Investigating the Connections Between Rotating Updrafts and Surface-Based Vorticity with New Theoretical Approach

By

Luke E. Odell

A dissertation submitted in partial fulfillment of the requirements for the degree of

Doctor of Philosophy

(Atmospheric Science)

at the

UNIVERSITY OF WISCONSIN-MADISON

2019

Date of final oral examination: 8/23/2019

The dissertation is approved by the following members of the Final Oral Committee:

Gregory J. Tripoli, Professor, Atmospheric Science
Jonathan E. Martin, Professor, Atmospheric Science
Michael C. Morgan, Professor, Atmospheric Science
Hart E. Posen, Professor, Business
Marcus L. Büker, Assistant Professor, Atmospheric Science
Leigh Orf, Research Scientist, Atmospheric Science

Investigating the Connections Between Rotating Updrafts and Surface-Based Vorticity with New Theoretical Approach

Luke E. Odell

Under the supervision of Professor Gregory J. Tripoli

At the University of Wisconsin-Madison

Abstract

Supercell tornadogenesis is a complex multi-scale atmospheric process involving the interaction of storm-generated and environmental flow and in particular, the interaction of their respective vorticity fields. A number of outstanding questions remain regarding the development and maintenance of rotation on the sub-storm scale during the evolution of a tornadic thunderstorm hampering our short-term predictability of tornadoes. Techniques currently used to study rotation in supercells are reviewed and, through application of research in fluid dynamics, new diagnostic technique is applied to study numerical simulations of supercells during tornadogenesis. Results from the analysis suggest a potentially important helical interaction between a supercell's outflow-generated baroclinic vorticity and low-level environmental streamwise vorticity in the storm's inflow layer, which is theorized to *dynamically couple* a supercell's updraft with surface-based baroclinic vorticity during tornadogenesis. The results of this work are discussed in the context of the current state of the atmospheric sciences and fluid dynamics literature and details of ongoing applications of the work to supercell tornadogenesis research are provided.

Aknowledgements

The research contributing to this dissertation involved significant departure from common progression for graduate work, which was motivated by my advisor Gregory Tripoli who always searches for the road less traveled. Professor Tripoli continually urged me to build from first principles, to find new scientific direction that could prove ground-breaking rather than build steadily in the direction of current literature. This approach is not easy and can be met with some resistance, in the words of my committee member Marcus Büker, "when breaking new ground, you will always hit some rocks". Despite this, the approach drove me to develop a deep, fundamental understanding of the dynamics of convective storms, which otherwise I do not believe I could have attained. This ultimately led to new approaches to studying the development of tornadoes in supercell thunderstorms that are presented in this dissertation and for that I whole-heartedly thank Professor Tripoli.

The road to completion of the degree was rife with academic challenges. Through this process, my committee members, Professors Jonathan Martin, Michael Morgan and Marcus Büker offered support and guidance to navigate me to reaching completion. Conversations with each Professor in the final months inspired me to keep going even in the toughest of times. To each I extend my gratitude. My sincere thanks also go out to Professor Matthew Hitchman, who was on the committee for several years. A number of highly stimulating conversations and regular words of support for my work provided boosts of motivation and morale throughout the research. I extend thanks to Professor Hart Posen of the Business School for stepping in at the last moment to replace Professor Philip Greenwood as my outside committee member.

Financial concerns during the latter stages of this research nearly prevented its completion but thanks to Professor Ankur Desai, who brought me on to work as mesoscale forecast support for the CHEESEHEAD field project at the very last minute, I was able to continue the dissertation research until conclusion. For this I am eternally grateful.

Pete “Poker Pete” Pokrandt is the most sought-after member of the Atmospheric and Oceanic Sciences department here at the University of Wisconsin-Madison. His technical expertise and willingness to always spare time to find a solution to your technical issues (even while on vacation) makes him well-worthy of his second nickname “Super Pete”. If I wasn’t running into a technical issue relating to numerical modeling or processing its output it was a highly unusual day. As in demand as he was, he’d always find the time to work to find a solution to the problem, for this I am very much in his debt.

Another technical wizard, Kelton Halbert, was a new graduate student in the Atmospheric and Oceanic Sciences department during the final year of my Ph.D. research. Kelton was an invaluable guide for the technical portions of the research and always spared time to help with running the CM1 model or post-processing the data from the simulations. I will always be grateful for the time he gave to me during the final few months.

I thank Dr. Leigh Orf for providing extremely high-resolution data for some of the analysis presented in this dissertation and for programming some of the new diagnostics developed through this research into the CM1 to allow comparisons with the UWNMS model data.

During my first few years as a graduate student, my office and research mate, Scott Trevorrow provided incredible support and guidance as well as daily stimulating and challenging conversation. Despite his departure to start a family and pursue a career, Scott frequently visited

to continue to help pursue the research that we were working on. His constant desire to help my research efforts provided a source of much needed discussion. I am extremely grateful for his help over the degree.

Another special mention goes out to Andrew Quigley, a junior undergraduate student who is currently pursuing a senior thesis in supercell dynamics with Professor Tripoli and I. His desire to learn and passion for the science has been apparent from day one. During the last 3 months of my dissertation research, Andrew provided incredible help with numerical modeling analysis that made many of the final plots possible. To him, I extend my thanks and best wishes for the future.

Outside of the Atmospheric and Oceanic Sciences department and from a more personal standpoint, I would like to extend thanks to Caity Dawson at the International Student Services here at UW-Madison. Caity and I met several times in the last 2 years of my graduate studies in a number of difficult circumstances. Caity was always extremely kind and supportive and did whatever she could to seek out assistance in each case. If it wasn't for some of the conversations and help that Caity provided, the last 2 years of my graduate studies would've been significantly more difficult.

In my personal life, my girlfriend Cathy Brunette was my rock for almost the entirety of my graduate studies. While this was assuredly not the best time to have met and developed a relationship with me, she was always there to give me the encouragement that I needed. Cathy is truly a kind-hearted soul and without her most loving support I am not sure what I would have done.

Living 5000 miles from home for almost 7 years is difficult even in the best of times. However, my parents, Amanda and Mark Odell, my grandparents, Shirley and Michael Odell

and my brother and sister, Sebastian and Ghislaine Odell provided whatever support they could from financial help to just lending an ear, their unwavering belief in me kept me going even when I thought I could not. I only hope the fruits of the labor will someday be able to provide for them in the same way they provided for me in my time of need.

Lastly, for their support throughout my graduate studies, there are a number of friends that deserve a special mention. First and foremost, Anthony "Panther" Wilcox, who has been a friend since I arrived in the U.S. for graduate school in 2013. During the following 6 years, he became much more like a brother to me and our frequent trips to chase storms constantly reinvigorated my passion for the science I present in this dissertation. The days of *Project Supercell* will always have a special place in my heart. Panther's absolutely insatiable desire to learn advanced supercell dynamics while jumping over years of fundamental physics in the process constantly kept me on my toes and drawing on napkins until the early hours of the morning. For his support, I am forever grateful. Another Mr. Wilcox not related to the first, Dane "Hondo" Wilcox, has been an incredible friend over the last few years, always making sure I feel at home even though I have been in such a new environment. His ornate sense of adventure has frequently provided much needed escape from the pressures of the degree. Adisen "Slim" Fenrich was an undergraduate who worked on her senior thesis with Professor Tripoli and I and was an extremely enthusiastic addition to the research. While her work was fantastic, it was her friendship and support during the last year that kept me pushing forward to finish this research. I wish her every success at Penn State in her own graduate studies. There was one friend from the United Kingdom who never let me forget my roots but who would remind me of the reason I was so far from home and constantly gave me the belief that I needed throughout my time as a graduate student, Tom "Pykey" Pyke. My god brother and friend since my day of birth, never

stopped providing encouragement and support despite not seeing each other for 3 or more years at a time. To develop a friendship like this means the world to me and I am truly grateful to him for all his support from so far away. Lastly, Tanner “String-Bean” Gibbs deserves my gratitude for his incredibly selfless attitude during a tough time in my life. I thank him from the bottom of my heart for his leveling and guiding conversations that led to a more positive outlook as I strove to finish this work.

TABLE OF CONTENTS

List of Acronyms

AGL – Above Ground Level
BRN – Bulk Richardson Number
CAPE – Convective Available Potential Energy
CFD – Computational Fluid Dynamics
CIN – Convective Inhibition
CM1 – Cloud Model 1
CM1-NOTOR – Cloud Model 1 NonTORnadic simulation
CM1-TOR – Cloud Model 1 TORnadic simulation
DPE – Dynamic Pipe Effect
DRC – Descending Reflectivity Core
EML – Elevated Mixed Layer
EL – Equilibrium Level
FFCB – Forward-Flank Convergence Boundary
FFDB – Forward-Flank Downdraft Boundary
FFD – Forward-Flank Downdraft
FFGF – Forward-Flank Gust Front
HP – High Precipitation
hPa – hecto-Pascals
LFC – Level of Free Convection
LCL – Lifting Condensation Level
LFCB – Left-Flank Convergence Bounday
LHS – Left-Hand-Side
LM – Left Moving (supercell)
LP – Low-Precipitation (supercell)
NOTOR – Non-tornadic NMS simulation
NMS – Nonhydrostatic Modeling System
RFD – Rear-Flank Downdraft
RFGF – Rear-Flank Gust Front
RHS – Right-Hand-Side
RM – Right-Moving (supercell)
SRH – Storm-Relative Helicity
SVC – Streamwise Vorticity Current
TDM – Triple Decomposition Method
TKE – Turbulence Kinetic Energy
TLV – Tornado-Like-Vortex
TOR-F – Tornado-like-vortex-Failure NMS simulation
TOR-S – Tornado-like-vortex-Success NMS simulation
TVS – Tornadic Vortex Signature
VPPGF – Vertical Perturbation Pressure Gradient Force
VORTEX2 – Verification of Rotation in Tornadoes Experiment
WK – Weisman-Klemp

List of Figures

List of Tables

Title	Description
Table 4.1	*UWNMS model configuration*
Table 4.2	*CM1 model configuration*

Chapter One: Introduction to supercells and overview of dissertation research

Part I. Introduction to supercell and tornado structure

1.1.1 Introduction

Despite their undisputed position as the most destructive form of middle-latitude deep moist convection, supercell thunderstorms are among nature's most breathtaking spectacles (Fig. 1.1). From a safe vantage point, the fortunate onlooker can witness the majesty of a deep, rotating cumulonimbus tower, the storm's mesocyclone (Fig. 1.2), twist up through the troposphere before crashing into the tropopause forming the "over-shooting top" and subsequently spreading out to form a large anvil of cirrus (Fig. 1.3). The incredibly varied cloud-scape that supercells produce draws "storm-chasers" from all over the world to the central Plains of the United States in the Spring where the greatest concentration of these storms occur (Fig. 1.4). The author of this dissertation frequently enjoys trips to the nation's most remote places to engage in a proverbial chess match with mother nature. The beauty and danger that this mesoscale phenomenon presents drives intense motivation to unlock the mysteries that they hold in their turbulent flows. Perhaps the most enigmatic feature of a supercell is the tornado (Fig. 1.5). Significant clues to their formation and persistence have been unearthed through a combination of theoretical, observational, and numerical work in the mesoscale atmospheric research community and yet a robust dynamical framework of their genesis continues to elude us. This dissertation presents the author's research of the dynamics of rotation in supercells during its tornadogenesis phase and aims to motivate intriguing new research direction in the

Figure 1.1: Supercell thunderstorm near Imperial, Nebraska on May 27, 2019 viewed from the south. Photo provided and permission for use provided by Scott Peake.

Figure 1.2: Supercell thunderstorm with clearly defined mesocyclone near Woodward, Oklahoma on April, 9, 2012. Photo provided and permission for use provided by Colt Forney.

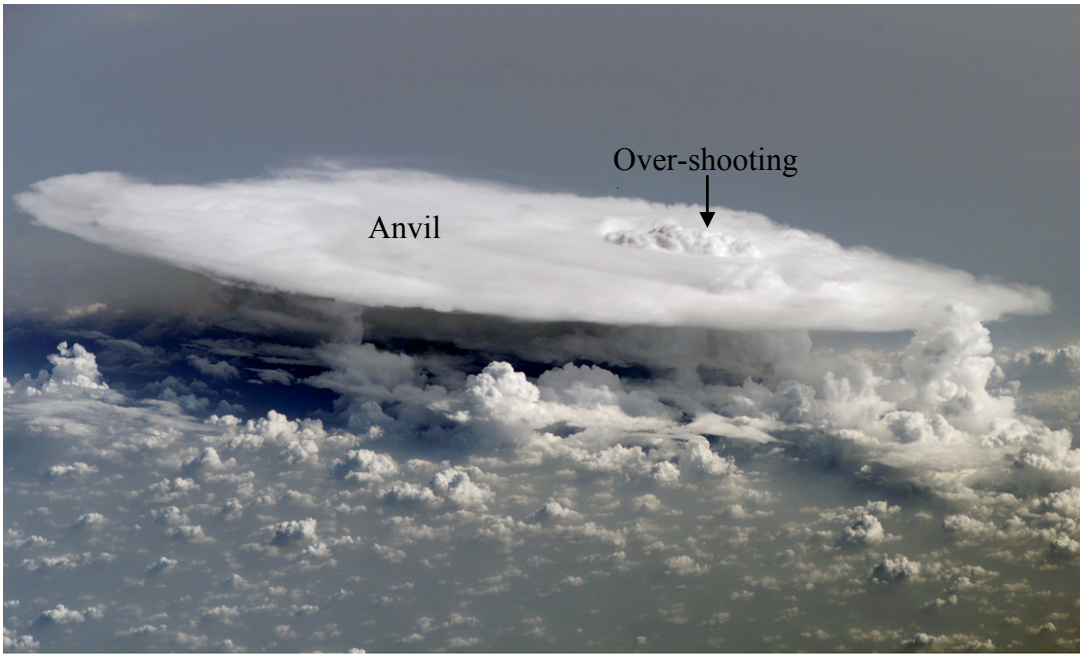

Figure 1.3: Supercell thunderstorm captured from the International Space Station. The overshooting top can be seen above the storm's updraft on the right side of a large anvil of cirrus spreading out downshear along the tropopause. Photo adapted from www.atmospheric-phenomena-ap.com. URL accessed at 22.30 UTC on August 7 2019.

Figure 1.4: Storm chasers on the side of the road viewing a supercell from the south-east. Photo and permission to use provided by Colt Forney.

study of supercell tornadogenesis. The following three sections are dedicated to describing the structure and features of a supercell and the supercell tornado to develop a basis from which to call upon throughout this document and to attempt to instill the same sense of awe for these storms that the author shares with vast numbers of scientists, storm-chasers and the public alike. Readers well-versed in basic supercell structure and dynamics will find these sections unnecessary to their overall understanding of this dissertation and are therefore encouraged to move on to parts two and three of this chapter, which layout research motivations and a dissertation roadmap respectively.

1.1.2 Supercell structure

One of the most visually recognizable structures of a supercell thunderstorm is the area of condensation that typically characterizes the base of its intense updraft known as the "wall cloud" (Figs. 1.6, 1.7). The wall cloud forms as rain falls out ahead of the storm and as it does so, evaporates into the air flowing into the incipient storm from downstream. The mixing ratio of these inflow air parcels increases and the temperature cools, bringing the air in the "forward-flank" region of the storm closer to saturation. As the air is lifted on its approach toward the updraft it often forms a "tail cloud" or "inflow band" that feeds into the storm's wall cloud where the inflow parcels are turned abruptly upward in the updraft (Fig. 1.1). Much of the storm's precipitation (including heavy rain and hail) falls in the forward-flank of the storm due to the strong vertical shear of the horizontal wind inherent in a supercell environment (see chapter two). Through water loading and evaporative cooling effects, a dominant downdraft and cold pool region is sustained *downshear* of the updraft in the forward-flank. A second, but not entirely

Figure 1.5: Large wedge tornado associated with a supercell near Tescott, Kansas on May 1, 2018. Photo and permission to use provided by Kirby, Wright (Top). Violent twin cyclonic tornadoes from a single supercell near Pilger, NE on June 16, 2014. Photo and permission to use provided by Kirby, Wright (Bottom).

Figure 1.6: Supercell with well-defined wall-cloud. Photo and permission to use provided by Colt Forney.

Figure 1.7: Supercell near Reed, Oklahoma on March 18, 2012 wall cloud, clear slot and tornado. Photo and permission to use provided by Colt Forney.

distinct cold pool region forms *upshear* of the updraft as the supercell's mid-level mesocyclone strengthens and advects precipitation upstream where it meets low equivalent-potential temperature (θ_e) air associated with the environment causing evaporation and cooling, which drives additional downdraft and cold pool development in the storm's "rear-flank" (refer to picture). Although classically, these two regions are distinct in models of supercell structure (Fig. 1.8), the author will often refer to the "outflow region" and "internal momentum surges" rather than distinguishing between rear- and forward-flank downdrafts (RFD and FFD respectively). The primary reason for this is that, in the author's modeling experience, downdrafts causing outflow momentum surging in the rear-flank may originate to the north and east (with respect to a cyclonically rotating supercell in the northern hemisphere) of the storm's updraft in what may be considered the forward-flank. That is, it is difficult to discern what constitutes a rear-flank and a forward-flank downdraft.

The outflow region of a supercell and in particular the sharp density gradients that are present internally and along its interface with environmental air have received substantial attention in the literature due to the prevalence of near-surface vorticity and convergence in these regions (returned to in more detail in chapter two). Where diverging air in the outflow region meets the relatively high θ_e air of the environment, a sharp wind shift and density gradient results, which are referred to as "gust fronts". The major gust fronts that form upshear and downshear of the rotating updraft are known as the rear-flank and forward-flank gust fronts (RFGF, FFGF) respectively. The RFGF tends to be the sharper, more distinctive boundary, while the FFGF tends to be more diffuse due to the relative θ_e differences between the regions of the outflow. *Internal* outflow convergence boundaries characteristically similar to the RFGF and FFGF form in response to internal (outflow) momentum surges. It has been shown that the

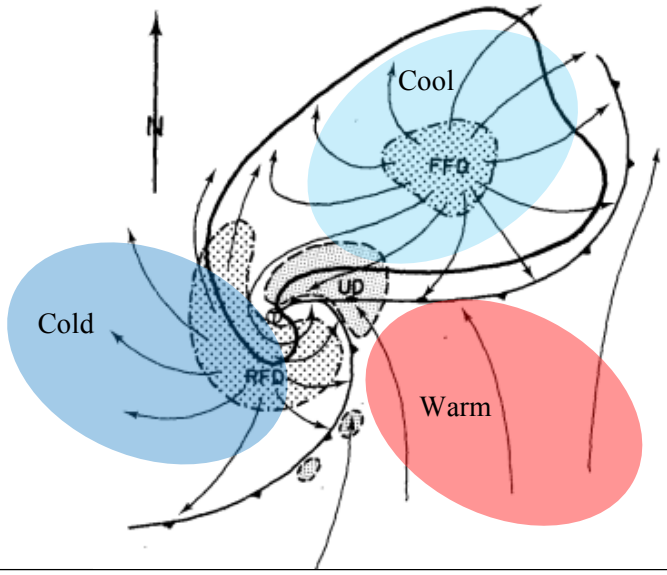

Figure 1.8: Conceptual model of a classic, right-moving supercell adapted from Lemon and Doswell, 1979. Arrows represent flow streamlines, lines with triangles indicate surface gust fronts, dark black bean-shaped contour indicates radar reflectivity and stippled and shaded regions represent the relative positions and structure of the forward-flank downdraft (FFD), rear-flank downdraft (RFD) and updraft (UD). The typical location of a supercell tornado (when present) is marked by a 'T'. Transparent colored ovals indicate relative temperature of the air around the supercell, where warmer colors are associated with warmer surface temperatures.

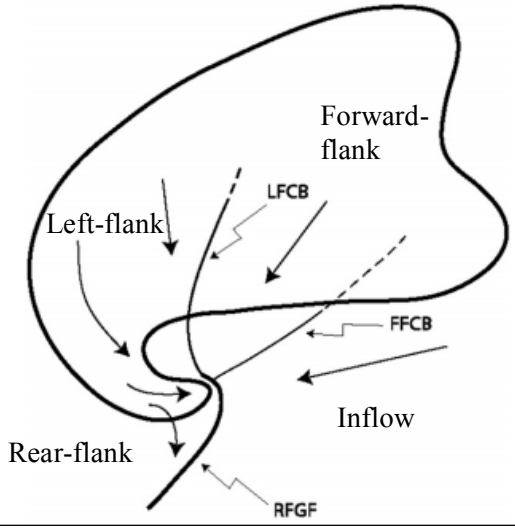

Figure 1.9: Steady state conceptual model of surface convergence boundaries in a RM supercell thunderstorm adapted from Beck and Weiss (2013). As in Fig. 1.8, bean-shaped black contour represents radar reflectivity. The remaining contours denote locations of surface-based convergence boundaries where the weight of the contour determines typical strength of convergence in these zones, dashed contours indicate that convergence becomes vanishingly weak along them. Arrows represent typical streamline pattern of near-surface flow.

dominant positions of the primary convergence boundaries associated with a supercell's outflow are out ahead of the storm's updraft, known as the forward-flank convergence boundary (FFCB; Fig. 1.9), along the RFGF and more transiently to the north of the updraft in what has recently been referred to as the storm's left flank convergence boundary (LFCB). Beck and Weiss (2013) introduced the term 'convergence boundary' to describe these regions of sharp density gradients in the left- and forward-flanks because there tend to be much less-well pronounced wind shifts across these regions compared with the RFGF and so do not always meet the criteria for the term "gust front". These 'boundaries' are in a constant state of flux as precipitation-generated downdraft surges and updraft-driven inflow acceleration continually modulate their structure, position and intensity.

Much of early supercell structural theory relied on visual clues such as those that may be afforded by the photographs in the preceding pages. Wegener (1928) termed the rotating storms as "mother whirls" that arose from the interaction of baroclinically-generated vorticity in the forward region of the supercell with environmental wind shear (Dahl, 2005). Brooks (1949) later indicated that tornadic supercells are made up of a "tornado cyclone" embedded in a larger scale vortex associated with the storm's updraft. More detailed structural insight was gained when supercells were first seen on radar in the early 1950's. The primary supercell features were then readily identified using radar reflectivity (Fig. 1.10). It was at this time the term "hook echo" was first used to describe the reflectivity appendage that develops upshear of the updraft in the storm's rear-flank due to storm rotation advecting precipitation upstream (Stout and Huff, 1953; Fujita, 1958; c. Dahl, 2005). Around this time, the first models of airflow through a supercell were developed by Browning (1964) and Fujita (1965) (Fig. 1.11). These models indicate that high-θ_e air enters the storm's updraft at low levels from downshear, rises almost vertically to

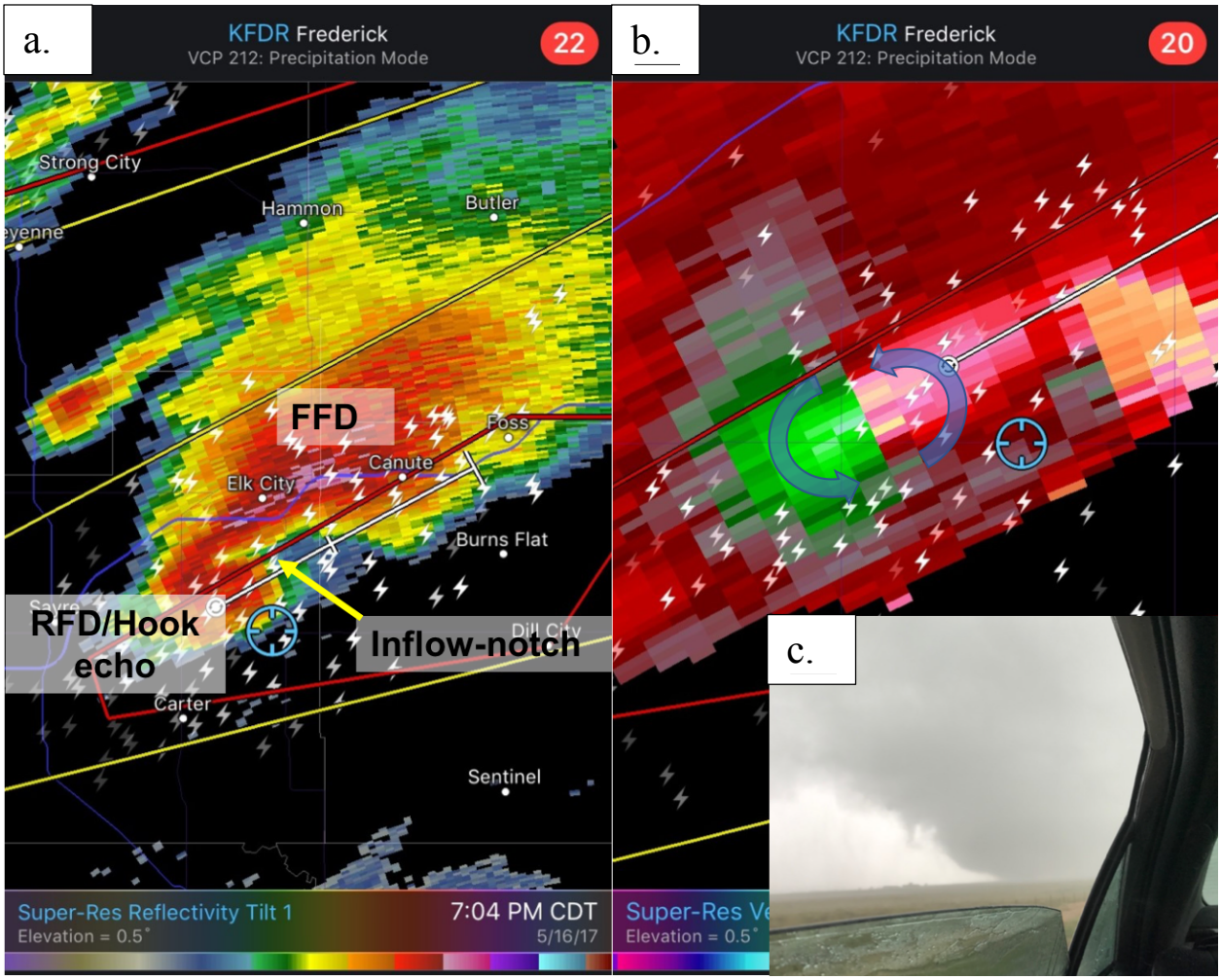

Figure 1.10: Radar imagery from a tornadic supercell thunderstorm near Elk City, Oklahoma on May 16, 2017 captured during a storm chase by the author. In the top-left panel (a) radar reflectivity is displayed over a local road map of the area with annotations to demonstrate the FFD, RFD and hook echo and inflowing air which causes an "inflow-notch" in the reflectivity. Bright colors near Elk City indicate very heavy rain and hail. In the top-right panel (b) horizontal velocities calculated using doppler radar are colored, greens indicate precipitation moving toward the radar while reds indicate precipitation moving away from the radar. Where the colors become brighter the velocities are greater and the variation of color from green to red is indicative of rotation about the vertical axis, blue arrows demonstrate the nature of this rotation. In both panels, (a) and (b), the blue circle signifies the author's location at the time of the radar image. Image inset on the bottom-right (c) is a screen-grab image of a tornado from the window of our vehicle at the time that panel (b) was captured. This tornado eventually went on to produce substantial damage in Elk City, Oklahoma.

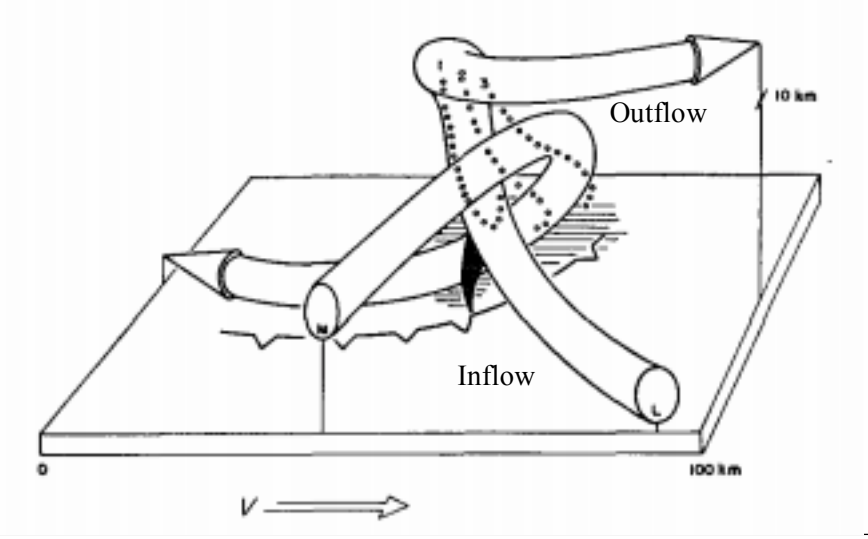

Figure 1.11: Browning (1964) three-dimensional airflow model through a supercell. Large arrows indicate quasi-steady updraft and downdraft circulations, where the updraft circulation begins with low-level inflow from the bottom right corner of the figure and exits to the right at upper-levels and the downdraft circulation begins at mid-levels and rotates cyclonically around the updraft airstream to the surface and exits to the left of the diagram. Surface frontal zone is denoted by black line with triangles.

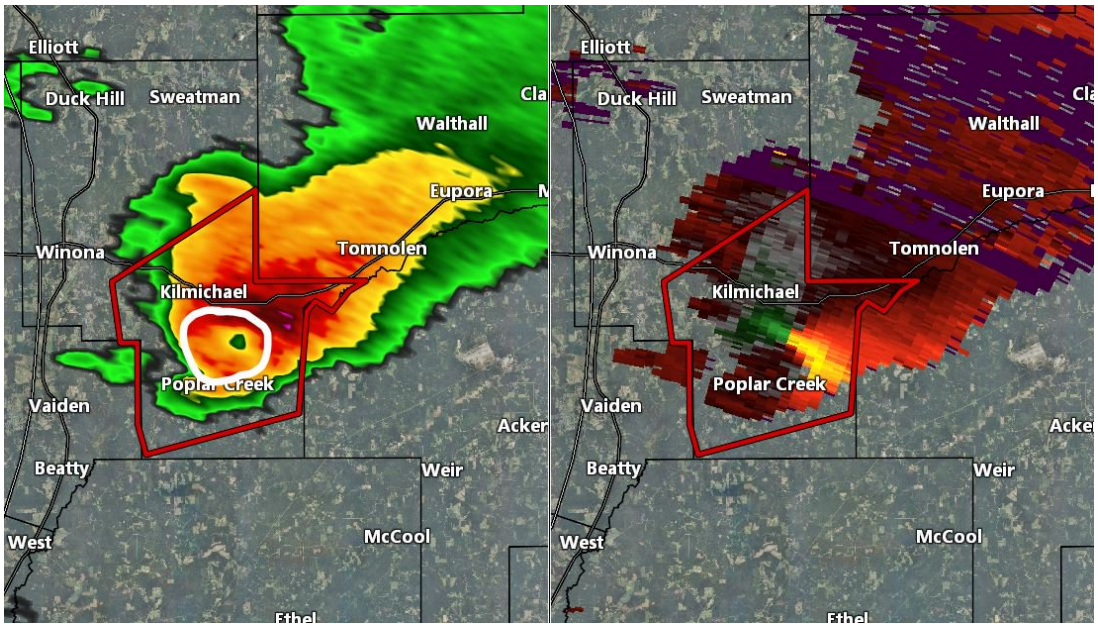

Figure 1.12: Bounded weak echo region (BWER) in radar reflectivity associated with mesocyclone rotation. White circle on left panel indicates the BWER. Permission to use given by Ari Salasari.

upper levels of the troposphere and flows outward in a downshear-direction again near the tropopause. Mid-level flow from upshear interacts with the storm's mesocyclone and precipitation regions and descends to the surface out ahead and in an arc around the storm's updraft. Following these models, Lemon and Doswell (1979) used radar and surface-based data to develop their seminal conceptual model of a supercell (Fig. 1.8).

The advent of an organized radar system in the United States during the 1970's and addition of doppler capabilities in the late 1980's enabled the National Weather Service (NWS) to remotely analyze rotation and other supercell characteristics in convective storms. This also led to the detection of certain distinguishing features of a *tornadic* supercell such as the Tornadic Vortex Signature (TVS), which is typically seen at mid-levels prior to tornado development (e.g. Lemon et al. 1978). In addition to the fixed WSR-88D radar network, mobile doppler radars (DOWs; e.g. Bluestein et al. 2007) were built for research purposes, capable of detecting finer-scale structures within a supercell and are increasingly used in field projects such as the recent Verification Of Rotation and Tornadoes EXperiment-2 (VORTEX2; Wurman et al. 2012) aimed at observing the evolution of rotation in supercell thunderstorms.

1.1.3 Supercell characteristics

Supercells can be described as quasi-steady, unicellular propagating convective storms. What distinguishes them from more common, ordinary single cell and multicell thunderstorms is their deep rotating updraft or *mesocyclone*. Unlike other cellular convection, supercells are able to reach a quasi-steady state due to the mesocyclone, a component of the flow associated with which becomes *inertially* (cyclostrophically; see chapter three) balanced. The inertially-balanced

component of the storm's updraft arises due to the correlation of vertical vorticity and vertical velocity enabling the storm to maintain a dynamic pressure minimum aloft (e.g. Klemp and Rotunno, 1983; Rotunno and Klemp, 1985; Markowski and Richardson, 2011, pp. 27; Bluestein, 2013, pp. 216; Eq. 1).

$$\alpha_0 \nabla^2 p' = -\left[\left(\frac{\partial u}{\partial x}\right)^2 + \left(\frac{\partial v}{\partial y}\right)^2 + \left(\frac{\partial w}{\partial z}\right)^2\right] - 2\left(\frac{\partial v}{\partial x}\frac{\partial u}{\partial y} + \frac{\partial w}{\partial x}\frac{\partial u}{\partial z} + \frac{\partial w}{\partial y}\frac{\partial v}{\partial z}\right) + \frac{\partial B}{\partial z} + f\zeta - \beta u \qquad 1.1$$

Where α_0 is the inverse of the reference state density, $\nabla^2 p'$ is the Laplacian of the perturbation pressure field, u, v and w are zonal, meridional and vertical components of velocity respectively, B is buoyancy, f is the Coriolis effect, ζ is relative vertical vorticity and β is the meridional gradient of the Coriolis effect. Eq. 1.1 is known as the (inviscid) *divergence equation* or the *diagnostic pressure equation* and is formed by taking the three-dimensional divergence of the momentum equation. The first six terms on the right-hand-side (rhs) of Eq. 1.1 are associated with inertial (dynamic) effects, the third term from the end of the rhs is associated with buoyancy effects and the last two terms are associated with Coriolis effects, which may be neglected for the purpose of studying rotation on the scale of a supercell. For well-behaved fields, $\nabla^2 p' \propto -p'$, neglecting Coriolis effects, Eq. 1.1 can be rewritten:

$$p' = e^2{}_{ij} - \frac{1}{2}|\omega|^2 - \frac{\partial B}{\partial z} \qquad 1.2$$

In Eq. 1.2 $e^2{}_{ij}$ is the square total three-dimensional deformation tensor and $|\omega|^2$ is the square of the total three-dimensional vorticity (this equation will be discussed further in chapter three). The first two terms on the rhs of Eq. 1.2 are associated with dynamic effects, where deformation is associated with local perturbation pressure maxima and vorticity is associated with local perturbation pressure minima. The dynamic pressure minimum associated with rotation aloft

generates an upward-directed vertical perturbation pressure gradient force (VPPGF; e.g. Rotunno and Klemp, 1982) allowing the storm to *dynamically* lift conditionally unstable air to its level of free convection and sustain its updraft (the concept of "dynamic lift" is returned to in later sections). The dynamics associated with the development of mid-level rotation of a supercell with be further discussed in chapter two.

The centrifugal force associated with the storm's rotating mesocyclone produces an outward-directed radial acceleration of precipitation in the updraft leading to a bounded weak echo region (BWER) in radar reflectivity at mid-levels (Fig. 1.12). The precipitation distribution around the updraft is a function of the environmental wind shear and the intensity of the mesocyclone. The interaction of precipitation with the environment leads to cold pool generation and outflow-driven convergence boundaries (Fig. 1.9). The amount and distribution of precipitation associated with the storm determines the visibility of the base of the storm. Low-precipitation (LP) supercells (Fig. 1.13), which tend to form in in environments with drier lower-troposphere's, are almost free of any precipitation at the updraft base and in the rear-flank. This can lead to visually stunning views of the structure of the storm's rotating updraft. These storms are not often characterized by wall clouds under the updraft due to the lack of precipitation associated with them and they rarely produce tornadoes (Moller et al. 1994). High-precipitation (HP) supercells (Fig. 1.14) are characterized by large amounts of precipitation in both the forward- and rear-flanks, which visually obscures most of the base of the storm's updraft. Tornadoes occur more frequently in these storms and are particularly dangerous because they often become shrouded in rain (rain-wrapped) preventing any visual confirmation that a tornado is on the ground. Classic supercells (Fig. 1.15) are the most prevalent tornado-producers. This class of supercell is often what storm chasers desire to witness as their updraft-bases tend to be

Figure 1.13: Low-precipitation (LP) supercell near Northfield, Texas on 23 May 2016. Photo and permission to use provided by Colt Forney.

Figure 1.14: Examples of high-precipitation (HP) supercells. Top photo taken near Tescott, Kansas on May 1, 2018 approximately an hour before the storm produced a ¾ of a mile-wide wedge tornado (Fig. 1.5), photo and permission to use provided by Kirby Wright. Bottom photo taken near Kingfisher, Oklahoma on May 29, 2012 as the supercell underwent a transition from classic structure to HP structure. Photo and permission to use provided by Alex Goldstein.

Figure 1.15: Examples of classic supercells. Top photo taken near Fairdale, Illinois on April 9, 2015 as a supercell and violent "wedge" tornado approached the highway from the west. Photo and permission for use provided by Walker Ashley. Bottom photo taken near Dodge City, Kansas on May 24, 2016 as a cyclic tornado-producing supercell had one tornado on the ground and began to develop a new tornado to its east associated with a new wall-cloud and low-level mesocyclone. Photo and permission for use provided by Alex Goldstein.

free from rain allowing the onlooker to witness the evolution of the storm's rotation and possible tornado formation.

1.1.4 Tornado structure

While supercell structure is readily diagnosed using a variety of remote sensing techniques and visual observations, diagnosing the structure of the tornado vortex, due to its relative scale, has relied primarily on laboratory experiments (e.g. Ward, 1972; Church et al. 1977; 1979), numerical simulation (e.g. Rotunno, 1979; Trapp and Fiedler, 1995; Lewellen et al. 1997; Fiedler, 2009; Nolan et al. 2017) and theroretical fluid dynamics (e.g. Lewellen, 1976; Fiedler and Rotunno, 1986; Lewellen and Lewellen, 2007; Rotunno, 2013). The structure of the tornado vortex is determined by its *swirl ratio* (Eq. 1.3).

$$S \equiv \Gamma^* r^* / m^* \qquad 1.3$$

In Eq. 1.3, Γ^* is the angular momentum of the vortex, r^* is the core width of the vortex and m^* is mass flux through the vortex. The swirl ratio is a non-dimensional parameter, which measures the ratio of the circulation (azimuthal flow) of the vortex to the volume flow rate of the updraft (Bluestein, 2013, pp. 392). With the right swirl ratio an optimal state for a *one-celled* vortex can be achieved as depicted in Fig. 1.16. Variations in the swirl ratio driven by the supercell's local environment and internal storm dynamics lead to variations in the structure of a tornado (Fig. 1.17; Davies-Jones, 1986; Davies-Jones et al. 2001; Bluestein, 2013, pp. 394). Low-swirl favors a one-celled tornadoes, whereas in high-swirl cases a strong central pressure deficit produces a downdraft at the tornadoes center and leads to vortex breakdown into multiple vortices.

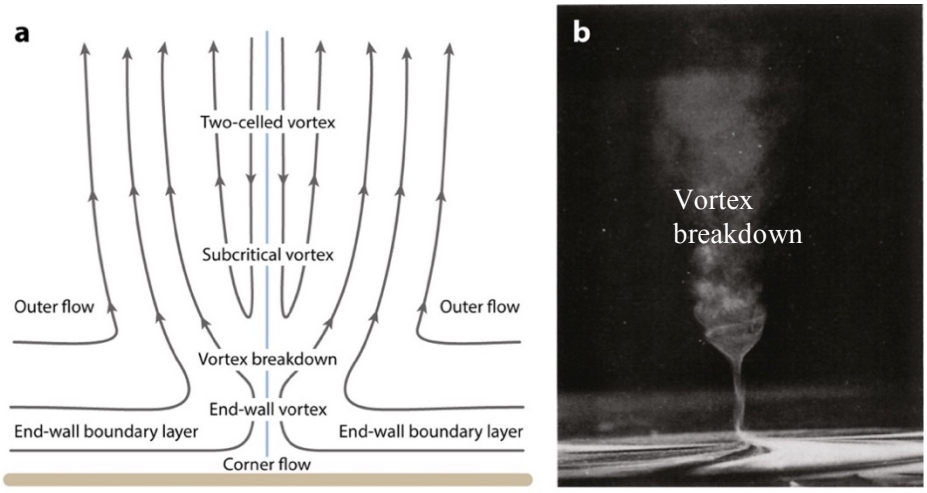

Figure 1.16: Idealized model of a one-celled vortex (a) and Ward tornado chamber laboratory experiment of a one-cell vortex (b). Figure adapted from Rotunno (2013) and reproduced with permission from Journal of Fluid Mechanics.

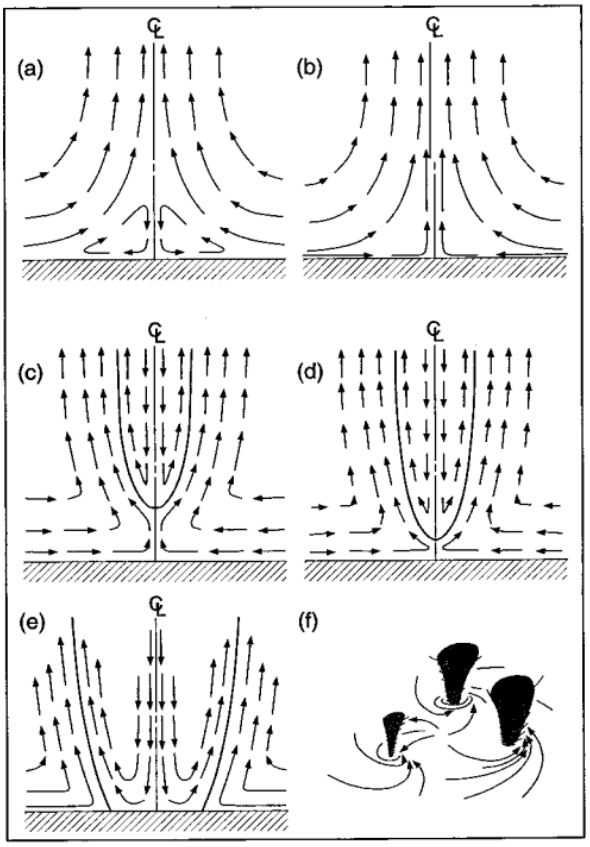

Figure 1.17: Effects of increasing swirl ratio of the structure of tornadoes. Arrows represent airflow within a tornado, C_L denotes the tornadoes center. Swirl ratio increases from (a) to (f). As the swirl ratio increases so does tendency for the vortex to develop a central downdraft, which eventually causes a transition from a one-cell to a two-cell tornado. As the swirl ratio further increases the vortex breaks down into multiple smaller vortices as is typical with a "multi-vortex" tornado (f). Figure adapted from Davies-Jones et al. (2001)

The structure of an idealized one-celled tornado vortex has an "inertial layer" of inflowing air, which is nearly laminar and can be approximated to be inviscid and is characterized by relatively low swirling motion (Fig. 1.18). Beneath this is the friction layer, which is in direct contact with the ground and is highly viscous with no swirling motion. Collectively these two layers are known as the tornado's *boundary layer*, which may be as little as 10 m in depth (Bluestein, 2013, pp.). Inflowing air in the inertial region makes an abrupt turn upwards at the base of the vortex in the "corner flow region", erupting vertically upward as a Bernoulli-driven jet (e.g. Davies-Jones, 2015; section 2.2.3b). Above this is the "core region" of the tornado, in which angular momentum (Γ) increases outward with radius and has strong swirling motion. Radially outward from the core region is the "outer flow region", which is characterized by strong swirling motion but by constant angular momentum with radius. The study of the structure of a tornado is a research area in its own right and so the reader is referred to Rotunno (2013) and references therein for more detailed theory.

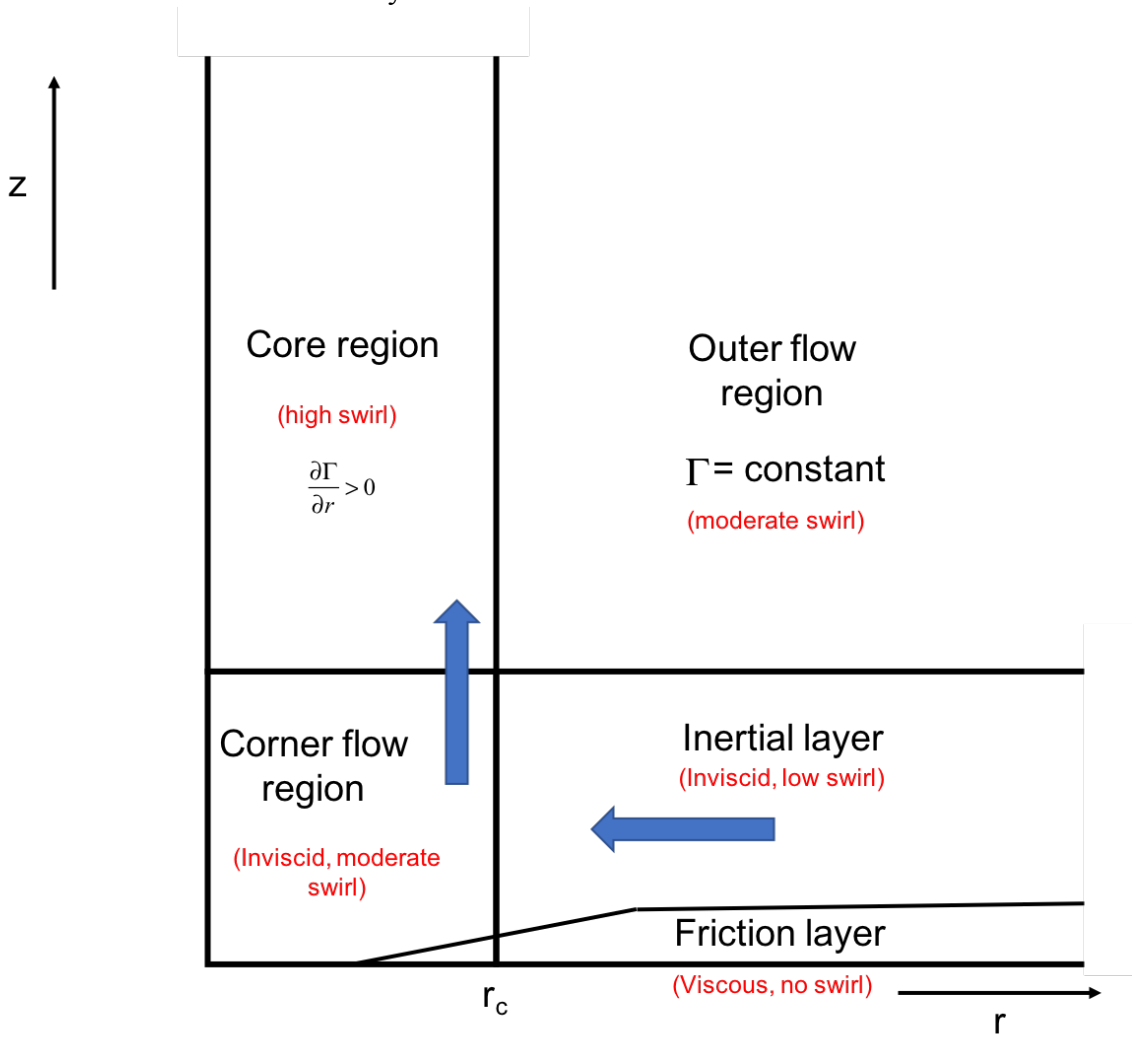

Figure 1.18: Idealized diagram of a one-celled tornado vortex adapted from Bluestein (2013). 'z' is height, 'r' is radius and 'r_c' is the core radius of the tornado. Each region is labeled and a sense of the strength of the swirling motion is given.

Part II. Research motivation

1.2.1 Summary

Supercell's are responsible for nearly all significant (>EF2 strength; Doswell et al. 2009) tornadoes on earth (Wurman et al. 2012) and, each year in the United States, tornadoes routinely rank among the costliest and deadliest of natural disasters (e.g. Boruff et al. 2003). Decades of research, installation and subsequent improvement of the WSR-88D radar network across the country has steadily improved our probability of detecting tornadoes and the warning lead time afforded to the public (Fig. 1.19; Wurman et al. 2012).

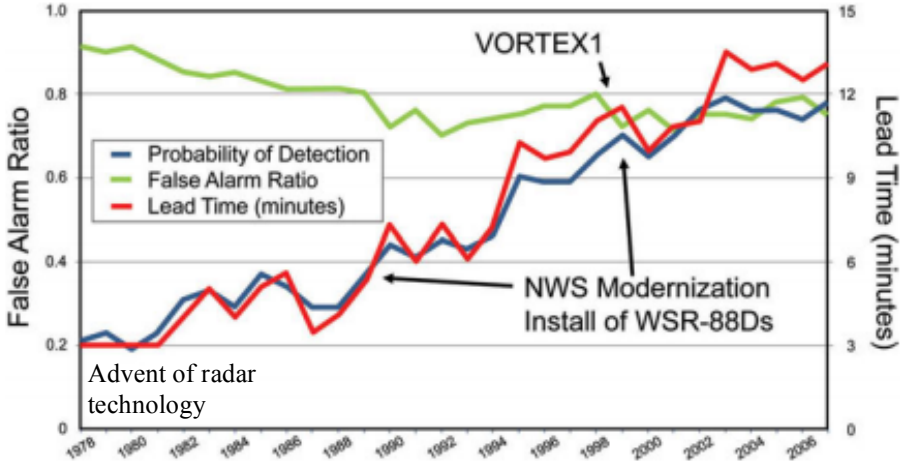

Figure 1.19: Trends in probability of detection (blue line), false alarm ratio (green line) and lead time (red line) over the last half-century. Clear improvements have been made in detecting tornadoes and length of lead time, while our false alarm ratio has remained nearly steady for the entire analysis period. Figure adapted from Wurman

Our false alarm ratio (FAR) has, however, remained nearly constant at 0.75 for the last 30 years (Barnes and Gruntfest, 2007; Brotzge et al. 2011). It is perhaps not all too coincidental that approximately only 25% of supercells are tornadic (Trapp et al. 2005). Despite improvements in our observational and model capabilities alongside a wealth of research, which has helped

develop parameters used in short-term forecasts to distinguish between tornadic and nontornadic environments (e.g. Doswell, 1991; Edwards and Thompson, 2000; Thompson and Edwards, 2000; Rasmussen, 2003, Grams et al. 2012), our short-term predictability of tornadogenesis remains poor. Recent analysis of the Storm Prediction Center's (SPC's) performance indicates that tornadoes remain the least well-predicted hazard associated with severe thunderstorms (Herman et al. 2018). Potential short-comings in our ability to predict and detect supercell tornadogenesis that result in high false alarm rates arise from an incomplete understanding of the dynamics associated with tornadogenesis, insufficiencies in our observational network and operational numerical weather prediction models. With an incomplete understanding of supercell tornadogenesis, operational forecasters rely on empirical connections between atmospheric environments and tornadic storms that often fail to discriminate between storms that do and storms that do not produce tornadoes in similar environments. While our short-term predictability of tornadogenesis in supercells is likely hampered by our ability to observe storm-scale processes in real-time, it is imperative that we develop a complete dynamical framework of tornadogenesis in order to improve our observational capabilities in a targeted manner.

It is evident that supercell tornadogenesis is strongly modulated by the atmospheric environment in which a storm evolves (e.g. Thompson et al. 2012) and yet it is also apparent that the process is somewhat stochastic and can occur in sub-optimal environments (Anderson-Frey et al. 2016; Coffer et al. 2017). The lack of a complete dynamical framework by which a supercell generates a tornado leads to difficulties in predicting how a supercell will respond to its local mesoscale environment and in detecting precursors to genesis of tornadoes operationally. Additionally, field campaigns targeting close-range observations of tornadogenesis are significantly benefitted by a knowledge of what to focus on during the storm's evolution. Model

representations of tornadic and nontornadic supercells are a powerful way to approach the outstanding questions related to the dynamics of tornadogenesis. It is, however, important to have a strong theoretical basis from which to work from when analyzing supercell simulations and to subsequently verify results with observations. The approach of the current work is to apply recent theoretical advancements in the study of rotational flow to the evolution of rotation in simulated supercell thunderstorms in order to illuminate key *coherent rotational structures*[1] involved in connections between the rotating updraft tornadogenesis. The ultimate goal is to confirm the presence and importance of these structures with direct observation.

[1]The term "coherent rotational structure" refers to connected fluid regions that are accompanied by a local pressure minimum, in which fluid rotates about a central axis. Although "vortex" could be used in place of "rotational" the author opts for this terminology because the term "vortex" is often used quite restrictively in the Atmospheric Sciences literature implying flow in cyclostrophic (or more generally, inertial) balance with the pressure field. In the physical atmosphere no vortex is ever truly in inertial balance and there are varying degrees to which a fluid region may be approximated to such an idealized state. Thus, "rotational" is more inclusive to all fluid regions that exhibit rotation or *swirling motion*.

1.2.2 Sustained updraft interaction with surface-based vorticity

Intensive theoretical, numerical, and observational research efforts during the last several decades have helped identify particular thermodynamic and kinematic characteristics of atmospheric environments more favorable for generating and sustaining low-level rotation (mesocyclones) and tornadoes in supercells (e.g. Klemp and Rotunno, 1983; Davies-Jones and Brooks, 1993; Wicker and Wilhelmson, 1995; Alderman et al., 1999; Markowski et al. 2012a,b; Dahl et al. 2014). As a result, our knowledge of the way *subtornadic* vertical vorticity is generated underneath supercells has increased markedly (the dynamics associated with which are discussed in detail in chapter two). However, environments that are generally thought to be favorable for tornadic storms have been found to produce a spectrum of tornadic and nontornadic supercells observationally and numerically (e.g. Coffer et al. 2017). Additionally, a wide-range of observational evidence suggests that almost all surface-based supercells have ample subtornadic vertical vorticity necessary for tornadogenesis and yet the significant majority fail to produce tornadoes (Coffer and Parker, 2015; 2017; 2018; Coffer et al. 2017).

Growing evidence suggests significant supercell tornadoes are favored in storms that can utilize surface-based vertical vorticity by generating and sustaining *low-level mesocyclones* that provide dynamic lifting of vorticity-rich outflow air (e.g. Markowski and Richardson, 2014; Coffer and Parker, 2015; 2018). ‘Dynamic’ lifting is distinguished from ‘buoyancy’ or more general ‘thermodynamic’ lifting in that the pressure-gradient forces responsible for the vertical accelerations are associated with inertia. Such inertia-driven lift includes rotational and deformational effects (which are covered in more detail in chapter three). Rotation is associated with a local perturbation pressure minimum and so if rotation increases with height above the

ground, such as underneath a low-level mesocyclone in a supercell, an upward-directed pressure gradient (VPPGF) provides a source of dynamic lift (e.g. Markowski and Richardson, 2014). Deformation is associated with a local perturbation pressure maximum and so if deformation increases toward the ground, such as is found along the leading edge of an outflow momentum surge, there is also an upward-directed VPPGF that provides a source of lift (e.g. Robertson, 2017). Both are known to be important sources of dynamic lift of low-level vorticity-rich air but the presence of sustained low-level mesocyclones and outflow surges are insufficient conditions for tornadogenesis (Brandes and Ziegler, 1993; Trapp, 1999; Markowski et al. 2011).

Despite this, Coffer and Parker (2018) concluded for the VORTEX2 field campaign sounding dataset (Wurman et al. 2012; Parker, 2014) that the lower-tropospheric wind profile was the greatest environmental discriminator between storms with ample surface-based, subtornadic, mesocyclonic-scale vertical vorticity that fail to contract and intensify rotation to tornado scale and those that do. They concluded that the wind profile modulated the intensity of the low-level mesocyclones in their simulated storms, which in turn modulated the strength of the dynamic lift of low-level vorticity-rich outflow air. The mechanisms by which the scale contraction between mesocyclone and tornado scale occurs are not well understood. It is of critical importance to improving the forecasting of supercell tornadoes to investigate the dynamical mechanisms by which the supercell updraft locally strengthens at low-levels prior to tornadogenesis causing an organization and intensification of surface-based vorticity on the tornado (miso) scale.

Technological advancements in high-performance computing has recently allowed the production of extremely high-resolution simulations of supercell thunderstorms that can help bridge the gap in knowledge of the processes on sub-mesocyclonic scales leading to low-level

updraft and vorticity intensification by explicitly resolving vortices involved in tornadogenesis. Orf et al. (2017) identified a *Streamwise Vorticity Current* (SVC) as an important helical, rotational misoscale structure in their high-resolution simulation of a violently tornadic supercell. The intensification of this feature appears to be linked to tornadogenesis through an increase in streamwise vorticity ingested by the low-level updraft. This is known to lead to an extraction of energy from the mean flow (Lily, 1986*a,b*; Brandes et al. 1988) and appears to be related to the intensification of the low-level updraft prior to tornadogenesis. Investigating dynamic, thermodynamic and microphysical processes associated with miso-vortex structures such as the SVC provides a promising direction to improve our dynamical understanding and short-term prediction of supercell tornadogenesis.

Throughout the research that contributed to this dissertation, the author has been motivated to develop better theoretical understanding of how the rotating updraft establishes a connection with vorticity that is rooted at the earth's surface. This intrigue has arisen through a lack of satisfaction with current explanations provided in the literature. It is popular to hear phrases such as "get enough vorticity underneath a strong enough updraft and it will be converged and stretched into a tornado". While the sentiment is not incorrect, a supercell tornado distinguishes itself from its non-mesocyclonic counterparts by its incredible potential intensity and methodical (non-random) development. Why some supercells produce tornadoes and others do not is still a burning question in supercell research and one which motivates this dissertation. Supercell tornadogenesis appears to be something of an *instability* in the storm's lifecycle, which once occurs, sets into motion a rapid structure and intensity change in the low-level vorticity field. In the author's experience, while it is possible that the timing of this instability is governed

by chaos, the evolution to a mature tornado vortex from the point of the instability appears to be far from it.

Part III. Approach and roadmap

1.3.1 Research models

Numerical modeling of supercells is an essential component of supercell tornadogenesis research. This approach affords the user the ability to analyze storm evolution at timescales not possible through observation. It is often not viable to test the veracity of new theoretical work using observations of real-world supercells alone. If theory can be confirmed through numerical analysis, methodology to detect components of the theory in the real-world can be developed more precisely. In order to produce physically-realistic realizations of supercell thunderstorms using a numerical model specific physics and microphysical requirements must be met that can adequately account for moist convective atmospheric processes (Bryan and Fritsch, 2002; Bryan et al. 2003). Two such models were used in this research, the specifications of which are outlined below.

a. University of Wisconsin-Nonhydrostatic Modeling System (UW-NMS)

The author has been fortunate enough at the University of Wisconsin-Madison to have been advised by one of the pioneers of nonhydrostatic numerical modeling for the purpose of studying moist convective processes. Professor Gregory J. Tripoli developed the University of Wisconsin-Nonhydrostatic Modeling System (NMS) with the intention of capturing the complex

interaction of atmospheric scales fundamental to convective weather systems (Tripoli, 1992). The NMS was built to resist the problem of nonlinear instability or 'numerical enstrophy cascade' (Sadorny, 1975) on the sub-grid scale through the implementation of an enstrophy conserving scheme. Enstrophy is the integral square of the vorticity field (Eq. 1.4) and its conservation in a numerical model prevents un-physical turbulence kinetic energy (TKE) dissipation on the sub-grid scale.

$$\varepsilon(\omega) \equiv \int_S |\omega|^2 dS \qquad 1.4$$

In Eq. 1.4 ε is enstrophy and S is an arbitrary surface. In addition, a fully three-dimensional form of the Lamb vector (Tripoli and Smith, 2014) serves as the basis for the dynamical formulation of the NMS. Combined with a three-dimensional extension of finite differencing techniques originally developed by Arakawa and Lamb (1981), this constrains the system against unphysical enstrophy production resulting from truncation error (Tripoli and Smith 2014). This makes the NMS uniquely capable of resolving three-dimensional vortex structures and interactions among numerical models used in mesoscale atmospheric research.

The NMS is a quasi-compressible, nonhydrostatic atmospheric model with a 2-moment bulk microphysics scheme and a 1.5-level turbulence closure and uses a three-dimensional Cartesian coordinate system. Additional information and the governing equations for the NMS can be found in Tripoli (1992) and in Tripoli and Smith (2014). In the current research, the NMS is employed in a nested-grid, full-physics format for horizontally-homogeneous idealized supercell simulations. All simulations presented in this dissertation make the use of two nested grids (three total grids) with 120 m horizontal resolution on the inner grid. More information on the specific model set-up can be found in chapter four.

b. Cloud Model 1 (CM1)

The most prominently used numerical research model in mesoscale dynamics is the Cloud Model 1 (CM1; Bryan, 2002; Bryan and Fritsch, 2002). The CM1 is a compressible, nonhydrostatic model using a split-time step technique to solve terms associated with acoustic fluctuations following Klemp and Wilhelmson (1978). As opposed to a nested-grid approach used by the NMS, the CM1 utilizes an inner and outer mesh with a stretching function (Wilhemson and Chen, 1982) between the two allowing for smoothly varying grid resolution. Inter-model comparison between the CM1 and the NMS is used herein to confirm the veracity of the numerical results. However, the CM1 is used much less frequently and so the reader is referred to Bryan and Fritsch (2002) and Fanelli and Bannon (2005) for more detailed information on the model design and its applications.

1.3.2 Roadmap

Ultimately, for a supercell to produce a tornado, updraft acceleration must be sustained at very low-levels to converge and stretch vorticity until it reaches tornadic strength. The focus of the current work is to illuminate misoscale rotational storm structures, through the use of new theoretical approach, that appear to be involved in a 'helical coupling' between a supercell's buoyantly-driven rotating updraft and outflow-generated, *surface-based* vorticity. It is shown that current tools used to study such coherent rotational structures in supercell research are insufficient for the analysis of such structures and so new diagnostics are developed from the fundamental fluid dynamics governing rotational motion in the atmosphere. A new conceptual model of supercell tornadogenesis is presented through studying the evolution of rotational

structures with these diagnostics to numerous numerical simulations of supercells with the research models outlined in section 1.3.1. Preliminary insight and assertions into the dynamical process and environmental controls associated with the model are discussed in the conclusions of this dissertation. Ongoing research efforts hope to isolate specific dynamical mechanisms by which this interaction takes place and to decipher more favorable storm environments capable of supporting such a sustained helical coupling.

This dissertation is separated into four subsequent chapters as follows:

Detailed review of relevant supercell and supercell tornadogenesis literature to date can be found in chapter two. This includes fundamental supercell dynamics and the interaction between a storm and its environment, followed by more recent advances of how low-level rotation develops and theories behind tornado formation.

Foundational theoretical fluid dynamics relevant to studying coherent rotational structures and their interactions in supercells is reviewed and extended in chapter three. Current methodology for studying rotation in supercells is first presented and then state-of-the-art techniques used in fluid dynamics research are covered. The short-comings of some of the current methods for the purposes of this work are discussed and new theoretical and diagnostic approaches are presented.

Chapter four presents numerical model results of supercell simulations using the NMS and CM1. The application of new theoretical diagnostics to these simulations is shown to help isolate key structures and interactions involved in the supercell tornadogenesis process. Tornadic and nontornadic environmental soundings from the VORTEX2 project are used as the basis for much of the idealized numerical analysis but other environments are also used to test the veracity of the findings. Specifically, cases of tornadogenesis success and failure in these idealized storms

are identified and rigorous, high-temporal analysis is performed on these portions of the simulations.

Chapter five provides a synthesis of the theoretical and numerical results obtained through this dissertation research. The culmination of which is a theoretical model of supercell tornadogenesis derived from theory developed in chapter three and analysis presented in chapter four. Discussion and assertions about the dynamical mechanisms involved in tornadogenesis through this model is then provided. Potential improvements to the methods are then addressed alongside ongoing and future research direction.

Chapter Two: Dynamics of supercell tornadogenesis

The following chapter provides a detailed overview of atmospheric environments that support supercells and tornadoes and the dynamics involved in the development of their rotation. Once again, the reader well-versed in supercell dynamics may wish to omit part one and the first section of part two of this chapter and pick up reading in section 2.2.1 without concern of missing details relevant to the results of this dissertation.

Part I. Supercell dynamics

The atmospheric environment in which deep moist convection develops is critical for determining its type, intensity and associated risk of sensible weather hazards. Of particular importance is the vertical thermodynamic and kinematic structure of a convective environment. The key components are reviewed in the sections below in the context of the dynamics involved in development of rotation in supercells.

2.1.1 Supercell environment

a. Thermodynamics

Like any other type of atmospheric deep moist convection, supercells require conditional instability or *convectively available potential energy* (CAPE). CAPE, determined by the integrated area on a Skew-T thermodynamic diagram between a potentially unstable air parcel's level of free convection (LFC) and its equilibrium level (EL), is a measure of the potential

kinetic energy a parcel can acquire through local buoyancy (Fig. 2.1). The greater the CAPE, the more potential energy exists for thunderstorm updrafts. A supercell environment is also typically characterized by a small amount of convective inhibition (CIN), which is a measure of the energy required to be overcome by a conditionally unstable air parcel to become positively buoyant with respect to its local environment. CIN is calculated by the integrated area between a parcel's lifting condensation level (LCL) and its LFC on a Skew-T. CIN results from "capping" inversions, preventing potentially unstable air parcel's from reaching their LFC until a forcing mechanism provides a source of lift to overcome the CIN. This allows the atmospheric boundary layer to become increasingly conditionally unstable, preventing weak, premature convection from otherwise mixing out the high θ_e air near the surface with air aloft. A typical supercell environment contains moderate to high CAPE (1000+ J/kg) and modest CIN (-10 to -50 J/kg; e.g. Weisman and Klemp, 1986; Johns and Doswell, 1992). The combination leads to what is colloquially referred to as a "loaded-gun sounding" (Fig. 2.1).

Atmospheric water vapor content, particularly at *low-levels*, is critical for determining the type and intensity of supercells (e.g. Moller et al. 1994; McCaul and Cohen, 2002). Drier boundary layers favor higher-based, LP storms while very moist boundary layers favor lower-based, HP storms. Furthermore, low-level moisture modulates the structure and intensity of supercell downdrafts, which are essential for generating and modulating low-level (0-1 km above ground level; AGL) rotation (Markowski, 2002; Markowski et al. 2002). The greater the relative humidity of the air below cloud-base, the less evaporation of falling precipitation occurs. This reduces the amount of evaporative cooling and, as a result, the intensity of negative buoyancy that can be achieved in a downdraft (Markowski, 2002). Boundary layers with higher relative humidity are characterized by lower LCLs and so lower cloud-bases, which also implies less

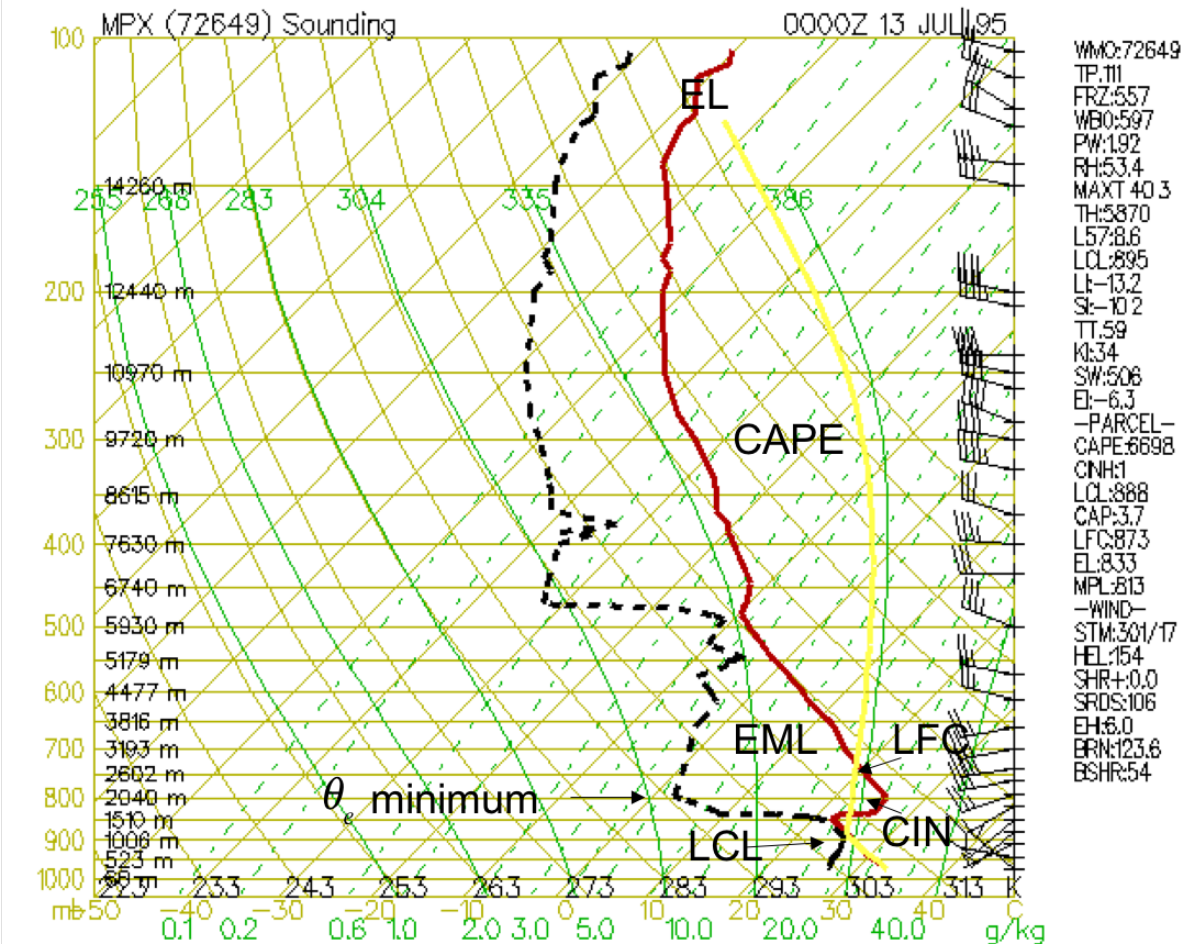

Figure 2.1: A "loaded-gun" sounding from radiosonde balloon launch at Minneapolis, Minnesota on July 13, 1995. Pressure levels (in millibars) and height above ground (in meters) are labeled on the left y-axis, mixing ratio and temperature are labeled on the axis and wind barbs are arrows on the right side. The red line is the observed vertical temperature profile and black-dashed line is the vertical dewpoint profile. The yellow line is the temperature a conditionally unstable surface air-parcel would have if lifted to its level of free convection (LFC), became unstable and rose to its equilibrium level (EL), the parcel's lifted condensation level (LCL) is also marked. The resulting convective available potential energy (CAPE; positive area) and convective inhibition (CIN; negative area) of this parcel are labeled as the regions between the parcel's temperature and its environment. Note the presence of a significant elevated mixed layer (EML) between 800 and 600 mb with a minimum in equivalent potential temperature (θ_e-minimum) at its base. Image modified from Plymouth State Weather Group (URL: https://vortex.plymouth.edu/ accessed on August 8, 2019 at 19.30 UTC).

evaporative cooling associated with downdrafts. In these environments there is a smaller distance over which a conditionally unstable air parcel must be lifted before condensational heating is added to a lifted parcel increasing its buoyancy relative to its local environment. Supercells that produce tornadoes tend to be preferred in atmospheric environments with moist boundary layers (low LCLs), high CAPE and weakly stratified or neutral boundary layers characterized by steep low-level lapse rates and minimal CIN (Parker, 2012).

The thermodynamics of the *middle* troposphere also significantly impacts the evolution of a supercell. Steep lapse rates increase buoyancy acceleration associated with unstable air parcels and reduce the energy lost to buoyancy oscillations (gravity waves). Additionally, a minimum in θ_e is typically found at mid-levels (often referred to as a "dry intrusion" e.g. Weisman and Klemp, 1982), which modulates the generation and maintenance of downdrafts and cold pools in supercells (Gilmore and Wicker, 1998). Once precipitation interacts with the dry, potentially cold air, negative buoyancy is produced through evaporative cooling and sustains a supercell's outflow by bringing low θ_e air to the surface. Therefore, supercell longevity is increased in atmospheric environments with weakly capped, moist boundary layers beneath steep mid-level lapse rates and a significant dry layer aloft that leads to substantial θ_e differences between mid-levels and the surface (Fig. 2.1). Additionally, moisture content of the middle troposphere modulates the efficiency and rate of hail growth (e.g. Johns and Doswell, 1992), which in turn impacts cold pool structure and ultimately storm morphology (e.g. Heever and Cotton, 2004; Snook and Xue, 2008).

b. Kinematics and development of mid-level rotation

Although intense atmospheric convection relies on thermodynamic properties of the atmosphere, supercell environments are distinguished from other types of cellular convective environments such as single and multi-cell thunderstorms by virtue of their *kinematic* environment. In order to assess the kinematic environment of a convective atmosphere, forecasters often use *hodographs* (Fig. 2.2). Hodographs are a type of kinematic diagram used to display a vertical profile of the horizontal atmospheric wind. Hodographs are a powerful tool used for forecasting severe convection. The vertical structure of the horizontal wind (vertical wind profile) determines the level of organization and therefore type of atmospheric convection that can evolve in a conditionally unstable atmosphere. Vertical wind shear (herein 'wind shear') leads to differential momentum advection by updrafts and downdrafts associated with convection (e.g. Dahl, 2017). In turn, this affects the amount of vertical vorticity generated by vertical motions and the structure of the updraft and outflow (Weisman and Klemp, 1982; 1984; Guarriello et al. 2018). Thunderstorm updrafts begin to acquire rotation about their vertical axis (mesocyclones) when the bulk wind vector difference (wind shear magnitude) is at least 20-25 ms^{-1} between the surface and 6 km AGL (Weisman and Klemp, 1982; 1984; 1986; Weisman and Rotunno, 2000; Thompson et al. 2007).

The supercell's mesocyclone is a deep rotating updraft, in which rotation is maximized between 2 and 8 km AGL. The mesocyclone distinguishes supercells from other types of cellular convection, allowing a supercell to persist substantially longer than the lifecycle of a single deep moist thermal. Mesocyclones arise through *tilting* and subsequent *stretching* of (storm-relative) "streamwise vorticity" present in the storm's inflow layer by a buoyant updraft (see sections 2.2.1 and 3.1.1). *Streamwise* vorticity (ω_s; Eq. 2.1) is present in an atmospheric flow when a

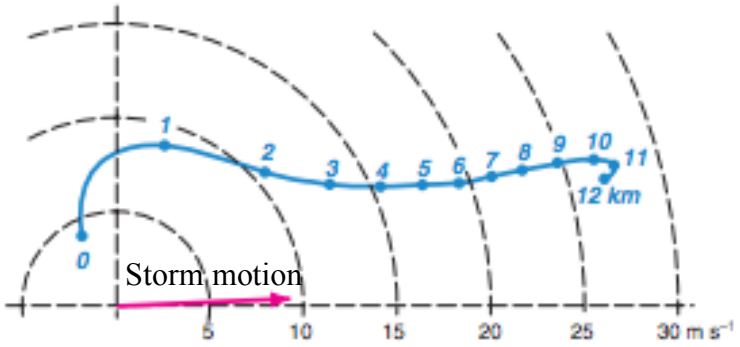

Figure 2.2: Composite hodograph of 400 soundings taken in supercell environments from Markowski and Richardson (2011). The blue line connects the wind vectors at each height, numbers marked are height above ground in kilometers. A vector pointing straight upwards on this diagram would indicate a southerly wind direction, such that the wind direction at the surface (0 km) is south-easterly and at 2 km above ground is south-westerly. The concentric dashed circular lines are wind magnitude (in ms^{-1}), westerly winds are positive values and easterly winds are negative. The wind shear magnitude between two heights can be calculated by subtracting the relevant points on the blue line. The magenta arrow is the mean storm motion for this composite of storms. Reprinted with permission from John Wiley and Sons.

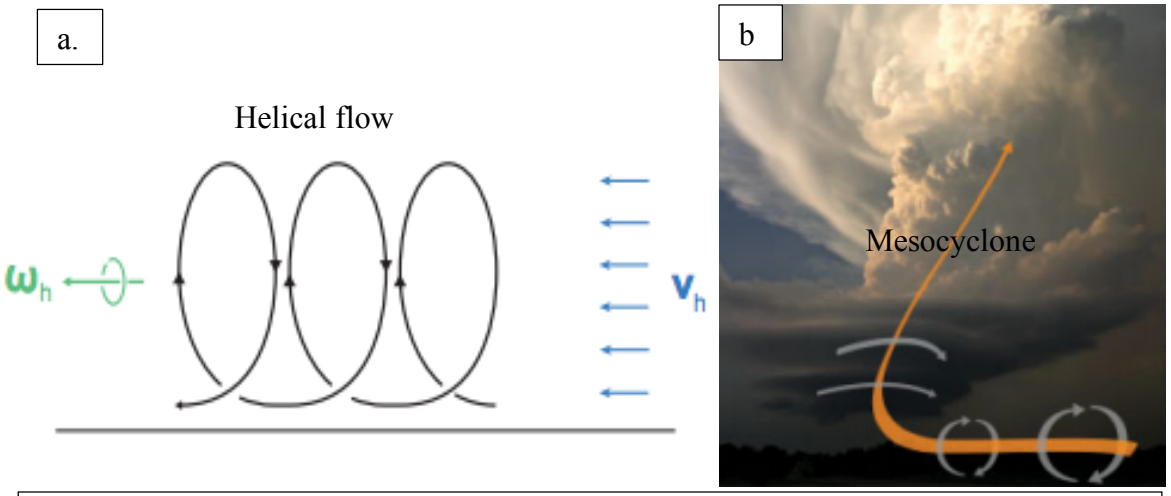

Figure 2.3: Schematic demonstrating the nature of flow associated with streamwise vorticity (a) and the development of rotation about the vertical axis upon being tilted (b). Green arrow in (a) indicates the horizontal vorticity vector ($\boldsymbol{\omega}_h$), while blue arrows indicate horizontal flow vectors ($\mathbf{v}_h$) and black arrows demonstrate the helical nature of the flow. Note that the black arrows do not necessarily indicate streamlines because flow may be characterized by streamwise vorticity and not physically rotate as depicted. Due to the streamwise nature of the vorticity, the orange arrow in (b) indicates both an environmental vortex line and a streamline and white arrows indicate sense of vorticity and subsequently rotation about the vertical axis as the flow is tilted by the incipient updraft and stretched. Figure adapted from Markowski and Richardson (2011).

component of the wind vector is parallel to the vorticity vector (Brandes et al. 1988; Lilly, 1986a; Fig. 2.3).

$$\omega_s = H = \vec{\mathbf{v}} \bullet \vec{\omega} \qquad 2.1$$

H in Eq. 2.1 is the local helicity density (Lily, 1986a). When streamwise vorticity associated with environmental wind shear is tilted by an incipient thunderstorm updraft, rotation will develop about the vertical axis because the vertical (buoyancy-driven) acceleration is aligned with the vorticity vector and is able to stretch the ambient vorticity (see chapter three for additional vorticity dynamics discussion).

Atmospheric environments in which the wind strengthens and changes direction with height are characterized by significant streamwise vorticity or *helicity*. Conversely, if the atmosphere is generally characterized by wind shear that does not change direction with height, the vorticity present is predominantly *crosswise* such that tilting by a convective updraft will lead to rotation on the left and right flanks of an updraft but not coincident with the maximum in buoyancy associated with the updraft (Fig. 2.4). More intense supercells and supercell tornadoes are favored in environments with larger magnitudes of *storm-relative* helicity in their inflow layers due to the prevalence of streamwise vorticity that may be intensified by horizontal and vertical flow accelerations (Eq. 2.2; Droegemeier et al. 1993; Weisman and Rotunno, 2000).

$$SRH = -\int_{z_0}^{z_1} \left[\left(\overline{\mathbf{V}} - \mathbf{c} \right) \bullet \omega_h \right] dz \qquad 2.2$$

Therefore, helicity is often calculated over layers of the lower-troposphere to assess the potential for updraft rotation and tornadoes. The 0-3 km layer is typically used to discriminate supercells from other types of deep moist convection and the 0-1 km AGL layer is used to assess the risk of tornadoes (e.g. Rasmussen, 2003). Furthermore, calculating SRH over an *effective inflow layer*

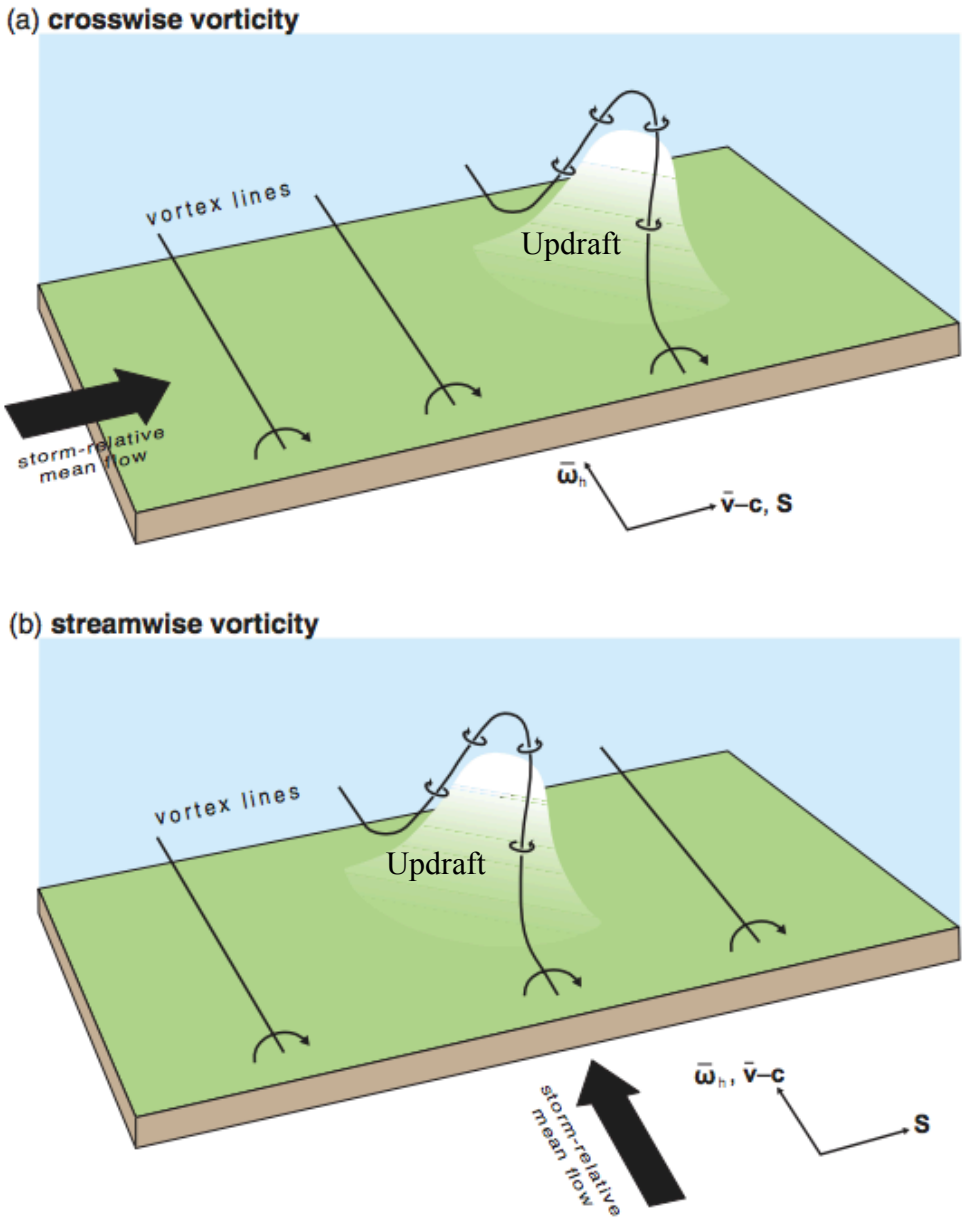

Figure 2.4: Development of vertical vorticity associated with an updraft embedded in an environment with a straight hodograph characterized by crosswise vorticity (a) and in a curved hodograph characterized by streamwise vorticity (b). Thin black lines are environmental vortex lines with arrows indicating vorticity orientation. Thick black line is the storm-relative flow, 'S' is the orientation of the environmental shear and 'c' is the storm motion. The white bump in the green surface is the updraft where *isentropes* are tilted upwards in the updraft. When the environment is characterized by significant crosswise vorticity, vertical vorticity develops on the flanks of the updraft, whereas in an environment characterized by significant streamwise vorticity, the vertical vorticity develops superimposed with the rising air. Figure adapted from Davies-Jones (1984) and Markowski and Richardson (2011) and reprinted with permission from John Wiley and Sons.

has proven to be one of the best environmental discriminators between supercell storms and other types of discrete convection (e.g. Thompson et al. 2007).

A supercell's mid-level mesocyclone derives its rotation from the environmental wind shear. The *vortex lines* (lines whose tangents are everywhere parallel to the local vorticity vector; e.g. Markowski et al. 2008) associated with the wind shear are reoriented and converged by the buoyancy-driven updraft and so mid-level rotation can develop before the storm's precipitation or downdrafts. This vorticity is known as *barotropic* vorticity and is associated with vortex lines that are frozen in the flow and are simply moved around as material surfaces. This differs from vortex lines that may be *generated* by *baroclinic* or frictional mechanisms (e.g. Dahl et al. 2014). The ability of a buoyant updraft to reorient and stretch barotropic vorticity present in the environment to sustain a supercell's mid-level mesocyclone depends on the relative magnitudes of buoyancy and wind shear present (Weisman and Klemp, 1982). Strong, sustained mid-level rotation is favored when one does not substantially dominate the other. The ratio of the CAPE to the 0-6 km bulk wind shear is known as the Bulk Richardson Number (BRN; Eq. 2.3, where v_{shear} refers to the magnitude of the wind shear between the surface and 6 km AGL), which was introduced by Weisman and Klemp (1982) and has been shown to be a good environmental discriminator between supercells and other forms of cellular convection (Thompson et al. 2003).

$$BRN = \frac{CAPE}{\frac{1}{2}\mathbf{v}_{shear}^{2}} \qquad 2.3$$

Cyclonic, right-moving (RM) supercells are favored in environments characterized by clockwise-curved hodographs in which an abundance of positive SRH is present (Weisman and Klemp, 2000; Thompson et al. 2007). A qualitative assessment of SRH can readily be made from a hodograph by comparing the approximate storm motion (Bunkers et al. 2000) with the

environmental wind. A quantitative measure of SRH can also be calculated from a hodograph by multiplying the area between the area swept out by the storm-relative wind by two (Fig. 2.5). RM supercells can be sustained for a wide-range of clockwise-curved hodographs with a variety of shapes and lengths (Parker, 2017). While the development of mid-level rotation is fairly insensitive to small changes in the shape of the hodograph (and in the vertical thermodynamic profile), the development of low-level rotation and tornadoes appears to be significantly impacted by relatively minor changes to the vertical kinematic and thermodynamic structure (e.g. Markowski and Richardson, 2011, pp. 201; Coffer et al. 2017).

Supercells most often form within the warm sector of developing mid-latitude cyclonic disturbances due to the differential horizontal temperature and moisture advections and wind shear associated with the upper-level jets that drive them (e.g. Uccellini and Johnson, 1979). In the northern hemisphere, these regions are typically characterized by veering and strengthening winds with height. As a result, *positive* helicity is found in the warm sector, which favors RM (cyclonic) supercells. The positive helicity implies ambient (environmental) streamwise vorticity for cyclonic supercells and leads to a prevalence of right-moving supercells across the United States.

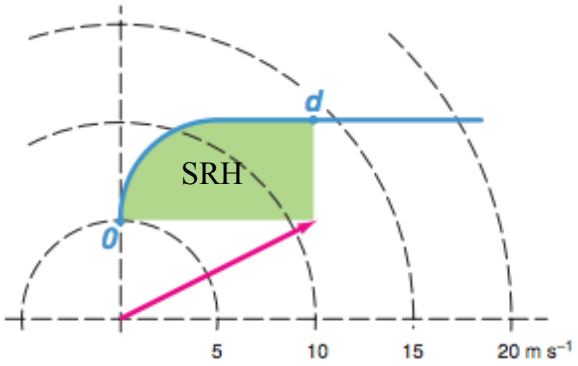

Figure 2.5: Calculating storm-relative helicity (SRH) using a hodograph. As in Fig. 1.19 but 'd' represents the depth of the layer that SRH is being calculated over and green is the area between the storm motion vector (magenta arrow) and the environmental wind (blue line). The environmental SRH in the layer between 0 and 'd' is equal to twice the green shaded region. Figure adapted from Markowski and Richardon (2011) and reprinted with permission from John Wiley and Sons.

c. Forcing mechanism

Even in environments that are thermodynamically and kinematically favorable for rotating convection, supercells may not develop. Initiation and sustenance of supercells requires a forcing (lifting) mechanism to lift conditionally unstable air parcels to their LFC's. Dynamic atmospheric lifting mechanisms include airmass boundaries such as fronts, drylines and convectively-generated cold pools from nearby or prior storms (Bluestein, 2008) and upper- and low-level jets (Doswell and Bosart, 2001). The combination of upper-level divergence and low-level convergence promotes lifting that can erode CIN and release conditional instability (Bunkers et al. 2006). Additionally, topography and other geographic inhomogeneities can lead to local convergence near the earth's surface that can generate the lift required for storm initiation (Kottmeier et al. 2008).

Most frequently, an upper level disturbance and associated surface synoptic-scale cyclone provides the necessary forcing for supercells. In the warm sector of the developing disturbance, low-level warm, moist advection collocated with cold air advection aloft can lead to a suitable thermodynamic environment for convection. In this region, the wind fields typically veer and strengthen with height generating a favorable kinematic environment for rotating updrafts. Finally, the presence of upper level divergence above the surface low and convergence along surface-based frontal boundaries provide a source of lift to initiate deep moist convection. Other potential forcing mechanisms associated with the warm sector of a developing synoptic cyclone include low-level isentropic lift caused by the upper-level jet's transverse (Sawyer-Eliassen; e.g. Shapiro, 1981) circulation and long-wavelength gravity waves generated by an advancing dense airmass (e.g. Weckwerth and Parsons, 2006; Parsons et al. 2019).

The central United States is uniquely placed geographically such that the combination of atmospheric conditions necessary for supercell development occur frequently, particularly during the Spring season. The Rockies lie upstream and, through intense surface heating, generate deep well-mixed layers with very steep lapse rates, which are regularly advected eastward over the Plains (Fig. 2.1). These *elevated* mixed layers (EMLs) can produce substantial CAPE and capping inversions at their bases due to the high-potential temperature (θ) values generated over the high terrain. These EMLs also provide a robust θ_e-minimum aloft for downdraft maintenance. To the south of the central U.S. lies the Gulf of Mexico, which provides a source of low-level moisture that is routinely advected northward underneath EML capping inversions in response to the approach of upper-level disturbances. As a result, loaded-gun soundings are common in the Spring across the central Plains (Fig. 2.1).

A semi-permanent dryline exists in the central U.S. between dry air in the lee of the Rockies and moist air over the Plains. This feature is characterized by significant low-level convergence and often provides the necessary lift for convective initiation (Buban et al. 2007; Bluestein, 2008; Wakimoto and Murphy, 2009). The presence of the Rockies also leads to a thermal upslope circulation, producing a significant ageostrophic acceleration of low-level flow directed upslope (e.g. Abbs and Pielke, 1986). The result is an enhancement of the low-level veering to the vertical wind profile generating a more favorable kinematic environment for supercells and tornadoes. Finally, frequent cyclonic disturbances are encouraged to develop in the lee of the high terrain particularly over eastern Colorado (Abbs and Pielke, 1986). The augmentation of the thermodynamic and kinematic environment by differential temperature, moisture and momentum advections is combined with dynamic lift associated with the disturbance to set the stage for frequent supercell thunderstorm development during the Spring.

2.1.2 Supercell propagation

Supercell formation occurs in conditionally unstable environments when at least 20 ms^{-1} deep layer (0-6 km AGL) shear is present. If the wind direction does not vary with height the wind shear is known as *unidirectional*. Supercells evolving in a unidirectional wind shear profile typically undergo several storm *splits* as precipitation and cold air load the initial updraft producing a central downdraft. Due to the prevalence of crosswise vorticity in these environments (straight hodographs), counter-rotating vortex maxima develop on the left- and right-flanks of the initial updraft (Figs. 2.4 and 2.6). This rotation is associated with a dynamically-induced low pressure and leads to upward-directed VPPGFs that promote new updraft development on the left and right sides of the original updraft (Rotunno and Klemp, 1982; 1985; Davies-Jones, 2002). Subsequent left- and right-moving supercells (with respect to the mean wind) develop, which are characterized by anticyclonic and cyclonic updraft rotation respectively (e.g. Fig. 2.5; Weisman and Klemp, 1984; Markowski and Richardson, 2011, pp. 240). Supercell propagation resulting from the tilting of crosswise vorticity and regular splitting is known as the *nonlinear* supercell propagation mechanism (e.g. Davies-Jones, 2002).

The left-moving storm develops anticyclonic mid-level rotation and the right-moving storm develops cyclonic rotation due to the presence of negative SRH (anti-streamwise vorticity) and positive SRH (streamwise) in their respective inflow layers (Fig. 2.6). This occurs as each storm propagates away from the mean wind direction, which generates a component of the storm-relative wind vector that is parallel (anti-parallel) to the environmental vorticity vector for right-moving (left-moving) storms even for unidirectional wind shear profiles. Left-moving

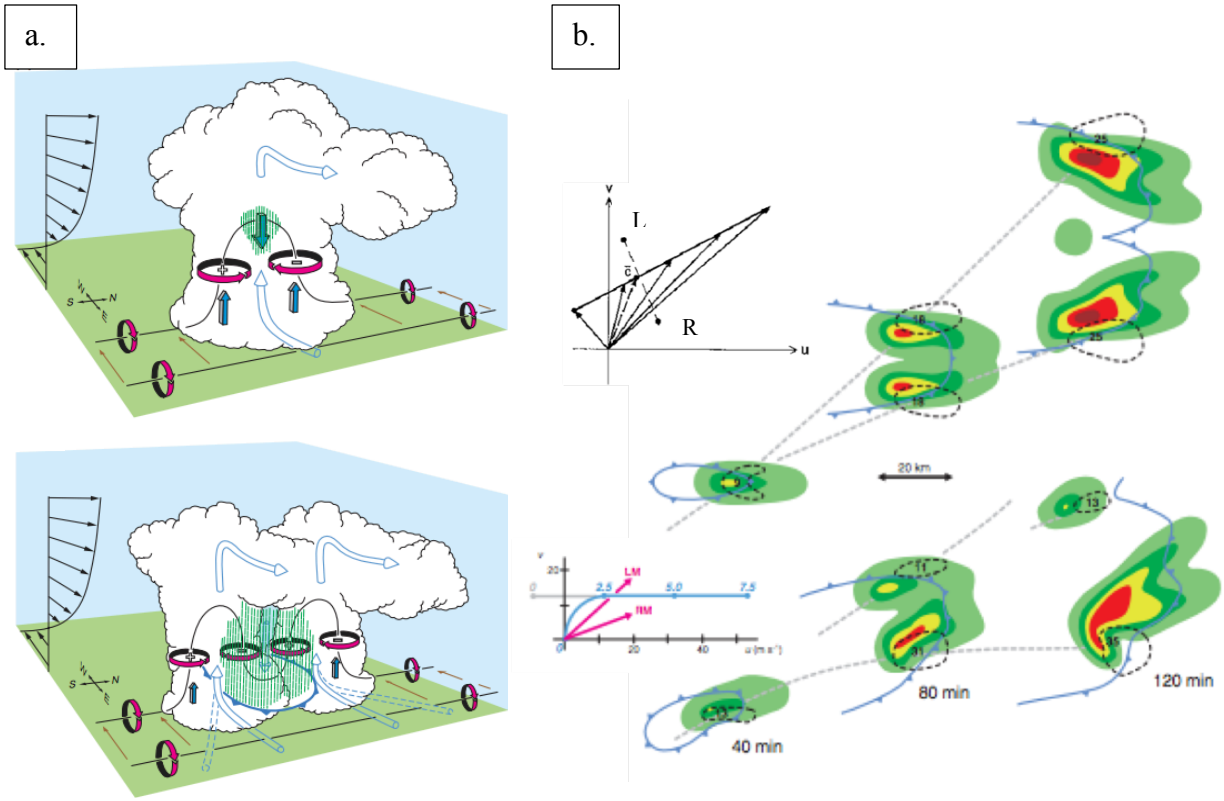

Figure 2.6: Supercell splitting process and the *nonlinear* supercell propagation mechanism. Panel (a) shows the evolution of an initial thunderstorm updraft in an environment with a straight hodograph such as that found in the top portion of (b). Note that while the wind changes direction and speed with height, the hodograph at the top of (b) is still straight implying predominantly crosswise environmental vorticity. In (a) and (b) black arrows represent wind vectors, large blue arrows in (a) indicate streamlines, black lines encircled by pink arrows indicate vortex lines with sense of rotation and positive and negative vertical vorticity labeled. In (c) color shading denotes radar reflectivity with warmer colors indicating more intense reflectivity, surface convergence boundaries are denoted by light blue lines with triangles and storm path is outlined by grey dashed lines. 'LM' and 'RM' denote the storm motion vectors associated with left-moving and right-moving supercell splits respectively. Supercells developing in environments with straight hodographs (top series of images in b.) will tend to split as seen in (a) due to the tilting of *crosswise* vorticity. Note how both LM and RM storms acquire equal magnitudes of negative and positive SRH respectively. Supercells developing in clockwise-curved hodographs (bottom series of images in b.) may initially split as precipitation loads the initial updraft but the RM storm will quickly become the dominant of the two as a result of the large positive SRH in its inflow layer. The LM storm is suppressed in this environment because it too, has positive SRH in its inflow layer, tilting of the streamwise vorticity associated with which leads to cyclonic vertical vorticity generation that destructively interferes with its anticyclonic rotation. Figure adapted from from Markowski and Richardson (2011) and Klemp (1987). Hodograph in (b) from Doswell (1991) and reprinted with permission from John Wiley and Sons.

supercells become favored (more intense) in environments in which the wind *backs* with height and right-moving supercells are favored in an environment where the wind *veers* with height (Markowski and Richardson, 2011, pp. 240).

Right-moving supercells are favored in environments with clockwise curved hodographs due to the prevalence of positive SRH in the inflow layer. The interaction between the storm's rotating updraft and the environmental wind shear produces upward-directed VPPGFs that encourage new updraft growth on the storm's right flank and suppress it on its left flank (Fig. 2.7; Rotunno and Klemp, 1982; 1985; Davies-Jones, 2002; 2015). As updraft development and mid-level rotation is continually forced on the right-flank, the supercell's rotating updraft will continually propagate to the right of the mean wind. This is known as the *linear* supercell propagation mechanism (e.g. Davies-Jones, 2002).

Primarily, supercell propagation depends on the evolution of VPPGFs associated with rotation developing on the flanks of their updrafts. However, a secondary effect associated with low-level convergence along the RFGF can also promote new updraft development by aiding in the dynamic lift of conditionally unstable air downstream of the updraft (Ziegler et al. 2010; Markowski and Richardson, 2014). The efficiency of this mechanism depends on the low-level wind shear (e.g. Markowski and Richardson, 2011, pp. 148). Greater low-level wind shear produces deeper, more vertically erect density interfaces between the storm's cold pool and the environment, which enhances low-level convergence and dynamic lift. Additionally, baroclinic vorticity generation along gust fronts can intensify low-level updraft rotation, which impacts storm propagation (Markowski and Richardson, 2014). A supercells motion relative to the mean wind determines the amount of streamwise vorticity ingested by its updraft, which in turn impacts the structure and intensity of the mesocyclone (e.g. Lilly, 1986a,b).

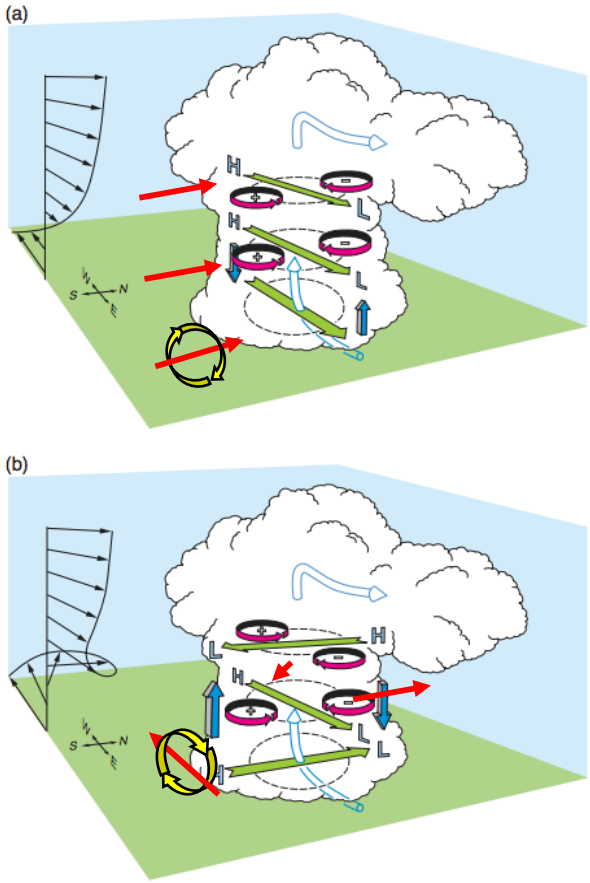

Figure 2.7: Orientation of perturbation pressure gradient forces associated with a supercell updraft in an environment with a straight hodograph (a) and clockwise-curved hodograph (b). As in Fig. 2.6 but here 'H' and 'L' represent perturbation high and low pressure respectively, green solid arrows indicate the direction of the environmental shear vector and consequently so too, the local horizontal perturbation pressure gradient force. Blue solid arrows indicate direction of vertical perturbation pressure gradient forces. The red arrows are vorticity vectors, which everywhere point at right-angles to the local shear, yellow circles indicate the sense of rotation with this orientation of vorticity. The pressure perturbations arise around the updraft due to the interaction with the environmental wind shear. The vorticity associated with the environmental wind shear opposes the upward motion and baroclinic vorticity generation associated with updraft where the shear vector points toward the updraft leading to local deformation and high pressure. However, where the shear vector points away from the updraft the environmental vorticity and updraft circulations work together to promote stretching of vorticity and local perturbation low pressure. Therefore, in an environment in which the wind shear vector does not change direction with height, high- and low-pressure perturbations are vertically stacked leading to weak VPPGFs. In an environment with a curved hodograph characterized by significant turning of the shear vector with height, the dynamically-induced pressure perturbations rotate with height leading to perturbation low-pressure above perturbation high-pressure. This promotes new updraft growth via dynamic lifting on the right-flank of the initial updraft such that the supercell will tend to propagate to the right of the mean wind. This is known as the *linear* supercell propagation mechanism. Figure adapted from Markowski and Richardson (2011) and reproduced with permission from John Wiley and Sons.

This research-focus of this dissertation is cyclonic right-moving supercells due to their prevalence in the United States and their associated dominance of supercell tornado production (Thompson et al. 2012). Therefore, the remaining background will focus on the evolution of rotation in this subset of storms.

Part II. Supercell tornadogenesis

2.2.1 Development of low-level rotation

a. The role of downdrafts

Mid-level rotation develops in response to tilting and stretching of vorticity present in the environment by the storm's updraft and so rotation develops as air is accelerated away from the ground (Davies-Jones, 1982). Low-level (0-1 km AGL) rotation is known to develop after precipitation regions mature around the updraft leading to downdrafts of air that introduce vertical vorticity near the ground where it is initially absent (e.g. Davies-Jones, 1982; Davies-Jones and Brooks, 1993). Relatively cold, dense outflow regions form around a supercell's updraft through precipitation-loading and evaporative cooling effects. Studies of the development of low-level rotation in supercells have generally focused on vorticity production in one of the two main downdraft regions around the updraft: the RFD and FFD. The FFD is associated with the primary precipitation region downwind of the storm's updraft. This region is known to be an important source of streamwise vorticity (both barotropic and baroclinic in

origin) for air parcels entering the storm's updraft at low-levels (Klemp and Rotunno, 1983; Rotunno and Klemp, 1985; Shabbot and Markowski, 2006; Rotunno et al. 2017; Orf et al. 2017).

During the past several decades of supercell tornadogenesis research, however, the RFD has received significantly more attention than the FFD. A number of factors likely contribute to this. A supercell tornado is often observed to develop on the left edge (looking downwind) of the hook echo (in radar reflectivity) between air sinking in the RFD and air rising in the updraft coinciding with the commonly observed cyclonic branch of vortex line arches that straddle the hook echo (e.g. Straka et al. 2007; Markowski et al. 2008; 2012a,b; Wurman et al. 2012; Fig. 2.8). Additionally, the RFD exhibits pulsing or surging that is associated with increased low-level convergence and vorticity, which has been found to correlate with successive tornadogenesis attempts (e.g. Marquis et al. 2008; Mashiko et al. 2009; Wurman et al. 2010; Lee et al. 2012; Kosiba et al. 2013; Skinner et al. 2014; Marquis et al. 2016).

Internal momentum surges associated with surging of the RFD can be driven by negative buoyancy or by downward-directed VPPGFs, some associated with a region of perturbation high pressure aloft (e.g. Schenkman et al. 2016) and some associated with intensification of rotation at the surface leading to an area of perturbation low pressure at ground level (e.g. Skinner et al. 2014; 2015). Significant surging of the outflow is often accompanied by descending pulses of precipitation known as *descending reflectivity cores* (DRCs), which have been shown to be associated with intensification of low-level rotation and tornadogenesis (Rasmussen et al. 2006; Kennedy et al. 2007; Byko et al. 2009; Markowski et al; 2012a,b; 2018; Fig. 2.9).

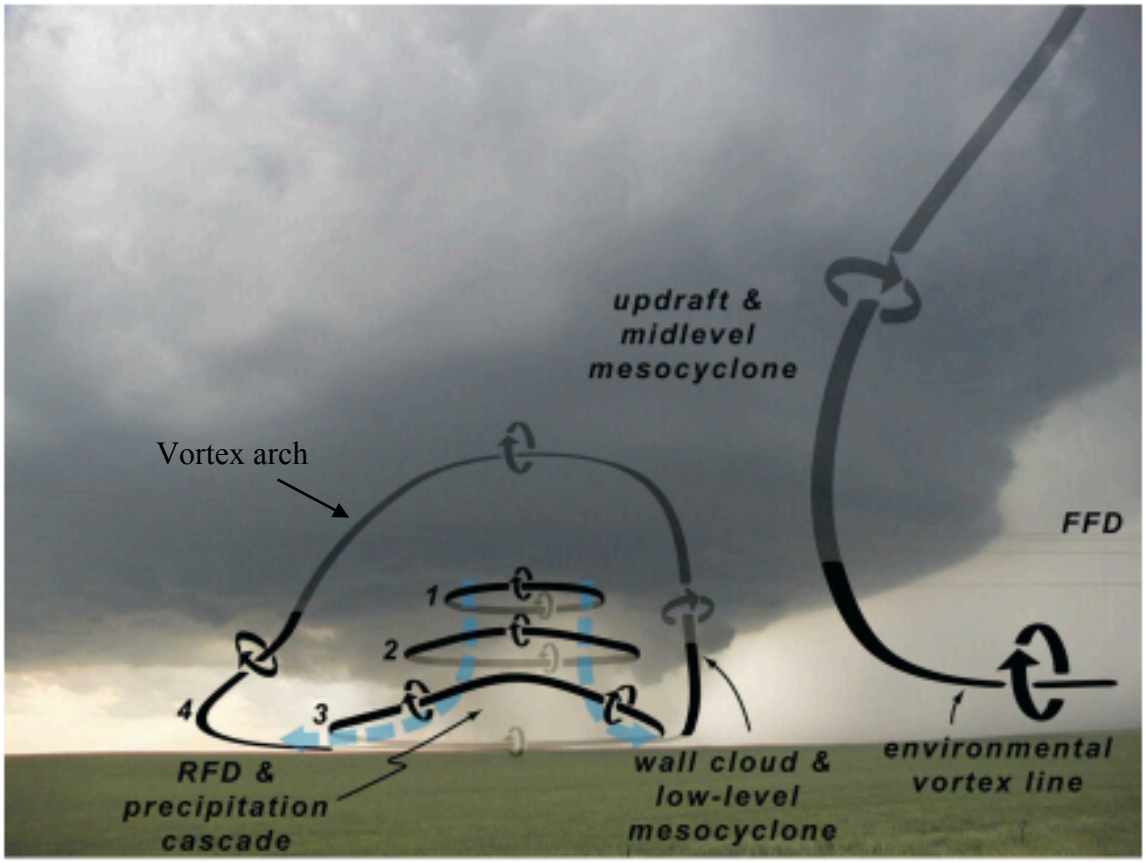

Figure 2.8: Model of the reorientation of vortex lines into vortex line-arches straddling an RFD surge adapted from Markowski et al. (2008). Vortex lines (thick black lines) were derived from observed three-dimensional wind synthesis from DOW data collected during the storm. Ascending numbers indicate four stages of vortex line orientation associated with a descending downdraft pulse (blue dashed arrows) in the storm's rear-flank. Figure reprinted with permission from Monthly Weather Review.

b. Origins of vorticity

Downdrafts are known to introduce vertical vorticity near the ground underneath supercells where it is initially absent (e.g. Davies-Jones, 1982). To gain a better understanding of the mechanisms by which this occurs it is useful to analyze the horizontal and vertical vorticity tendency equations (Eq. 2.4a,b):

$$\frac{\partial \boldsymbol{\omega}_h}{\partial t} = -\mathbf{v} \bullet \nabla \boldsymbol{\omega}_h + \boldsymbol{\omega} \bullet \nabla \mathbf{v}_h + \nabla \times \left(B\mathbf{k} \right) + \nabla_h \times \mathbf{F} \qquad 2.4a$$

$$\frac{\partial \zeta}{\partial t} = -\mathbf{v} \bullet \nabla \zeta + \boldsymbol{\omega}_h \bullet \nabla_h w + \zeta \frac{\partial w}{\partial z} + \mathbf{k} \bullet \left(\nabla \times \mathbf{F} \right) \qquad 2.4b$$

Eq. 2.4a and Eq. 2.4b are the horizontal and vertical vorticity tendency equations respectively, which are developed by taking the curl of the equations of motion. The Boussinesq approximation has been made such that buoyancy (B) only appears in the horizontal vorticity equation (e.g. Klemp and Rotunno, 1983; Markowski and Richardson, 2011, pp. 20). $\mathbf{F}$ is friction, away from the surface the frictional term tends to be orders of magnitude smaller than the other terms in Eq. 2.4a,b. The first term on the rhs of Eq. 2.4a is associated with advection of horizontal vorticity, the second term is often referred to as the "twisting-tilting" term involved with velocity gradients in the flow that reorient (tilt) and stretch (twist) vorticity. The third term is associated with buoyancy gradients in the flow. In the vertical vorticity tendency equation, the buoyancy term no longer appears due to the Boussinesq approximation and the twisting-tilting term has been separated into a tilting (second term on rhs of 2.4b) and a stretching (third term on rhs of 2.4b) term.

Downdrafts can contribute to the development of low-level rotation by generating vorticity baroclinically (via the solenoidal term in the horizontal vorticity equation; Eq. 2.4a;

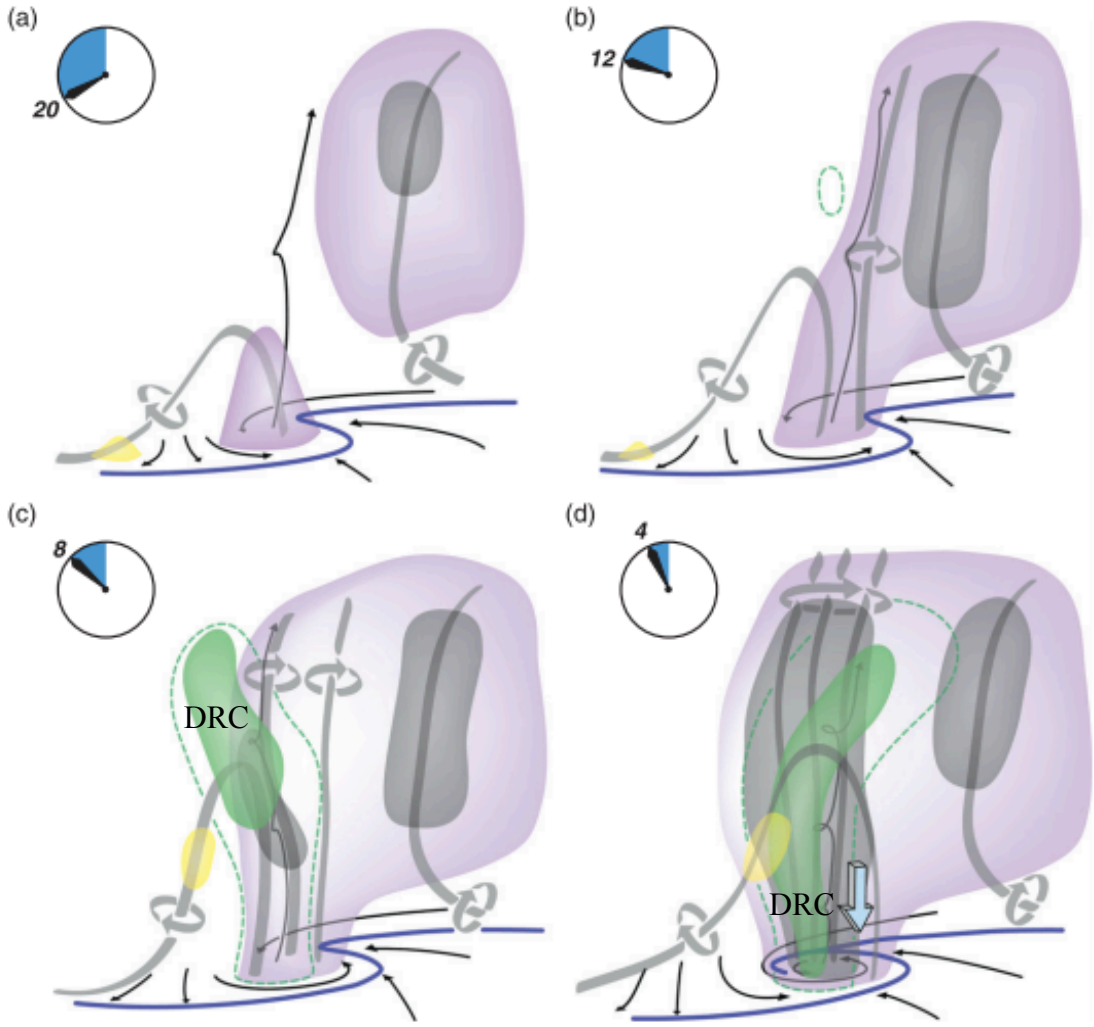

Figure 2.9: Schematic of vortex lines (grey lines encircled by sense of rotation) in the Goshen, County, Wyoming tornadic supercell observed during the VORTEX2 field campaign by Markowski et al. (2012a). Times in the top-left corner of each panel are minutes before tornadogenesis. Streamlines are black arrows, blue lines at the surface indicate positions of surface gust fronts, yellow and purple isosurfaces are regions of significant anticyclonic and cyclonic vertical vorticity respectively and darker isosurface indicates even larger cyclonic vertical vorticity magnitudes. The green dashed line and isosurface indicate the 50 and 55 dBZ reflectivity contours, which indicates the presence of a *descending reflectivity core* (DRC) during tornadogenesis. Figure reprinted with permission from Monthly Weather Review.

Klemp and Rotunno, 1983) in buoyancy gradients along their periphery and subsequently tilt and advect this vorticity toward the ground (Eq. 2.4b). Additionally, downdrafts may tilt and advect frictionally-generated or environmental (barotropic) vorticity associated with wind shear toward the ground. A number of barotropic mechanisms of near-surface vertical vorticity generation have been proposed that involve the importation of high-angular momentum air down from aloft by downdrafts converging this air underneath the storm's updraft (e.g. Davies-Jones, 2001; Markowski et al. 2003; Davies-Jones, 2008; Parker, 2012). These mechanisms are discussed in more detail in Dahl et al. (2014) and references therein.

The orientations of vortex lines in outflow regions of numerical and observed tornadic supercells has cast some doubt on the aforementioned barotropic mechanisms acting as the dominant processes by which low-level rotation develops in a supercell (Markowski et al. 2008; Dahl et al. 2014). Vortex lines associated with such barotropic mechanisms of vertical vorticity generation would lead to depressed vortex lines where the downdraft subsides (e.g. Fig. 2.10; Straka et al. 2007), which is not commonly observed (e.g. Markowski et al. 2012a,b). Using idealized supercell simulations, Dahl (2015) recently found that baroclinic dominated barotropic generation of low-level vertical vorticity in all but the weakest downdrafts. Additionally, in low-level wind profiles that favor sustained low-level rotation (significantly curved hodographs in the lowest 3 km AGL), the background streamwise vorticity ends up horizontally oriented near the surface following descent in a downdraft. Despite this, it has recently been shown that air parcels associated with near-ground rotation about the vertical axis are not necessarily required to exhibit vertical vorticity at the nadir of their trajectory (Rotunno et al. 2017).

Frictional generation of initially horizontal vorticity is another possible mechanism by which low-level rotation may develop near the ground under supercell storms (e.g. Schenkman et

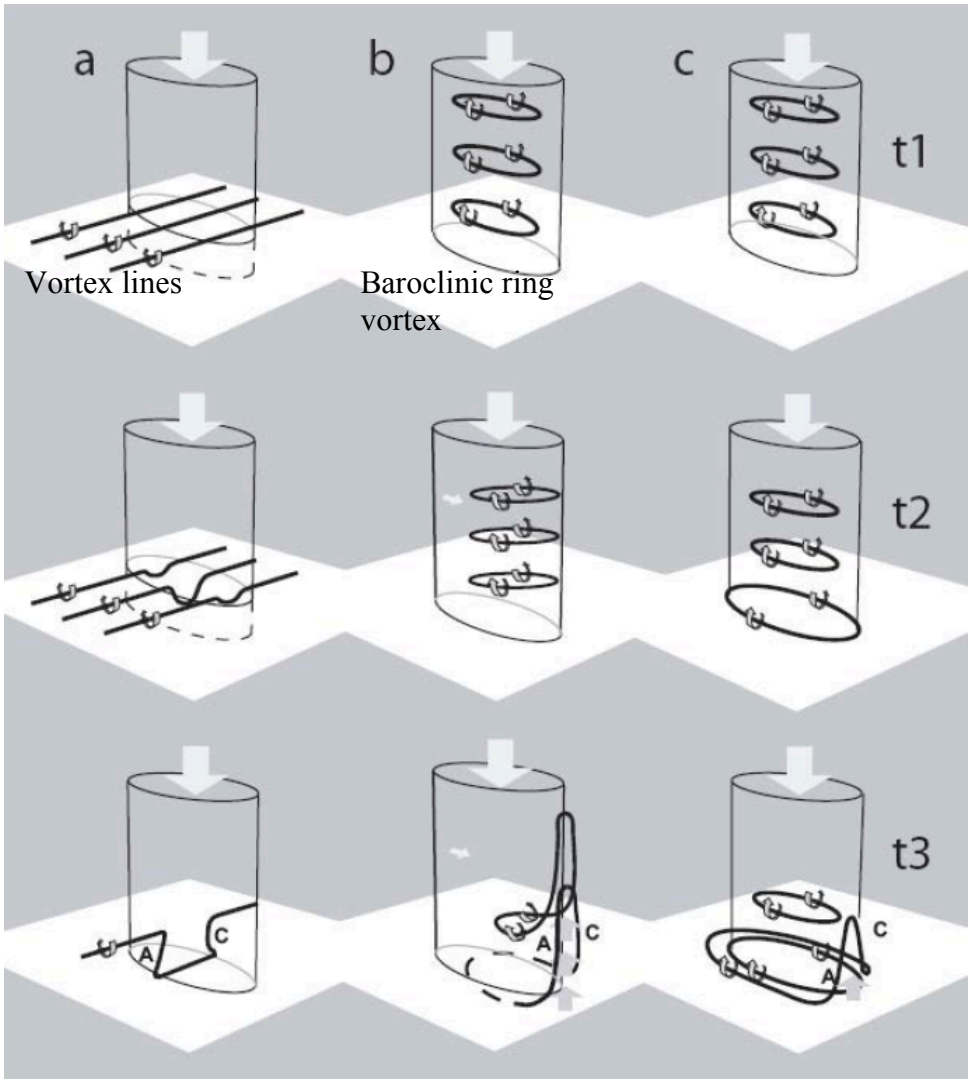

Figure 2.10: Orientations of vortex lines associated with a downdraft pulse as conceptualized by Walko (1993) and Straka et al. (2007). Each proposed mechanism (a-c) results in counter-rotating vortices on the flanks of the downdraft pulse. The left column of schematics (a) is a *barotropic* mechanism of counter-rotating vortex production characterized by depressed vortex lines whereas the center and right columns involving tilting of initially horizontal *baroclinic* vorticity generated by the downdraft. In (b) the downdraft falls in close proximity to an updraft causing tilting of the horizontal vortex ring, while in (c) the baroclinic ring subsides to the surface, spreads out and is subsequently lifted forming an arch. It has since been shown that the right-side progression (c) is unlikely to operate in supercells because air approaching the head of the density current associated with the downdraft will be forced upwards out ahead of the surge due to deformation in the flow (Davies-Jones and Markowski, 2013). Additionally, the deformation and high pressure leads to vortex "squashing" reducing the rotation in the flow during this process.

al. 2014; Roberts and Xue, 2017). In addition to providing a direct source of vorticity, heterogeneous surface roughness varies the orientation and velocity of the storm-relative flow, which alters the magnitude of streamwise vorticity ingested by an incipient storm. Our deficiency in understanding the interaction of flow with the surface (e.g. Rotunno, 2013) and difficulty modeling the lower boundary to account for physically realistic frictional effects in numerical simulations is the subject of ongoing research (e.g. Markowski, 29th Conference on Severe Local Storms). Quantifying the contribution of friction to generation and intensification of low-level rotation remains an outstanding problem.

c. The baroclinic mechanism

There is a growing body of literature, however, that suggests the prominent mechanism by which a supercell develops low-level rotation is baroclinically in association with air-parcel trajectories that descend through downdrafts before being turned sharply upwards near the ground in strong vertical motion gradients (e.g. Rotunno and Klemp, 1985; Davies-Jones and Brooks, 1993; Wicker and Wilhelmson, 1995; Markowski et al. 2012a,b; Kosiba et al. 2013; Parker and Dahl, 2015; Davies-Jones, 2015; Mashiko, 2016; Rotunno et al. 2017). This mechanism of near-surface vertical vorticity generation was proposed theoretically by Davies-Jones and Brooks (1993) and expanded upon by Davies-Jones et al. (2001) and was later confirmed to operate in idealized numerical simulations (e.g. Markowski and Richardson, 2014; Dahl et al. 2014; Parker and Dahl, 2015).

The so-called “baroclinic mechanism” occurs along air parcel trajectories descending through a downdraft in which, initially horizontal, crosswise vorticity is generated baroclinically

and as the flow progresses, the vorticity vectors become oriented at an elevated angle relative to descending streamlines (Fig. 2.11; Dahl et al. 2014; Dahl, 2015). This 'slippage results from

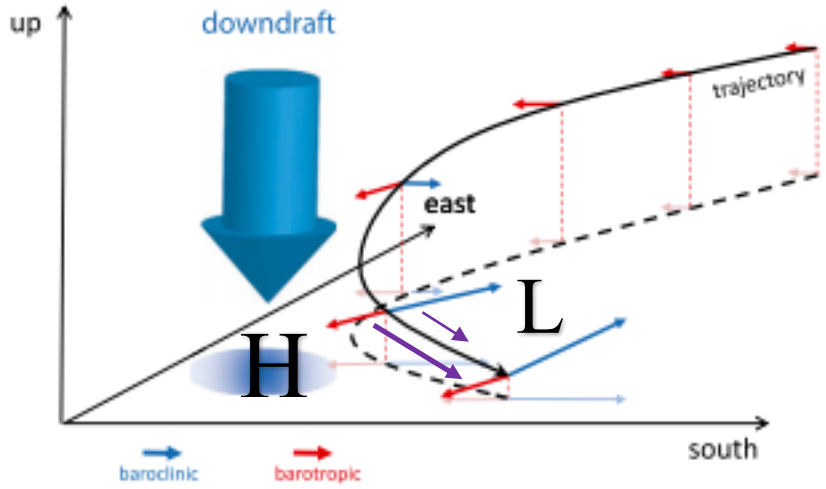

Figure 2.11: Conceptual model of the "baroclinic mechanism" leading to near-ground vertical vorticity generation associated with flow trajectories traversing the periphery of a downdraft modified from Dahl (2015). Baroclinic vorticity vectors are blue and barotropic vorticity vectors are red. As the trajectory (black line) approaches the downdraft it begins to descend toward the ground. Barotropic vorticity is frozen in the flow and so these vectors begin to tilt downwards but are soon reoriented by baroclinic vorticity generated along the periphery of the downdraft. Due to continued baroclinic vorticity generation along the trajectory, vorticity vectors become elevated relative to the descending trajectory. The flow descends in a "feet-first" fashion due to the barotropic effect (purple lines indicate relative magnitudes of flow close to and just above the surface), which reorients the trajectories upwards as the flow approaches its nadir even in the absence of an updraft. Due to the relative positions of high-pressure ('H') associated with the downdraft and low-pressure ('L') associated with the inflow low of a supercell's updraft region, the flow is forced to curve similarly to water moving around a bend in a river ("river-bend effect") such that the initially crosswise-oriented baroclinic vorticity vectors become progressively streamwise along the trajectory. Figure reprinted with permission from Monthly Weather Review.

continued baroclinic vorticity production along the trajectory, which modifies the orientation of the vorticity vectors relative to descending streamlines. Because the flow descends 'feet first' in a density current fashion the "barotropic effect" reorients the vorticity vectors into the vertical as the flow approaches its nadir. Initially crosswise, the vorticity becomes progressively streamwise along the trajectory due to the "riverbend effect", where flow is forced to curve due to pressure gradients between higher relative pressure of the outflow and lower relative pressure of the inflow (Fig. 2.11; Davies-Jones and Brooks, 1993; Dahl et al. 2014; Parker and Dahl, 2015). The resulting vertical vorticity is subsequently ingested by the overlying updraft and stretched if the dynamic (non-buoyancy related) lifting is strong enough (e.g. Coffer and Parker, 2018). The sustained connection between low-level updraft acceleration and surface-based vorticity is what ultimately leads to tornadogenesis, which is the focus of the next section.

2.2.2 Connections between surface-based vorticity and the updraft

a. Overview

While our understanding of how low-level vorticity is produced under supercells has been significantly improved over the last several decades, a wide-range of observational evidence suggests that almost all *surface-based* supercells have ample subtornadic surface-based vertical vorticity for tornadogenesis and yet the majority fail to produce tornadoes (Coffer and Parker, 2017; 2018). No matter how surface-based, vertical vorticity arrives under the storm's updraft it must be converged, lifted and stretched to attain tornadic strength (Fig. 2.12). This process requires a communicative effort between surface-based vorticity and the storm's updraft.

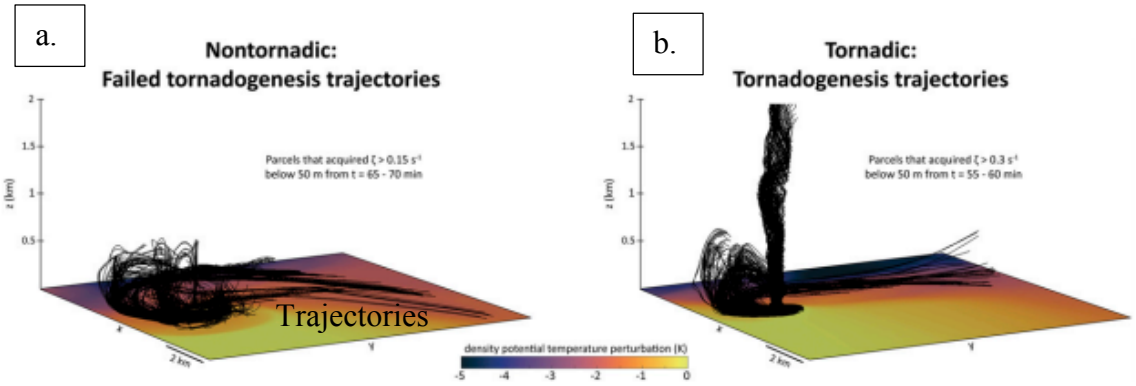

Figure 2.12: Coffer and Parker (2017) air parcel trajectories (black lines) that attained large vertical vorticity over the lowest 50 m AGL in simulations of nontornadic (a) and tornadic (b) storms using the composite VORTEX2 nontornadic and tornadic soundings using the CM1 model. Surface is shaded by perturbation density potential temperature (θ'_ρ) at the lowest model grid point. While a substantial portion of the trajectories in the tornadic storm ascend from near the surface deep into the overlying updraft all of the nontornadic trajectories fail to ascend above 500 m AGL. Also note that the tornadic trajectories are significantly more coherent in their origins along a low-level density gradient to the north of the updraft and tend to exhibit descent during their approach. The nontornadic trajectories originate from a much sparser region of the storm's outflow from closer to the surface and more predominantly from the east as opposed to the north. Figure reprinted with permission from Monthly Weather Review.

The LFC in a typical supercell environment is approximately 2 km above ground (e.g. Davies, 2004), and so although a number of thermodynamic and microphysical effects significantly modulate an inflow parcel's buoyancy, the lifting and stretching of vorticity-rich air parcels in the lowest kilometer above ground requires *dynamic* forcing associated with rotation and deformation rather than directly through buoyancy alone.

Sustained rotational structures such as the low-level mesocylone can provide the necessary upward-directed dynamic VPPGFs associated with low-level updraft intensification (e.g. Guarriello et al. 2018). The vertical gradient of rotation (that can be approximated by the vertical gradient of the square of the vorticity magnitude) is responsible for the strength of the dynamic lifting associated with the low-level mesocyclone (e.g. Markowski and Richardson, 2014). Stronger low-level wind shear, more environmental streamwise vorticity (e.g. Rotunno and Klemp, 1982; Coffer and Parker, 2015) and better vertical alignment of the mid- and low-level mesocylones (e.g. Wicker and Wilhelmson, 1995; Wakimoto et al. 1998; Alderman et al. 1999; Snook and Xue, 2008) tends to produce stronger low-level dynamic lifting.

Upward-directed VPPGFs can also result from internal momentum surges that produce intense near-surface deformation zones, which are associated with local perturbation high pressure (Davies-Jones, 2002; Bluestein, 2013, pp. 218, Davies-Jones and Markowski, 2013; Jeevanjee and Romps, 2015; Robertson, 2017; see chapter three for further details). These surges have been shown to generate new updraft growth from low-levels that can couple with the storm's main updraft above and have been associated with tornadogenesis through the stretching of near-surface vertical vorticity (e.g. Markowski et al. 2012a,b; Kosiba et al. 2013; Skinner et al. 2014; Marquis et al. 2016; Markowski et al. 2018). Despite this, significant tornado generation in supercells does not appear to occur without the presence of a strong, persistent low-

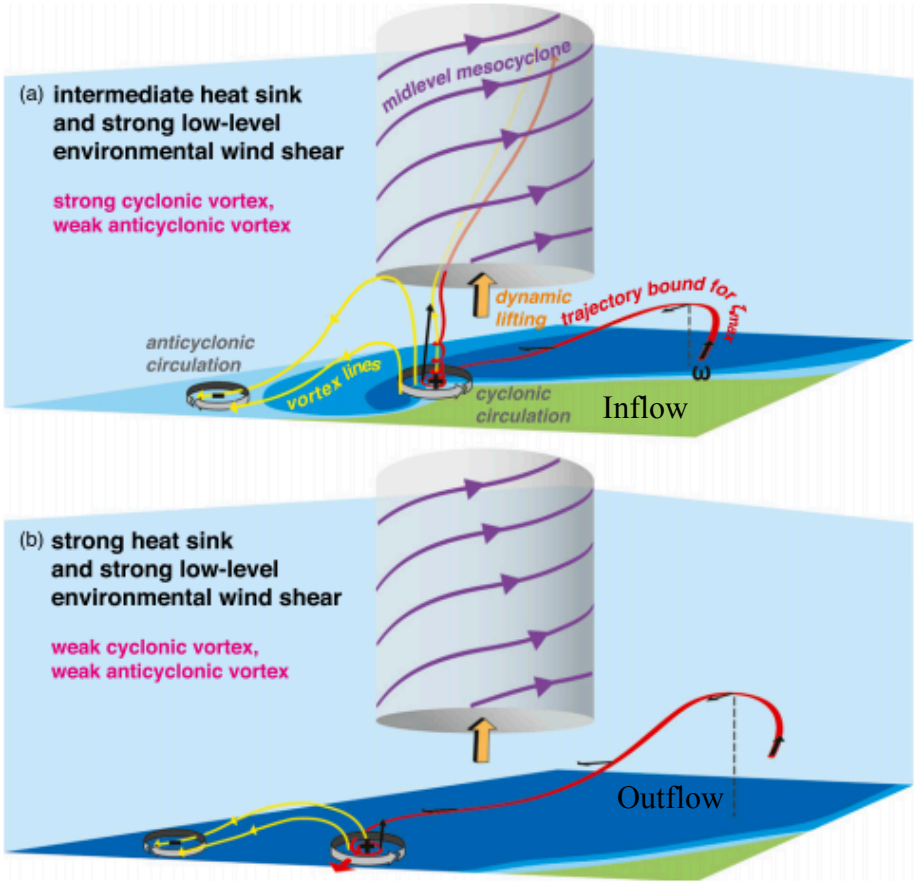

Figure 2.13: Conceptual model developed from numerical simulations of highly-idealized heat sink and heat sources with the CM1 by Markowski and Richardson (2014). White shaded region with purple arrows indicates the supercell's rotating updraft, yellow lines are vortex lines and red lines are air parcel trajectories that attain maximum near-surface vertical vorticity. Bold orange arrow indicates dynamic lifting under the mesocyclone and grey circular arrows at the surface are ground-based circulations with positive and negative vorticity indicated. The surface is shaded by temperature where darker blues are colder temperatures. The characteristic trajectory with intermediate heat sink and strong low-level shear (a) follows a similar path to the Coffer and Parker (2017) tornadic trajectory set and ascends deep into the mesocyclone from near the surface. Conversely, the characteristic trajectory in the case with a strong heat sink fails to ascend from the surface. Figure reprinted with permission from Journal of the Atmospheric Sciences.

level mesocyclone (Coffer and Parker, 2017). Persistent low-level mesocyclones are also insufficient for tornadogenesis, however (e.g. Markowski et al. 2011). Our knowledge of the processes involved in abruptly intensifying low-level dynamic acceleration and deep vertical vorticity growth during tornadogenesis is incomplete. To improve upon this theory, it is critical to study processes on the misoscale (sub-mesocyclonic scale) at which this sudden organization and intensification of vorticity takes place.

The thermodynamic characteristics of a supercell's outflow are critical to determining the ability of dynamic forcing to lift air into the overlying updraft (Fig. 2.13). If the air is too negatively buoyant, air parcels are less likely to be lifted significantly in the vertical (e.g. Trapp, 1999; Markowski, 2002; Markowski and Richardson, 2009; 2014; Markowski et al. 2011; Weiss et al. 2015). Relatively warm (and therefore less negatively buoyant) outflow surges tend to occur in environments in which less evaporative cooling occurs (moist boundary layers with low LCLs) and in surges dominantly forced by downward-directed dynamic VPPGFs as opposed to negative buoyancy (e.g. Schenkman et al. 2016). Despite growing evidence that strong dynamic lifting combined with weakly negatively buoyant outflow favors tornadic storms, the ability to predict tornadogenesis from an environmental perspective remains a challenge (e.g. Anderson-Frey et al. 2016).

b. Vortex arches

Downdrafts can tilt and advect barotropic vorticity associated with low-level wind shear toward the ground or baroclinically generate vorticity through the *solenoidal* term in the vorticity equation (Eq. 2.4a). Vorticity generated baroclinically by downdrafts tends to be in the form of horizontal "ring" vortices (assuming a local relatively circular downdraft structure) around the

downdraft's periphery (Fig. 2.8). If a downdraft subsides in close proximity to an updraft, the baroclinic ring vortex may be tilted by differential vertical motions across it to produce counter-rotating vertical vortices forming a vortex "arch" over the descending downdraft (Straka et al. 2007; Markowski et al. 2008; Markowski et al. 2012a,b; Figs. 2.8, 2.9 & 2.10).

The observed orientation of vortex lines in real-world and numerical supercell storms in the RFD region almost ubiquitously exhibit vortex arches (Brandes, 1984; Bluestein et al. 1997; Wakimoto et al. 1998; Wakimoto and Cai, 2000; Bluestein and Gaddy, 2001). Due to the orientation of observed vortex lines in supercell cold pools, it has been proposed that vortex arches are baroclinically generated as opposed to resulting from rearrangement of barotropic vorticity, which would exhibit depressed vortex lines in the downdraft region (Markowski et al. 2008). It has been hypothesized that the cyclonic branch of the vortex arch provides the rotation associated with low-level mesocyclones and, if the downdraft is not too negatively buoyant and dynamic lifting is strong enough, for the tornado itself (Straka et al. 2007; Markowski et al. 2008; Markowski et al. 2012*a,b*).

Markowski and Davies-Jones (2013) demonstrated that low-level flow approaching an outflow surge is characterized by local perturbation high pressure due to deformation in the flow and as a result forces vertical motion out ahead of the surge and so is unable to lift baroclinic vorticity generated upshear in the cold pool. Additionally, air parcels are deformed in this region resulting in a reduction in their vorticity as they are lifted into the overlying updraft. However, using idealized downdraft simulations with the NMS model, Trevorrow (2014) demonstrated that downdrafts subsiding through significant low-level shear can produce vertically erect vortex arches, particularly in the presence of surface-friction, without the need for an interaction with an updraft (Fig. 2.14). These experiments showed that vorticity was predominantly baroclinically

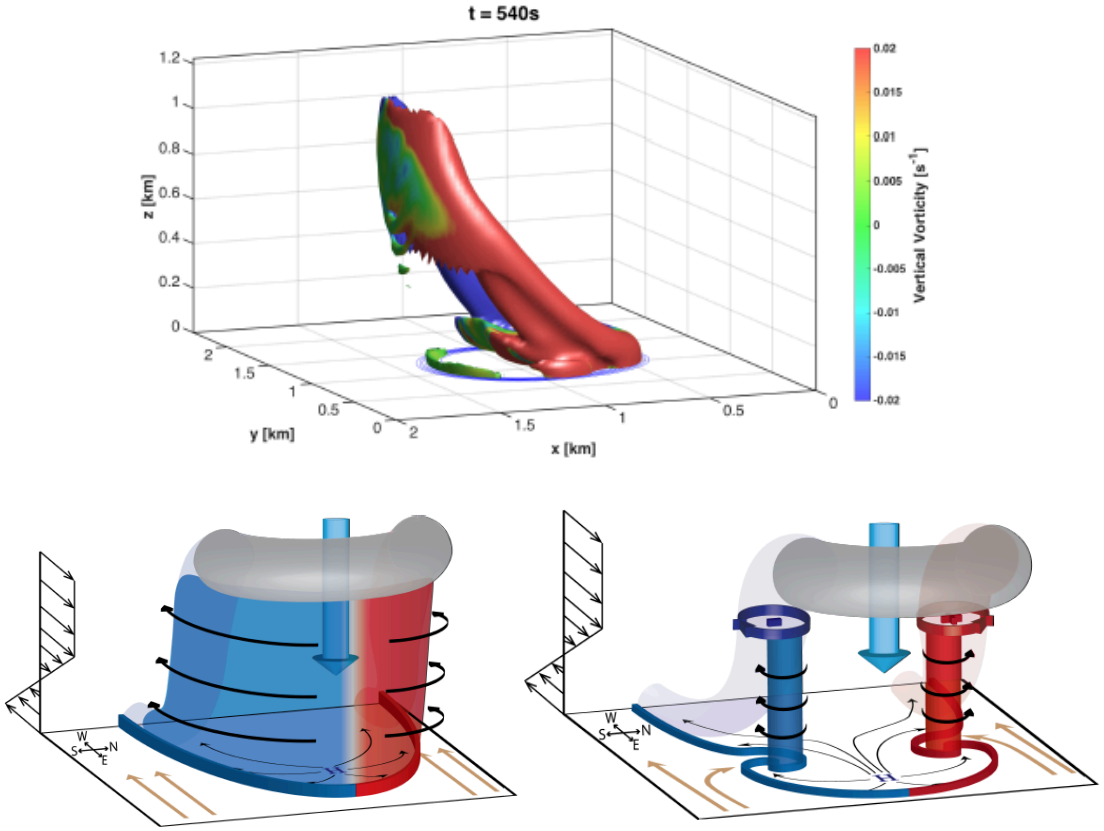

Figure 2.14: Idealized downdraft experiment with the UWNMS at 540s into the simulation (a) and conceptual model of vorticity and vortex evolution during the downdraft's descent through a unidirectional shear profile (b) and (c), from Trevorrow et al. (2016; manuscript rejected). Red shading in all three panels is cyclonic vertical vorticity and blue is anticyclonic vertical vorticity. Environmental surface flow is indicated by gold arrows and the surface flow associated with the outflow is marked by black arrows at the base of (b) and (c). The core of the downdraft is denoted by the thick blue arrow in (b) and (c), the orientation of downdraft-relative streamlines is given by bold black arrows. The conceptual model suggests that "sheet-like" baroclinic vorticity along the downdrafts periphery can be "rolled-up" onto incipient cyclonic (thick red shading in (c)) and anticyclonic (thick blue shading in (c)) branches producing surface-based counter-rotating vortices on the periphery of the downdraft surge.

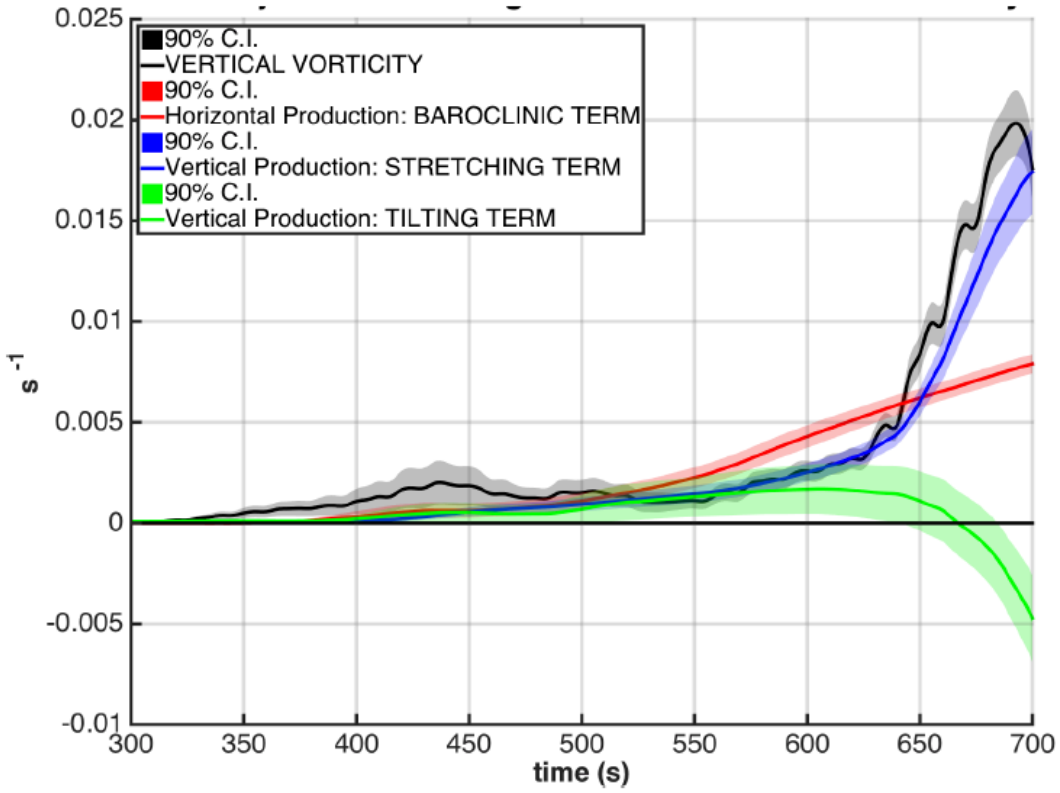

Figure 2.15: Vorticity tendency analysis along 250 trajectories subsiding through the downdraft in the idealized downdraft experiment in Fig. 2.14 from Trevorrow (2016; manuscript rejected). Vertical vorticity is plotted in black, baroclinic production is plotted in red and the tilting and stretching contributions are blue and green respectively.

generated along the edge of the subsiding downdraft and subsequently tilted and stretched to generate a vertically-arched vortex structure similar to observations (Fig. 2.15). Additionally, Trevorrow (2014) showed that the cyclonic branch of downdraft-driven baroclinic vortex arches becomes more intense in environments characterized by positive helicity in the 0-1 km layer due to preferential vertical vorticity aggregation by the cyclonic vortex in these environments.

Through interaction with surface-friction, a horizontally-accelerating momentum surge at the ground may root vortex lines to the ground connected with its arched ring vortex that extends over the head of the surge (Trevorrow, 2014). The baroclinically generated, surface-based vortex may subsequently interact with the overlying updraft of a supercell thunderstorm if a sustained dynamical interaction between its vortex lines and the updraft can been maintained. The position, structure and intensity of vertical vorticity associated with such outflow-driven momentum surges is strongly modulated by the low-level wind profile and relative position and strength of the overlying mesocyclone (Guarriello et al. 2018).

c. The streamwise vorticity current

The current proposed mechanism for how vorticity generated in the outflow regions interacts with mid-level rotation is a "vortex-line surgery" process, in which vortex lines associated with outflow-generated rotation are "severed and reattached" to those associated with the mid-level mesocyclone (Markowski and Richardson, 2014; Fig. 2.16). While useful in an illustrative sense, the dynamical process by which this occurs is unclear. In a recent high-resolution simulation of a violently tornadic supercell, Orf et al. (2017) identified a *Streamwise Vorticity Current* (SVC), which is a helical misoscale structure that intensified during tornadogenesis (figure). The SVC develops rotation about the horizontal axis baroclinically as it

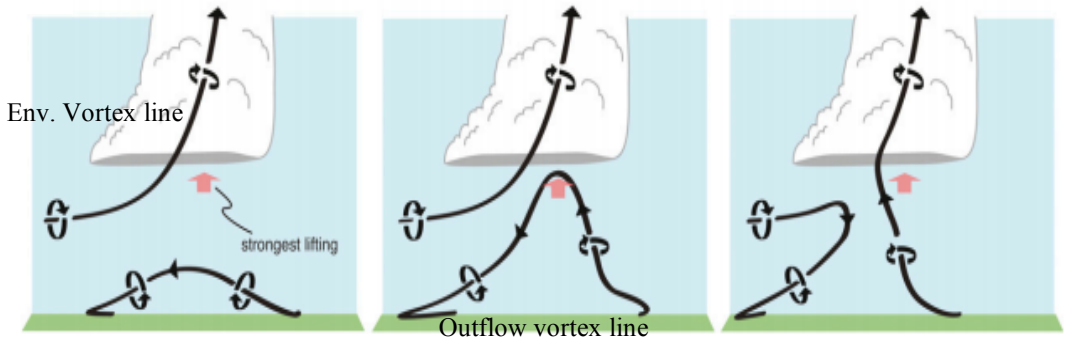

Figure 2.16: Conceptual model by which arched vortex lines associated with baroclinically-generated vorticity may interact with the mesocyclonic vorticity associated with a supercell's updraft. Black lines with arrows are vortex lines with sense of rotation superposed and dynamic lifting is indicated by the pink arrow. Theoretically, vortex lines originating deep within the cold pool may become arched through the baroclinic mechanism as air parcel trajectories approach the base of the updraft near the surface. In favorable environments; not-too negatively buoyant outflow and strong dynamic lifting from above, these parcels may ascend into the storm's updraft lifting the vortex line arches with them. These vortex lines may then sever and reattach to the vortex lines associated with the rotating updraft through diffusion. Figure reprinted with permission from Journal of the Atmospheric Sciences.

approaches the low-level updraft from the storm's forward flank along the cool side of the forward-flank downdraft boundary (FFDB), which is equivalent to the LFCB in the Beck and Weiss (2013) conceptual model (Fig. 2.17). The horizontal rotation associated with the SVC becomes tilted upward as it is ingested into the storm's updraft supporting significant dynamic pressure deficits in a bent, tube-like fashion over the lowest few kilometers above ground (Fig. 2.17). Such dynamically supported pressure deficits associated with the SVC produce low-level horizontal and vertical momentum accelerations that lead to intensification of the low-level updraft and inflow (Orf et al. 2017).

Orf et al. (2017) found that the SVC supported numerous surface-based misovortices, which were transported along it rearwards in a storm-relative sense, subsequently ingested by the storm's updraft and stretched (Fig. 2.18). In recent numerical simulations by the author, a similar helical structure was identified in associated with the LFCB as outflow parcels accelerated toward the updraft from the north along a baroclinic zone (Fig. 2.19). This structure appeared to be related to genesis of a tornado-like vortices in these simulations via near-surface tilting and lifting of vorticity produced baroclinically along the periphery of an internal momentum surge. The helical structure appeared to provide a mechanism of communication with the overlying updraft as the cyclonic surface-based vortex grew vertically from the ground upward. The primary difference between the simulation with the NMS (Fig. 2.19) and the Orf et al. (2017) simulation (Fig. 2.17) was the clear initiating mechanism of an intense internal momentum surge driven by an intense downdraft pulse to the north of the storm's updraft.

The SVC is an example of a coherent rotational structure that is capable of providing a sustained dynamical connection between surface-based vorticity generated in the outflow and the storm's updraft. To study the role of the SVC and other potentially important dynamic structures

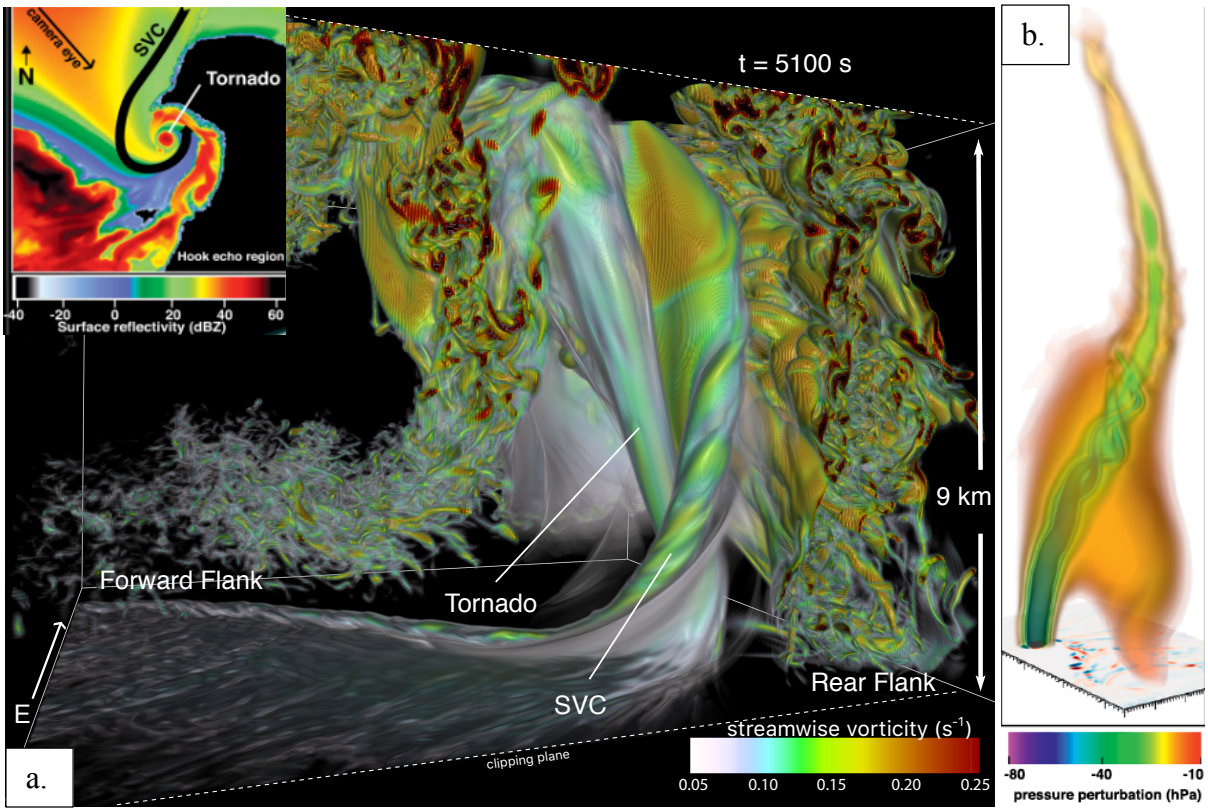

Figure 2.17: View of a streamwise vorticity current (SVC) and tornado from the north-west through the left-flank of a numerical simulation of a violently tornadic supercell at 5100 s into the simulation (a) and pressure perturbation associated with these structures viewed from the north-east at 6580 s into the simulation (b). The inset in (a) is a top-down plane view of simulated surface 'reflectivity' with the relative positions of the SVC and tornado marked. The volume rendering in (a) is streamwise vorticity (s^{-1}) and the volume rendering in (b) is pressure perturbation (hPa). The tube of streamwise vorticity can be seen ascending along the forward-flank downdraft boundary (FFDB) as it approaches from the north of the updraft (a). Collocated with this structure is a significant negative pressure perturbation (b). Figure reprinted with permission from Bulletin of the American Meteorological Society.

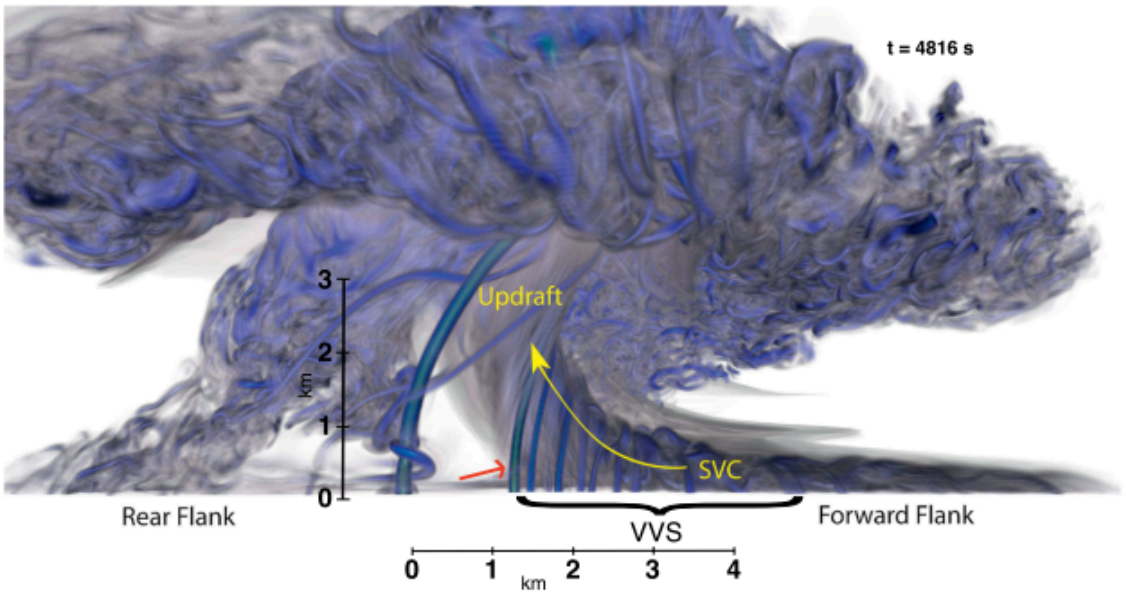

Figure 2.18: Volume rendering of total vorticity magnitude of the numerical simulation in Fig. 2.17 viewed from the south at 4816 s into the simulation. Sheet-like vorticity in association with the SVC appears to break down into discrete misovortices during its approach and ascent into the storm's updraft (yellow line). Figure adapted from Orf et al. (2017) and reprinted with permission from Bulletin of the American Meteorological Society.

such as vortex arches in supercell tornadogenesis, it is desirable to be able to distinguish these structures from the total three-dimensional vorticity field. This dissertation develops new diagnostic approaches for illuminating and classifying rotational structures in a supercell and, through this, presents insight gained about the interaction between surface-based vorticity and the storm's rotating updraft aloft during tornadogenesis and tornadogenesis failure in simulated supercell thunderstorms.

2.2.3 Theories for development of the tornado vortex

A vortex such as a tornado differs from the local spin associated with vorticity by virtue of its sustained interaction with a local pressure minimum (e.g. Kolar, 2007; Markowski et al. 2011; Bluestein, 2013, pp. 366; see chapter three). Numerous theories for how the tornado vortex forms from local vorticity exist in the literature, none of which have been explicitly confirmed.

a. Dynamic-pipe effect

The advent of radar technology led to the detection of a *tornadic vortex signature* (TVS) at mid-levels in a supercell, a region of more intense rotation on a scale smaller than the parent mesocylone that preceded tornado development at the ground (e.g. Lemon et al. 1978; Brandes, 1981; Wieler, 1986; French et al. 2013). This prompted the theory that a misoscale vertical vortex initially developed aloft and descended to the surface through the so-called "dynamic-pipe effect" (DPE; Snow, 1984; Fiedler, 1998; Bluestein, 2013, pp. 352; Fig. 2.20). The DPE involves the convergence of flow characterized by non-zero vorticity beneath a developing vortex in

cyclostrophic (inertial) balance acquiring rotation as it is accelerated toward the vortex by the pressure gradient associated with its lower end. Due to the horizontal cyclostrophic balance associated with a vertically oriented vortex, flow cannot be radially converged into the vortex from the sides but can be at the ends of the vortex where the rotation terminates, such that the vortex acts like a "pipe". Theoretically, as a result of conservation of angular momentum, the rotation would increase beneath the vortex as vorticity-rich air parcels converge towards the central low pressure. Subsequently the inflowing air beneath the vortex also develops toward cyclostrophic balance with a dynamic pressure minimum. This theoretical mechanism is known as a "top-down" mechanism of tornado development and requires minimal static stability and significant ambient vorticity in the layer below the developing vortex. Observations of tornadogenesis in numerical and real-world supercells have found that vertical vorticity intensification associated with tornado development occurs rapidly, if not simultaneously, over a deep layer (e.g. French et al. 2013). These findings suggest that the DPE is not the dominant mechanism by which a tornado vortex develops because the growth of vertical vorticity would require significantly more time to reach the surface than is observed.

b. Non-dynamic-pipe effect

The short-comings of the DPE theory to explain observed modes of tornadogenesis motivated subsequent theoretical research by Trapp and Davies-Jones (1997) who proposed an alternative to the DPE consistent with observed rapid intensification of vertical vorticity over a deep layer. Their "non-DPE" theory for tornado vortex development requires the existence of a deep layer of converging, inflowing air between the base of a vortex aloft and the surface (Fig. 2.20). If ambient vorticity and convergence is nearly constant with height over this layer, high-

angular momentum air converges over the whole layer simultaneously. In this model, vertical vorticity may initially intensify at the surface due to enhanced radial inflow resulting from surface frictional effects and subsequently intensify upwards rapidly.

c. Convergence boundaries

Due to the prevalence of vorticity along convergence boundaries within and along the periphery of a supercell's outflow regions, a number of mechanisms for surface-based vortex development in these regions have been suggested. Recall from section 2.3 that a downdraft subsiding in close proximity to an updraft may generate, baroclinically, a counter-rotating vortex couplet joined by arching vortex lines (Figs. 2.8, 2.9, 2.10 & 2.14). Additionally, a downdraft subsiding through significant low-level shear will bring air to the surface with different horizontal momentum relative to the ambient near-surface flow, which will lead to horizontal momentum acceleration (surging) along the ground. As the flow surges outward along the surface, horizontal shear along the periphery with the ambient environment will also lead to vertical vorticity production associated with horizontal shear. Interestingly, in this conceptual mechanism, the vortex lines will effectively terminate at the ground via the surge's interaction with surface-friction.

Shearing instability along gust fronts and convergence boundaries has been proposed as a mechanism by which vorticity, initially in the form of *vortex sheets* (Figs. 2.14 & 2.18; Markowski et al. 2014b) can organize into discrete vortex centers. Convergence boundaries are generally regions of maxima in horizontal wind shear, which generates local maxima in vertical vorticity arranged in a thin line along the boundary as a sheet-like structure. Barotropic (shear)

instability can develop along such sheets of vorticity leading to vortex formation, which is referred to as a "vortex sheet roll-up process" (Drazin and Howard, 1966). This process is the generally accepted mechanism by which non-mesocyclonic tornadoes such as landspouts and waterspouts develop (Wakimoto and Wilson, 1989; Lee and Wilhemson, 1997; Marquis et al. 2007). In supercell flows, Markowski et al. (2014) demonstrated that vortex sheets can develop along gust fronts through the baroclinic mechanism discussed in section 2.2.1. Mobile doppler radar and mobile mesonet surface observations have been used to demonstrate that such shear-instability driven vortex generation occurs along supercell gust fronts and has been linked to tornadogenesis via vertical stretching of vortices developing underneath a strong low-level updraft (Bluestein et al. 2003; Lee et al. 2012). Further, Gaudet and Cotton (2006a,b) found that anisotropic horizontal convergence interacted with vortex sheets along gust fronts in a simulated supercell producing local vortex sheet roll-up underneath an idealized supercell updraft, which led to tornado-like genesis.

d. Low-level mesocyclone contraction

In what he refers to as "stage 3" of supercell tornadogenesis, Davies-Jones (2015) recently outlined a general theory of tornado development in a supercell. Davies-Jones theorizes that blocking of high-angular momentum air by the RFD leads to the concentration of low-level rotation, which, subject to surface friction, upsets the cyclostrophic balance associated with the low-level mesocyclone causing air to "overshoot its cyclostrophic equilibrium radius" and contract to a new cyclostrophic equilibrium accompanied by a vertical jet driven by the Bernoulli effect. Why such a scale contraction would occur in some supercells and not others is not apparent from this theory.

e. The streamwise vorticity current

Recent high-resolution modeling work by Orf et al. (2017) highlighted the potential importance of a misoscale, helical rotational structure they termed the streamwise vorticity current in supercell tornadogenesis (see section 2.2.2). In their simulation the sustained helical structure transported numerous misovortex structures toward the incipient supercell updraft at which point they were converged and stretched. During this process no specific "trigger mechanism" for tornadogenesis was identified, instead tornado development appeared to be a steady process until a critical threshold of vertical vorticity was converged under the updraft leading to tornado development.

Although by no means confirmed as the dominant mechanism of supercell tornado production, there is clear theoretical attractiveness of tornadogenesis process involving the interaction of a sustained helical misovortex such as the SVC and crosswise misovortex structures (generated by shear instability or otherwise). The helical rotation associated with the SVC can support (if such a structure can maintain a connection with the buoyancy-driven updraft) a sustained dynamic pressure minimum from the updraft aloft to very low-levels within the supercell's vorticity rich outflow region, which supports a robust dynamical connection between the buoyancy-driven updraft aloft and the low-level vorticity field. The misovortices, resulting from their crosswise orientation, have vortex lines that effectively terminate at the ground capable of supporting the necessary surface-based circulation required for a tornado to form. While the crosswise misovortex structures likely start out as arches or hoops due to the requirement that vortex lines cannot terminate in the interior of a fluid (e.g. Wu et al. 2005, pp. 73), the interaction with the helical rotational structure at their upper end presents a plausible mechanism by which the vortex lines may be severed and reconnected (such has been suggested

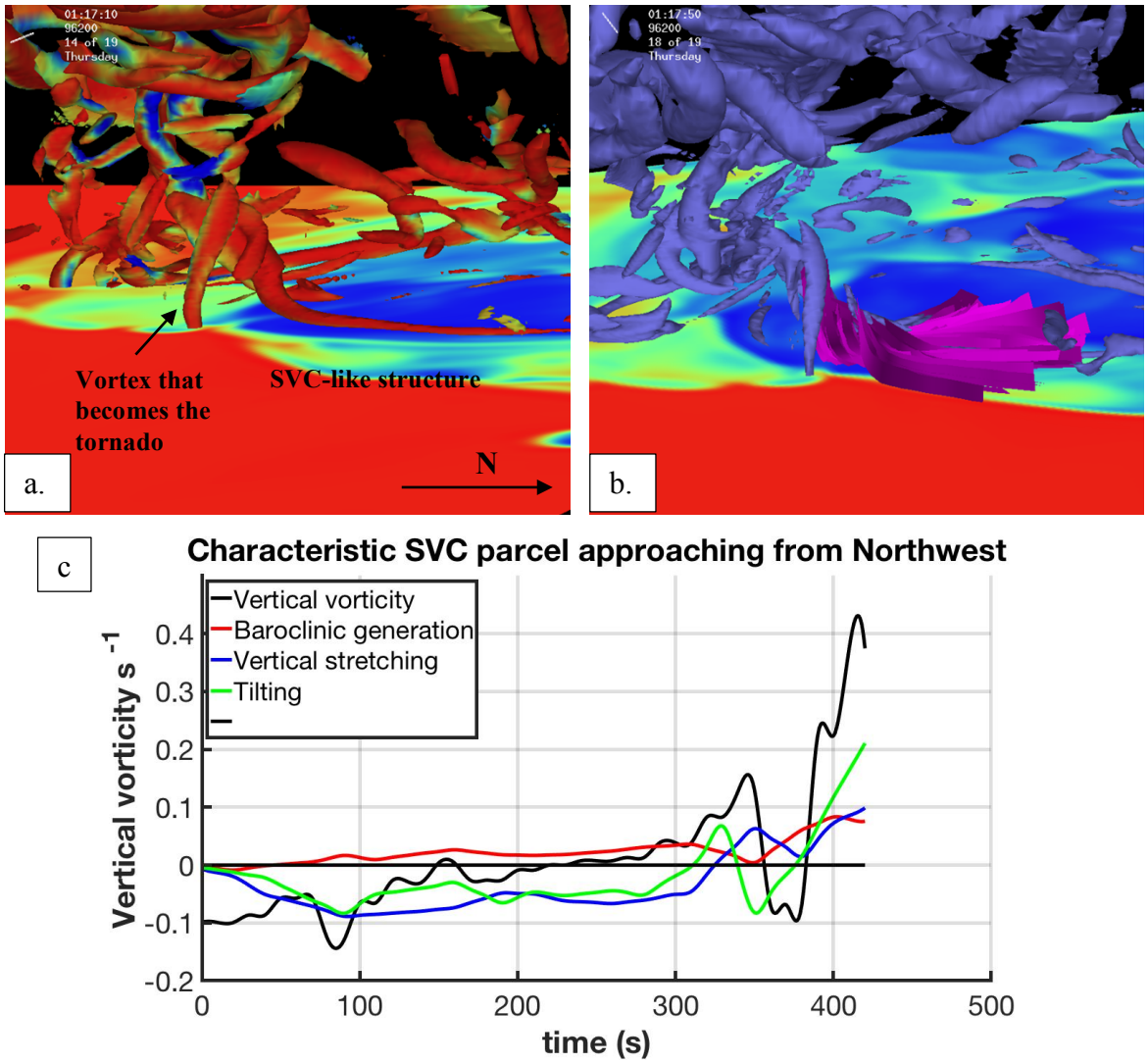

Figure 2.19: Numerical simulation of a tornadic supercell with the NMS approximately five minutes before tornado-like genesis looking from the east ((a) and (b)). The surface in (a) and (b) is shaded by perturbation equivalent potential temperature (θ_e), the isosurface is the rotational component of vorticity as outlined in chapter three contoured at 0.5 s^{-1} and the purple ribbons are air-parcel trajectory paths associated with the incipient tornado-vortex. The trajectories that enter the developing tornado-like vortex and ascend to the tropopause through the storm's updraft tend to originate in the cold pool to the north of the updraft on the cool side of the LFCB. As they approach the updraft from the north they descend slightly before being sharply turned upward on the warm side of this boundary and the SVC-like structure. Calculations of vorticity tendency along these trajectories indicate that horizontal baroclinic vorticity production occurs along their path (c). At approximately 340 s along the trajectory integration the air parcels are suddenly tilted toward the ground during which time negative vertical vorticity is generated, abruptly soon after the tilting reverses sign and positive vertical vorticity is rapidly generated as the parcels are lifted upward on the warm side of the boundary. The horizontal resolution of the inner grid used in this simulation is 120 m and the vertical resolution is 40 m until 1 km AGL where it is steadily stretched to 360 m by approximately 6 km AGL and then remains 360 m to the top of the domain at 20 km AGL.

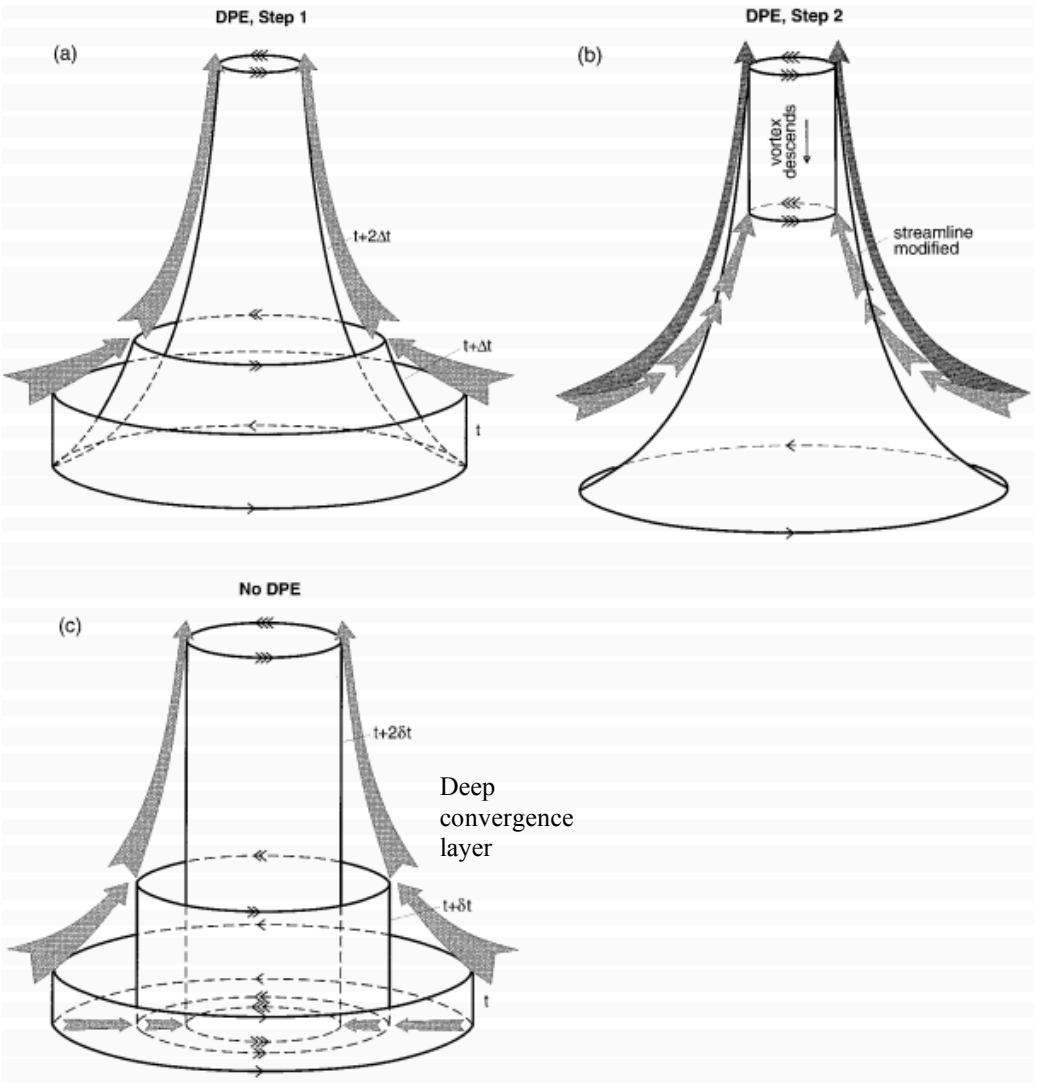

Figure 2.20: Theoretical development of a surface-based misoscale vortex within and under a rotating updraft. (a) and (b) are stages in the development of a vortex initially aloft in association with converging flow with significant vertical vorticity as envisioned by the dynamic-pipe effect (DPE) theory. The flow steadily becomes cyclostrophically balanced between outward-directed radial inertial acceleration from the convergence of vorticity and a local dynamic pressure minimum. This vortex subsequently builds toward the surface by accelerating flow with significant vertical vorticity inwards toward the axis of rotation, which too (via the conservation of angular momentum constraint) develops cyclostrophic balance. Trapp and Davies-Jones (1997) proposed a different mechanism of vertical vortex-genesis that does not involve the DPE (c). In this model, if convergence is constant over a deep layer beneath the rotating updraft, the radial convergence of high-angular momentum air can occur simultaneously over this layer without needing to descend slowly from aloft. Figure adapted from Trapp and Davies-Jones (1997) and reprinted with permission from Journal of the Atmospheric Sciences.

by Markowski and Richardson (2014)) with those associated with the helical rotation. Once this occurs, mass can be drawn up through the initially crosswise vortex structure leading to surface pressure falls and penetration of the vortex by radial inflow near the surface. As a result, the vortex becomes progressively helical and vertical stretching is intensified. This dynamical theory will be explored in greater detail in subsequent chapters of this dissertation.

Chapter Three: Theoretical investigation of the dynamics of rotation

In the author's opinion, outstanding gaps in our knowledge of supercell tornadogenesis are most likely to be resolved through a combination of advances in theoretical physics and high-resolution numerical modeling. Albeit, all advancements as a result of this work must be subsequently confirmed by observations of real-world supercells. Theoretical work involving vorticity and helicity dynamics, primarily in the 1980s (e.g. Davies-Jones, 1982; 1984; Rotunno and Klemp, 1982; 1985; Klemp and Rotunno, 1983; Lily, 1983; 1986a,b; Brandes, 1984; Klemp, 1987; Brandes et al. 1988; Brooks et al. 1993), has shaped our current understanding of rotation in supercells, much of which has been recently "confirmed" through numerical model analysis as our computing capabilities continue to advance. It is essential, now that we have the technological capability to realistically simulate the development of rotation on the tornado-scale in supercell thunderstorms, to continue to advance our theoretical approach in order to develop theories from numerical simulations that are grounded by the physical laws that govern fluid flows.

Advancing the theory of tornado development requires analysis of the fluid dynamics associated with rotational flow. Fluid dynamics theory, such as the concept of swirl ratio, has been extensively applied to understand the structure and evolution of a mature tornado vortex (e.g. Harlow and Stein, 1974; Fiedler, 1994; Rotunno, 1977; 2013; Trapp and Fiedler, 1995; Nolan, 2005; section 1.1.4). Relatively little attention, however, has been directed toward studying the dynamics of coherent rotational fluid structures in a supercell other than the tornado. This dissertation will show that the lineage of rotational structures in the time leading up to tornado development can illuminate how a thunderstorm develops vertically coherent dynamic

mechanisms of communication between the intense updraft aloft and the surface-based vertical vorticity.

In part one of this chapter, techniques currently employed by the research community to analyze the development and evolution of rotation in supercells are reviewed. In the context of relevant fluid dynamics theory, the shortcomings of these techniques for the purposes set out herein are discussed. This theory is extended to develop new diagnostic techniques for studying rotational structures in supercells.

Part I. Current methods of identifying rotational flow in supercells

3.1.1 Vorticity framework

a. Vorticity

Rotation in fluid flows such as the earth's atmosphere is primarily governed by the distribution and intensity of vorticity (e.g. Brown, 1991). Therefore, in order to explain the processes involved in development and intensification of rotation in supercells we need to invoke the (prognostic) vorticity tendency equation. The Coriolis effect is generally ignored to study vorticity dynamics in supercells because the timescales of significant rotational structures are typically one to three orders of magnitude smaller than those affected by planetary scale rotation. Eq. 3.1 is the three-dimensional vorticity tendency equation, in which an assumption of incompressibility has been made.

$$\underbrace{\frac{D\left(\nabla\times\mathbf{v}\right)}{Dt}}_{\text{local tendency}}=\underbrace{\frac{\partial\omega}{\partial t}}_{\text{local tendency}}+\underbrace{\left(\mathbf{v}\bullet\nabla\right)\omega}_{\text{advection}}=\underbrace{+\left(\omega\bullet\nabla\right)\mathbf{v}}_{\text{tilting/stretching}}+\underbrace{\frac{1}{\rho^{2}}\nabla\rho\times p}_{\text{solenoidal generation}}+\underbrace{\nabla\times\mathbf{F}}_{\text{viscous effects}} \qquad 3.1$$

The contribution of each term to local vorticity tendency is labeled. The third term on the rhs of Eq. 3.1 is the *solenoidal* term, which generates vorticity in baroclinic regions of the atmosphere where pressure gradients exist along constant density (ρ) surfaces. A common simplification of the solenoidal term, one which does not significantly affect the assessment of local vorticity tendency in supercells (e.g. Klemp and Rotunno, 1983), is made by invoking the Boussinesq approximation (ignoring density variation unless multiplied by gravity). Eq. 3.1 then becomes:

$$\frac{\partial \omega}{\partial t} = -\left(\mathbf{v} \bullet \nabla\right)\omega + \left(\omega \bullet \nabla\right)\mathbf{v} + \nabla \times B\mathbf{k} + \nabla \times \mathbf{F} \qquad 3.2$$

Where, $B = \frac{\rho'}{\overline{\rho}} g$. Eq. 3.2 can be split into Eq. 2.4a and Eq. 2.4b to analyze the tendency of horizontal and vertical vorticity separately. The third term on the rhs of Eq. 3.2 is the baroclinic term and arises due to relative differences in weight of the overlying atmosphere such that sharp regions of horizontal density gradient generate horizontal vorticity baroclinically. For the reasons discussed in chapter two, it is also common to separate the vorticity into streamwise and crosswise components by taking the dot product of the horizontal velocity vector and the horizontal vorticity vector (Eq. 2.4a; e.g. Markowski and Richardson, 2011, pp. 40).

The primary way to study the development and evolution of rotation in supercells has thus far been analysis of horizontal and vertical vorticity tendencies using Eq. 2.4a,b. Through this approach we have learned that supercells derive their mid-level updraft rotation from tilting and subsequent stretching of environmental streamwise vorticity in the storm-relative flow (Davies-Jones, 1984; Brandes, 1984). This is known as a barotropic vortex generation mechanism, which results from updraft reorientation of initially horizontal ambient vorticity associated with the environmental wind shear. Supercell mesocyclone development is relatively insensitive to the vertical kinematic structure of the atmosphere as long as the wind shear

magnitude is at least 20 ms^{-1} (Parker, 2017). The vorticity framework also explains that, in the absence of pre-existing surface vertical vorticity (such as may be associated with low-level wind shift lines), a supercell's downdrafts are required to introduce vertical vorticity near the surface where it is initially absent (e.g. Davies-Jones, 1982). While mid-level rotation in supercells can be sustained for a wide-variety of vertical wind profiles, the development of low-level (0-1 km) rotation is highly sensitive to minor changes in the wind profile, particularly in the lowest kilometer above ground (e.g. Markowski and Richardson, 2011, pp. 201; Coffer and Parker, 2015; 2017; 2018; Coffer et al. 2017).

Vorticity tendency analysis is typically performed along integrated air-parcel trajectories derived from model output (e.g. Noda and Niino, 2010; Wurman et al. 2010; Beck and Weiss, 2013; Naylor and Gilmmore, 2014; Schenkman et al. 2014; Nowotarski et al. 2015) or approximated from observed wind fields using dual-doppler wind synthesis (e.g. Markowski et al. 2012*a*). The sources and processes involved with intensification of vorticity in specific regions of a supercell can then be determined. To understand where a tornado acquires its rotation it is particularly pertinent to study the evolution of vorticity associated with air parcels which develop significant vertical vorticity near the ground underneath a supercell's updraft. Through such analysis it has largely been concluded that baroclinic generation along air parcel trajectories that descend in or along the periphery of precipitating downdrafts is almost certainly the dominant mechanism by which a supercell acquires low-level rotation on the mesocyclonic- and probably on the tornado-scale (e.g. Dahl et al., 2014; Dahl, 2015; Parker and Dahl, 2015). It has also been shown that supercells with greater *environmental* streamwise vorticity in their inflow layers tend to be associated with stronger upward-directed dynamic VPPGFs in the lowest kilometer above the surface, which is known to be necessary for low-level lifting of vorticity-

rich outflow air (Markowski and Richardson, 2014a; Coffer and Parker, 2017). The currently proposed theory for this is the mid- and low-level mesocyclones can develop significant rotation at lower altitudes more efficiently than storms in environments with more substantial crosswise orientation of vorticity in their inflow layers (Coffer and Parker, 2015; 2018).

b. Vortex lines

Tornado development is associated with rapid intensification of surface-based vertical vorticity. For this to happen, air parcels with near-ground vertical vorticity must "participate" in the vertical acceleration associated with the supercell's rotating updraft (Markowski et al. 2011). Due to the prevalence of vorticity in supercells it is difficult to assess how this interaction occurs. However, a useful qualitative assessment of vorticity interaction can be made through the use of vortex lines (Fig. 3.1; Markowski and Richardson, 2009; 2014). Vortex lines are everywhere tangent to the local vorticity vector and so their orientation and evolution relies on vorticity

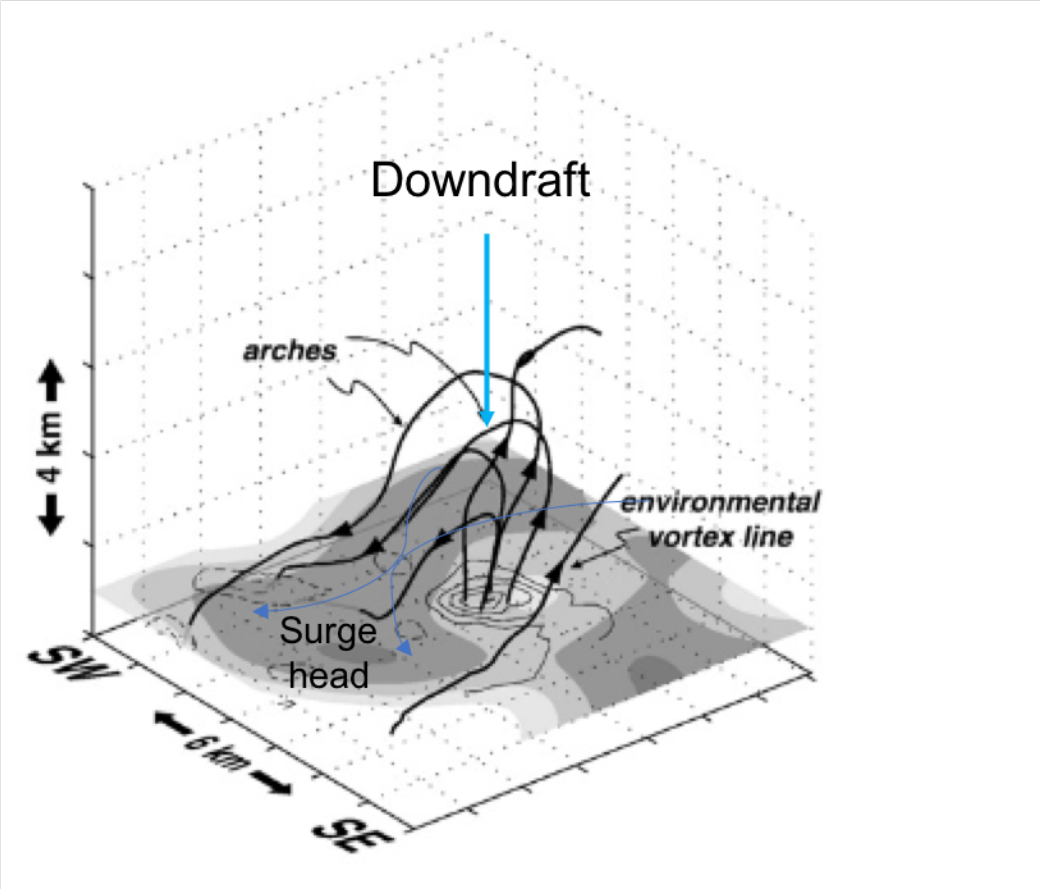

Figure 3.1: Vortex line arching over the downstream head of a supercell's outflow region. Surface is shaded by equivalent radar reflectivity (dBZ) at 1 km above ground. Vortex lines are black lines with arrow heads indicating the orientation of vorticity. The relative position of the downdraft and surge head are marked. Blue lines provide a sense of the near-surface streamlines emanating from the downdraft leading to counter-rotating vertically oriented vortices at the left and right flanks of the surge head. Figure adapted from Markowski and Richardson, 2009 and reprinted with permission from Springer.

tendency source terms in Eq. 3.1. Vortex lines are not material surfaces in baroclinic and viscous flows due to the generation of vorticity by these effects, which creates, severs and reconnects vortex lines (Markowski et al. 2008). Despite this, analysis of vortex lines in numerical and observed storms has provided insight into the structure of the vorticity field at low-levels in supercells (Markowski et al. 2012*a,b*). Notably, vortex line arches in downdraft regions of supercells has provided further supporting evidence for the theory of baroclinic generation of low-level rotation (Markowski and Richardson, 2014).

Due to the requirement that vortex lines must terminate at boundaries and not in the interior of a fluid, vortex lines in the atmosphere generally form loops such as those associated with baroclinic ring vortices generated by updrafts and downdrafts or extend "infinitely" in the horizontal such as those associated with environmental wind shear. Vortex lines must effectively terminate at the ground for rotation to form at the surface, which can be forced through viscous interaction of flow with the surface. Notably this can occur due to horizontal momentum surging caused by downward vertical transport of differential horizontal momentum. This introduces horizontal shear near the surface, which is associated with vortex lines that terminate at the ground.

It is well known that a tornado is, at least in part, a helical vortex structure associated with a vertical jet which erupts upward in the *corner-flow region* (e.g. Rasmussen et al. 1994; Davies-Jones 2015, section 1.1.4). Mass is drawn through the vortex by the updraft aloft causing vortex stretching and lowering surface pressure. Interestingly, however, vortex lines that terminate at the ground associated with baroclinic generation by a downdraft are crosswise in orientation. Vortices oriented crosswise relative to the flow, by definition, do not have mass flux through them. Therefore, while the surface-based vertical vorticity that precedes tornado

development is likely crosswise, it must interact with helical (streamwise) vortex lines that participate in the updraft in a way that causes mass flux through the surface-based vortex. Using vortex lines as a conceptual basis, Markowski and Richardson (2014) theorize vertically-arched, baroclinically-generated, vortex lines in a supercell outflow "sever and reconnect" with those associated with the storm's rotating updraft (Fig. 2.16). The dynamical mechanisms associated with the lifting of the surface-based vortex structure and the subsequent interaction with the helical flow of the updraft are not well understood.

c. Three-dimensional vorticity analysis

While analysis of vortex lines provides a useful qualitative assessment of vorticity field in a supercell and can be readily calculated from dual-doppler observations, the one-dimensional perspective does not explicitly help visualize the interaction of three-dimensional vortex structures. Total (three-dimensional) vorticity magnitude is another technique used to qualitatively study the evolution and interaction of vorticity structures in model realizations of supercells (Fig. 3.2; e.g. Odell et al. 2014, 94th AMS Annual Meeting; Orf et al. 2017). Orf et al. (2017) used volume and isosurface renderings of the three-dimensional vorticity field to highlight the importance of a dominant helical rotational structure that they termed the streamwise vorticity current, which intensified during tornadogenesis (Fig. 2.17).

Three-dimensional vorticity analysis has been used to demonstrate the structural differences in the vorticity field such as vorticity sheets associated with shear lines and vorticity tubes associated with discrete vortex centers (Fig. 3.2). Studying the evolution of the full three-

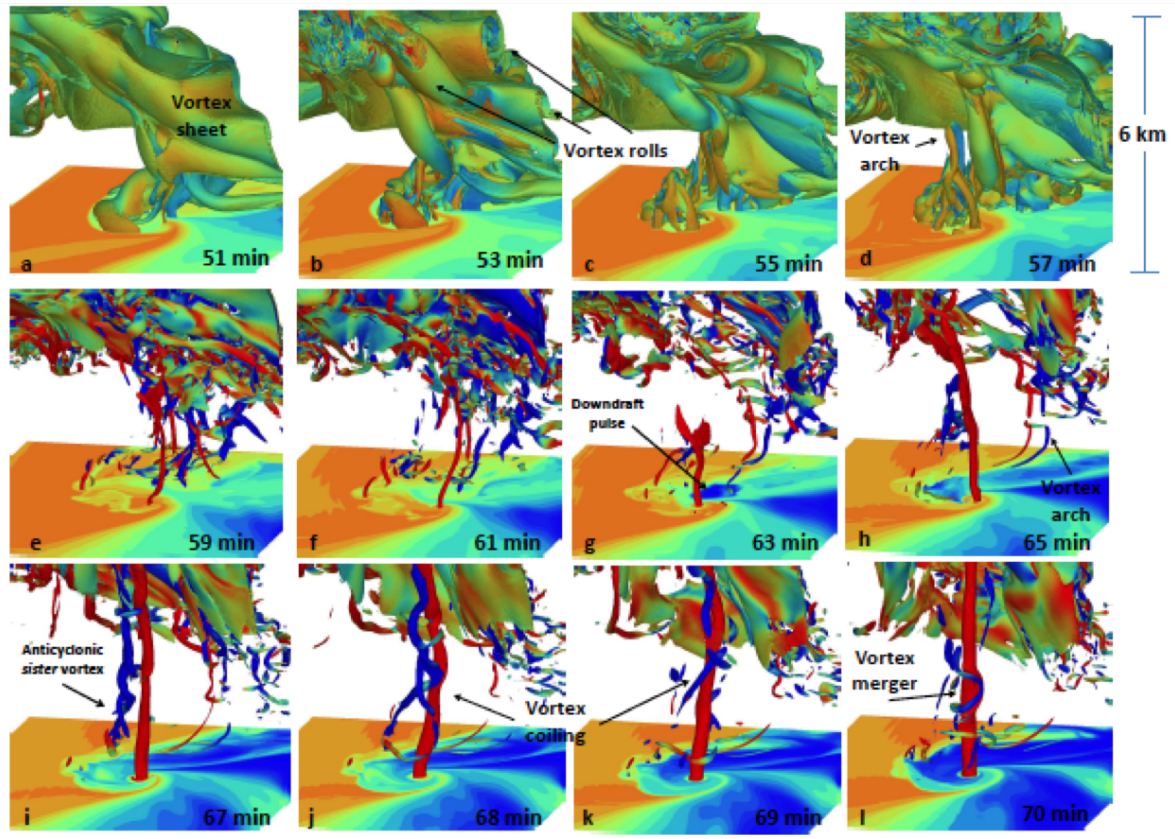

Figure 3.2: Total three-dimensional vorticity isosurface analysis during the genesis of a tornado-like vortex with the UWNMS model. In all panels, the surface is shaded by equivalent potential temperature with warmer colors indicating larger values, simulation time is indicated at the bottom right of every panel. In (a)-(d) vorticity is the three-dimensional isosurface at 0.05 s^{-1} shaded by the vertical component of vorticity. In (e)-(I) total vorticity isosurface is contoured at 0.15 s^{-1}. This analysis highlights the utility of studying the total vorticity field in the evolution of a supercell where a number of different vortex structures can be detected.

dimensional vorticity field is a powerful way to visualize the origins, interaction and intensification of vorticity in a supercell (e.g. Bernard, 2019).

d. Shortcomings of the vorticity framework for studying rotational structures in supercells

Despite these advancements, it is still unclear how or why some supercells rapidly contract and intensify its low-level rotation into a tornado while others do not. Almost all surface-based supercells have ample surface-based vertical vorticity required for tornadogenesis and numerous vorticity structures such as arches are common to both tornadic and nontornadic supercells (e.g. Markowski et al. 2008; Markowski and Richardson, 2014a). This gap in our understanding may partly result from the inability of vorticity analysis to distinguish between the intensification of shear and the development of rotational flow (e.g. Markowski et al. 2011). Because vorticity is a local measure of spin in a fluid, it is large in regions of substantial shear in the flow and in regions of strong rotation (e.g. Hunt, 1988; Kolar, 2007). Vorticity tendency analysis is therefore, unable to elucidate whether local vorticity intensification is associated with an increase in shear or the development of a discrete vortex. The rotational flow associated with a vortex requires centripetal acceleration resulting from pressure-gradient acceleration, while local maxima in shear do not (e.g. Rotunno and Klemp, 1985; Davies-Jones, 2002; Haller, 2005). As a result, the tendency of vorticity associated with air parcel trajectories does not directly provide information of how vorticity contributes to the overall *rotation* associated with vortex structures within a supercell. Furthermore, the orientation of rotational structures relative to the local flow (whether they are helical or crosswise) significantly impacts their characteristics and role in the evolution of a supercell's rotation. While three-dimensional vorticity analysis provides a good rough assessment of orientation and nature of vortex structures it does not

explicitly distinguish shear from rotation nor which vortices are helical and which are crosswise. From a diagnostic perspective, additional tools are required to distinguish rotation and its characteristics from the total vorticity field.

3.1.2 Relationships between vorticity, deformation and helicity

a. Momentum divergence and inertial balance

Vorticity in the atmosphere is a measure of local spin associated with air parcels resulting from gradients in the velocity of the flow. Vorticity is present in both regions of significant wind shift, which do not exhibit rotation or local pressure minima and vortex structures that do (e.g. Haller, 2005). This is because vorticity is only part of the total contribution to pressure (mass) forcing by the three-dimensional inertia-acceleration. To investigate this further it is useful to study momentum divergence through the use of the divergence equation.

The three-dimensional *anelastic* momentum equation governing fluid motion in supercells can be defined:

$$\frac{\partial \mathbf{v}}{\partial t} = -\mathbf{v}.\nabla\mathbf{v} + \frac{\rho'}{\overline{\rho}}g - \frac{1}{\overline{\rho}}\nabla p' + \mathbf{F} \qquad 3.3$$

In Eq. 3.3 the effects of Coriolis acceleration are neglected. A steady-state, Boussinesq reference atmospheric state is assumed (e.g. Klemp and Rotunno, 1983; Davies-Jones, 1984). It has been pointed out that the determination of this reference state is arbitrary and that a more physical partitioning can be achieved by splitting the momentum equations into hydrostatic and nonhydrostatic components (e.g. Davies-Jones, 2002; 2003). Additionally, the buoyancy term (second on the rhs of Eq. 3.3) in this form does not include the effects of the *back-reaction* produced by the interaction of a buoyant air parcel with its environment as it rises or sinks (e.g.

Krueger et al. 1996; Xu and Randall, 2001; Jeevanjee and Romps, 2015). To avoid this issue in buoyancy calculations, the pressure is often split into components associated with buoyancy and inertia, from which the buoyancy portion can be combined with third term on the rhs of Eq. 3.3 to form an 'effective buoyancy' term (Davies-Jones, 2003; Doswell and Markowski, 2004; Jeevanjee and Romps, 2015). However, for the purposes of studying rotational structures herein, Eq. 3.3 can be used with no loss of substance.

Taking the three-dimensional divergence of Eq. 3.3 gives:

$$\frac{\partial\left(\nabla\bullet\mathbf{v}\right)}{\partial t}=\frac{\partial DIV}{\partial t}=-\nabla.\left(\mathbf{v}.\nabla\mathbf{v}\right)+\nabla.B\mathbf{k}-\frac{1}{\bar{\rho}}\nabla^{2}p^{'}+\nabla.\mathbf{F} \qquad 3.4$$

Eq. 3.4 is the divergence tendency equation where DIV is divergence. The first term on the rhs of Eq. 3.4 is associated with the tendency of the flow to diverge due to inertia acceleration, the second term on the rhs is related to buoyancy-driven divergence, the third term is associated with local extrema in the pressure field and the last term is associated with frictional effects. Therefore, atmospheric divergence tendencies arise due to pressure gradient, gravitational (buoyant) and inertial forcing. Competing effects (terms with opposing signs in Eq. 3.4) between flow accelerations can lead to local cancelation of divergence tendency such as is the case in a hydrostatic atmosphere in which gravitational and pressure-gradient acceleration oppose one another. Perturbations from equilibrium states, in which one forcing dominates its opposing forcing, generates a divergence tendency. Divergence tendencies are associated with local density changes in a compressible flow, which results in a change in the local pressure field. Acoustic adjustment to divergence tendencies occurs through sound wave propagation and quickly equilibrates the flow to an anelastic state. Continued divergence forcing, for example; sustained buoyancy-induced stretching of a tornado in a supercell updraft, requires constant acoustic adjustment, which is why tornadoes can be "heard" via infrasound detection techniques

from thousands of miles away (e.g. Georges and Greene, 1975; Bedard and Georges, 2000). In the interest of studying coherent rotation evolving significantly slower than the speed of sound, it is adequate to ignore such effects and study the resulting (anelastically) adjusted effect on the structure of the pressure field.

Therefore, we can ignore the local divergence tendency and form the diagnostic pressure equation:

$$\nabla^2 p' = -\bar{\rho}\left[\nabla.\left(\mathbf{v}.\nabla\mathbf{v}\right)\right] + \bar{\rho}\frac{\partial B}{\partial z} \qquad 3.5$$

Viscous effects have been neglected in Eq. 3.5 due to their relative insignificance away from the surface. Eq. 3.5 is an elliptic partial differential equation for the perturbation pressure field. The lhs of Eq. 3.5, the Laplacian of the perturbation pressure, is positive when the combined effects of inertia and buoyancy terms on the rhs are positive. Such an elliptic solution to Eq. 3.5 implies low-frequency (slow-manifold) evolution of the perturbation pressure field associated with balanced flow (e.g. Knox, 1997; Bourchtein and Bourchtein, 2010). A quasi-steady mesocyclone associated with the rotating updraft of a supercell is an example of a flow in which the combined effects of buoyancy and inertia produce ellipticity of the perturbation pressure field. Misoscale rotational structures in a supercell primarily require a cooperative interaction between inertia and pressure gradient acceleration, which forms an *inertial* balance. Therefore, it is typical to ignore buoyancy effects to study their interaction with the perturbation pressure and write Eq. 3.5 (Bradshaw and Koh, 1981; Brandes, 1984; Davies-Jones, 2002):

$$\nabla^2 p' = -\bar{\rho}\left[\nabla.\left(\mathbf{v}.\nabla\mathbf{v}\right)\right] = -\bar{\rho}\left[e_{ij}e_{ij} - \frac{|\omega|^2}{2}\right] \qquad 3.6$$

. In Eq. 3.6, $e_{ij}e_{ij}$ is the square of the three-dimensional deformation tensor where $e_{ij} = \frac{1}{2}\left[\frac{\partial v_i}{\partial x_j} + \frac{\partial v_j}{\partial x_i}\right]$. In well-behaved flows (in which Green's theorem applies; e.g. Davies-Jones, 2002), positive Laplacian of perturbation pressure correlates with a local minimum in pressure. It can readily be seen then, that (the square of) the absolute magnitude of vorticity is associated with local minima in pressure and (the square of) the total deformation is associated with local maxima in pressure (e.g. Jeevanjee and Romps, 2015). This illuminates the well-understood concept that rotation (local maxima in vorticity and minima in deformation) is associated with local low pressure.

b. Shear vs. rotation

Armed with Eq. 3.6 it is possible to mathematically discuss the differences between shear and rotation in a fluid. To approach this, it is useful to consider an idealized region of pure shearing motion and an idealized region of pure rotational motion (Fig. 3.3). In this thought experiment we can assume that the magnitude of vorticity is equivalent in both regions. In the pure-shear region fluid parcels both rotate and deform through viscous interaction with neighboring parcels. However, in the region of pure rotation the parcels simply rotate and do not undergo deformation. This is to say that regions of shear are characterized by both deformation and vorticity, while the inertia field in pure rotational motion (*solid-body* rotation) is characterized by vorticity alone. From Eq. 3.6 we find that the deformation and vorticity terms exactly cancel in a region of pure shear such that the net acceleration of inertia imposed on the pressure field is identically zero. In the region of solid body rotation where the

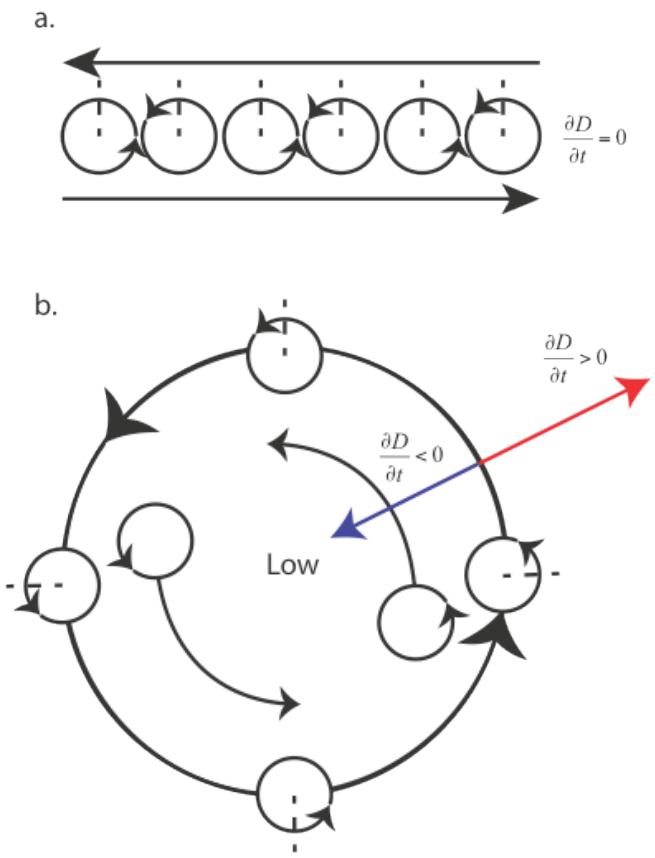

Figure 3.3: Conceptual diagram of a viscous fluid region of pure shear (a.) and solid body rotation (b.). Black arrows indicate nature of the flow field, white circles are fluid parcels with cyclonic vorticity, the blue arrow pointing toward the center of the vortex in b. is convergence tendency supplied by pressure gradient while the red arrow is divergence tendency resulting from inertia. If a *solid* particle was placed into the two flow regimes it would rotate in both cases. The key difference between these two flow configurations is that *fluid* parcels *do not* rotate in a. and thus do not supply a divergence tendency or pressure forcing, whereas they *do* rotate in b. and therefore provide opposing divergence forcing to that of the pressure gradient.

total deformation is zero and vorticity is large, there is a net positive divergence forcing imposed by inertia acceleration, which sustains the local pressure minimum associated with a vortex.

Deformation, therefore, negatively impacts the ability for a fluid to sustain a local pressure minimum and therefore the ability for the flow to rotate. Horizontal shearing zones that characterize gust fronts and convergence boundaries are associated with local vertical vorticity maxima but also local horizontal deformation maxima and so generate vortex sheets but not rotation unless it transitions from pure shearing motion into local *curved* flow that can support a pressure minimum. The deformation associated with a shearing zone of this nature is aptly referred to as *shearing deformation*. Fluid parcels may also deform through stretching effects associated with local momentum divergence referred to as *stretching deformation*. Stretching deformation is also referred to as irrotational strain (e.g. Kolar, 2007) or fluid extension (Rotunno and Klemp, 1982; 1985). Stretching deformation is responsible for the downscale turbulence kinetic energy cascade by breaking larger vortex structures down into progressively smaller structures (e.g. Wang et al. 2006). However, stretching of vorticity is also known to lead to intensification (Eq. 3.3). This seemingly paradoxical effect of stretching will be discussed in section 3.3.1.

A crosswise-oriented rotational structure is characterized by flow streamlines oriented perpendicular to the rotational axis and so experiences significant deformation along its interface. In the case of a crosswise vortex, no flow penetrates its core and so the flow is unable to intensify the rotation through stretching. A vortex must develop a helical component, in which flow penetrates the rotation to allow intensification through stretching effects. If this occurs, the vortex becomes progressively less susceptible to the detrimental effects of deformation of

viscous interaction with its relative flow field (Lily, 1983; 1986*a,b*; Brandes et al. 1988; Brooks et al. 1993).

c. Helicity

Helicity results from the correlation of the local velocity and vorticity vectors (Eq. 2.1). If the velocity vector and vorticity vector are everywhere parallel the flow is known as Beltrami (Davies-Jones, 1984; 2002). In such idealized flow, there is zero deformation and viscous dissipation of TKE is not possible (Lily, 1986*a,b*; 1990). Lily (1983;1986*a,b*) attributed the relative strength and persistence of a supercell's rotating updraft to the presence of significant helicity in its inflow layer that reduced the loss of energy through the effects of eddy viscosity (Bluestein, 1993). Through this stabilizing effect, the rotating updraft is able to acquire kinetic energy associated with its storm-relative flow such that there is, locally, an upscale growth of TKE of the disturbance.

If the storm-relative environmental shear is streamwise then a mass perturbation such as is generated by an updraft will acquire rotation (see section 2.2.1*b*). Rotation is associated with curving flow and inertial acceleration that supports a radial pressure gradient, which in effect *traps* the mass perturbation initially generated by buoyancy. Thus, convection evolving in an environment with significant streamwise vorticity or storm-relative helicity, will convert kinetic energy associated with the environmental wind shear into rotational kinetic energy of the storm's mesocyclone. On the other hand, the same buoyancy-driven mass perturbation associated with an updraft evolving in an environment entirely characterized by crosswise vorticity (zero helicity everywhere) will be rapidly lost via gravity wave dissipation, which is typical of ordinary-cell thunderstorms. Supercells interacting with significant low-level helicity are therefore able to

efficiently generate low-level updraft rotation. This concept will be important for the conceptual model of tornadogenesis presented in chapter four of this dissertation.

3.1.3 Current diagnostic solutions applied to supercells

a. Pressure minimum

Rotation of a fluid is necessarily associated with a local pressure minimum. Therefore, analysis of the perturbation pressure field has been used to study development of vortex structures in supercells (Eq. 3.7; e.g. Wicker and Wilhelmson, 1995; Grasso and Cotton, 1995; Noda and Niino, 2005; Mashiko, 2016).

$$\nabla^2 p' > 0 \cong p' < 0 \qquad 3.7$$

While pressure minimum is ultimately required for rotation it can be difficult to use for diagnosing rotational structures. Pressure fluctuations arise from a number of atmospheric effects including buoyancy-, acoustic- and inertia-effects. Analysis of the pressure field alone can therefore be difficult in determining the reason for the perturbation in highly baroclinic flow of a supercell, in which buoyancy-driven pressure perturbations are significant. Additionally, the pressure field is difficult to accurately calculate from remote sensing observations of supercells.

b. The Okubo-Weiss number

The knowledge that deformation in the flow is detrimental to sustained rotational structures has been understood for some time in a vast array of different fluid dynamic disciplines. Through theoretical work by Okubo (1970) and Weiss (1991), a parameter was developed to isolate

vertical rotation from the total vorticity field initially intended to isolate the rotational part of quasi-two-dimensional ocean eddies, which was later termed the Okubo-Weiss number (W ; Eq. 3.8).

$$W = \zeta^2 - D_H{}^2 \qquad 3.8$$

In Eq. 3.8, D_H is total *horizontal* deformation including shearing and stretching effects. If the magnitudes of deformation and vorticity are both non-zero but equal then the vertical vorticity is entirely associated with shear. If the horizontal deformation is zero but the vorticity is non-zero then the flow about the vertical axis is in solid-body rotation. If the vorticity is zero but the deformation is non-zero the flow is purely deformational. The Okubo-Weiss number is calculated along a constant height surface such that an implicit assumption of rotation in a horizontal plane is made. W has recently been employed in supercell literature to distinguish rotation associated with the developing tornado vortex from the total vorticity field (e.g. Markowski et al. 2011; Atkins et al. 2014; Coffer and Parker 2017).

While the Okubo-Weiss parameter accurately isolates rotation about the vertical axis from the total vertical vorticity field it is not useful for studying three-dimensional rotational structures that are partly or wholly horizontally oriented. Evidenced by the recent identification of the SVC by Orf et al. (2017), the study of such three-dimensional rotational structures is likely critical to our understanding of supercell tornadogenesis.

c. The kinematic vorticity number

In two-dimensional flow, most methods for identifying rotation are dynamically equivalent to the Okubo-Weiss number (Eq. 3.6; Wu et al. 2005, pp. 310-321; Dahl, 2017). Which, in effect, is a measure of how much vorticity prevails over the deformation (strain rate). For studying three-

dimensional structures, the Okubo-Weiss number is insufficient. The problem of identifying a vortex in three-dimensions becomes significantly more complex due to the consideration of *axial strain* (deformation perpendicular to the vortex axis; Wu et al. 2005, pp. 318-321). In a qualitative sense, the relative local magnitudes of deformation and vorticity at a point in the flow can be compared to assess the *quality* of local rotation, which is known as the kinematic vorticity number (N_k ; Truesdell, 1954; Haller, 2005; Schielicke, 2016; Dahl 2017).

$$N_k = \frac{||\omega||}{||D||} \qquad 3.9$$

In Eq. 3.9, $\|\omega\|$ and $\|D\|$ are the absolute magnitudes of total vorticity and deformation respectively. Eq. 3.9 does not quantitatively measure the intensity of rotation and like many other techniques (see section 3.2.1), it suffers bias in regions of significant axial strain (see section 3.2.1).

d. Computational methods

The problem of three-dimensional vortex detection is critical in the study of computational fluid dynamics (CFD). A number of algorithmic methods have been developed for this purpose from fundamental fluid dynamics theory (e.g. Sujudi and Haimes, 1995; Roth and Peikert, 1998; see section 3.2.1) and have been shown to be useful for isolating vortex structures in supercell simulations (e.g. Orf et al. 2007). However, these methods have been used relatively infrequently to date. One reason for this may be, until recently, our ability to adequately numerically resolve misoscale rotational structures and their interactions in supercells has been limited. Another

possibility is that our theoretical approach to understanding tornadogenesis has not demanded such tools.

Part II. Theoretical dynamics of fluid rotation

3.2.1 Vortex identification

a. Identifying rotational structures

A necessary consideration for identifying vortex structures in complex flows is dependence on frame of reference. The total vorticity magnitude is a Galilean *invariant* (frame-independent) property of the flow and so therefore, ideally, the definition of a vortex structure should be too. For example, although the identification of spiraling streamlines is a good heuristic approach to detecting a vortex (Lugt, 1979), streamlines are not Galilean invariant and so the actual swirling strength and orientation cannot be determined by this technique. Similarly, partitioning total vorticity into *shear* and *curvature* vorticity components in a normal coordinate system (e.g. Bell and Keyser, 1993) or calculated along isobaric-(e.g. Viudez and Haney, 1996) and height-surfaces (e.g. Dahl, 2017) are all Galilean *variant* techniques. Flow doesn't move along isobaric or height surfaces and therefore the decomposition of vorticity into shear and curvature components along these surfaces is arbitrary. Additionally, calculating shear and curvature vorticity along streamlines is another arbitrary decomposition because the vortex does not move with the mean flow and so whether the vorticity is locally associated with shear or rotation and therefore its resulting inertial forcing of the pressure field is not adequately resolved by this

partition (Fig. 3.4). Through Eq. 3.6 and discussion in section 3.1.2*b* it is readily apparent that only flow exhibiting elliptic curvature in absolute three-dimensional space can supply the opposing inertial forcing to support a local pressure minimum associated with rotation. Shear is not associated with a tendency for the flow to diverge and so has no net forcing on the pressure field. Arbitrary decompositions of the vorticity field into shear and curvature parts can lead to misleading conclusions about the relative quantities and roles of shear and curvature.

Therefore, a number of Galilean invariant techniques have been developed in the fluid dynamics literature to attempt to elucidate the true rotational motion from the total vorticity field. A popular technique is the Q-criterion (Eq. 3.10; Hunt et al. 1988), which is a three-dimensional variation of the Okubo-Weiss number and follows from Eq. 3.6.

$$Q = \frac{1}{2}\left[\left\| \boldsymbol{\Omega} \right\|^2 - \left\| \mathbf{S} \right\|^2 \right] \qquad 3.10$$

In Eq. 3.10, ω has been replaced by $\boldsymbol{\Omega}$, which is the antisymmetric part of the *velocity gradient tensor* ($\nabla \mathbf{v}$) or *vorticity tensor,* $\boldsymbol{\Omega} = \frac{1}{2}\left[\nabla \mathbf{v} - \left(\nabla \mathbf{v} \right)^{\mathbf{T}} \right]$, and is equivalent to the total vorticity magnidtude. D has been replaced by $\mathbf{S}$, which is the symmetric part of the velocity gradient tensor, the *deformation tensor*, $\mathbf{S} = \frac{1}{2}\left[\nabla \mathbf{v} + \left(\nabla \mathbf{v} \right)^{\mathbf{T}} \right]$, and is equivalent to the total magnitude of deformation. Q is positive for regions in which the total three-dimensional vorticity magnitude (rate of rotation) dominates the three-dimensional deformation (rate of deformation or *strain*). The net divergence forcing by inertia must be then be positive implying elliptically flow curvature, which necessarily has to be associated with a local pressure minimum.

Still, there are some drawbacks to using Q to identify coherent vortex structures. Of primary interest here is the fact that this criterion does not allow for arbitrary axial strain. For

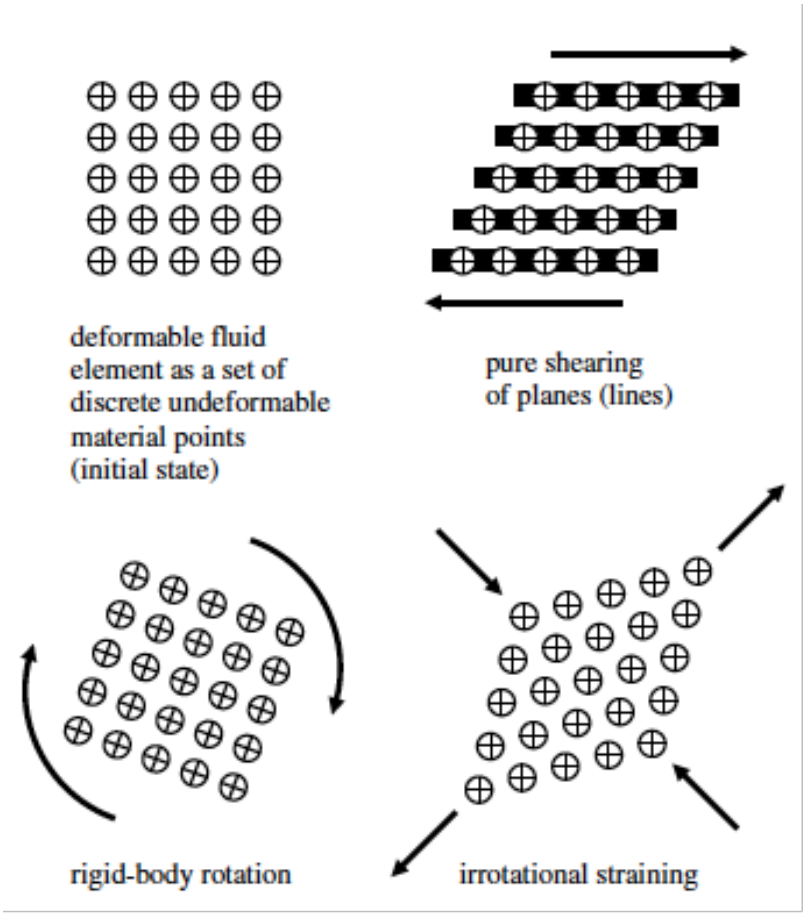

Figure 3.4: Kolar (2007) depiction of the Triple Decomposition Method (TDM). Material points in the flow are represented by white circles with black crosses, several of these make up a deformable fluid element (top left panel). The flow can be split into pure shear (top right), solid-body rotation (bottom left) and irrotational straining motion (bottom right). The vector associated with solid-body rotation is the vector associated with the portion of vorticity responsible for divergence tendency that can resist pressure gradient-induced convergence tendency. Figure reprinted with permission from the International Journal of Heat and Fluid.

example, in the case of a vertically-oriented vortex that is experiencing intense vertical stretching, the magnitude of the total three-dimensional deformation is large and may exceed the magnitude of the total three-dimensional vorticity. This in fact, through the stretching term in the vorticity equation, would strengthen the vortex and yet Q would be negative in these regions exhibiting a broken structure where in fact the vortex and sectional pressure minimum is still present. This has motivated additional research to define a three-dimensional vortex diagnostic that does not suffer this drawback. One approach taken by Jeong and Hussain (1995) was to decompose the inertia contribution to the pressure field into symmetric and antisymmetric components:

$$\underbrace{\frac{1}{\rho}p_{,ij}}_{\text{pressure tensor}} = \underbrace{\left(\frac{D}{Dt}S_{ij} + \Omega_{ij}\Omega_{kj} + \mathbf{S}_{ik}\mathbf{S}_{kj}\right)}_{\text{symmetric}} + \underbrace{\left(\frac{D}{Dt}\Omega_{ij} + \Omega_{ik}\mathbf{S}_{kj} + \mathbf{S}_{ik}\Omega_{kj}\right)}_{\text{antisymmetric}} \qquad 3.11$$

In Eq. 3.11, the components of the deformation and vorticity tensors are associated with $\mathbf{S}$ and Ω above. For a voriticty-induced pressure minimum to exist in a plane of motion, λ_2 must be negative (e.g. Jeong and Hussain, 1995; Wu et al. 2005, pp. 313).

$$\lambda_2 = \mathbf{S}\cdot\mathbf{S}^{\mathrm{T}} - \Omega\cdot\Omega^{\mathrm{T}} \qquad 3.12$$

However, while shown to be an improvement on the Q-criterion, λ_2 can also exhibit unphysical disjointedness in some regions of highly turbulent flow (Wu et al. 2005, pp. 316).

To further improve on the shortcomings of the Q and λ_2 criteria, Kolar (2007) employed a theoretical technique called the triple decomposition method (TDM). The TDM decomposes relative motion near a point in the flow into rotational, irrotational strain and shearing components (Fig. 3.4). From this qualitative theory, Kolar defined a "residual vorticity" vector ($\vec{\omega}_{RES}$; Eq. 3.13) by extracting an effective pure shearing motion from the total vorticity to

isolate the motion associated with solid body rotation. This was achieved by splitting the velocity gradient tensor into parts associated with shear ($\omega_{SH} = \mathbf{S}_{SH}$), residual (irrotational) strain following the removal of shear ($\mathbf{S}_{RES}$) and residual (solid-body) vorticity (ω_{RES}).

$$\vec{\omega}_{RES} = \omega - \omega_{SH} = \left(\operatorname{sgn}\omega\right)\left[\left|\omega\right| - \left|S\right|\right] \quad \text{for } \left|S\right| \le \left|\omega\right| \qquad 3.13$$

In Eq. 3.13, $\operatorname{sgn}\omega$ is the sign of the total vorticity (either positive or negative) in the plane of solid-body rotation as defined by ω_{RES}, which determines the direction of the rotation relative to the plane of swirl. This technique adequately determines the direction and magnitude of a vortex. However, determining the plane of effective shearing motion in order to remove it from the total vorticity field requires an expensive optimization process at each point in the flow, which limits its applicability (Liu et al. 2018, herein L18).

L18 recently developed what should probably become the gold standard for identifying vortex structures in fluids from a Eulerian perspective, which they called the "Rortex" vector ($\vec{\mathbf{R}}$; Eq. 3.14). Again, the underlying method was to decompose the total vorticity vector into a shear ($\vec{\mathbf{S}}$) component and a curvature ($\vec{\mathbf{R}}$) component:

$$\nabla \times \mathbf{v} = \vec{\mathbf{R}} + \vec{\mathbf{S}} \qquad 3.14$$

To find , L18 rotate the velocity gradient tensor, $\nabla\mathbf{v}$, from an original *xyz*-frame to a new *XYZ*-frame using a rotation matrix, M, such that the solid-body rotation axis vector, $\vec{r}$, is parallel to the Z-axis (Eq. 3.15). This condition is met in the plane in which there is no shear in the perpendicular axis, $\frac{\partial u}{\partial Z} = 0$ and $\frac{\partial v}{\partial Z} = 0$. L18 employ the real Schur decomposition method (Schur, 1909) to prove the existence of the axis of rotation, $\vec{r}$.

$$\vec{r} = M^T \begin{bmatrix} 0 \\ 0 \\ 1 \end{bmatrix} \qquad 3.15$$

Once this axis has been determined, the two-dimensional deformation and vorticity are calculated in that plane to determine a magnitude of the Rortex vector. This is done using the new reference frame (*XYZ*) such that the total deformation, α, is:

$$\alpha = \frac{1}{2}\sqrt{\left(\frac{\partial v}{\partial Y} - \frac{\partial u}{\partial X}\right)^2 + \left(\frac{\partial v}{\partial X} + \frac{\partial u}{\partial Y}\right)^2}$$

and vorticity, β, is:

$$\beta = \frac{1}{2}\left(\frac{\partial v}{\partial X} - \frac{\partial u}{\partial Y}\right)$$

$\vec{\mathbf{R}}$ is defined:

$$\vec{\mathbf{R}} = R\vec{r} \qquad 3.16$$

Where,

$$R = \begin{cases} 2\left(\beta - \alpha\right), & \text{if } \alpha^2 - \beta^2 < 0,\ \beta > 0, \\ 2\left(\beta + \alpha\right), & \text{if } \alpha^2 - \beta^2 < 0,\ \beta < 0, \\ 0, & \text{if } \alpha^2 - \beta^2 \geq 0 \end{cases}$$

In summary, the Rortex vector is defined by finding the plane in which the solid-body component of fluid motion resides (if one exists) and determining its magnitude by subtracting the effects of total deformation in that plane. This technique does not suffer from the same bias as Q and λ_2 in regions of intense axial strain because it simply calculates the deformation in the plane of rotation (i.e. ignores the deformation in the axial direction). As a result, unlike many of the other techniques outlined in the preceding pages of this chapter, the choice of magnitude of

$\vec{\mathbf{R}}$ for contouring purposes is not arbitrary. Any *connected* region of $\vec{\mathbf{R}} \neq 0$ is characterized by fluid rotation and therefore can be called a "vortex".

However, like any local vortex definition, the user must determine a *scale* at which to apply it. Every physical atmospheric vortex is made up of smaller scales, which may not necessarily have the same characteristics as the global flow in which it is embedded. For example, a tornado vortex can reasonably be assumed to be in cyclostrophic balance, which would imply the flow in the vortex core is in steady solid-body rotation. However, it is well known that tornadoes contain smaller suction-type vortices among other inhomogeneities and therefore is made of up of regions of more intense and less intense rotation. Of course, a vortex such as a tornado is never really "balanced" or it would never develop, intensify or weaken. Through the interaction of compressible and viscous effects imposed by friction and buoyancy accelerations, even a single isolated vortex will continually be forced away from true inertial balance. All atmospheric vortices, independent of scale, are fractal phenomena, made up of progressively smaller scales each with their own governing dynamics based on the Navier-Stokes equations all the way down to the molecular scale of motion. Or more eloquently put by Lewis Fry Richardson,

Big whirls have little whirls that feed on their velocity

and little whirls have lesser whirls and so on to viscosity.

Part III. Extending theory to supercell dynamics

3.3.1. Diagnostics and considerations

a. Application of the Q-criterion as the square of the inertial frequency

This chapter has thus far set out theoretical basis for decomposing the three-dimensional inertia into rotational and deformational components to study the ability of the flow to *resist* pressure gradient acceleration, which permits inertial balance that supports rotational flow. This ability can be measured for three-dimensional flow by Q (Eq. 3.10). The stability of rotational flow depends the relative equilibrium between pressure gradient and inertia acceleration ($\nabla^2 p' \cong Q$). This equilibrium is the basic atmospheric 'infrastructure' for building a vortex on the supercell-scale. This relationship does not hold for vorticity magnitude alone. Interestingly, while Q suffers some drawback for objectively determining vortex structure in complex turbulence, it contains the complete three-dimensional inertial contribution to momentum. Let us return for a moment to the hypothetical scenario of a vertically-oriented vortex undergoing intense axial stretching by an updraft. If such a region is characterized by greater deformation magnitude vs vorticity magnitude, $Q < 0$. This is not inaccurate, the inertia forcing of momentum divergence truly is dominated by linear momentum acceleration in this region, which is what is driving the local stretching. If it wasn't for the updraft acceleration in this region, which provides the source for the linear momentum acceleration and therefore stretching deformation imposed on the rotation, the vortex would be destroyed in this region because the deformation-dominated flow is associated with local perturbation high pressure. However, the buoyancy is also providing a stabilizing influence through its associated $\nabla^2 p' > 0$, which offsets

the negative effects of the deformation. It is, therefore, difficult to separate the effects of buoyancy and inertia to study the evolution of vortex structures in highly baroclinic flow. This will be returned to in part b of this section.

Following the preceding discussion, it is useful to recast Eq. 3.5 in a manner similar to Brandes (1984):

$$\bar{\theta}\nabla^2\pi' = -\nabla\cdot\left(\mathbf{v}\cdot\nabla\mathbf{v}\right) + \frac{g}{\bar{\theta}}\frac{\partial\theta'}{\partial z} \qquad 3.17$$

Eq. 3.17 is defined by taking the three-dimensional divergence of the momentum equations in perturbation Exner-function (π') form (e.g. Brandes, 1984). θ is potential temperature with mean ($\bar{\theta}$) and perturbation (θ') parts and g is gravitational acceleration. Coriolis, friction and compressible effects have been ignored to form Eq. 3.17. It is possible to write Eq. 3.17:

$$\nabla^2\pi' = \frac{I^2}{\bar{\theta}} + \frac{1}{\bar{\theta}}\left(\frac{g}{\bar{\theta}}\frac{\partial\theta'}{\partial z}\right) \qquad 3.18$$

Where $\frac{g}{\bar{\theta}}\frac{\partial\theta'}{\partial z}$ is similar to the square of the buoyancy frequency and I^2 is herein referred to as the square of the inertial frequency. This rather simple relationship between inertia, buoyancy and pressure a useful way to understand flow stabilities in a mesoscale baroclinic atmosphere. Where the collective contribution to the rhs of Eq. 3.18 is positive, periodic solutions exist for π' indicating stable, oscillatory motions (such as gravity waves, inertia-gravity waves or inertial oscillations). Where the collective contribution to the rhs is negative, hyperbolic solutions for π' result, indicating unstable, growing disturbances. If the magnitude of the local vertical perturbation potential temperature gradient is large, the atmospheric motions are likely governed by buoyancy dynamics. If its sign is positive and exceeds the magnitude of I^2, this will result in *local* hydrostatic stability supporting gravity wave (buoyancy oscillations). If its sign is negative

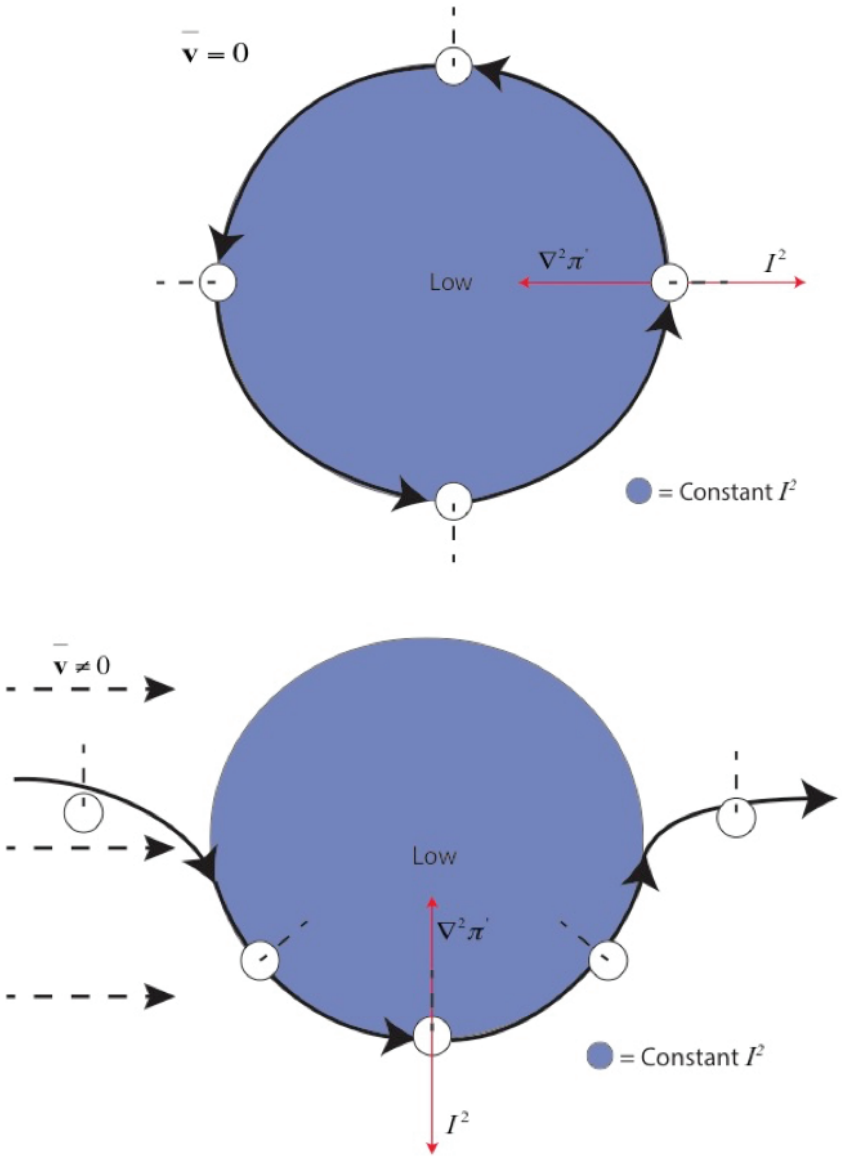

Figure 3.5: Conceptual diagram of an isolated cyclonic vortex in solid body rotation (a.) and the same vortex embedded in mean flow (b.). Solid black arrows indicate streamlines, dashed arrows in b. are mean flow vectors, white circles are fluid parcels and dashed lines are to indicate orientation of fluid parcels. The blue shading is a region of constant positive I^2 and 'Low' indicates center of low pressure. Red arrows indicate the divergence forcing associated with pressure gradient ($\nabla^2\pi'$) and inertia (I^2).

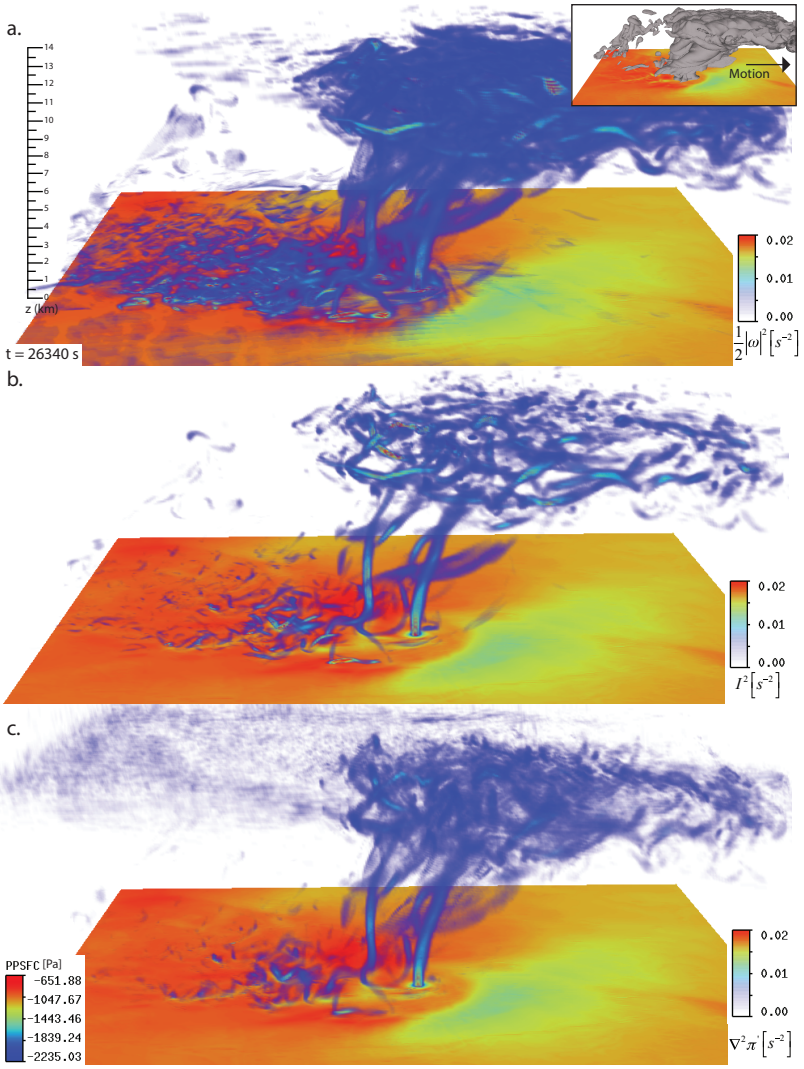

Figure 3.6: Oblique view from the south at the mature stage of a numerical simulation of the Goshen County, Wyoming tornadic storm of June 5, 2009. Each panel is the same simulation time of t = 26340 s (the insert in a. is an isosurface of total precipitation and cloud water, which illustrates the three-dimensional structure of the full storm). As in Fig. 3, the UWNMS is used with a nested grid domain, but in this case the model run is initialized with North American Regional Reanalysis Data. The third nested (fourth) grid is being viewed here, which has 120 m horizontal resolution. The surface in is shaded by pressure perturbation (PPSFC), half of the square of the total vorticity magnitude ($\frac{|\omega|^2}{2}$) is plotted as a volume rendering in a., the square of the inertial frequency, I^2 and the Laplacian of the nonhydrostatic pressure $\nabla^2\pi'$ are plotted using volume rendering with an identical scale in b. and c. respectively. I^2 and $\nabla^2\pi'$ exhibit significant differences to $\frac{|\omega|^2}{2}$. Three-dimensional dynamic balance between I^2 and $\nabla^2\pi'$ is evident supporting vortices within the storm, however only a portion of the vorticity is involved with these structures.

and exceeds the magnitude of I^2, buoyancy-driven instabilities such as convective updrafts and downdrafts will result. On the other hand, I^2 is proportional to the gradient of absolute angular momentum (I^2; Pendergrass and Willoughby, 2009), and so too, is a measure of stability.

$$I^2 = \frac{1}{r^3}\frac{\partial M_A}{\partial r} \qquad 3.19$$

r in Eq. 3.19 is radius from the axis of rotation. Regions in which I^2 dominates the rhs of Eq. 3.18 are dominated by inertia-dynamics. For example, large and positive regions I^2 indicates the azimuthal flow stability associated with a vortex. Conversely, where I^2 is large and negative regions of I^2 indicates strongly deformational (unstable) flow.

In this context, I^2 is a useful atmospheric parameter through which we can study the stability of rotational flow in a supercell. For example, Fig. 3.6 demonstrates how the square of the inertial frequency (I^2) nearly identically matches the $\nabla^2\pi'$ field in the three-dimensional flow of a numerically simulated supercell thunderstorm. Numerous vortex structures in the simulated supercell storm are depicted with total vorticity magnitude but not all are associated with a pressure tendency or minima. The use of I^2 not only has a superior fundamental basis but is also significantly more efficient than total vorticity magnitude at locating rotational regions of the flow with a supporting pressure field.

Further, comparing the positive part of I^2 to the total vorticity magnitude (Eq. 3.20) provides a useful metric of the proportion of vorticity actively supporting local pressure gradient acceleration. This is referred to as the pressure-efficiency diagnostic because it determines how efficient the inertia is at maintaining local pressure gradients.

$$P_{eff} = \frac{\max\left(0, I^2\right)}{\frac{1}{2}\left|\omega\right|^2} \qquad 3.20$$

P_{eff} refers to the local geometry of the flow; the greater the degree of local elliptic curvature, the closer P_{eff} is to unity. $P_{eff} = 0$ implies no net divergence tendency results from inertia, which says that (in the absence of intense axial stretching by buoyancy) vorticity is entirely associated with shear. $P_{eff} = 1$ indicates solid body rotation. Therefore, P_{eff} is a measure of how close the flow is to solid-body rotation.

b. Rotational vorticity vector

Buoyancy gradients may impose intense acceleration and axial strain that results in vortex stretching. In this scenario, the magnitude of the buoyancy-driven deformation can exceed the magnitude of vorticity. Although parcels will be elongated in the direction of the acceleration they can still follow curved trajectories as is the case with strongly stretched helical rotational structures such as the SVC. As outlined in section 3.2.1, it is possible to define diagnostics of rotation that do not suffer from the bias associated with axial strain. A simplification of Eq. 3.13 for computationally expensive supercell simulations is presented below, which will be referred to as *rotational vorticity*.

Following recent methodology in fluid dynamics (e.g. Kolar, 2007), the total deformation and total vorticity fields can be decomposed into parts associated with shear (D_{shear} ; ω_{shear}), irrotational strain (fluid extension; D_{irot}) and rotation (ω_{rot}). This is performed by starting with I^2 split into these respective components.

$$I^2 \cong \omega_{rot} + \omega_{shear} - D_{shear} - D_{irot} \qquad 3.21$$

Because $|\omega_{shear}| = |D_{shear}|$, the square of the inertial frequency depends simply on $I^2 \cong \omega_{rot} - D_{irot}$

Where rotational vorticity is defined (following Kolar, 2007) as $\omega_{rot} = \omega - \omega_{shear}$.

Rotational vorticity (ω_{rot}) is a Galilean invariant property of the flow. It separates vorticity associated with rotation from the total vorticity such that it defines the portion of vortex lines associated with rotation. It is unaffected by irrotational strain (stretching deformation) and so it is able to identify three-dimensional rotation in buoyancy (or dynamically) accelerated flow even in regions of intense stretching where I^2 can suffer bias.

It is possible to define a vector quantity for rotational vorticity that defines the direction of rotation, which is readily calculated on a standard cartesian model grid. This is done by subtracting the shearing deformation magnitude from the vorticity in each plane about a point in the flow and multiplying by the sign of the vorticity in each plane:

$$\vec{\omega}_{rot} = \left[\sqrt{\left(\max\left(0, |\omega_x|^2 - |\mathbf{S}_{SH,x}|^2\right)\right)} \cdot \operatorname{sgn}\omega_x\right]\hat{i} + \left[\sqrt{\left(\max\left(0, |\omega_y|^2 - |\mathbf{S}_{SH,y}|^2\right)\right)} \cdot \operatorname{sgn}\omega_y\right]\hat{j}$$
$$+\left[\sqrt{\left(\max\left(0, |\omega_z|^2 - |\mathbf{S}_{SH,z}|^2\right)\right)} \cdot \operatorname{sgn}\omega_z\right]\hat{k} \qquad 3.22$$

From Eq. 3.22, it is readily seen that $\vec{\omega}_{rot}$ is simply equal to the three-dimensional vorticity vector for flow in solid body rotation. By neglecting the effects of deformation, $\vec{\omega}_{rot}$ incurs a useful quality that none of the other methods discussed in this chapter possess. Rotational vorticity is a vector field and a subset of the total vortex lines in the flow, therefore traditional vortex line analysis can be combined with rotational vorticity lines to determine where the vorticity in a supercell acquires rotation. It is pertinent to draw attention to, however, that while the above planar decomposition of rotational vorticity is a very efficient method of calculation it incurs Galilean variance. The Galilean-invariant alternative is the Kolar (2007) method, which

appears not to be a reasonable method for calculating the parameter in large-data supercell simulations. It is asserted that the differences between these methods is negligible, but in future work it will be necessary to demonstrate this numerically.

c. Dynamic considerations of rotation in buoyancy-forced flow

The preceding analysis shows that a portion of the vortex lines in a given fluid volume are associated with shear and a portion are associated with rotational flow. The significance of this is that while vortex lines must not begin or end in the interior of a fluid, rotation can. If one were to define the rotational flow of a vortex using traditional vortex lines, they are put in the awkward position of saying that a vortex does not have "ends". However, rotation of the three-dimensional flow associated with a local concentration of vortex lines may have a finite length. This concept can be illustrated by starting with a theoretical field of equidistant vortex lines in an inviscid, inertial flow such as would be found in a region of constant shear (Fig. 3.7a). Locally "bundling" the vortex lines in a symmetric fashion relative to those surrounding this region demands local flow rotation (curvature) in response and an accompanying pressure minimum to provide a supporting centripetal acceleration. In this idealized thought experiment the vortex lines extend infinitely (do not have ends) but a local region of rotation exists along their length where they have been concentrated (Fig. 3.7b). There is now a local region of fluid rotation with finite length. A physical example of this idealized thought problem is a supercell's mesocyclone. Vortex lines in the background environment are horizontally oriented and entirely associated with vertical wind shear (assuming negligible horizontal shear). The vortex lines are tilted and subsequently stretched to form local rotation in the vicinity of the mesocyclone where they are bundled together and eventually, they return to being associated entirely with shear in the far-

field environment. Thus, we can partition the vortex lines into parts associated with shear and parts associated with rotation.

Continuing with this thought experiment, in the radial direction relative to the axis of rotation we can reasonably assume that some compensatory relationship (degree of balance) exists between pressure gradient acceleration ($\frac{1}{\rho}\nabla p'$) and advection ($\mathbf{v} \bullet \nabla \mathbf{v}$; inertial or *centrifugal* acceleration, Fig. 3.8). However, in the axial direction a pressure gradient exists directed toward the center without an opposing acceleration. If we integrate forward in time from Fig. 3.7b, even in an inviscid flow the central pressure minimum will be eroded by axial mass convergence and the local rotation will weaken and eventually be destroyed (Fig. 3.8b). For larger scale disturbances such as tropical cyclones the central pressure minimum associated with its rotational flow is protected from destructive axial mass entrainment by static stability forming quasi-two-dimensional rotation. This is not the case in thunderstorm-generated vortices as the flow tends to be moist adiabatic in the buoyant updraft regions, which implies that misoscale rotational structures are fundamentally three-dimensional. Therefore, the maintenance and intensification of convective rotational structures is dependent on updraft forcing that can prevent destructive axial mass convergence.

Significant updraft acceleration in supercells can subject rotational flow to intense vertical stretching. Discussed earlier in this section, the deformation (irrotational strain) magnitude may exceed the vorticity in these regions. Fluid parcels associated with such helical structures will be deformed as they are accelerated vertically but will also follow curved trajectories as long as the total Laplacian of perturbation pressure is positive ($\nabla^2 p' > 0$) and there is non-zero rotational vorticity (Eq. 3.22; Fig. 3.9). Considering only the dynamic portion of the nonhydrostatic pressure or the full inertial forcing such as is done by many of the

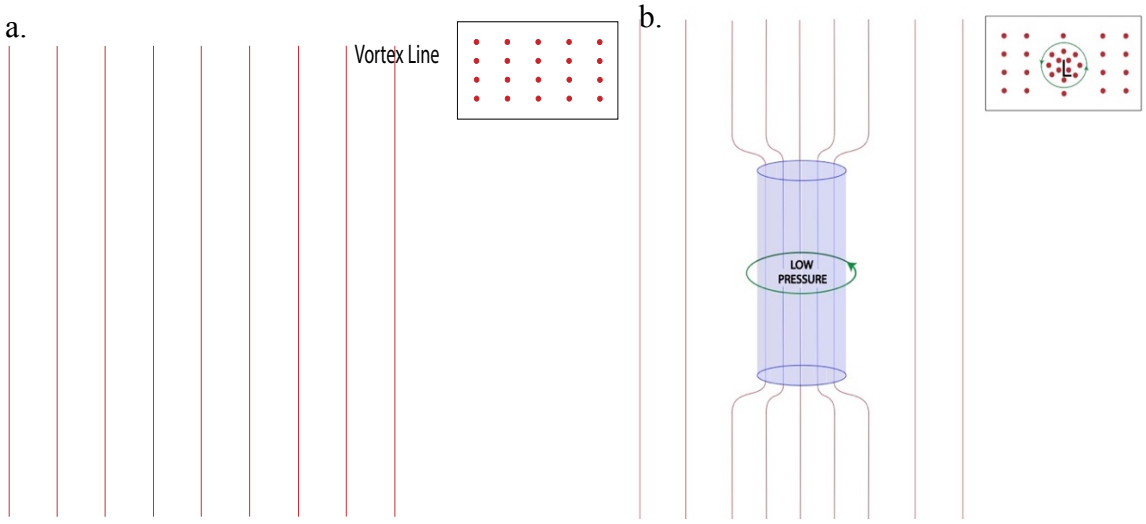

Figure 3.7: Theoretical diagram of vortex line concentration. (a) field of equidistant vortex lines (red lines), inset demonstrating three-dimensional nature of vortex lines. (b) local, symmetric concentration of vortex lines requiring central pressure minimum (blue shaded region) and flow curvature (green arrow).

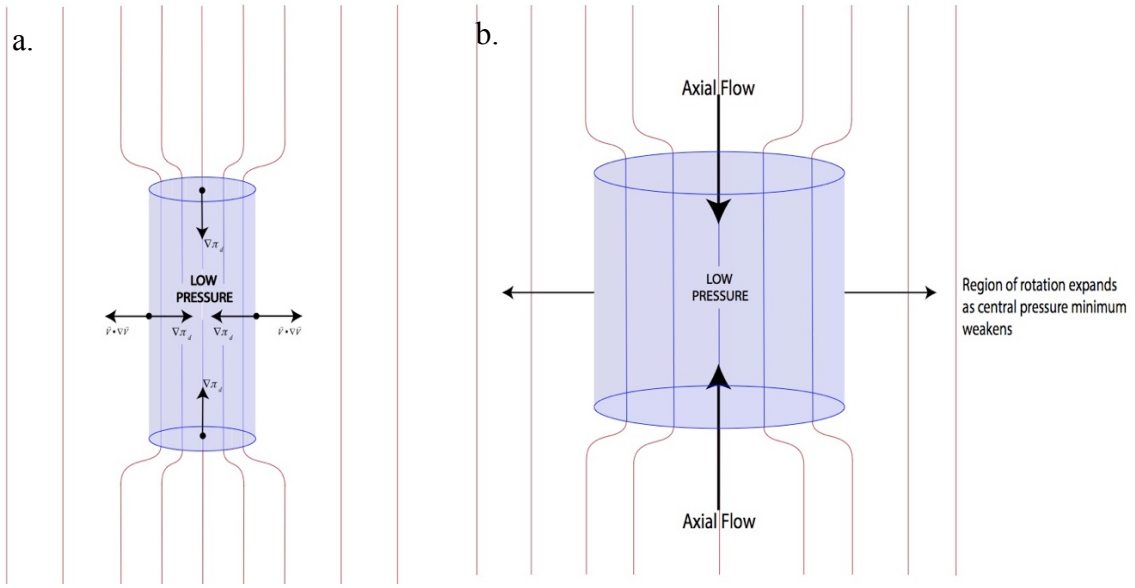

Figure 3.8: Theoretical diagram of three-dimensional unforced vortex evolution. Same as Fig. 3.7 but now considering the evolution of rotational flow. If some arbitrary forcing causes local vortex line concentration as in Fig. 3.7 but then abates, then central pressure minimum will produce an unmatched axial pressure gradient directed towards the center of the region of rotation. Axial mass convergence will raise the central pressure and weaken the region of rotation until it becomes entirely divergent.

diagnostics presented earlier in this chapter can therefore be misleading when diagnosing rotation in baroclinic flow. While the dynamic portion of the Laplacian of nonhydrostatic pressure may be negative ($\nabla^2 p'_d < 0$) owing to substantial deformation in a region of intense stretching, the full Laplacian of perturbation pressure may still be positive owing to the effects of buoyancy. In these regions, the buoyancy contribution to the perturbation pressure can offset the portion of nonhydrostatic pressure associated with deformation and maintain the rotational component of the flow in three-dimensions. Fig. 3.9a illustrates this process by modifying the thought experiment in Figs.3.7,3.8 by imposing positive buoyancy in the region of rotational flow, which supplies an opposing forcing protecting the core pressure minimum.

To illustrate the significance of this, consider a parcel with no vorticity accelerated through a region of updraft acceleration. The parcel will be elongated (deformed) while following a straight trajectory (Fig. 3.9*b*). However, if the parcel has some initial vorticity, the local $\nabla^2 p' > 0$ associated with the updraft acceleration will allow some rotational vorticity to evolve as it is accelerated vertically. The magnitude of deformation may still exceed the vorticity and the parcel will again deform as it rises but, in this case, it will also follow a curved trajectory (Fig. 3.9*b*). This does not affect the ability of the parcel to sustain radial pressure gradients because generally, buoyancy imposes symmetric radial convergence on region of rotation and so does not destructively deform the flow in the radial direction. It is in these regions that rotational vorticity (Eq. 3.22) and the Rortex vector (Eq. 3.16) can elucidate developing rotation and connections with forcing where other commonly used diagnostics can suffer bias.

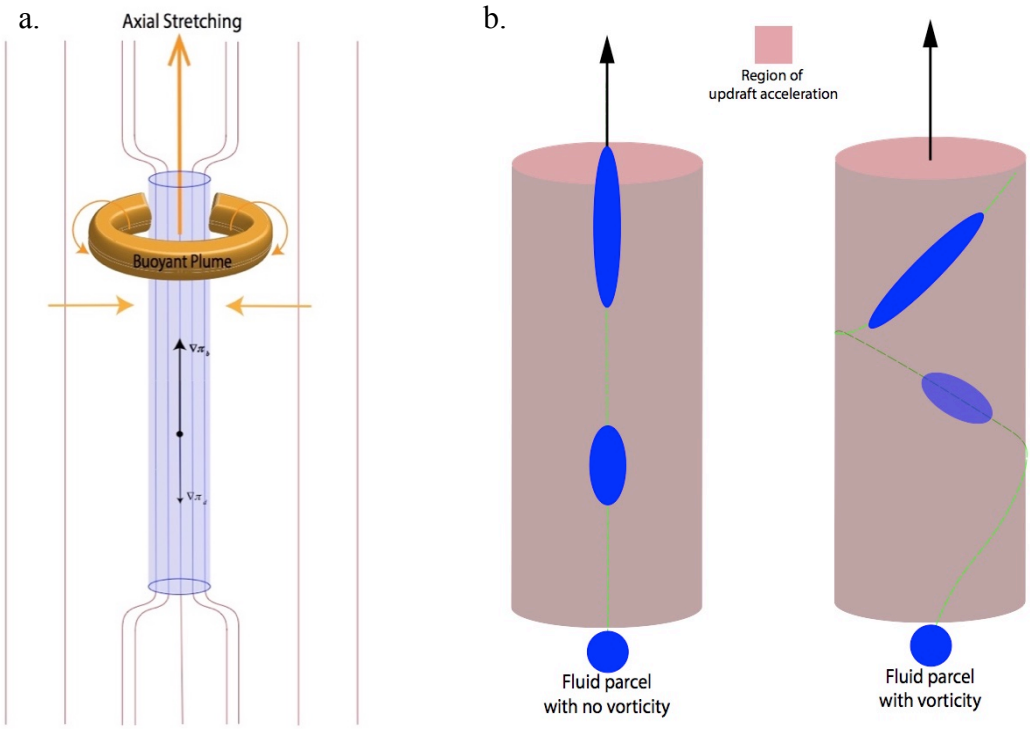

Figure 3.9: Theoretical fluid rotation in buoyancy-forced flow. (a) As in figure 3.8 but now a theoretical buoyant plume superimposed on the region of concentrated vortex lines producing a pressure gradient acceleration that opposes the downward-directed axial pressure gradient acceleration associated with the rotation. (b) Fluid parcel (blue circle) trajectory (green dashed line) through a region of updraft acceleration (pink shaded area) with no initial vorticity (left) and with initial vorticity (right).

d. Helical vs. crosswise rotation

This chapter has outlined in detail numerous possible methods for isolating the rotational component of the total vorticity field and demonstrated the simplicity and efficacy of two such methods (I^2 and $\vec{\omega}_{rot}$) for studying coherent rotational structures in numerical simulations of supercells, which will be used in the analysis portion of this dissertation. However, neither of these methods, nor any other available in the literature at the time of writing, are designed to separate the rotational structures that are predominantly helical in nature from those which are predominantly crosswise. This distinction has been shown throughout this document to be of utmost importance to understand the dynamics of supercell rotation. Specifically, a critical characteristic difference is in the efficiency of vortex stretching by an incipient supercell updraft. The ability to stretch crosswise structures is highly limited due to the lack of flow penetration of their core. In the case of helical structures, however, horizontal and vertical flow accelerations such as those associated with the inflow and updraft region of a supercell can readily stretch rotation that has a significant helical component. *Local maxima in stretching of vorticity, therefore, are generally correlated with helical rotational structures*. Given this, our subsequent analysis demands a diagnostic approach capable of differentiating rotational structures that are helical from those that are crosswise.

Using rotational vorticity as a basis, it is quite straightforward to develop a diagnostic of three-dimensional *helical* rotation. Helicity of the flow is found by projecting the local three-dimensional velocity vector onto the local three-dimensional vorticity vector (accomplished by the dot product of the two vector fields) and so, instead, projecting the three-dimensional velocity vector onto the three-dimensional *rotational* vorticity vector, a diagnostic of helical rotation is readily acquired:

$$\omega_{rothel} = \mathbf{v} \bullet \vec{\omega}_{rot} \qquad 3.23$$

Although the optimum approach to forming a diagnostic of true helical rotation appears to be by taking the dot product of the Rortex vector (Eq. 3.16) with the local velocity vector, these parameters adequately isolate helical rotation for the purposes of this dissertation (Fig. 3.10). Therefore, a comprehensive approach to studying the development, evolution and interaction of rotational structures during a supercell's lifecycle can be achieved through combined analysis of the total vorticity, rotational vorticity, I^2 and rotational helicity fields.

3.3.2 Flow separation, reconnection and helical vortex interaction

Additional work in the fluid dynamics discipline of interest to studying the dynamics of the interaction between a supercell and its local environment is briefly described in the following section, which motivates the development of a new conceptual model of tornadogenesis in chapter five of this dissertation.

a. Flow separation in an unsteady boundary layer

Initially laminar boundary layer flow can become unsteady and *separate* from the surface forming rotational structures when flow is forced to move against an adverse pressure gradient by a *shock* or disturbance (e.g. Lighthill, 1963; Smith and Duck, 1977; Na and Moin, 1998; Wu et al. 2005, pp. 246-252). This area of fluid dynamics research has been particularly important from an engineering standpoint to control flow in turbines and jets (e.g. Lin et al. 1990; Sondergaard et al. 2002). When the boundary layer flow undergoes such an unsteadiness it tends

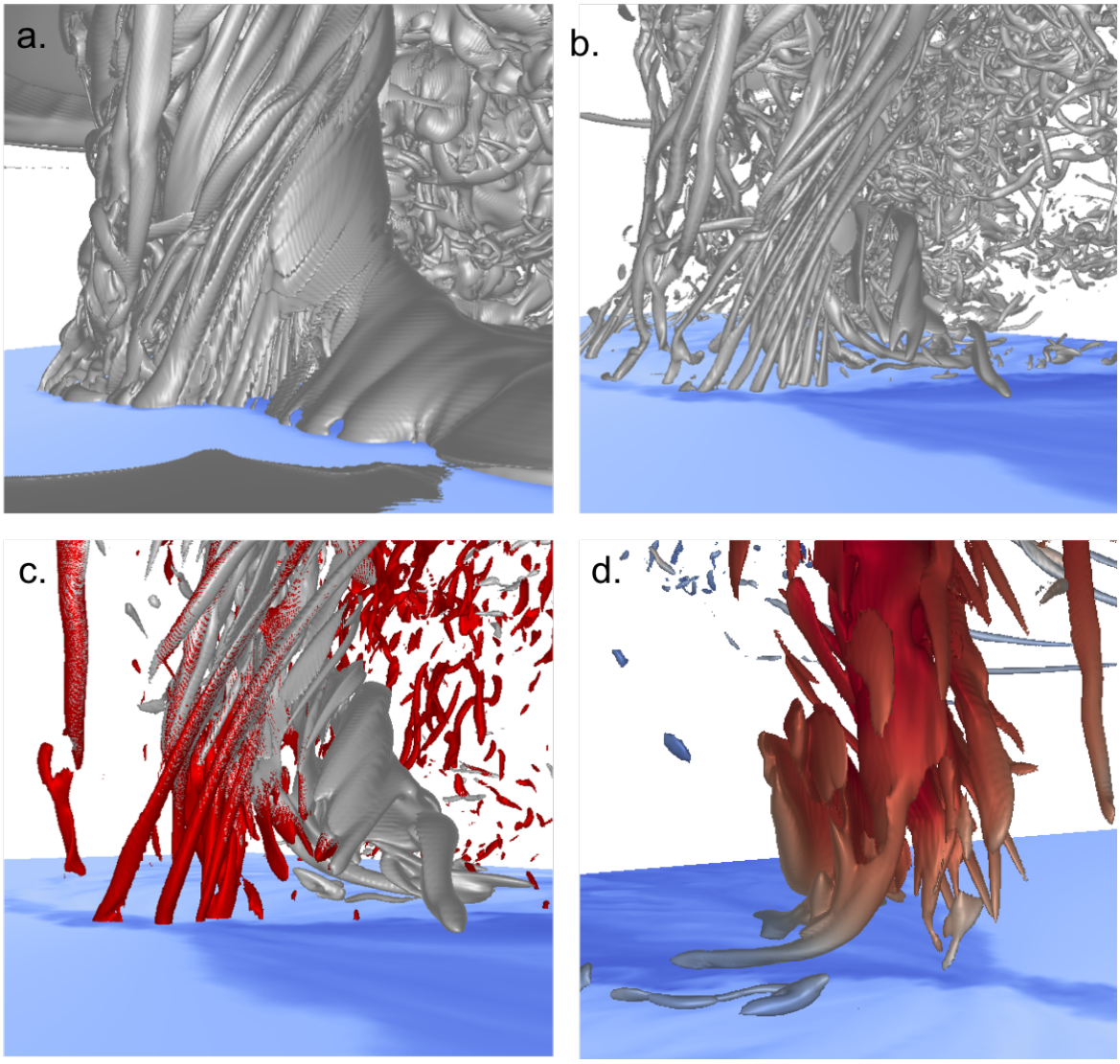

Figure 3.10: May 24 2011 30 m isotropic simulation (Orf et al. 2017) showing utility of new diagnostics. Isosurfaces in each panel above are from 3500 s simulation time and displayed between the surface and approximately 3 km above ground level. The viewing angle for (a)-(c) is from the north looking south whereas (d) is from the south looking north. (a) is a total vorticity magnitude isosurface of 0.075 s^{-1}. (b) is a rotational vorticity magnitude isosurface of 0.075 s^{-1}. (c) is a rotational helicity isosurface of 3 ms^{-2} (the storm-relative velocity varies from 20 to 60 ms^{-1} from near the surface to the top of the plot) in grey and a vertical vorticity isosurface of 0.15 s^{-1} in red. (d) is the same rotational helicity isosurface as in (c) but now viewed from the south and shaded by vertical motion.

to bifurcate and turn away from the adverse pressure gradient toward the interior of the fluid (Fig. 3.11; Dollamann, 1988). Additionally, behind the jet engines of an aircraft, sudden intense pressure gradients cause initially laminar flow to separate into counter-rotating spanwise (crosswise) vortex rolls ((Fig. 3.12; e.g. Smith, 1947). Due to the downstream acceleration of the flow, a portion of the crosswise vortex structure becomes streamwise through conversion of vorticity associated with shear on the upper portion of the crosswise vortex roll (e.g. Zhou and Zhong, 2010; Jukes and Choi, 2013).

A similar process occurs in as supercell thunderstorm outflow region where downdrafts interact with the boundary layer flow. In this region, frequent downward and subsequent horizontal surging in momentum leads to the baroclinic generation of crosswise vortex rolls similarly to the Fujita (1981) downburst model (Fig. 3.13). At the downwind head of the horizontal portion of the surge the flow bifurcates and turns outward leading to the commonly observed structure of counter-rotating vortices (e.g. Straka et al. 2007; Lee et al. 2012). The vortex lines associated with such a transition initially begin as baroclinic rings around the subsiding dense air but a portion are severed and reconnect over the head of the surge forming an arch connecting the cyclonic and anticyclonic branches of the separated flow at the downstream edge of the surge (e.g. Markowski and Richardson, 2009; Fig. 2.14).

Therefore, while baroclinic vorticity generated by a supercell downdraft near the ground is initially crosswise in nature, through horizontal flow acceleration in the presence of viscosity a crosswise to streamwise conversion can occur along the surge periphery. The result is an elevated streamwise vorticity maxima surrounded on its environmental periphery with a sheet-like vorticity. This flow configuration is remarkably similar to recent dual-pol RHI scanning radar observations of a supercells outflow periphery (Fig. 3.14; Schueth et al. 29th Conference on

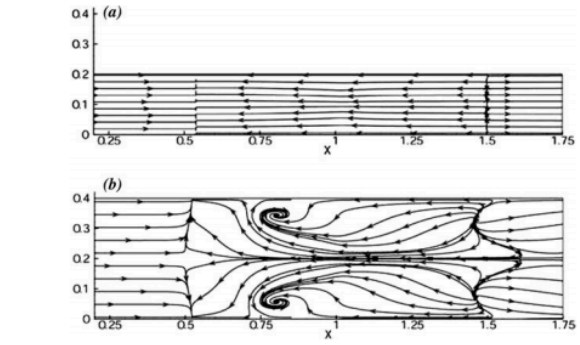

Surface streamlines on the plate, $L_z = 0.2$ (**a**), $L_z = 0.4$ (**b**), $\theta = 32°$

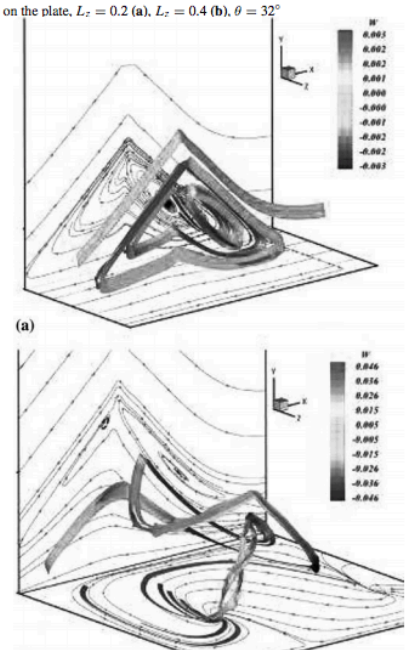

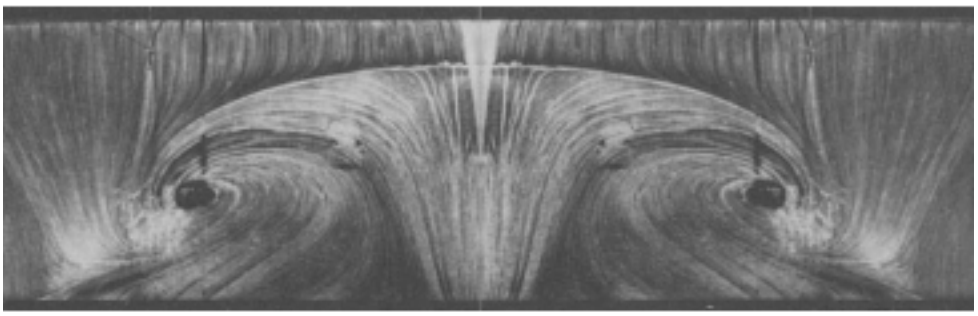

Figure 3.11: (a) Flow separation caused by a shock to an initially laminar boundary layer. (b) Flow separation leading to boundary layer flow bifurcation and counter-rotating vortices at the downstream head of the surge. Figures modified from Dollamann (1988) and Bippes (1987).

Figure 3.12: Jet-induced flow separation leading to crosswise (spanwise) vortex rolls in its wake and streamwise vortices at their core.

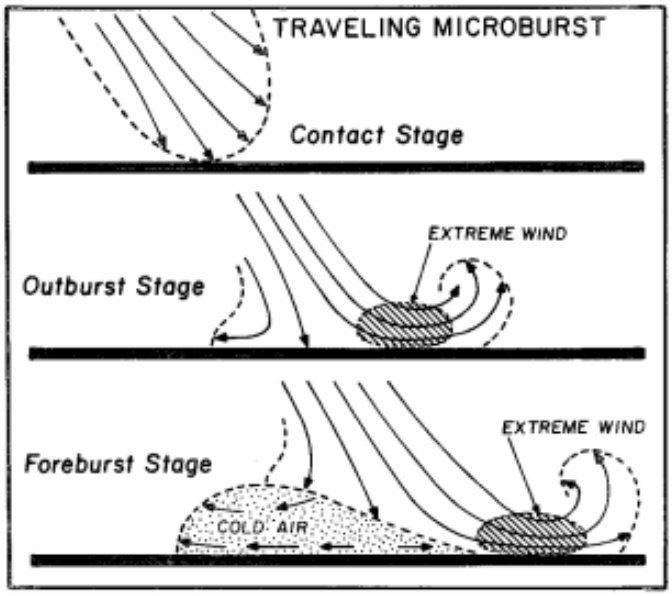

Figure 3.13: A momentum surge impacting the boundary layer from Fujita (1981). Figure reprinted with permission from Journal of the Atmospheric Sciences.

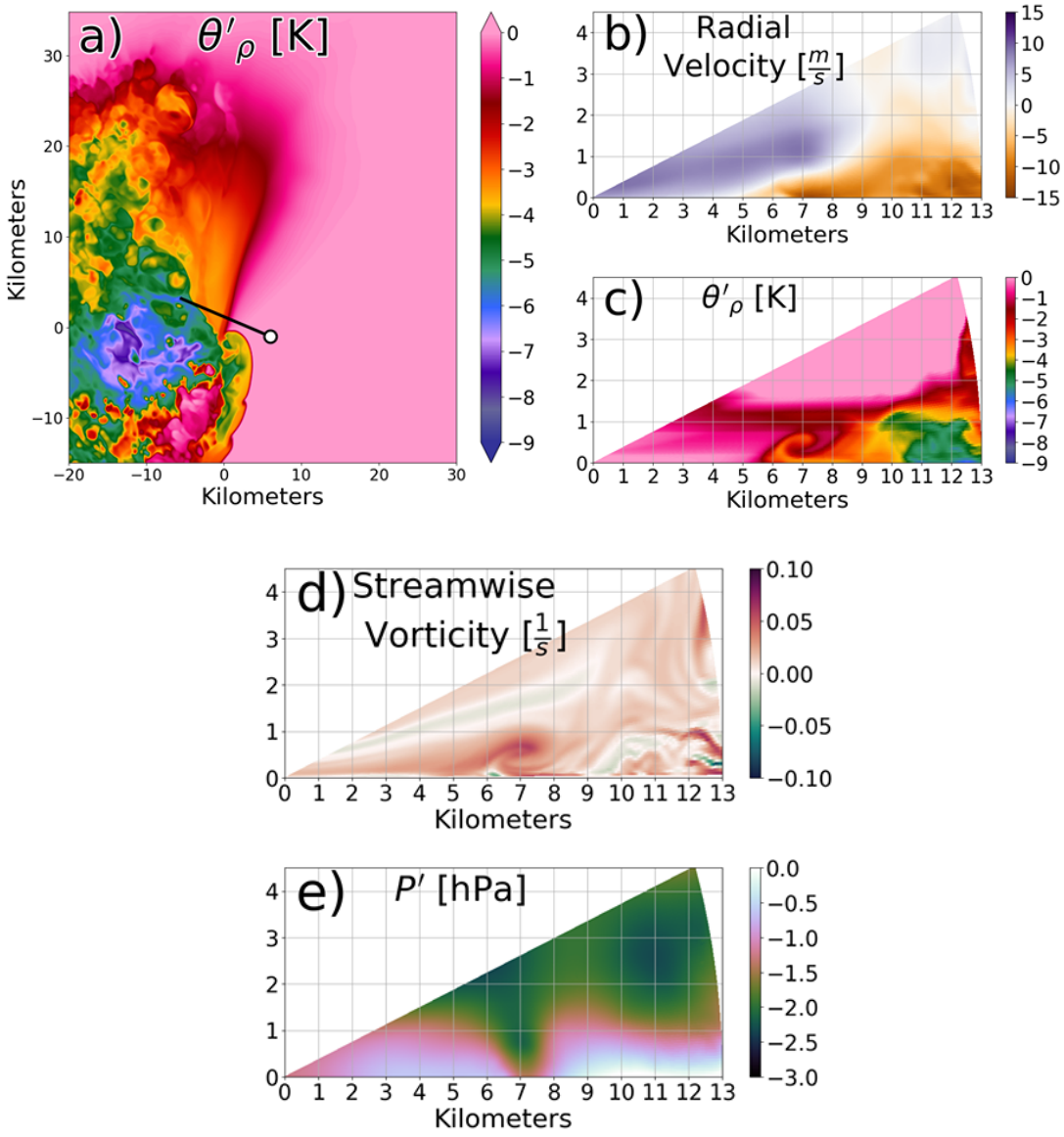

Figure 3.14: Simulated radar from a numerical simulation of a supercell thunderstorm. Figure provided by Alex Schueth.

Severe Local Storms). Schueth found Kelvin-Helholtz-type billows in this region accompanied by a streamwise vorticity maxima, which has recently been referred to as the SVC (Fig. 2.17; Orf et al. 2017).

b. Flow reconnection

To investigate further, the effects of such a flow separation in a low-level supercell environment, it is pertinent to discuss the flow *reconnection*. Flow reconnection is a fluid phenomenon found to occur when flow is forced to diverge around an obstacle (e.g. Wu et al. 2000). Through boundary layer separation effects discussed in part a of this section, vorticity is generated and frequently leads to downstream streamwise vortex generation (e.g. Liu and Chen, 2011). Subsequently and a result of the vorticity generation, the separated flow interacts downstream and undergoes a reconnection process (Fig. 3.15; e.g. Wu et al. 2000). The significance of this is that vortex lines associated with the separated flows interact and wind helically around one another through a *mutual induction* mechanism (e.g. Nemes et al. 2015). Once again to return to the dynamical interest for supercell flow, baroclinic streamwise vortex lines along the periphery of a surging region of outflow can interact with streamwise vortex lines of the storm-relative environmental flow in a similar manner. Initially, due to its stark density characteristics relative to the ambient flow and its closed, looped vortex lines, the outflow air of a supercell does not readily interact with its ambient environment. However, surging of the outflow at the surface presents a mechanism by which the vorticity of the outflow and low-level environment can interact via boundary layer separation and subsequent reconnection of helical vortex lines.

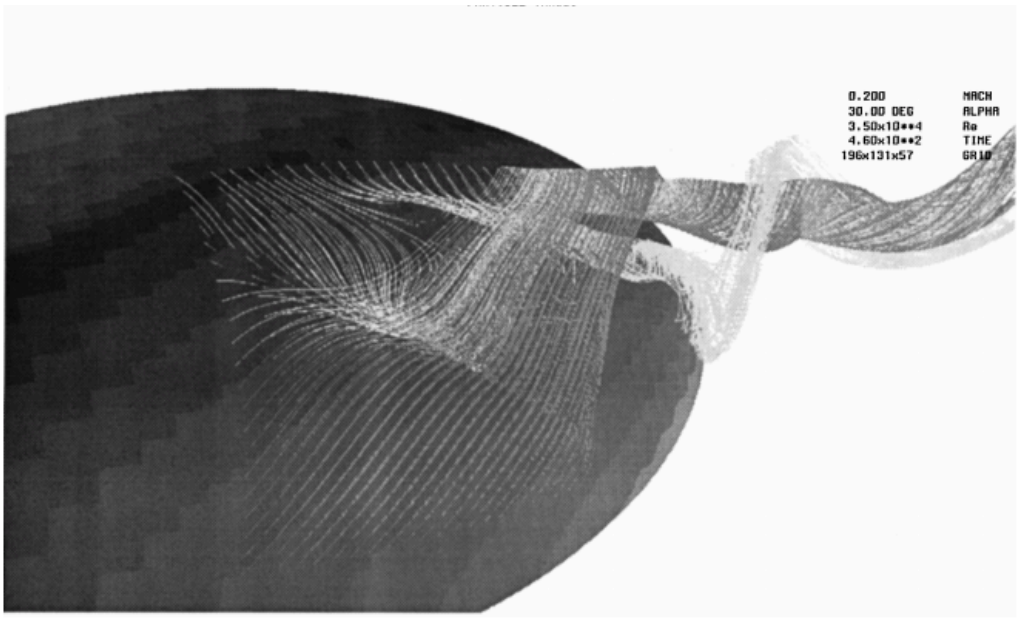

Figure 3.15: Reconnection of separated flow. Adapted from Wu et al. (2000).

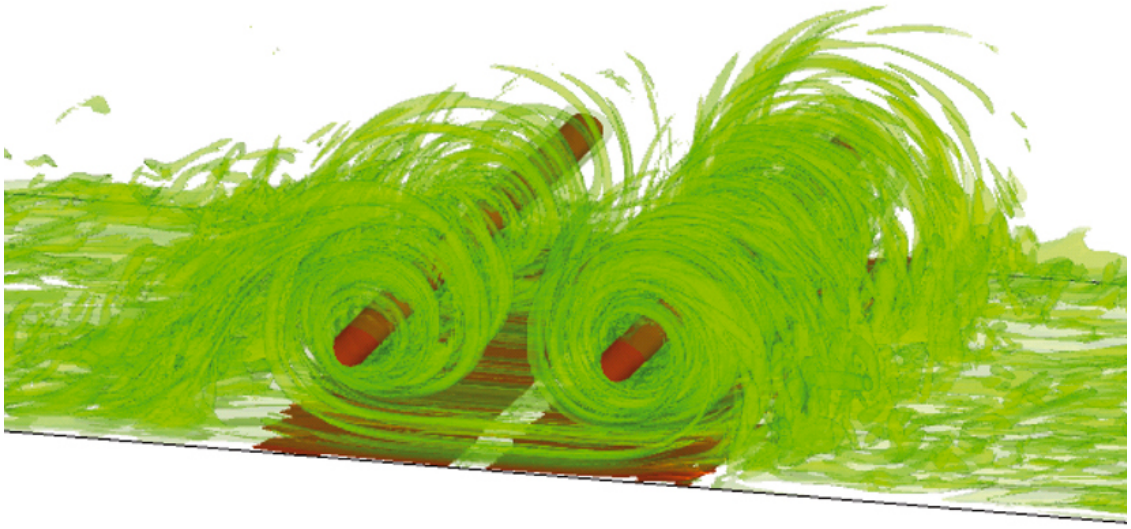

Figure 3.16: Numerical simulation of counter-rotating crosswise (spanwise) vortex structures resulting from flow separation behind a jet engine. Red isosurface is streamwise vorticity and green is crosswise vorticity.

The downward acceleration of low-level flow into a supercell outflow region by *dynamic* forcing is a well-known mechanism by which downdraft surging can be induced (e.g. Skinner et al. 2014; 205, see section 2.2.1). In contrast to downdraft surging resulting from local negative buoyancy, dynamically-driven downdraft acceleration is known to produce warmer and therefore less negatively buoyant outflow momentum surges. This suggests that the air accelerated to the surface is from the nearby, ambient low-level environment, which requires minimal low-level static stability in order for such vertical excursions of air parcels (e.g. Parker, 2012). Intense near-surface divergence of air occurs just on the internal periphery of simulated flow in Fig. 3.16. It is reasonable to extrapolate this to the internal edge of the outflow periphery where intense streamwise rotation has been found to occur in a supercell. Such dynamically-driven near-surface divergence resulting from momentum surging and streamwise vorticity intensification presents a mechanism by which low-level environmental air associated with the supercell's inflow may be forced down into the surging outflow around the baroclinic head of the outflow's periphery.

c. Helical interactions

Due to the known importance of streamwise vorticity in the development and intensity of supercell rotation it is critical to our theoretical understanding of supercells to study helical flow interactions. This is another area heavily researched area in the fluid dynamics literature, which the author believes demands substantially more attention from the supercell research community. Of relevance to the current discussion is the interaction between two nearby helical (streamwise) vortex structures. Two neighboring vortex features, in the presence of viscosity, will tend to interact, which can occur in a variety of ways depending on their relative orientations and

intensities. For brevity and relevance to current application, the author will restrict this discussion to a small, specific subset of these interactions.

Following from the discussion in parts *a* and *b* of this section, consider a baroclinically generated streamwise vortex line parallel in orientation to a neighboring environmental streamwise vortex line associated with the low-level inflow. As the two air-streams are drawn together in the manner described above, the vortex lines associated with the streamwise vorticity of the environment and of the outflow will begin to interact (through mutual induction) in a winding manner such that a portion of the vortex lines associated with the low-level inflow and outflow become associated with the same rotational structure (Fig. 3.17; Scheeler et al. 2014; 2017; Nemes et al. 2015). The result of this interaction on the evolution of the three-dimensional rotational structure depends on the local forcing. For example, helical vortex structures tend to undergo "writhing" in most circumstances due to local crosswise viscous-stretching effects (Scheeler et al. 2014; 2017). However, in the presence of intense axial stretching, which is known as "compression" in fluid dynamics, the helical structure will tend to "twist" (Scheeler et al. 2014; 2017).

Interestingly, the author has found evidence supporting both types of helical vortex evolution in numerical simulations of supercells through application of the diagnostics presented in section 3.3.1. Fig. 3.18 is associated with a failed tornadogenesis period in a numerical simulation of a supercell with the UWNMS model. Note how the vortex structure along the outflow periphery undergoes a *writhing*-type evolution near the surface close to the base of the updraft. This would be consistent with a helical rotational structure experiencing viscous deformational effects with insufficient axial stretching for twisting. In their simulation of a violently tornadic supercell, Orf et al. (2017) highlighted a dominant helical rotational structure, which was intensely stretched in

the horizontal and vertical during tornadogeneis through interaction with the storm's buoyant updraft aloft (Fig. 2.17). This structure appears to exhibit a *twisting* mode of helical vortex evolution consistent with the intense axial stretching it experiences. The preceding theoretical discussion will be called upon throughout the remainder of this dissertation and helps form the basis of a conceptual model of supercell tornadogenesis that draws from much of the theory in this section.

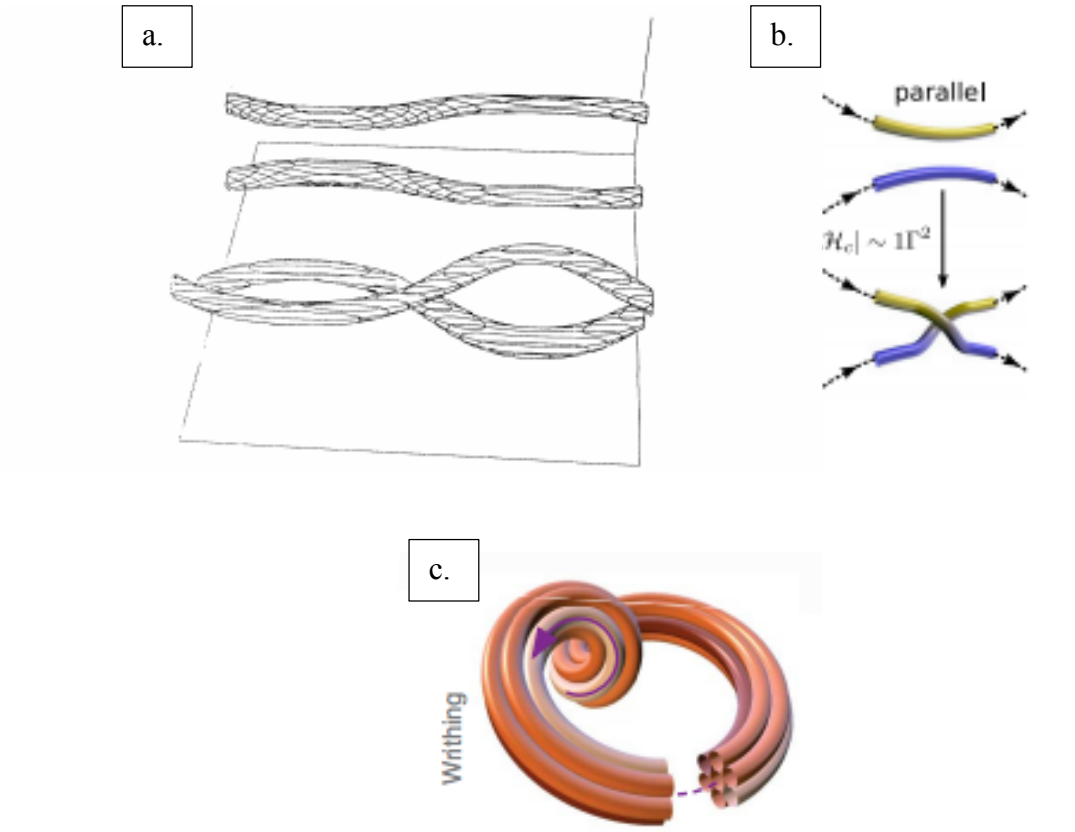

Figure 3.17: Helical vortex interaction between two parallel streamwise vortices. (a) and (b) demonstrating how parallel vortices interact coiling and (c) demonstrating writhing of a helical vortex through deformational effects. Figures adapted from Dallamann (1988) and Scheeler et al. (2014).

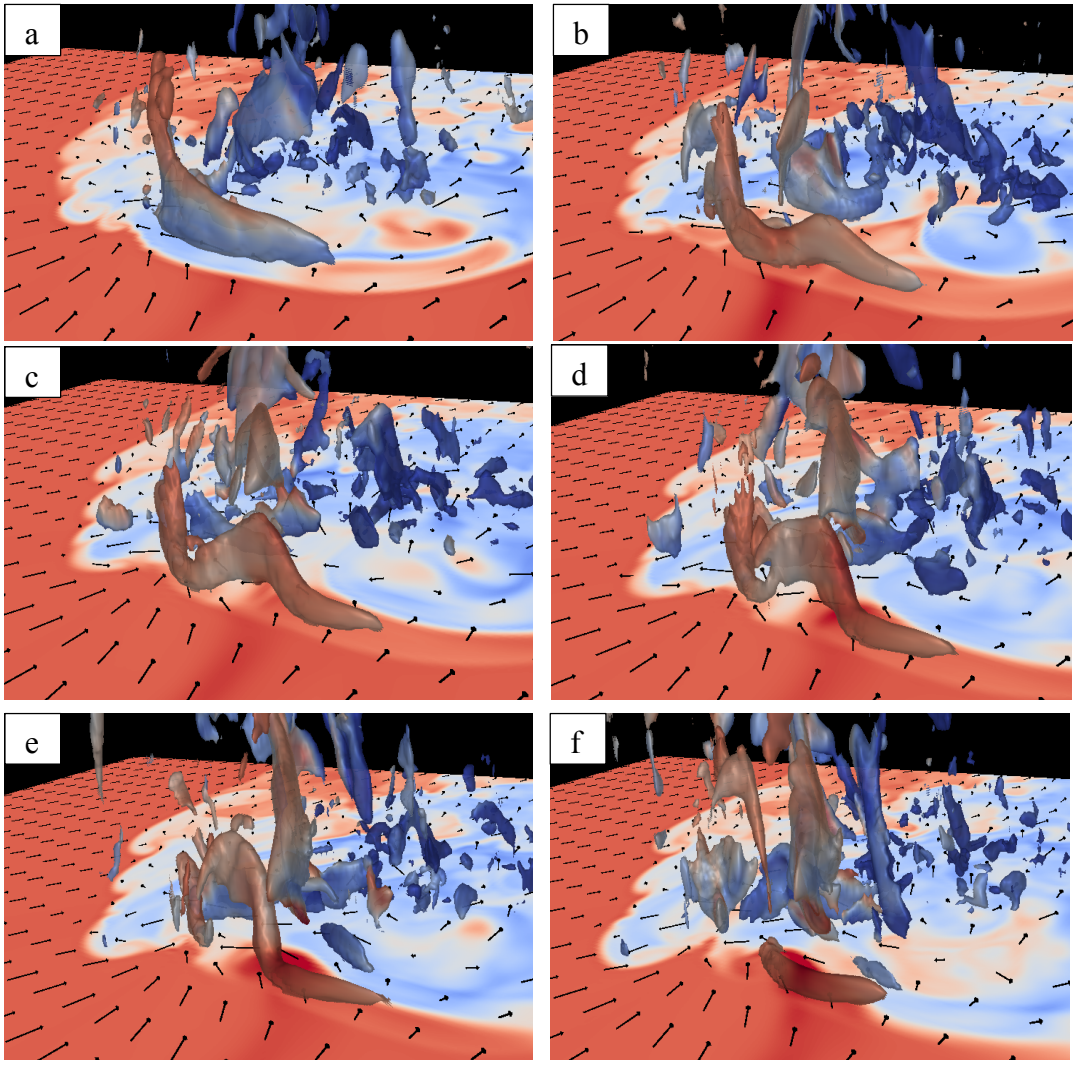

Figure 3.18: Evolution of a helical rotational structure along the periphery of a supercell downdraft surge during a tornadogenesis failure event in a numerical simulation of a supercell with the UWNMS. Surface is shaded by equivalent potential temperature with warmer colors indicating higher values. Surface (lowest model level) wind bards are black arrows. Isosurface is rotational helicity of magnitude 0.5 ms^{-2} and is shaded by the vertical component of vorticity. Simulation time of (a) is 7100 s and then (b)-(f) is every 50 s from 7250 – 7500 s

Chapter Four: Identification of coherent rotational structures in tornadic and nontornadic supercells

In the following chapter, diagnostic approach discussed theoretically in chapter three is applied to study the development and evolution of coherent rotational structures on the sub-mesocyclonic scale during supercell tornadogenesis and failure in numerical supercell simulations. Applying the new diagnostics through similar methods used already to study vorticity evolution in a supercell, key rotational structures and processes involved in supercell tornadogenesis are found to be illuminated from the total vorticity field. In particular, the apparent role of a helical coupling mechanism is discovered, which prompts a new conceptual model of supercell tornadogenesis, consistent with current literature, presented in chapter five.

Part I. Experimental design

a. Numerical model configuration: NMS and CM1

Introduced in section 1.3.1, the UWNMS (herein, NMS) is a nonhydrostatic enstrophy-conserving model capable of competently modeling the sub-storm scale rotational structures of interest. For all of the simulations presented in this chapter the NMS was employed in a two-nested grid approach with $\Delta x = \Delta y = 120m$ horizontal resolution and $\Delta z = 40m$ vertical resolution (stretched to $\Delta z = 360m$ between 1.6 km and 9 km above ground) on the inner grid (third grid; Fig. 4.1; Table 4.1). Each run was initialized with a bubble-shaped potential

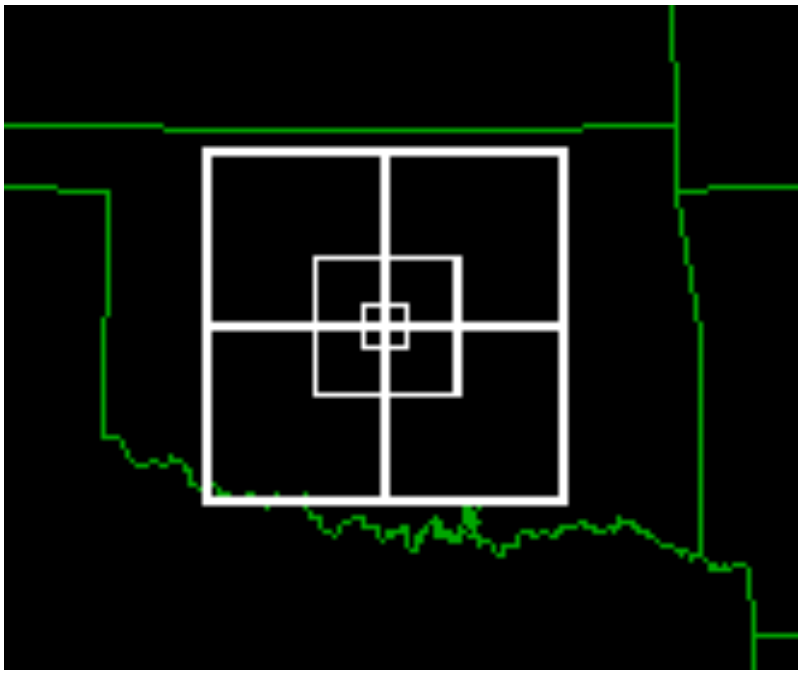

Figure 4.1: UWNMS nested grid set-up. Rotated spherical grid centered over Oklahoma.

NMS model configuration	
Parameter	**Description**
Inner nested domain dimensions	50 x 50 x 20 km
Grid spacing	$\Delta x = \Delta y = 120m, \Delta z = 40m \rightarrow 360m\left(1.6 - 9km\right)$
Numerics	6th order flux-form Crowley (scalars; Tremback et al. 1987), 2nd order enstrophy conserving and quasi-compressible closure
Microphysics	Morrison double moment (Morrison et al. 2005)
Turbulence closure	1.5-level closure, TKE prediction and filter (4th order horizontal; 6th order vertical)
Cloud forcing	Warm bubble
Long time step	0.4 s
Short time step	(0.4/12) s
Pressure-solver	Time-iterative quasi-compressible closure
Lower boundary condition	No-slip (logarithmic profile below 10 m)
Lateral boundary condition	Open radiative

CM1 model configuration	
Parameter	**Description**
Inner mesh dimensions	160 x 160 x 20 km
Grid spacing	$\Delta x = \Delta y = 120m, \Delta z = 40m \rightarrow 360m\left(480m - 9km\right)$
Numerics	RK2 (Wicker and Skamarock, 1998), fifth-order
Microphysics	Morrison et al. (2009) dual moment
Turbulence closure	Smagorinsky (1963)
Cloud forcing	Updraft nudging (Naylor and Gilmore, 2012)
Long time step	0.2 s
Short time step	(0.2/10) s
Pressure-solver	Klemp-Wilhelmson time splitting, vertically implicit
Lower boundary condition	Free slip
Lateral boundary condition	Open radiative

Tables 4.1 and 4.2: UWNMS and CM1 model configuration respectively.

temperature perturbation of +4 K with a vertical diameter of 3 km and a horizontal diameter of 10 km, which was centered at 1.5 km above ground in the center of the third grid. The domain was horizontally homogeneous with the initial tornadic and nontornadic composite environments (see part *b* of this section). The lateral boundaries were open radiative and the upper boundary was rigid with a 3-kilometer absorbing layer beneath the domain top. The lower boundary was no-slip, in which the wind is assumed to follow a logarithmic profile between 10 m and the surface. Each simulation was run for 9000 s.

The CM1 simulations used the same model configuration as Orf et al. (2017; Table 4.2) but the horizontal resolution was decreased to match that used with the NMS. Each of these simulations were also run for 9000 s but were forced with an "updraft-nudging" technique (Naylor and Gilmore, 2012) instead of the potential temperature perturbation (see part c of this section). Additionally, the lower boundary was free-slip as opposed to no-slip as in the NMS.

b. Supercell environments: VORTEX2 and Weisman and Klemp idealized soundings

Recent sounding data collected in the VORTEX2 field campaign was used as basis from which to study the differences in evolution of a supercell's sub-storm scale rotation in tornadic and nontornadic environments (Wurman et al. 2012; Parker, 2014). These data were chosen because they offer the best quality, close-range (convectively-uncontaminated environments downstream of mature supercells) analysis of vertical atmospheric structure in physical supercell environments to date (Parker, 2014).

Fig. 4.2 is the composite sounding and hodograph data from seven radiosonde launches in the downstream environment of *tornadic* supercells used in the tornadic supercell simulations and

Fig. 4.3 is the composite sounding and hodograph data from five downstream environments of *nontornadic* supercells used for the nontornadic supercell simulations. Both composite soundings

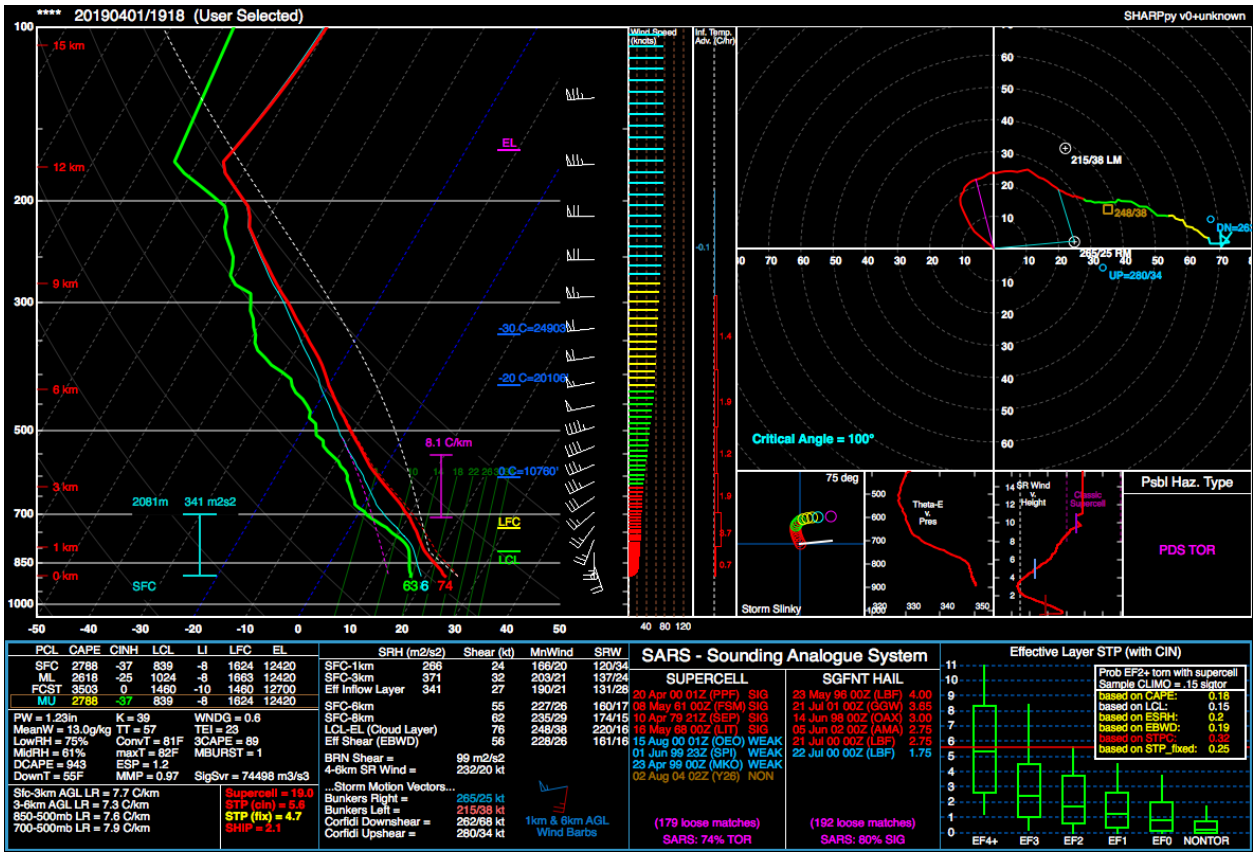

Figure 4.2: Composite VORTEX2 tornadic environment sounding and hodograph. Vertical temperature profile is the red line on the Skew-T and the vertical dewpoint profile is the green line. Wind barbs are plotted at the right edge of the Skew-T and the corresponding hodograph is plotted in the top right of the figure. Computed values of common thermodynamic and kinematic parameters used for assessing a severe thunderstorm environment are given beneath the sounding and hodograph. Figure created using SHARPpy, data originally provided by Dr. Brice Coffer.

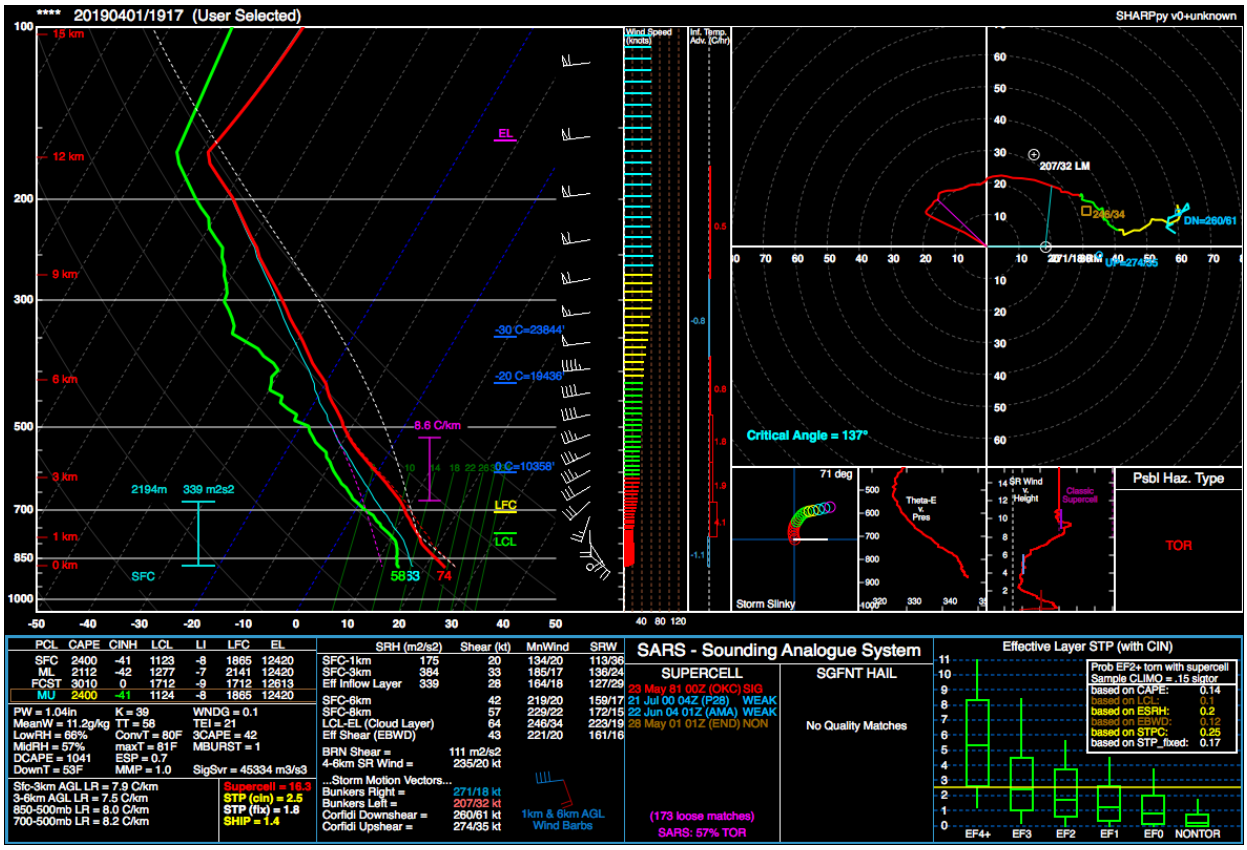

Figure 4.3: VORTEX2 composite nontornadic sounding and hodograph. As in Fig. 4.2 but for the composite VORTEX2 *nontornadic* environments.

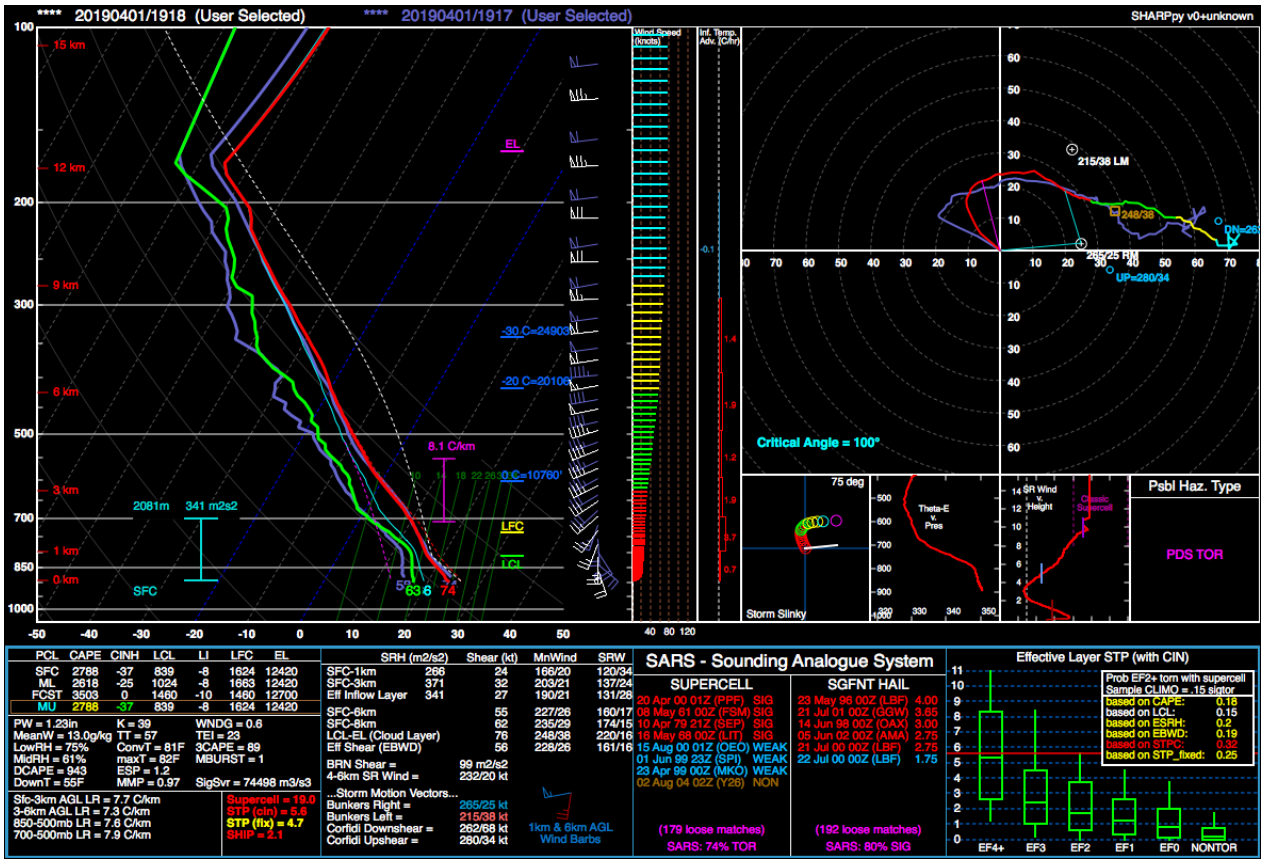

Figure 4.4: Overlay of tornadic and nontornadic composite soundings. As in Fig. 4.2 but both composite soundings are plotted (nontornadic is in purple behind the tornadic sounding and hodograph).

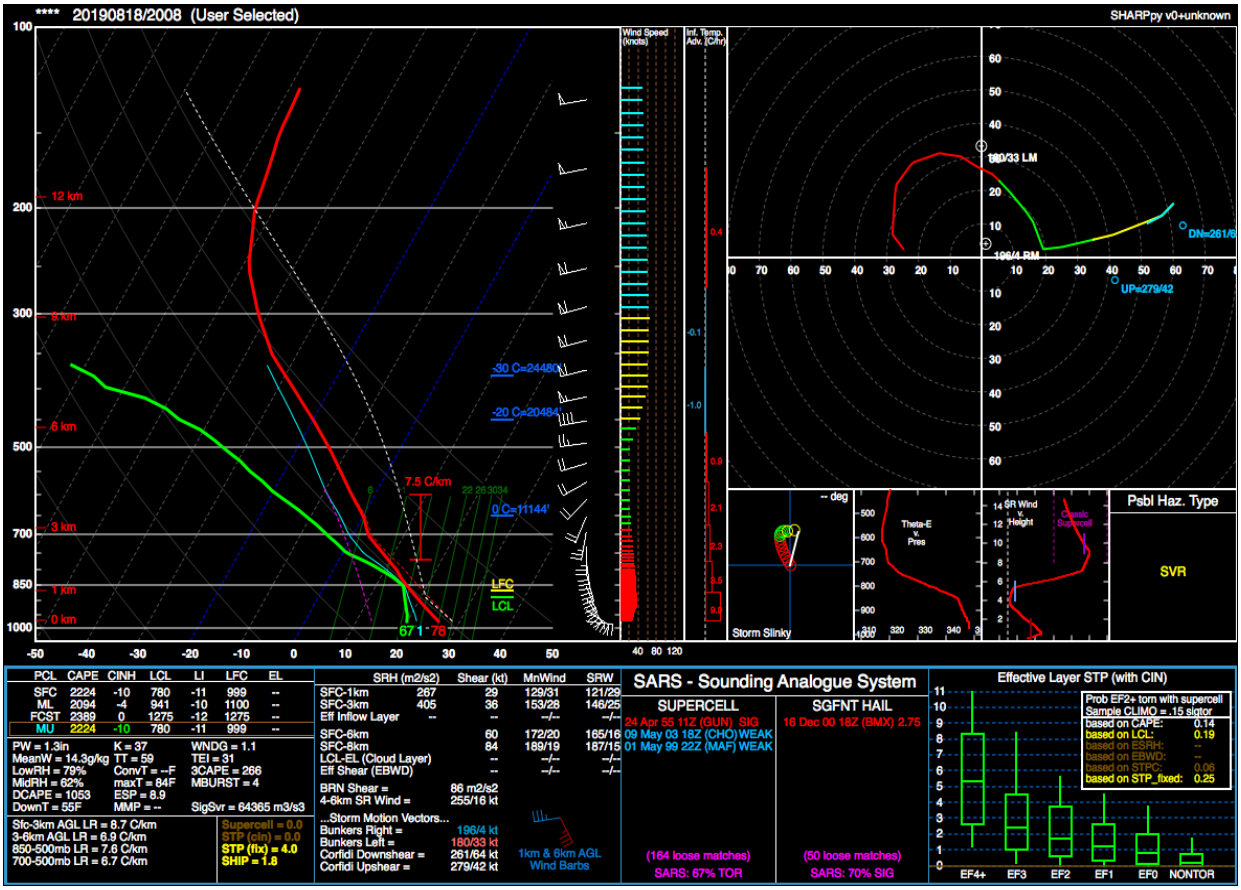

Figure 4.5: Weisman-Klemp idealized sounding. As in Fig. 4.2 but for the Weisman-Klemp idealized sounding, which has been slightly modified from the original by Weisman and Klemp (1982).

a.

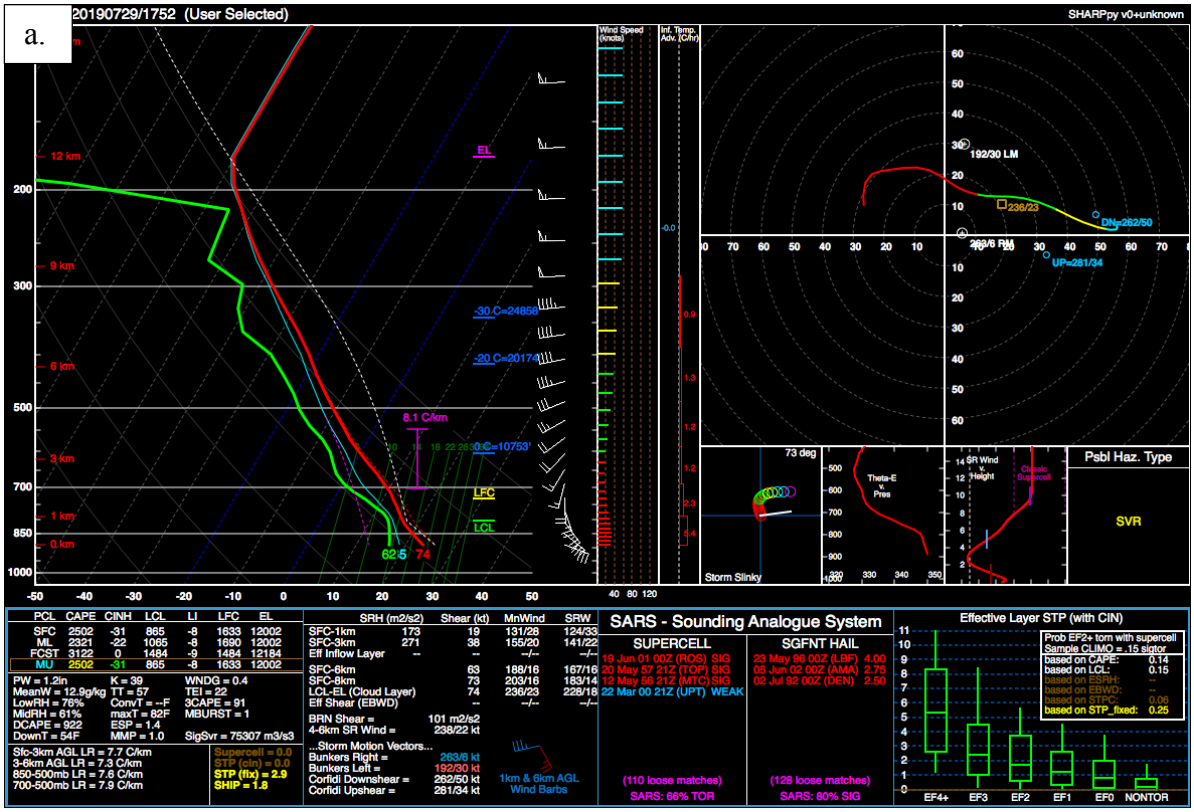
20190729/1752 (User Selected)
SHARPpy v0+unknown
EL
12 km
9 km
6 km
3 km
1 km
0 km
-30 C=24856
-20 C=20174
8.1 C/km
0 C=10753'
LFC
LCL
62
5
74
192/30 LM
236/23
DN=282/50
UP=281/34
73 deg
Storm Slinky
Theta-E vs. Pres
SR Wind vs. Height
Classic Supercell
Psbl Haz. Type
SVR
PCL CAPE CINH LCL LI LFC EL
SFC 2502 -31 865 -8 1633 12002
ML 2321 -22 1065 -8 1690 12002
FCST 3122 0 1484 -9 1484 12184
MU 2502 -31 865 -8 1633 12002
PW = 1.2in K = 39 WNDG = 0.4
MeanW = 12.9g/kg TT = 57 TEI = 22
LowRH = 76% ConvT = --F 3CAPE = 91
MidRH = 61% maxT = 82F MBURST = 1
DCAPE = 922 ESP = 1.4
DownT = 54F MMP = 1.0 SigSvr = 75307 m3/s3
Sfc-3km AGL LR = 7.7 C/km
3-6km AGL LR = 7.3 C/km
850-500mb LR = 7.8 C/km
700-500mb LR = 7.9 C/km
Supercell = 0.0
STP (cin) = 0.0
STP (fix) = 2.9
SHIP = 1.8
SRH (m2/s2) Shear (kt) MnWind SRW
SFC-1km 173 19 131/28 124/33
SFC-3km 271 38 155/20 141/22
Eff Inflow Layer -- -- --/-- --/--
SFC-6km 63 188/16 167/16
SFC-8km 73 203/16 183/14
LCL-EL (Cloud Layer) 74 236/23 228/18
Eff Shear (EBWD) --/--
BRN Shear = 101 m2/s2
4-6km SR Wind = 238/22 kt
...Storm Motion Vectors...
Bunkers Right = 283/6 kt
Bunkers Left = 192/30 kt
Corfidi Downshear = 262/50 kt
Corfidi Upshear = 281/34 kt
1km & 6km AGL Wind Barbs
SARS - Sounding Analogue System
SUPERCELL
19 Jun 01 00Z (ROS) SIG
20 May 57 21Z (TOP) SIG
12 May 56 21Z (MTC) SIG
22 Mar 00 21Z (UPT) WEAK
(110 loose matches)
SARS: 66% TOR
SGFNT HAIL
23 May 96 00Z (LBF) 4.00
05 Jun 02 00Z (AMA) 2.75
02 Jul 92 00Z (DEN) 2.50
(128 loose matches)
SARS: 80% SIG
Effective Layer STP (with CIN)
Prob EF2+ torn with supercell
Sample CLIMO = .15 sigtor
based on CAPE: 0.14
based on LCL: 0.15
based on ESRH: --
based on EBWD: --
based on STPC: 0.06
based on STP_fixed: 0.25
EF4+ EF3 EF2 EF1 EF0 NONTOR

b.

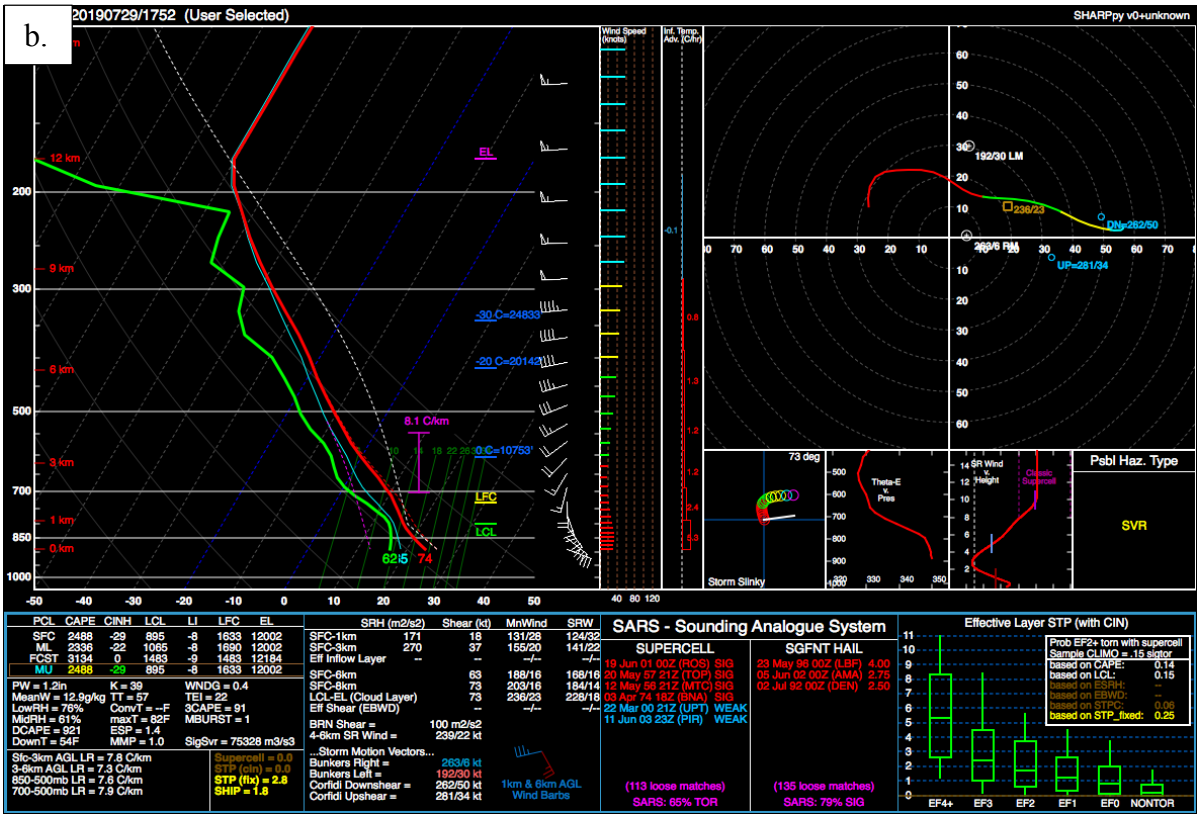
20190729/1752 (User Selected)
SHARPpy v0+unknown
EL
12 km
9 km
6 km
3 km
1 km
0 km
-30 C=24833
-20 C=20142
8.1 C/km
0 C=10753'
LFC
LCL
62
5
74
192/30 LM
236/23
DN=282/50
UP=281/34
73 deg
Storm Slinky
Theta-E vs. Pres
SR Wind vs. Height
Classic Supercell
Psbl Haz. Type
SVR
PCL CAPE CINH LCL LI LFC EL
SFC 2488 -29 895 -8 1633 12002
ML 2336 -22 1065 -8 1690 12002
FCST 3134 0 1483 -9 1483 12184
MU 2488 -29 895 -8 1633 12002
PW = 1.2in K = 39 WNDG = 0.4
MeanW = 12.9g/kg TT = 57 TEI = 22
LowRH = 76% ConvT = --F 3CAPE = 91
MidRH = 61% maxT = 82F MBURST = 1
DCAPE = 921 ESP = 1.4
DownT = 54F MMP = 1.0 SigSvr = 75328 m3/s3
Sfc-3km AGL LR = 7.8 C/km
3-6km AGL LR = 7.3 C/km
850-500mb LR = 7.6 C/km
700-500mb LR = 7.9 C/km
Supercell = 0.0
STP (cin) = 0.0
STP (fix) = 2.8
SHIP = 1.8
SRH (m2/s2) Shear (kt) MnWind SRW
SFC-1km 171 18 131/28 124/32
SFC-3km 270 37 155/20 141/22
Eff Inflow Layer -- -- --/-- --/--
SFC-6km 63 188/16 168/16
SFC-8km 73 203/16 184/14
LCL-EL (Cloud Layer) 73 236/23 228/18
Eff Shear (EBWD) --/--
BRN Shear = 100 m2/s2
4-6km SR Wind = 239/22 kt
...Storm Motion Vectors...
Bunkers Right = 283/6 kt
Bunkers Left = 192/30 kt
Corfidi Downshear = 262/50 kt
Corfidi Upshear = 281/34 kt
1km & 6km AGL Wind Barbs
SARS - Sounding Analogue System
SUPERCELL
19 Jun 01 00Z (ROS) SIG
20 May 57 21Z (TOP) SIG
12 May 56 21Z (MTC) SIG
03 Apr 74 18Z (BNA) SIG
22 Mar 00 21Z (UPT) WEAK
11 Jun 03 23Z (PIR) WEAK
(113 loose matches)
SARS: 65% TOR
SGFNT HAIL
23 May 96 00Z (LBF) 4.00
05 Jun 02 00Z (AMA) 2.75
02 Jul 92 00Z (DEN) 2.50
(135 loose matches)
SARS: 79% SIG
Effective Layer STP (with CIN)
Prob EF2+ torn with supercell
Sample CLIMO = .15 sigtor
based on CAPE: 0.14
based on LCL: 0.15
based on ESRH: --
based on EBWD: --
based on STPC: 0.06
based on STP_fixed: 0.25
EF4+ EF3 EF2 EF1 EF0 NONTOR

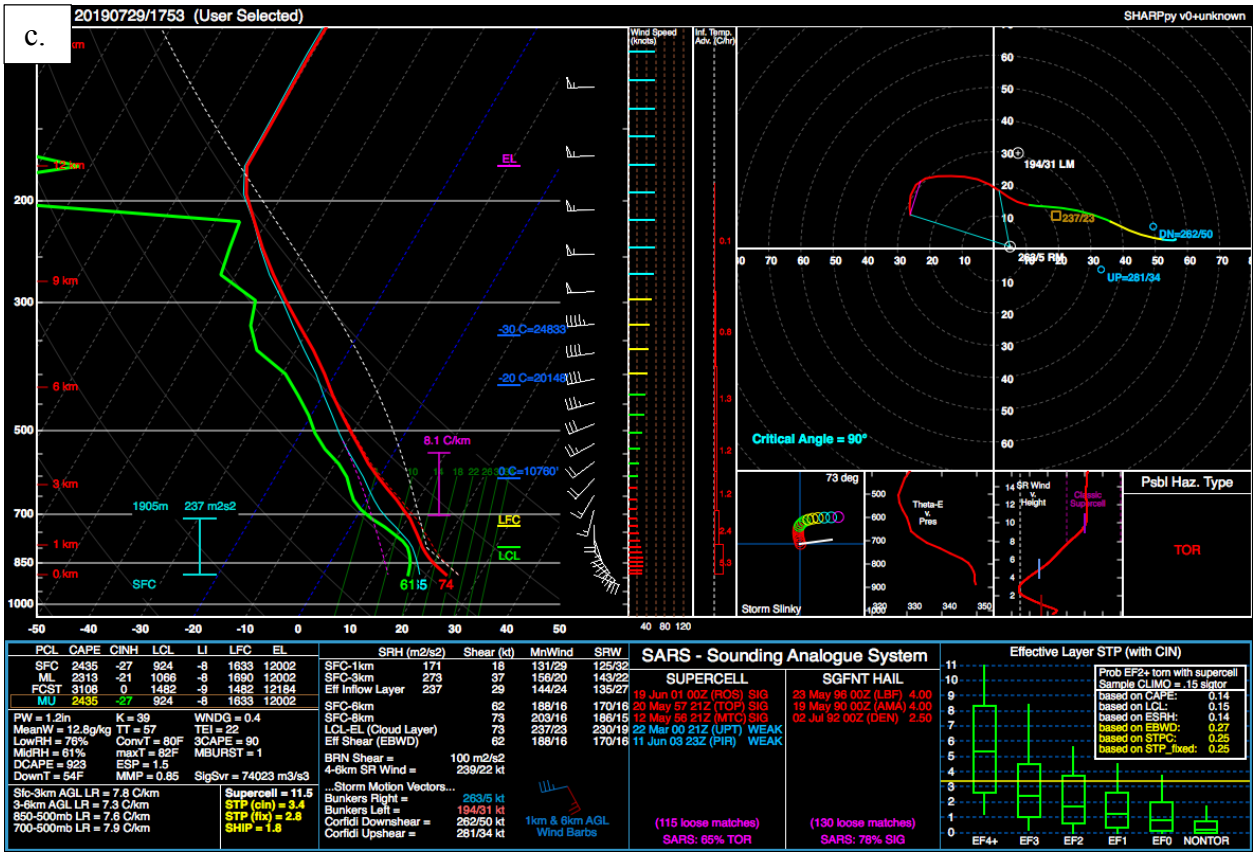

Figure 4.6: Warm bubble initialization. Sounding and hodographs plotted from model data 30 km to the South East of the initial "warm bubble" perturbation at 600 s (a), 1200 s (b) and 1800 s (c) into the simulation.

a.

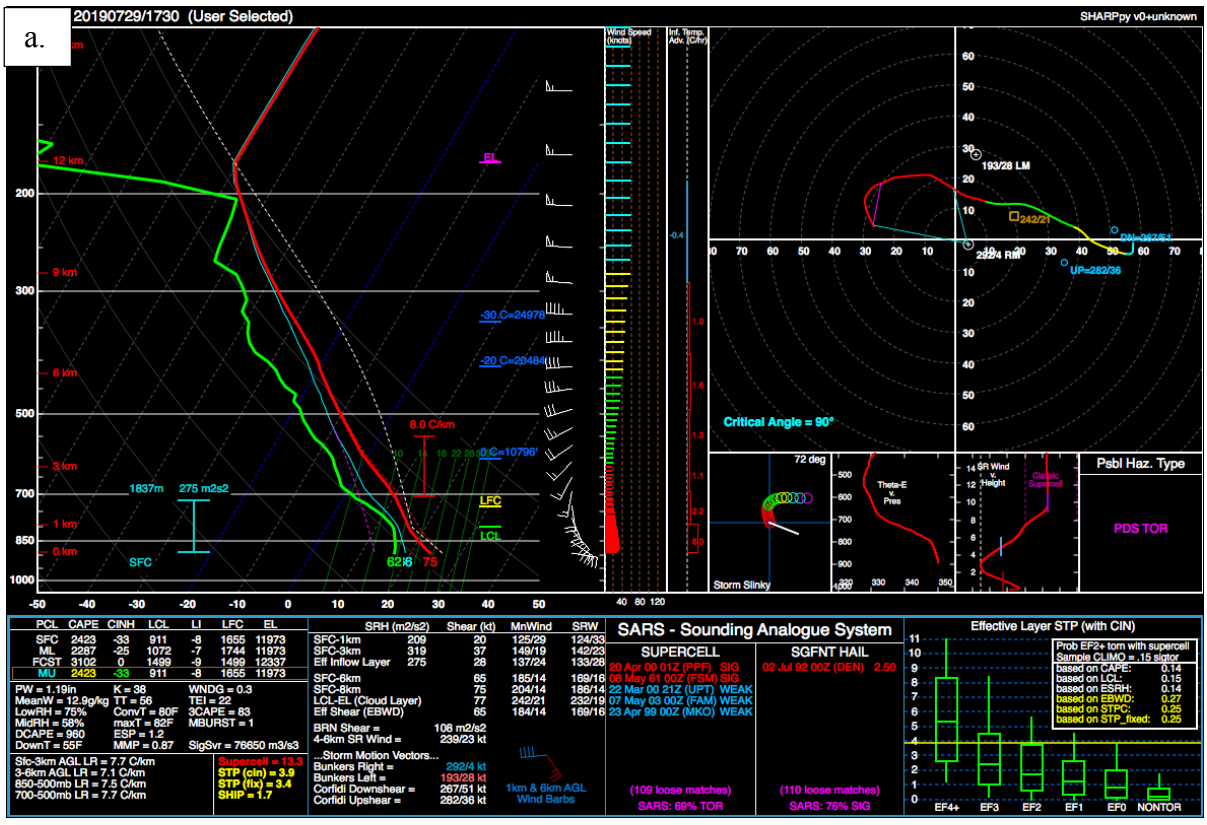
20190729/1730 (User Selected)
SHARPpy v0+unknown
Critical Angle = 90°
Psbl Haz. Type
PDS TOR
SARS - Sounding Analogue System
SUPERCELL
SGFNT HAIL
02 Jul 92 00Z (DEN) 2.50
(109 loose matches)
SARS: 69% TOR
(110 loose matches)
SARS: 76% SIG
Effective Layer STP (with CIN)

b.

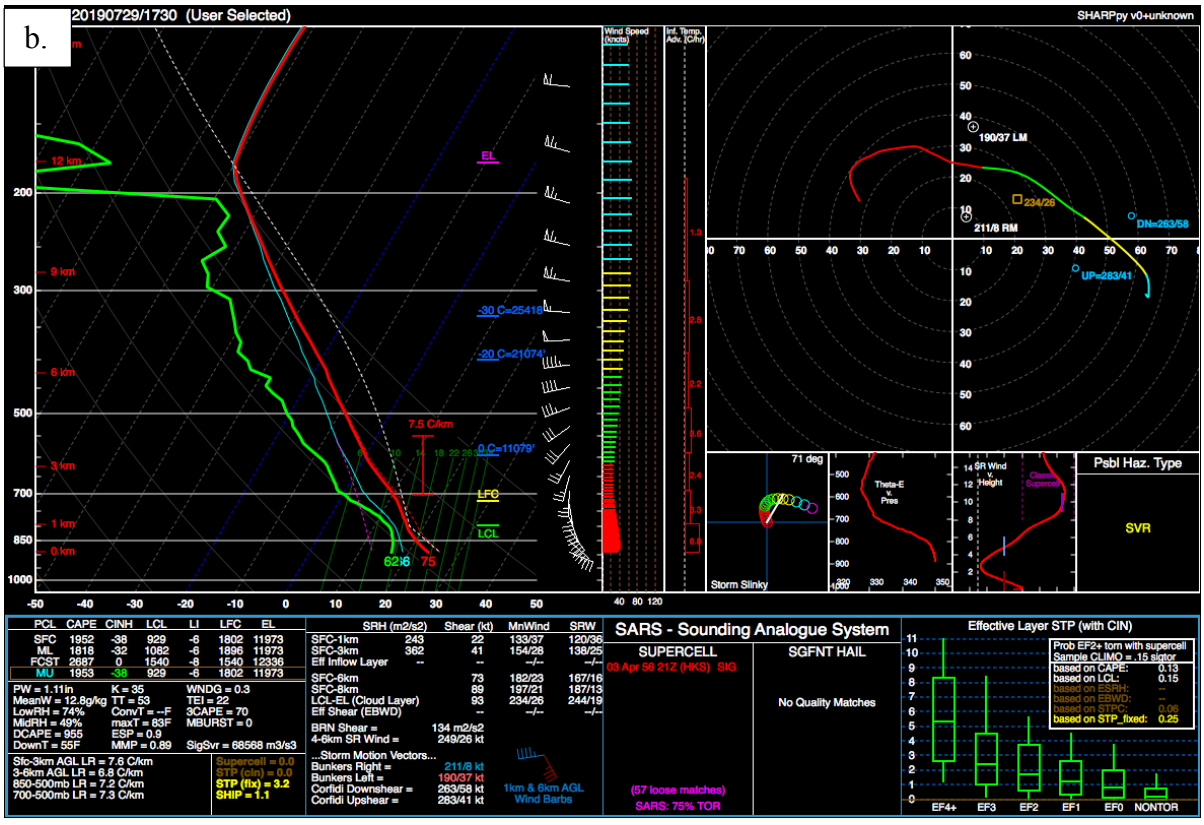
20190729/1730 (User Selected)
SHARPpy v0+unknown
Psbl Haz. Type
SVR
SARS - Sounding Analogue System
SUPERCELL
SGFNT HAIL
No Quality Matches
(57 loose matches)
SARS: 75% TOR
Effective Layer STP (with CIN)

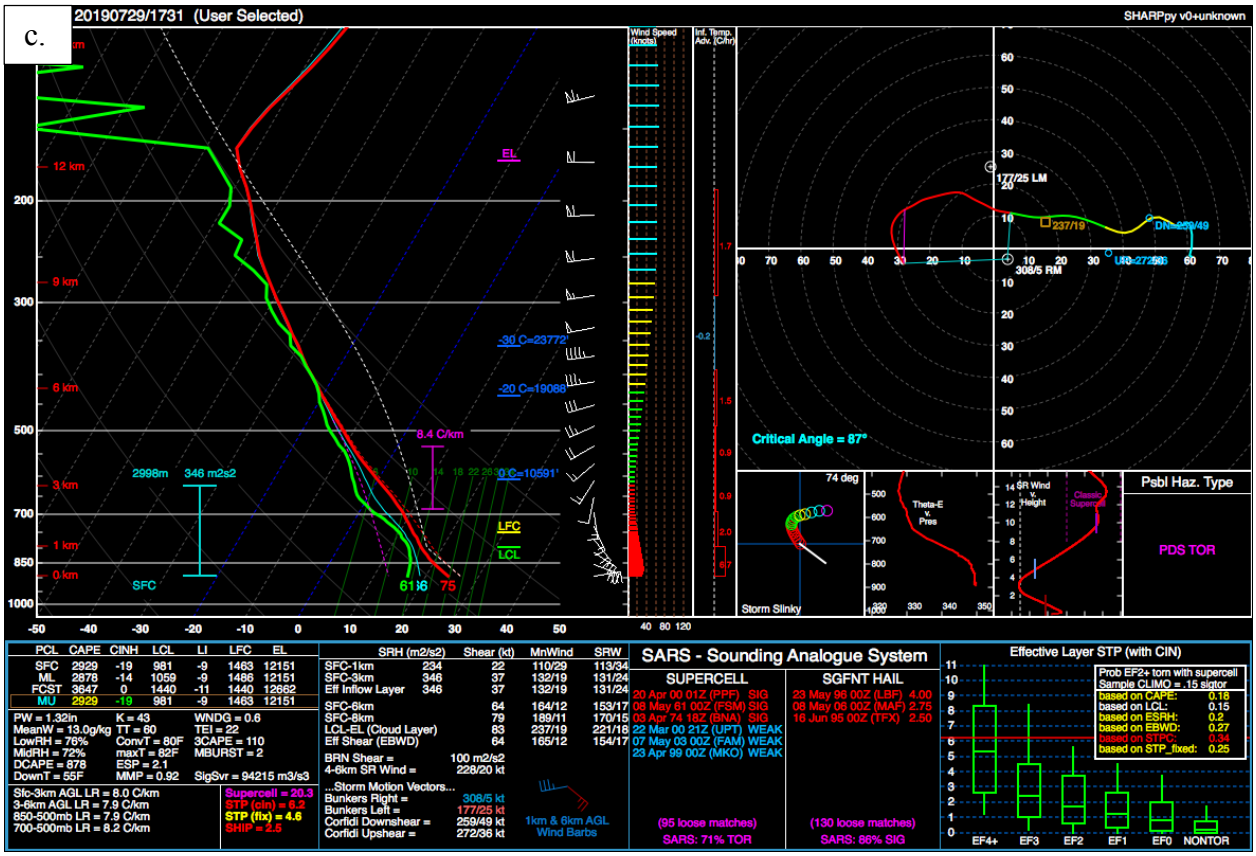

Figure 4.7: Updraft-nudging initialization. As in Fig. 4.6 but now displaying the "updraft nudging" initialization technique.

exhibit the necessary thermodynamic and kinematic characteristics required for supercells (see section 2.2.1). In each environment, there is ample CAPE and wind shear and both vertical wind profiles veer and strengthen considerably with height. Initially, recalling discussion in chapter two, both environments appear favorable for low-level rotation and potentially tornadoes. Superposing the two soundings shows only minor, but potentially significant differences (Fig. 4.3). There is substantial SRH in each of the 0-1 km, 0-3 km and approximate effective inflow layers in the tornadic and nontornadic environments. However, while the SRH is of comparable magnitude, the nontornadic environment exhibits a "kink" in the hodograph in the lowest few hundred meters above ground. Below this height the low-level storm-relative environmental vorticity is predominantly crosswise in orientation. In the tornadic environment, no such kink is present in the hodograph and the environmental shear is associated with predominantly streamwise vorticity, which is known to be important at low-levels to sustain rotation of the low-level mesocyclone. Two other potentially significant structural differences between the soundings are the quality of boundary layer moisture, which is greater in the tornadic environment and a dewpoint inversion and second hodograph kink at 6 km above ground level (AGL) in the nontornadic environment, which is not present in the tornadic composite sounding. Evidence of these two structural differences was apparent throughout the author's simulations, in which cloud bases were significantly lower in the tornadic environments and a stable layer that frequently developed around 6 km AGL in the nontornadic simulations, which was largely absent in the tornadic simulations (see sections 4.2.1 and 4.2.2).

For several decades, a popular sounding to initialize supercell simulations has been the idealized sounding from Weisman and Klemp (1982; Fig. 4.5). This sounding successfully

produces TLVs almost invariably with adequate grid resolution and so it is employed as a comparison with the results from the VORTEX2 environments in section 4.3.

c. Initialization technique: Using updraft nudging vs. bubble perturbation

The methods by which to perturb the initially horizontally homogeneous model domain has been the subject of debate over the last several decades (Naylor and Gilmore, 2012). All such methods are artificial and each present their own concerns over contaminating the environment that the user intends on studying and the ability to physically study the process by which a supercell develops and evolves in the real atmosphere. The traditional approach is to use a warm potential temperature "bubble" (which is used here to initialize the NMS) that locally causes the atmosphere to become convectively unstable and develop deep convection (e.g. Weisman and Klemp, 1982). Recently, it has become more popular to initialize mesoscale research models such as the CM1 with a so-called "updraft nudging" technique, which simply forces vertical motion locally within the domain. Naylor and Gilmore (2012) demonstrated that, with the CM1, it was more effective at generating stronger, longer-lived supercells, which is likely the primary reason for its popularity. The instantaneous effects of this cloud-forcing technique on the domain environment to which it is imposed are severe, however the domain subsequently undergoes rapid compressible adjustment to remove the perturbation after the forcing is turned off and so it has largely been assumed that the lasting impact of the technique is minimal. Although the goal of this research is not to compare the two commonly used initialization techniques, the author noticed significant differences in supercell structure and evolution when using both to generate supercells with the NMS (not shown) and so a brief note on these differences and reasoning for choosing the bubble technique is warranted.

To qualitatively interpret the differences between the supercells produced with the NMS with the updraft nudging and warm-bubble techniques, soundings were generated from 30 km to the south-east of the initial perturbation in convectively uncontaminated inflow over the first 1800 s of the simulation. Fig. 4.6 displays the vertical structure of the environment at 600, 1200 and 1800 s after the warm bubble perturbation. While the effects of the perturbation are apparent in the acceleration of the low-level wind field, the remainder of the sounding remains consistent with the original (compare with Fig. 4.2). This was repeated for the updraft nudging technique with vastly different results (Fig. 4.7). The kinematic structure changed dramatically over the 1800 s, not only in its magnitude but also in direction. Possibly the most concerning however, was the substantial changes to the thermodynamic profile. Both the vertical temperature and dewpoint profiles are considerably different to the original sounding and the bubble initialization after 1800 s, which leads to drastic changes in the CAPE and relative humidity in the environment. These differences between the initialization techniques arises from the substantial differences in pressure perturbation generated by imposing each forcing. The bubble initialization generates a surface pressure perturbation of approximately 2 hPa, while the updraft nudging generates approximately 40 hPa. While it is evident that the model atmosphere adjusts rapidly to this initial perturbation, its effects are apparent in most model fields for a significant period of the simulation. Additionally, 4 K temperature contrasts are commonly observed between the boundary layer rolls and so the magnitude of the warm-bubble perturbation is not unphysical. The size of the perturbation however, is unphysical and leads to mesocyclogenesis through significantly different mechanisms than real-data simulations of supercells studied by the author using the NMS model.

While this is by no means a comprehensive or conclusive study of the differences between the methods and may only apply to the NMS model, it is sufficient reasoning for choosing the bubble initialization for the NMS portion of the numerical simulations. The CM1 simulations were initialized using the updraft nudging technique to be consistent with the model configuration used by Orf et al. (2017).

d. Methods of analysis

Integral data

Several methods of analysis were applied to study the evolution of rotation in the simulated storms. The first of which are plots of diagnostic fields calculated at the model time step and output in an integral sense throughout the simulation. These *integral plots* are used to measure extremes in the model domain, which produces a guide for which times to focus on in more detail. The focus of the integral data is on the lowest kilometer above ground because this is the region in which rotation must intensify to permit tornadogenesis. It is also below the level at which buoyancy associated with the updraft has a direct role in vorticity evolution and so the evolution of rotational structures is critical to the development and sustenance of pressure perturbations and updraft acceleration in this layer.

While this method is highly efficient for isolating major events in the simulation such as tornadogenesis, it affords very little information on the processes involved in the development of such extrema and so more detailed analysis is required once a time frame of interest has been established.

Time vs. height plotting

Adding height as a dimension to an integrated field significantly improves the quality of information attained. Time vs. height analysis is a popular technique for diagnosing the evolution of vorticity and vertical velocity in simulated supercells. It is applied here to assess where local maxima in rotation and helical flow develop initially and whether they evolve upwards or downwards with time. Studying the evolution of the vorticity field in this manner has been found to be useful for identifying tornadogenesis and failure events but because large values of (vertical) vorticity develop almost instantaneously over a significant portion of the lower-troposphere, it does not afford much explanation for the sudden intensification. However, applying new diagnostics presented in chapter three with this technique illuminates much greater insight, the results from which will serve as a basis for much of the discussion throughout this chapter.

Vapor 3D visualization

To fully visualize the three-dimensional structure of rotational flow it is necessary to render many of the diagnostic fields outlined in chapter three with a visualization program such as *Vapor*. Vapor is state-of-the-art software designed specifically for visualizations and analysis of atmospheric and oceanic flows and is highly competent for three-dimensional rendering such as is intended in this dissertation. One only has to look at the renderings used by Orf et al. (2017) to get a sense of its capabilities (Fig. 2.17; Fig. 2.18). Three-dimensional analysis is critical to studying development and interaction of misoscale rotational structures in a supercell. Rendering the new diagnostics with this tool highlights critical structures and their interactions from the total vorticity field demonstrating their utility in studying numerical realizations of supercells

and will be used extensively in the following sections. It is important to point out, however, that using three-dimensional isosurfaces to study the development and evolution of rotation can be misleading due to the arbitrary choice of isosurface magnitude set by the user. Therefore, it is often necessary to use isosurface analysis alongside other techniques.

SHARPpy sounding analysis

It is well established that the development and intensification of low-level rotation in supercells is highly dependent on the vertical kinematic and thermodynamic structure of the storm's local environment (see chapter two). Therefore, to determine the local vertical atmospheric structure in a variety of regions around the simulated supercells the author uses the SHARPpy program to plot soundings and hodographs from the model data. Used alongside the other methods outlined in this section can help develop a better understanding of how the storm is interacting with its environment particularly at times of rapid intensification of rotation. The vertical atmospheric structure varies significantly from one region to another and so several soundings from each region analyzed were taken to ensure a characteristic profile of this region was sampled. The regions that are analyzed from this perspective include the supercell's "left-flank", on the cold side of the dominant outflow convergence boundary that extends to the north from the updraft in most of the simulations. This boundary has been referred to as the "left-flank convergence boundary" (e.g. Beck and Weiss, 2013) and the "forward-flank downdraft boundary" (e.g. Orf et al. 2017). Additionally, soundings are taken just on the relatively warm side of this boundary to the east, further downstream in the forward flank precipitation region and in the supercell's near-inflow region. These regions are marked on Fig. 4.8 using a characteristic example of the supercell's outflow structure from a tornadic supercell in the NMS.

Part II. Evolution of rotational structures in tornado-like genesis and failure in VORTEX2 environments

Tornadogenesis is referred to herein as *tornado-like* genesis because the numerical grid resolution used does not permit physical surface pressure minima or wind speeds that are observed in real-world tornadoes. While we have the capability to model in resolutions that do adequately resolve the tornado and its associated strength (e.g. Orf et al. 2017), this would limit the number of different simulations that can be studied and so for the purpose set out in this dissertation the author opted for coarser resolution with greater variety. Defining what is and what is not a *tornado-like vortex* (TLV) then becomes somewhat user-defined. Herein, the author uses a combined approach of surface pressure perturbation at least 200% lower than the background steady state (which was generally -2 hPa, and so -6 hPa was a typical threshold used), collocated with a local maximum in I^2 and surface wind speed of at least 30 ms^{-1} associated with the vortex (approximately the threshold used for an EF0 tornado).

10-member ensemble simulations were performed using both the tornadic and nontornadic composite VORTEX2 environments with random perturbations imposed on the initial warm bubble. All 20 produced long-track right-moving supercells lasting more than 3 hours. All of the supercells evolving in the *tornadic* environment produced TLVs at some stage in their lifecycle but the time at which they occurred varied significantly. Additionally, there were frequent cases of TLV-*failure* in the tornadic supercells at different stages of their lifecycle.

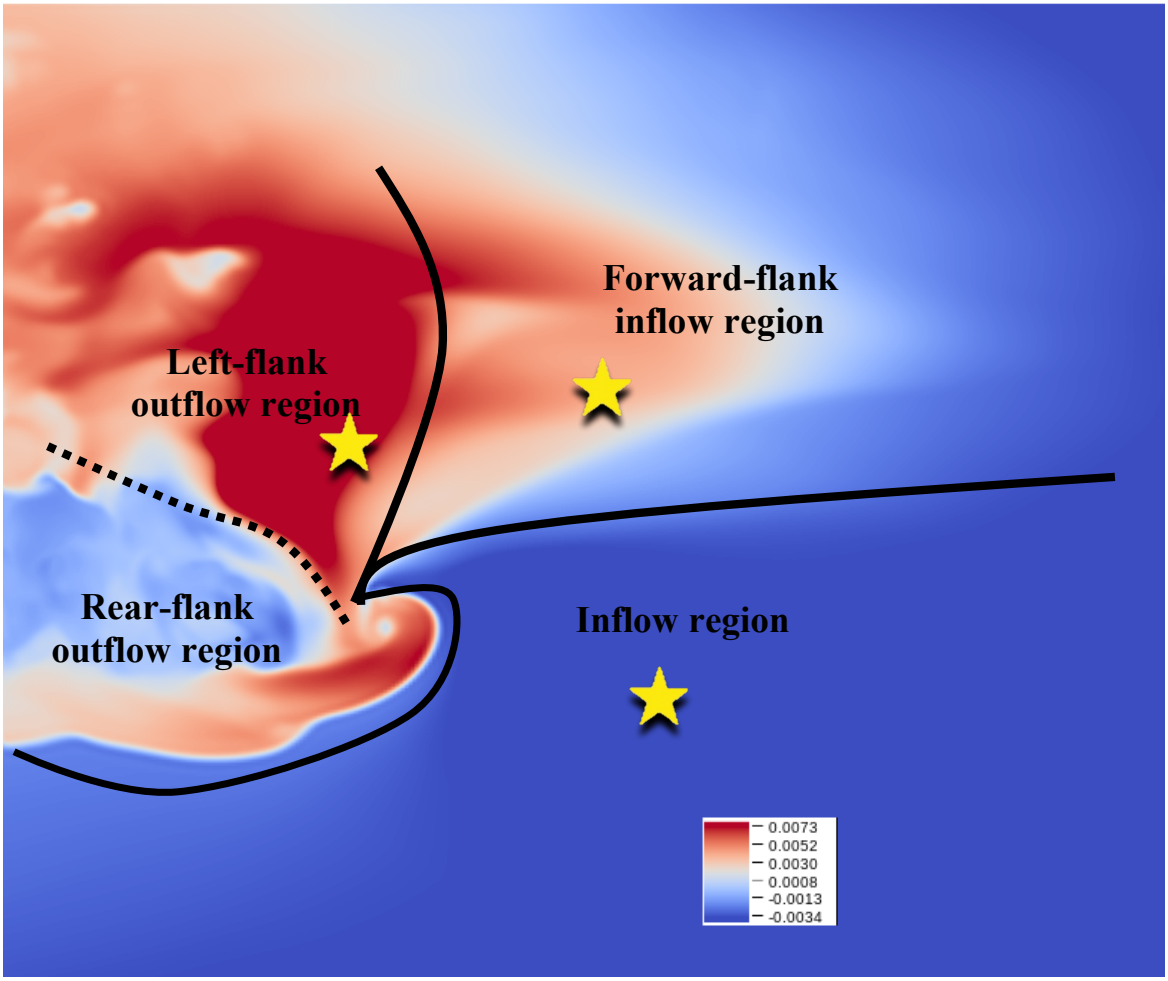

Figure 4.8: Regions of a typical cyclonic, right-moving supercell. The surface is shaded by density perturbation and the black solid lines indicate zones of convergence. The dashed black line is a transient convergence boundary. Stars depict the locations of model soundings taken in each region.

Here, "TLV-failure" refers to a storm that produces a deep, surface-based vortex with a local pressure minimum but which does not meet the thresholds for pressure perturbation or wind speed. None of the supercells evolving in the nontornadic environment produced TLVs, although deep misoscale vortices resembling the structure of a tornado developed in several simulations, their intensity was wholly unimpressive. This variety of different supercell evolution with both TLV success, failure and non-events provides a wealth of data from which to study the

development and intensification of rotation from the theoretical perspective outlined in chapter three.

In the following section supercells from the tornadic environment are presented. To study specific rotational structures and their potential roles in TLV-genesis, the author chooses to focus on a case of TLV-success (TOR-S) and a case of TLV-failure (TOR-F) from two different simulations.

4.2.1 VORTEX2 simulations: Tornado-Like-Vortex success

Common to all of the tornadic and nontornadic supercell simulations with the NMS, a deep updraft develops in response to the bubble forcing and begins producing precipitation that reaches the surface after approximately 30 minutes (1800 s). The initial updraft subsequently undergoes a splitting process generally during the 1800 s to 3000 s time period of the simulation, thereafter, a dominant cyclonic, right-moving supercell develops and persists through 9000 s. In this section, a characteristic case of TLV-success is analyzed in detail from a tornadic simulation with the NMS.

a. TLV genesis in the TOR-S simulation

The TOR-S storm went through the splitting process described above and at approximately 3000 s through the model integration and evolved into a dominant, intense right-moving supercell soon afterwards (Fig. 4.9). Several deep, surface-based vortex structures developed during the 3000-5000 s period, none of which intensified into a TLV (Figs. 4.10, 4.11).

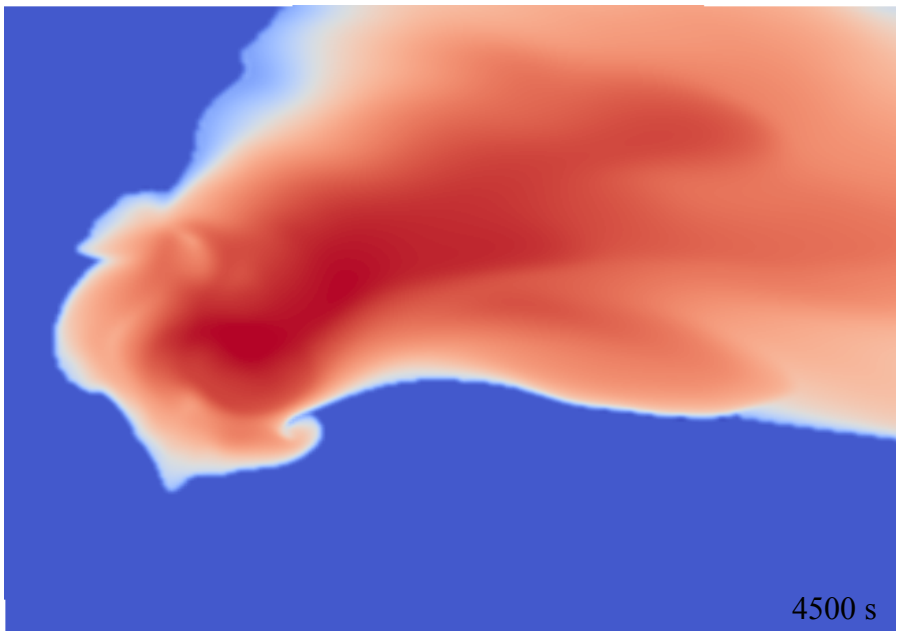

Figure 4.9: TOR-S surface condensate at 4500 s. Total condensate is shaded at the lowest model level where darker reds indicate higher condensate mixing ratio and blue indicates no surface condensate. This can be thought of as surface reflectivity.

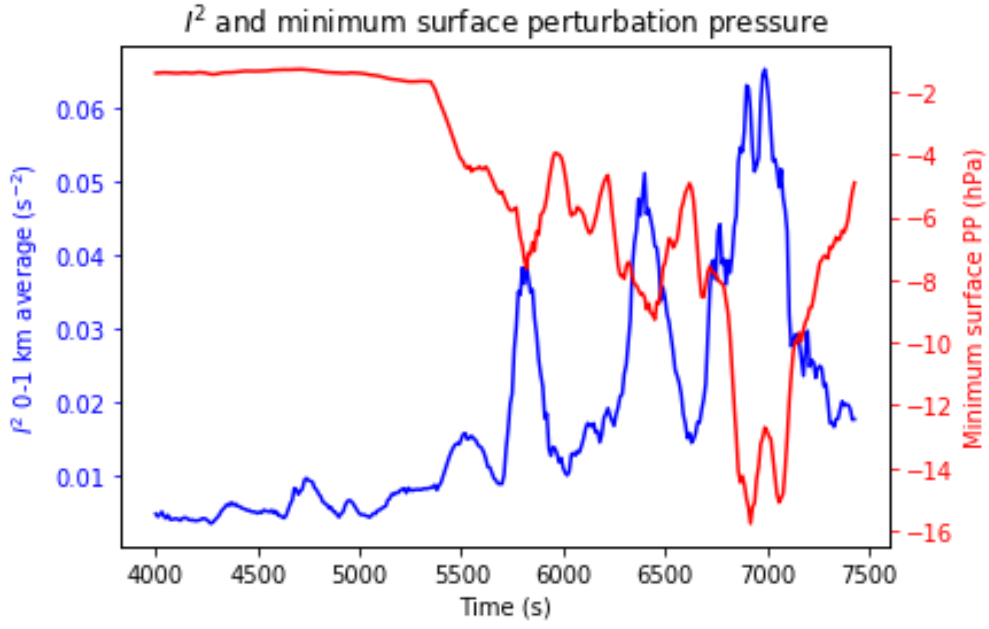

Figure 4.10: Evolution of I^2 and surface pressure perturbation in the TOR-S simulation. Blue line is maximum I^2 and red line is minimum pressure perturbation at lowest model level.

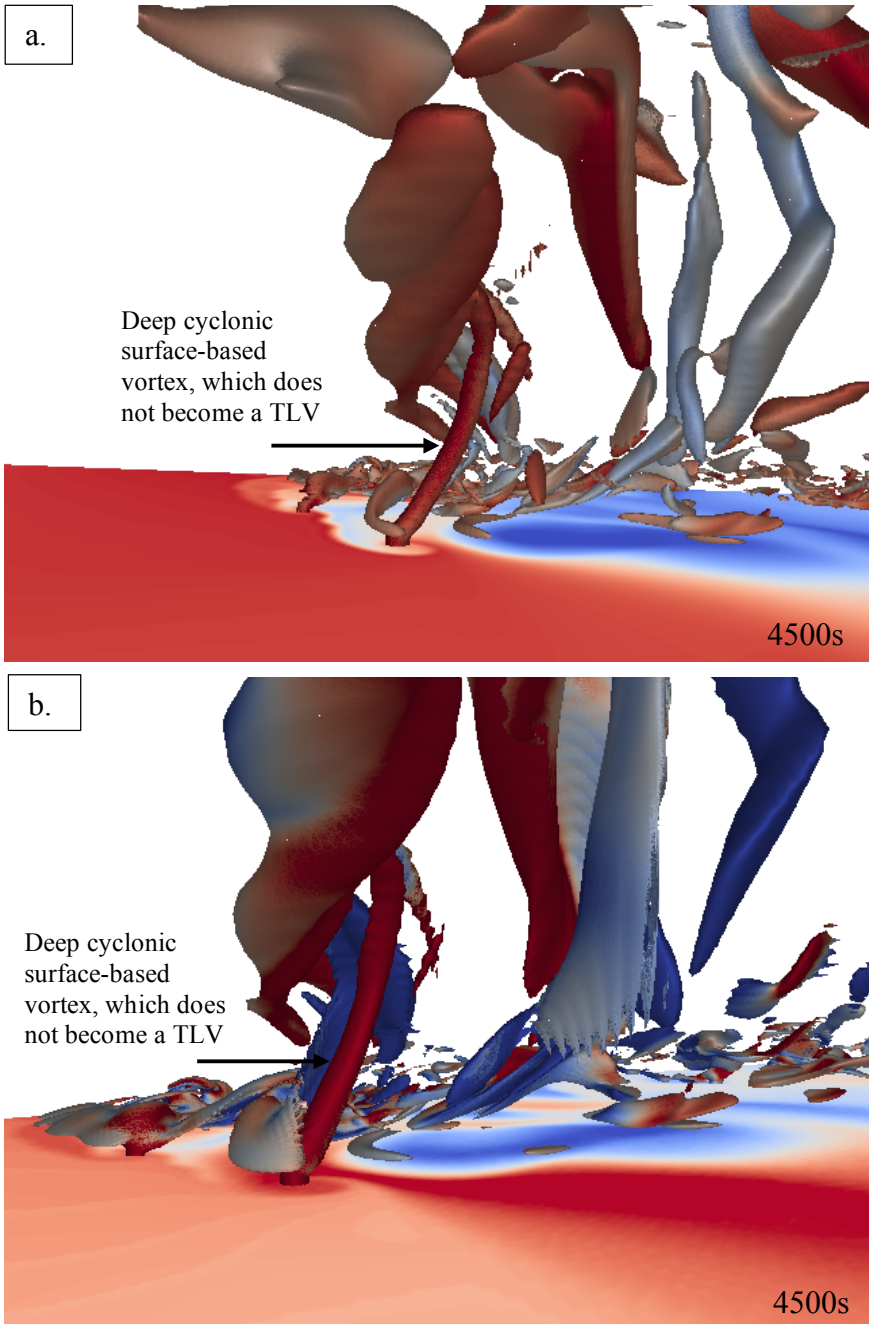

Figure 4.11: Surfaced-based vertical vortex that fails to become a TLV. Isosurfaces of I^2 (0.0025 s^{-2}; panel a) shaded by the vertical component of vorticity and total vorticity magnitude (0.05s^{-1}; panel b) shaded by the vertical component of vorticity. With surface shaded by equivalent potential temperature in (a) and saturation point in (b), where warmer colors indicate larger values of both. The view is from the east in (a) and the south-east in (b). The model time is 4500 s, 1000 s before TLV-genesis.

At 5500 s, the surface pressure perturbation rapidly dropped from -2 hPa to -8 hPa and I^2 doubled in magnitude, indicating that TLV-genesis had occurred (Figs. 4.10 & 4.12). Both total vorticity and I^2 adequately identify this event from an integral perspective, however, neither indicate a period of interest in the time prior to genesis. However, when analyzing rotational helicity integral data, a period of interest before TLV-genesis becomes apparent (Fig. 4.12). Between 4500 and 5000 s, a substantial maximum of rotational helicity develops in the lowest 500 m AGL, and is accompanied by a maximum in the surface vertical vorticity, which appears to intensify just after the helical flow (Fig. 4.13). Additionally, maxima in vertical stretching and saturation point are correlated with the maximum in rotational helicity (Figs. 4.14, 4.15). Finally, a stark contrast between the rotational vorticity and rotational helicity parameters during this timeframe indicates that a conversion of rotational vorticity to rotational helicity is taking place during this time (Fig. 4.16). During the TLV-phase of the TOR-S simulation, maxima in rotational vorticity and rotational helicity are significantly better correlated as would be expected if the dominant rotational structure in the storm domain was also helical. Although a TLV doesn't develop until approximately 5500 s, there is evidence to suggest the storm is undergoing structural changes in the 4500 – 5500 s period that demand more detailed investigation.

Time-height analysis of this period of interest was then used to learn more about the origins of the intensification of helical flow and its evolution at low-levels during the pre-TLV period. From 4500 s to 5400 s rotational helicity develops and intensifies in the lowest 500 m AGL in the left-flank region of the supercell's outflow (Fig. 4.17). Large values of helical flow associated with the mesocyclone between 1 and 4 km AGL are also apparent at the start of this period but weaken substantially in this layer by 5400 s. At 5200 s, the rotational helicity exhibits

a rapid intensification in the lowest 500 m and appears to interact with a distinct region of helical flow in the 1000-1500 m layer that intensifies during the upward intensification of helical flow.

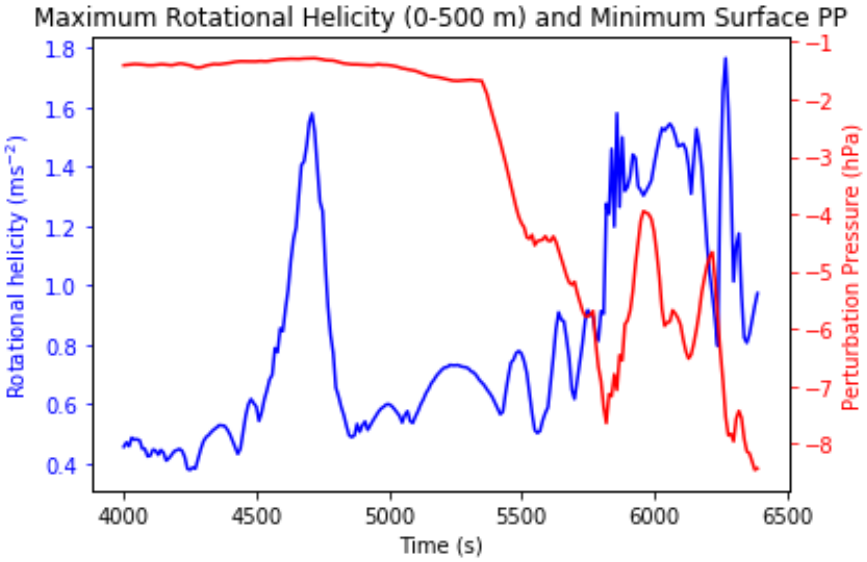

Figure 4.12: Rotational helicity and surface pressure perturbation during TLV-genesis. Evolution of maximum rotational helicity averaged over the lowest 500 m AGL (blue) and minimum surface pressure perturbation (PP, red) between 4000 and 6500 s of the TOR-S simulation.

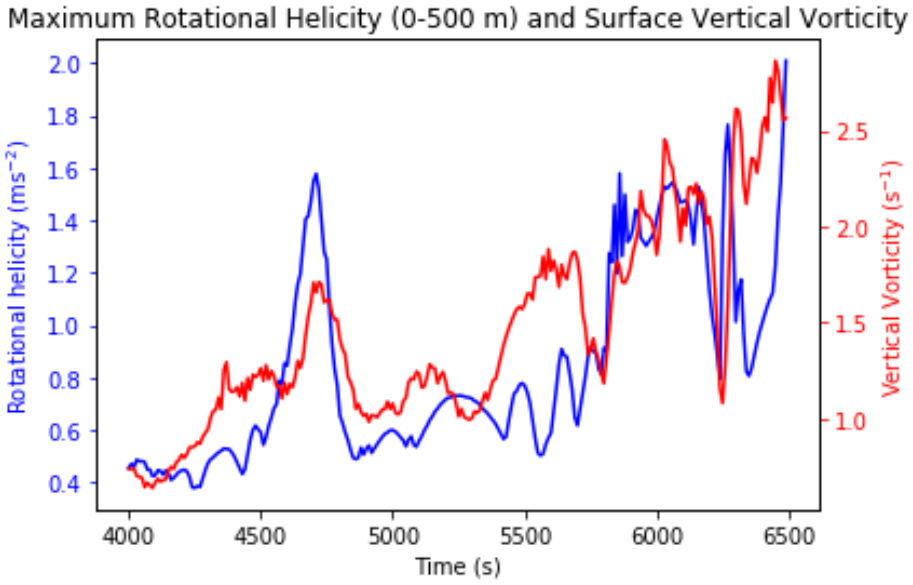

Figure 4.13: Rotational helicity and surface vertical vorticity during TLV-genesis. As in Fig. 4.12 but with the red line indicating evolution of maximum surface vertical vorticity.

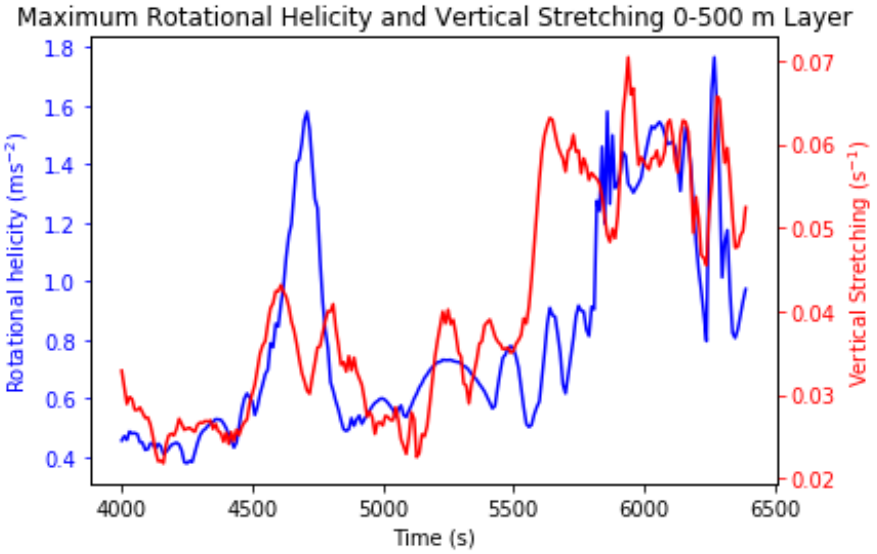

Figure 4.14: Rotational helicity and vertical stretching during TLV-genesis. As in Fig. 4.12 but with the red line indicating evolution of maximum vertical stretching in the lowest 500 m AGL.

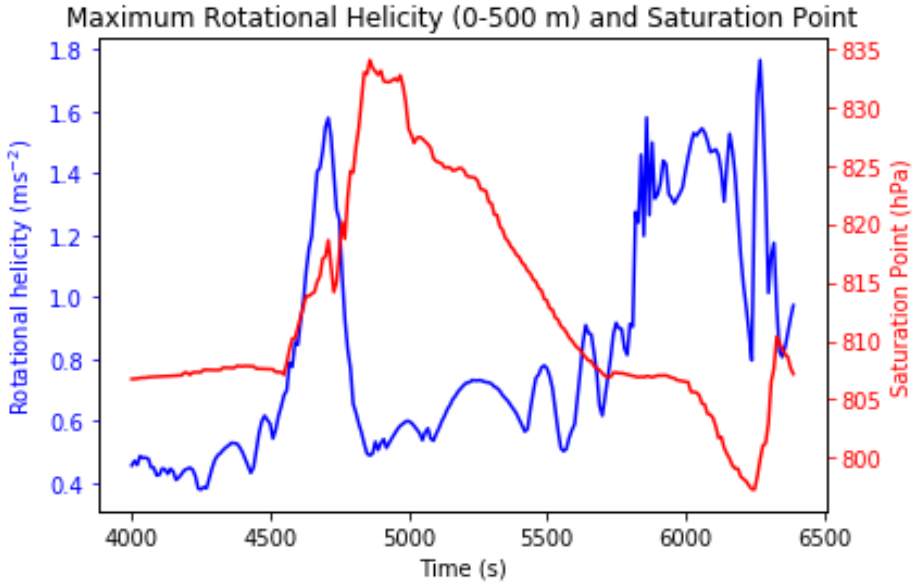

Figure 4.15: Rotational helicity and saturation point during TLV-genesis. As in Fig. 4.12 but with the red line indicating evolution of maximum saturation point.

The upward intensification of rotational helicity is accompanied by a rapidly upward propagating vorticity maximum (Fig. 4.19*b*) and pressure minimum (Fig. 4.20*b*). This feature moves out of the outflow box domain but soon after an intensification in vorticity and rotational helicity

accompanied by a lowering of pressure is evident in the broader storm domain over the 0-4 km layer (Figs. 4.18*a*, 4.19*a* & 4.20*a*). This suggests that the intensification of helical flow in the lowest 500 m in the storm's left flank region preceded the upward development of substantial vorticity involved in TLV genesis. Furthermore, the upward development appears to be associated with an interaction of two distinct regions of helical flow; one in the lowest 500 m AGL and the other in the 1000-1500 m layer. During the time of this interaction the helical flow intensifies in the upper layer and remains substantial during TLV genesis. Upward intensification of rotation appears to be associated with this interaction. Fig. 4.21*a* provides a closer inspection of this interaction and upwards intensification, in which it can be clearly seen that the two regions of helical rotation are initially separated in height until 5300 s during which time explosive upward growth of vertical vorticity occurs (Fig. 4.21*b*).

Analysis of the total vorticity does not illuminate this important dynamical interaction in either domain due to the prevalence of vorticity in a low-level supercell region. Additionally, while vorticity highlights the vertically propagating region of rotation well in the outflow domain (Fig. 4.19*b*), it is significantly different in the full storm domain (Fig. 4.19*a*) due to the larger values of vorticity directly under the updraft. Rotational helicity is qualitatively similar in both domains (Fig. 4.18*a,b*) such that the choice of area over which to analyze the development of helical rotation using rotational helicity in a time vs. height sense is less critical.

Using rotational helicity, the preceding analysis revealed the development of helical rotation in the storm's left flank that intensified upward with time appearing to interact with a separate region of helical rotation aloft, which was associated with explosive upward growth of vertical vorticity. To learn more about this potential interaction, a more detailed two and three-dimensional analysis is performed with Vapor.

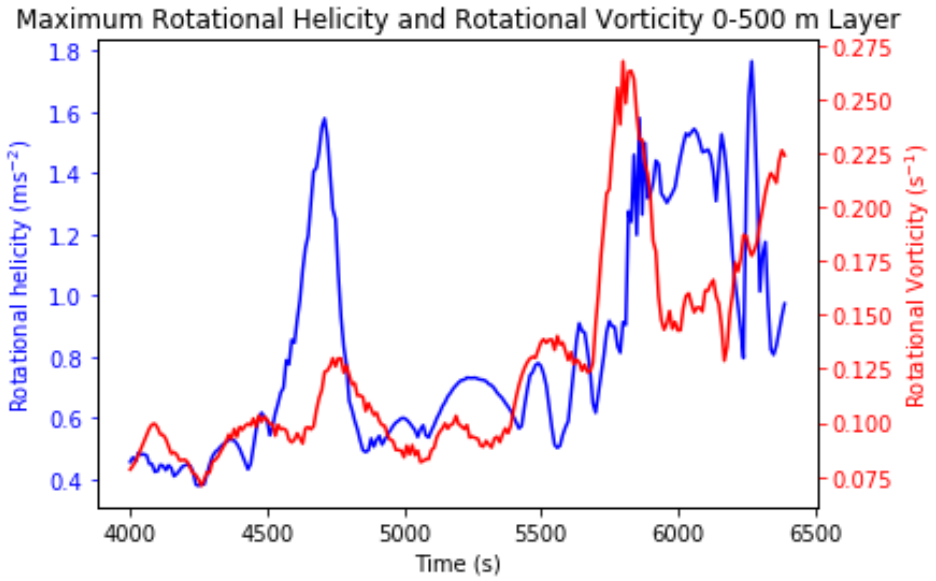

Figure 4.16: Rotational helicity and rotational *vorticity* during TLV-genesis. As in Fig. 4.12 but with the red line indicating evolution of maximum rotational vorticity in the lowest 500 m AGL.

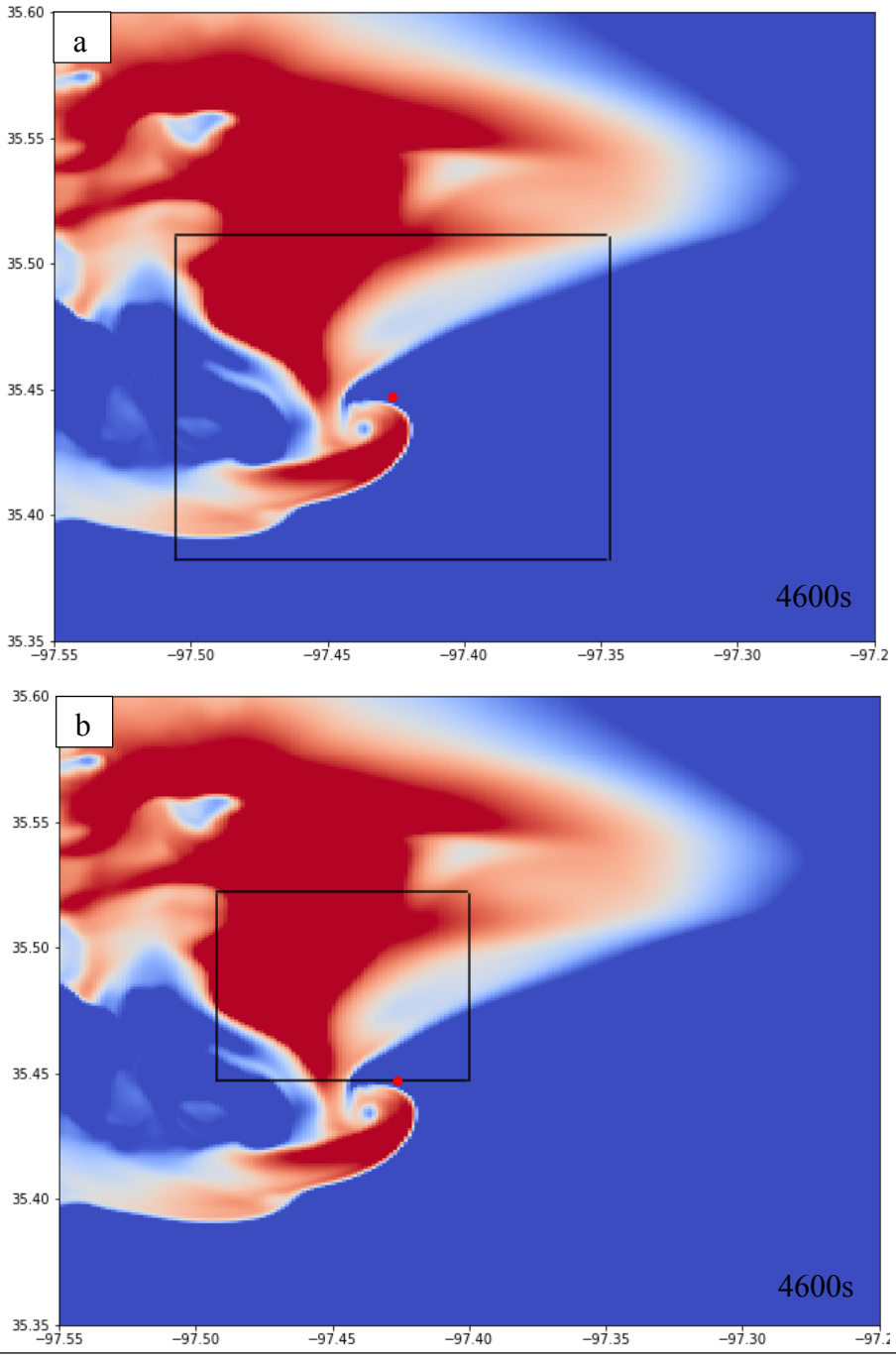

Figure 4.17: Box areas for time-height analysis. Areas are selected relative to storm updraft maximum at 4 km AGL (red dot). The surface is shaded by a characteristic perturbation density structure exhibited by tornadic simulations in the NMS. (a) is the area analyzed in the "storm domain" and (b) is the region analyzed in the "outflow domain". The location of the updraft maximum was determined by applying a Gaussian smoothing function on the vertical velocity data such that the box areas chosen to analyze were quasi-steady relative to the propagation of the storm's updraft center.

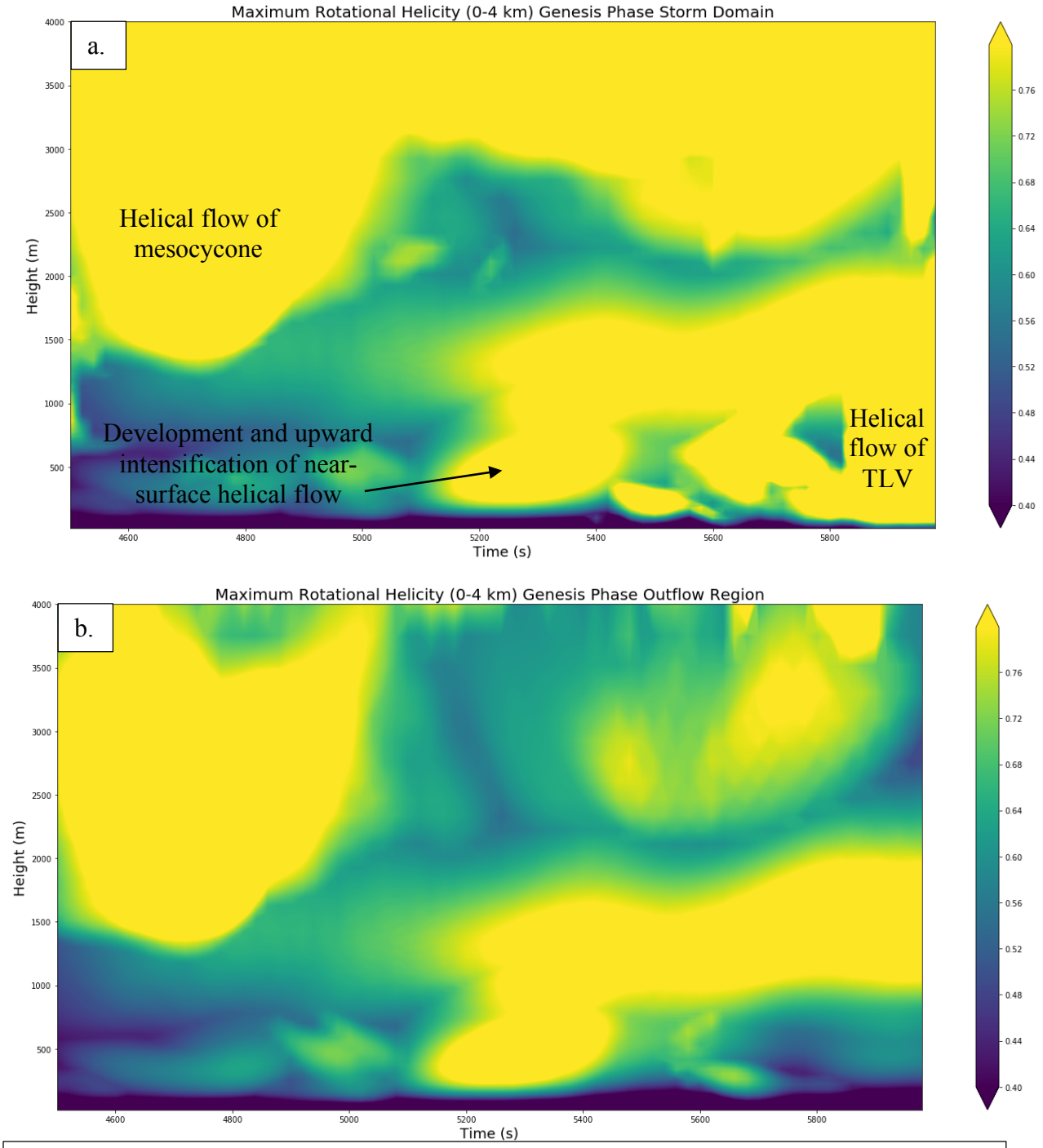

Figure 4.18: Rotational helicity time vs. height during TLV-genesis. Color shading is maximum rotational helicity over the 0-4 km layer in a larger storm domain (a) and more restrictive outflow domain (b).

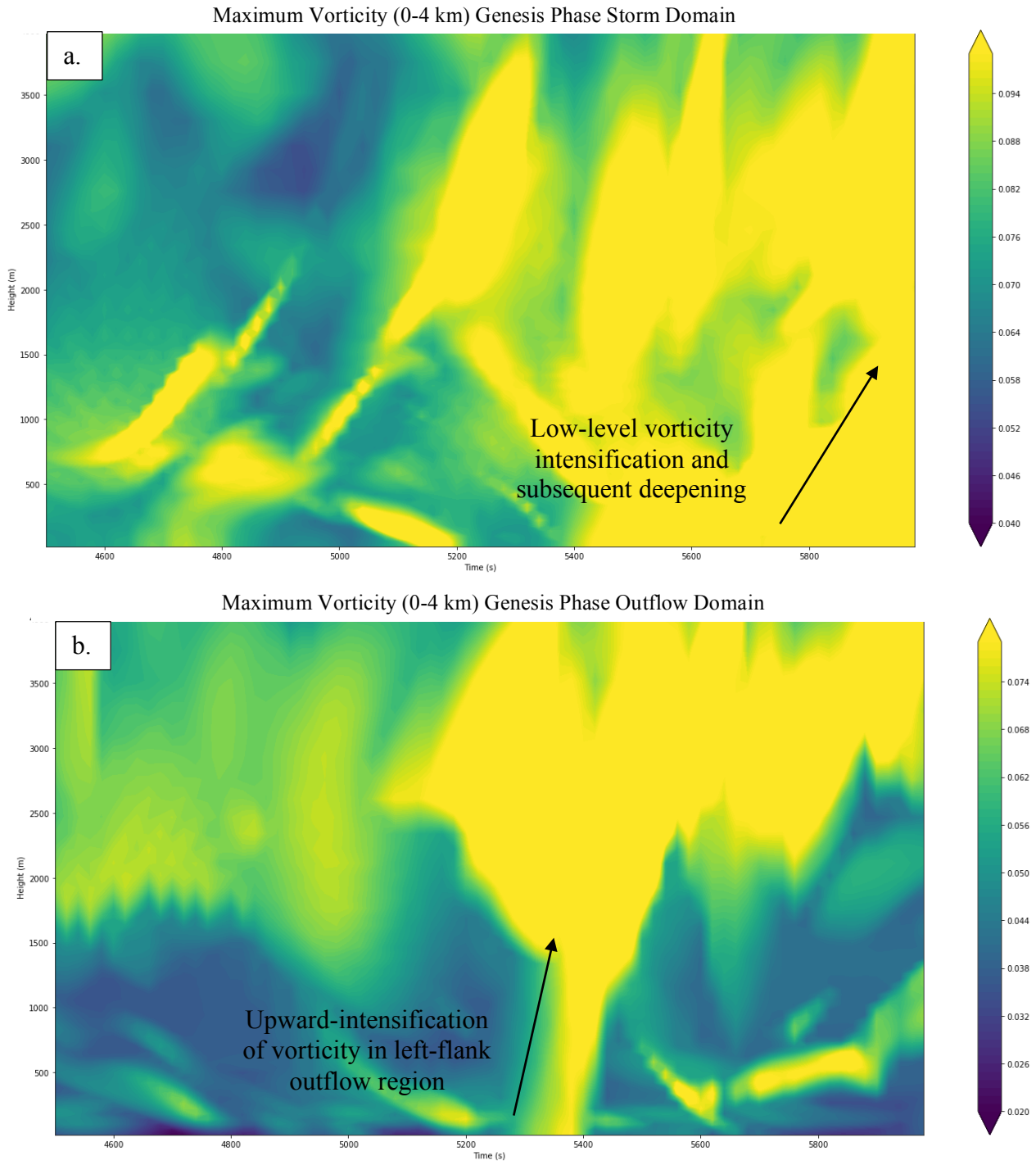

Figure 4.19: Total vorticity time vs. height during TLV-genesis. Color shading is maximum vorticity over the 0-4 km layer in a larger storm domain (a) and more restrictive outflow domain (b).

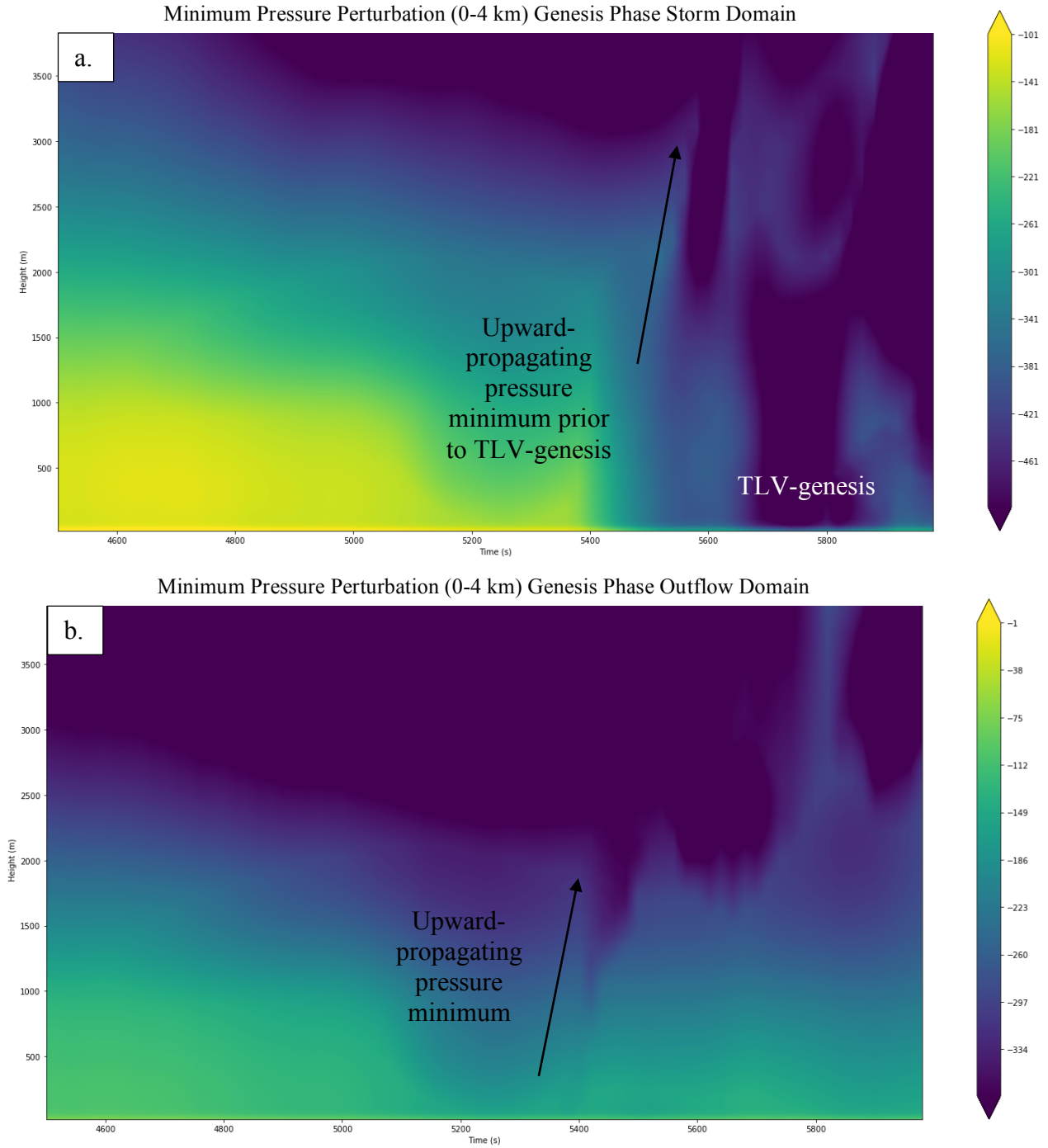

Figure 4.20: Pressure perturbation time vs. height during TLV-genesis. As in Fig. 4.16 but with pressure perturbation shaded.

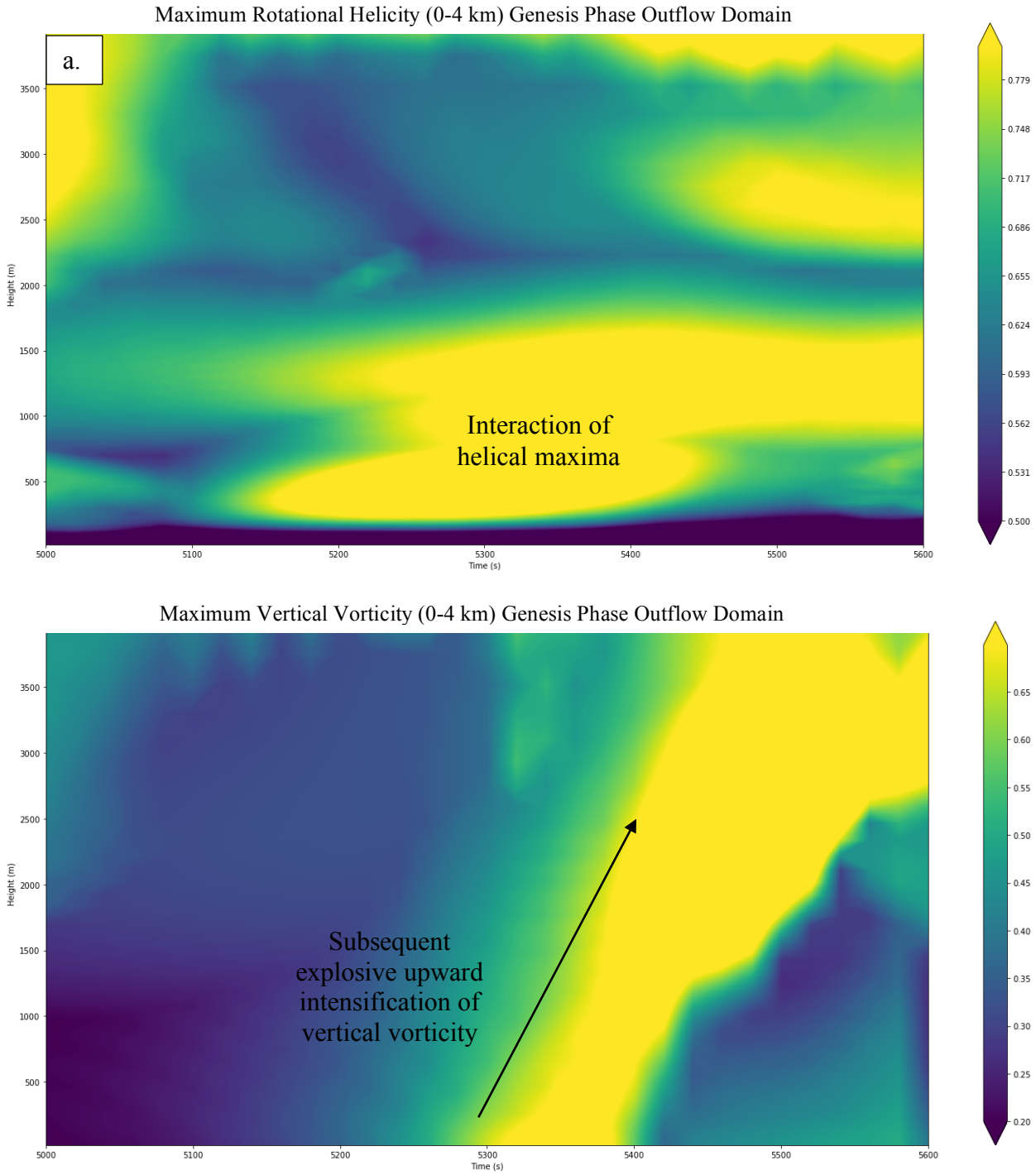

Figure 4.21: Rotational helicity and vertical vorticity time vs. height during TLV-genesis in the left-flank outflow region. Maximum rotational helicity is shaded in (a) and maximum vertical vorticity is shaded in (b) during the 5000-5600 s period of the TOR-S simulation.

During the development and intensification of helical flow in the storm's left-flank region prior to TLV-genesis, the outflow region underwent significant structural reorientation. The surface perturbation density increases markedly several kilometers north of the updraft, which appears to reorient the outflow orientation with respect to the low-level inflow in the forward flank (Fig. 4.22). The cold pool regions to the north and west of the updraft and mesocyclone become significantly more organized as density gradients to the north of the updraft increase. At 4900 s, a north-south oriented band of higher density becomes separated from the larger region of dense air in the left-flank by a region of lower density that broadens with time (Fig. 4.22). This suggests that the outflow air is being locally mixed with environmental air entrained from the low-level forward flank inflow region. At 5400 s, this region of outflow air interacts with the surface-circulation of the developing TLV. Relatively low-density air to the north of the updraft is sustained in the outflow region through 5600 s as the TLV develops.

The reorganization of the cold pool in the TOR-S left-flank region is driven by a core of high condensate, which descends from aloft and is associated with a maximum in hail mass (Figs. 4.23 & 4.24). Intensification of surface divergence occurs in response to this descending condensate maximum and is oriented in a north-south direction along the periphery of the cold pool (Fig. 4.23). Subsequently, a *surge* in momentum occurs horizontally in a southward direction toward the storm's updraft. Associated with which is a reorientation and intensification of the low-level wind field and strengthening convergence along its periphery with the low-level inflow from the forward flank.

Along the periphery of the increasingly dense left-flank outflow air and the low-level inflow, rotational helicity develops in very close proximity to the surface (Fig. 4.25). This helical flow subsequently intensifies as it approaches the low-level updraft from the north, during which

it can be seen to interact with a separate maximum in helical inflow associated with the storm's updraft.

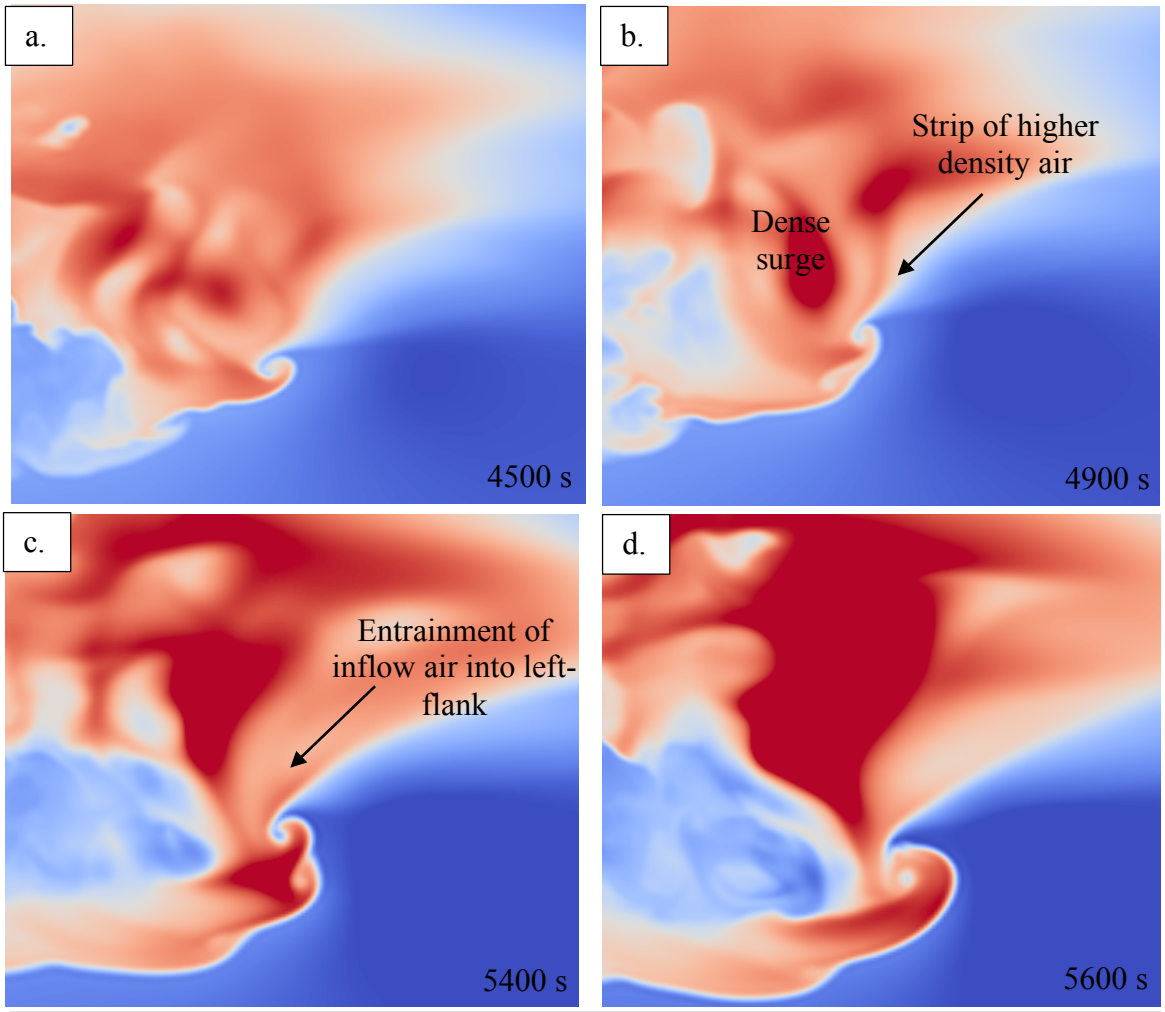

Figure 4.22: Surface perturbation density during TLV-genesis. Warmer colors represent positive values of perturbation density and cooler colors represent negative values. A gradual zoom-in between (a) and (d) is used to focus on the region of interest.

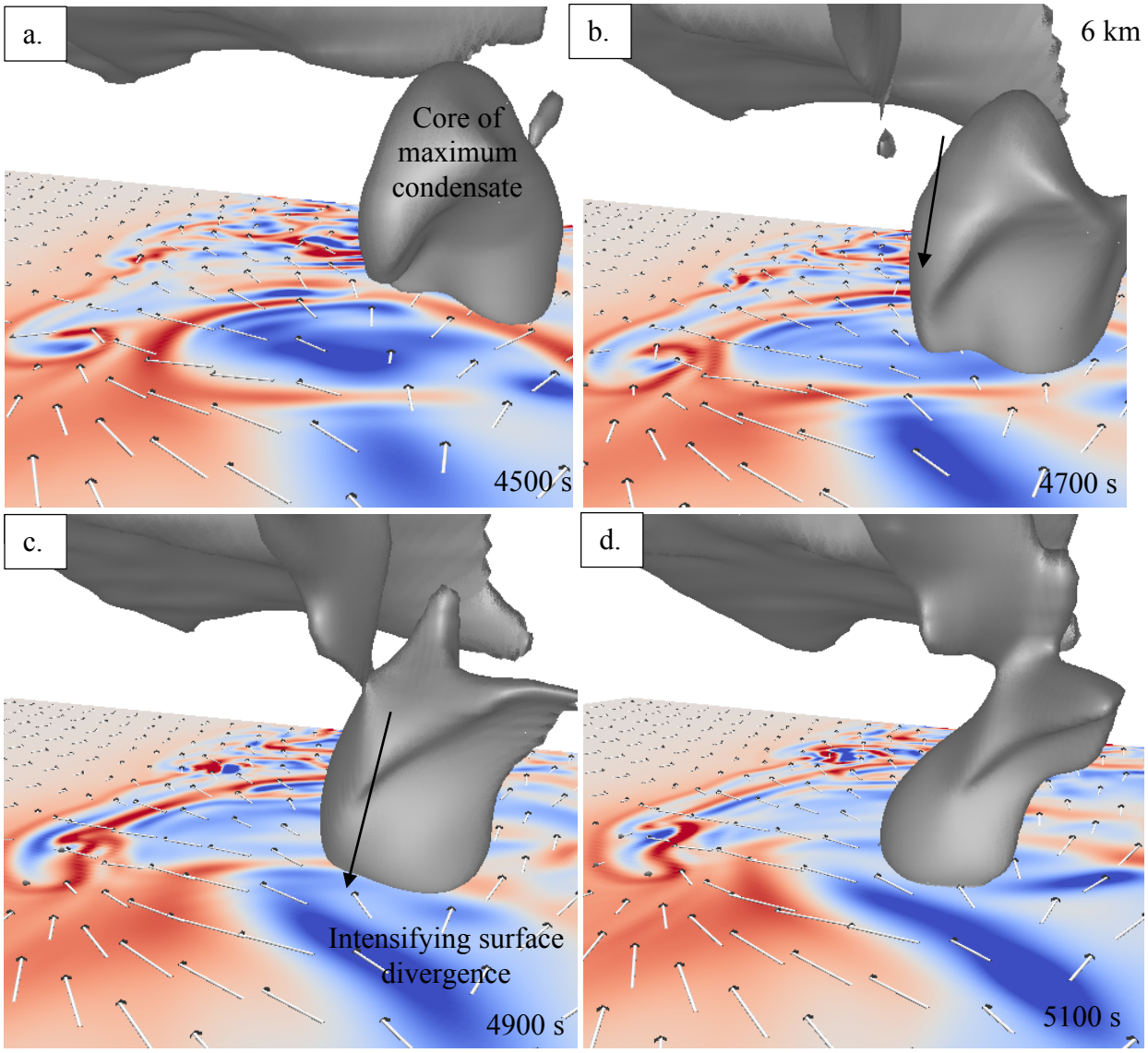

Figure 4.23: Descent of a maxima in condensate in the left-flank outflow region prior to TLV-genesis. Total condensate mixing ratio is rendered at 0.65 gm^{-3}, surface is shaded by surface convergence where warmer colors indicate positive values of convergence and cooler colors indicate divergence. Surface (lowest model level) wind vectors are also plotted where length corresponds to their magnitude. View is from the north-east. Model time is displayed in each panel.

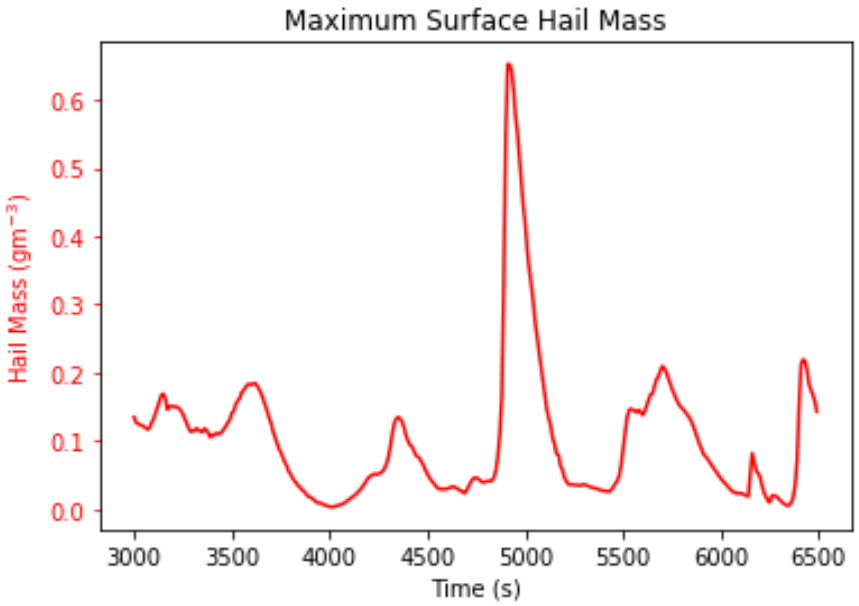

Figure 4.24: Maximum surface hail mass in TOR-S simulation.

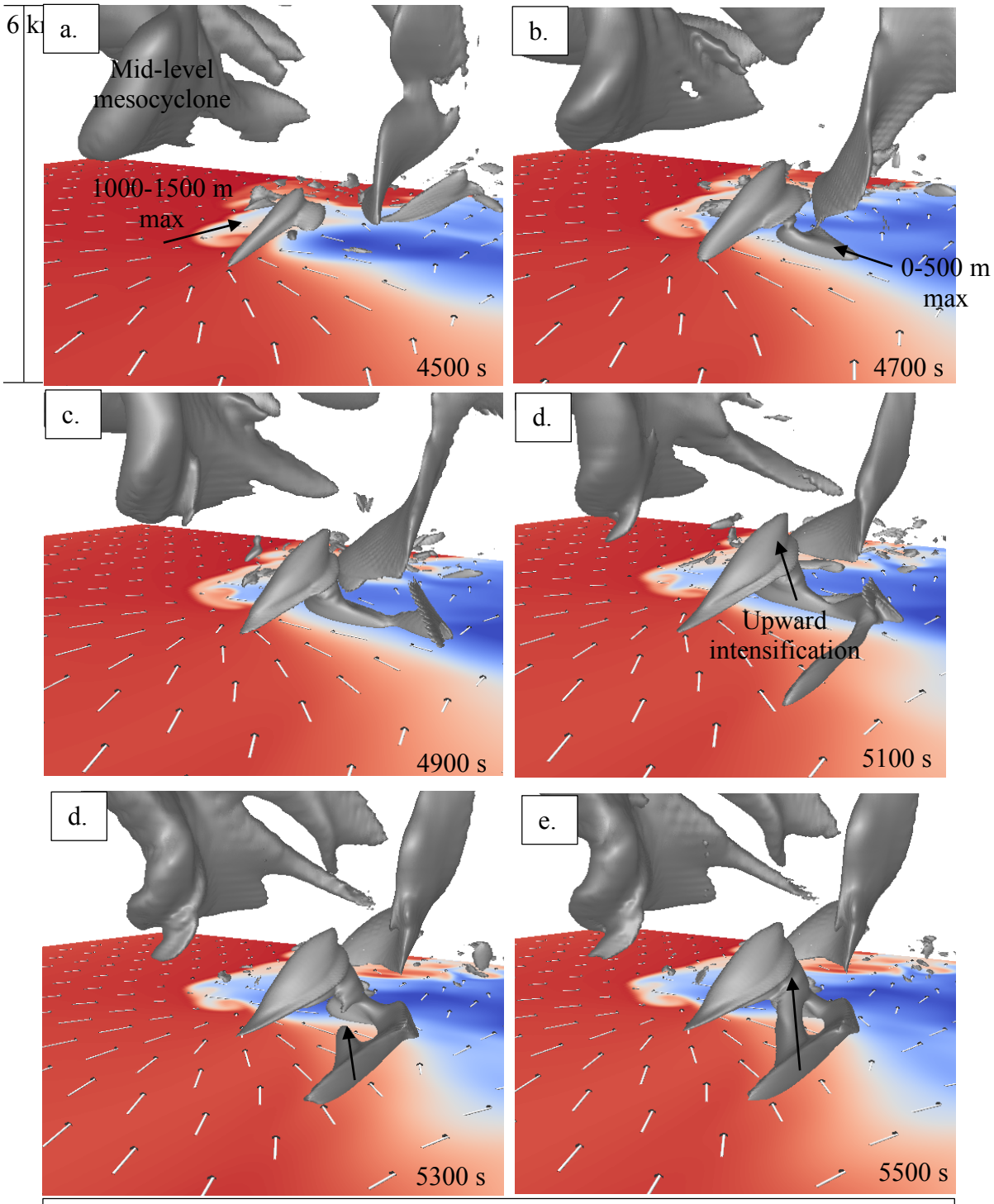

Figure 4.25: **Rotational vorticity development and intensification in the left and forward flank regions during pre-TLV period.** Gray isosurface is rotational helicity contoured at 0.45 ms^{-2}, surface is shaded by equivalent potential temperature where warmer colors correspond with greater values and is overlaid by wind vectors at the lowest model level. View is from the north-east.

A baroclinic roll structure evolves along this convergence boundary and, just on the cool side of which, helical rotation quickly intensifies (Fig. 4.26). As the baroclinic roll and helical structure intensify, positive values of perturbation virtual-virtual temperature (θ'_{vv}; Tripoli and Smith, 2014*a,b*) descend into the outflow region on the cool side of the helical structure. Positively buoyant air is entrained downwards into the outflow along the internal edge of the helical rotation. To confirm the downward transport of environmental air, a vertical slice of potential temperature is taken through the developing helical structure, which shows that larger values of potential temperature descend into the outflow along its cool edge (Fig. 4.27).

As the helical structure develops southward toward the updraft along the periphery of the near surface divergence in the left-flank, it *couples* with the helical inflow from the forward-flank region of the storm (Fig. 4.25). Negative perturbation pressure in the lower portions of the rotating updraft intensifies and lowers during this process (Fig. 4.27*a*). With this low-level intensification, the updraft also intensifies on its lower left side (relative to its forward propagation) and the helical rotation is ingested from the north (Fig. 4.27*b*). Significant surface-based vertical vorticity develops along the structure and is also ingested into the rotating updraft (Fig. 4.27*c*). During the 5200 – 5400 s period, which the time-height analysis indicated explosive upward growth of vertical vorticity, the perturbation pressure field intensifies rapidly over the lowest several kilometers in a tube-like structure indicating the formation of the TLV (Fig. 4.27*d*). At the time of the vertical intensification of helical flow and vertical vorticity evident in the time-height analysis (Fig. 4.21), there was also a *descending* intensification of helical flow from the coupled structure, which is initially just elevated from the surface, to the lowest model level between 5600 and 5800 s (Fig. 4.18*a* & Fig. 4.29). This downward intensification was associated with the formation of the TLV.

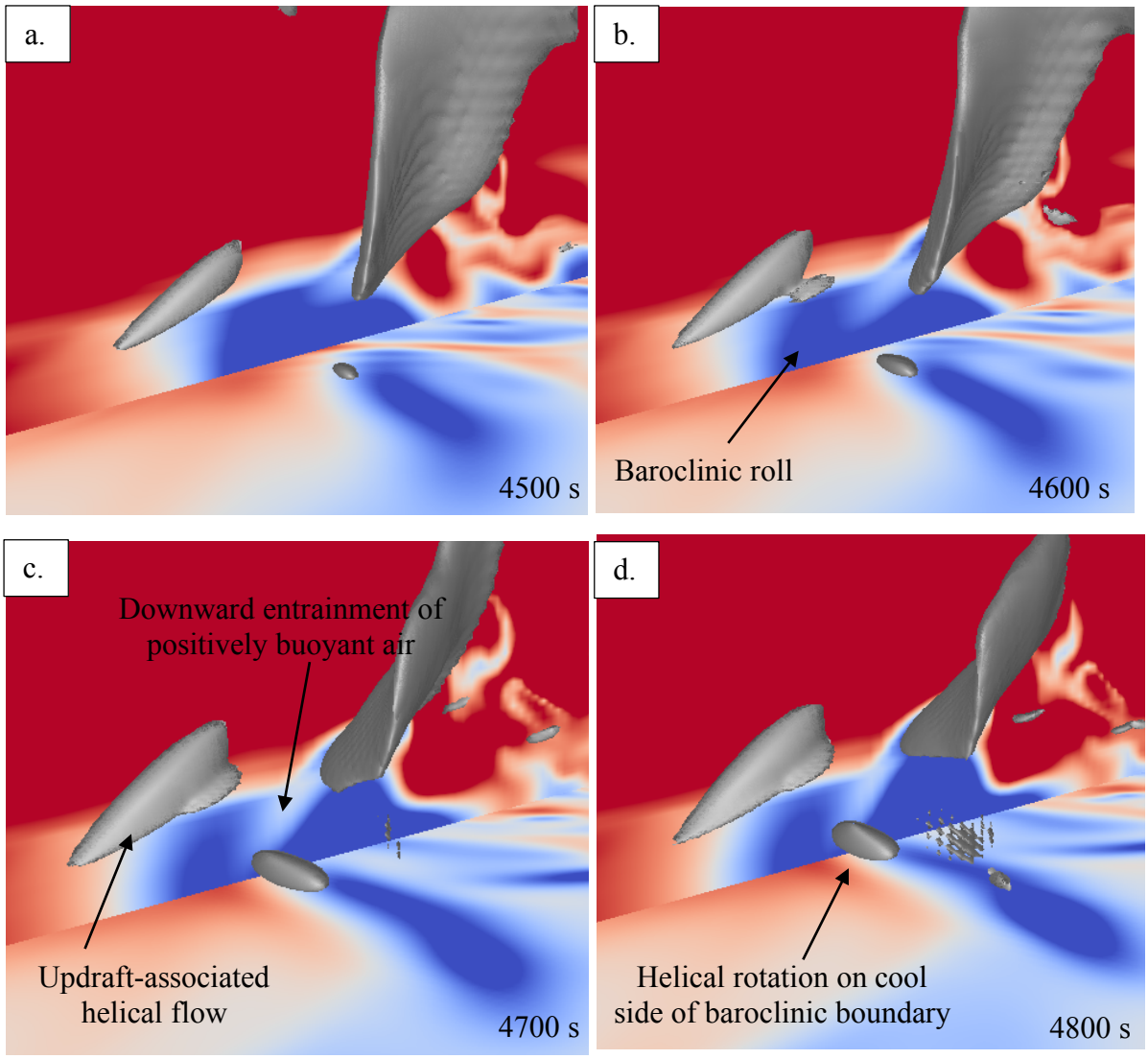

Figure 4.26: Generation of helical rotation prior to TLV-genesis. Development of baroclinic roll structure and helical rotation along the environmental periphery of an outflow momentum surge preceding TLV genesis during the TOR-S simulation. East-west oriented vertical slice of perturbation virtual-virtual potential temperature (θ'_{vv} , which is qualitatively similar to perturbation equivalent potential temperature; Tripoli and Smith, 2014*a,b*) in which cooler colors are associated with negative perturbation θ'_{vv} and warmer colors are associated with positive perturbation θ'_{vv} . The surface is shaded by convergence to match Fig. 4.23 and gray isosurface is rotational helicity at 0.5 ms^{-2}. View is from the north-east as in Fig. 4.23.

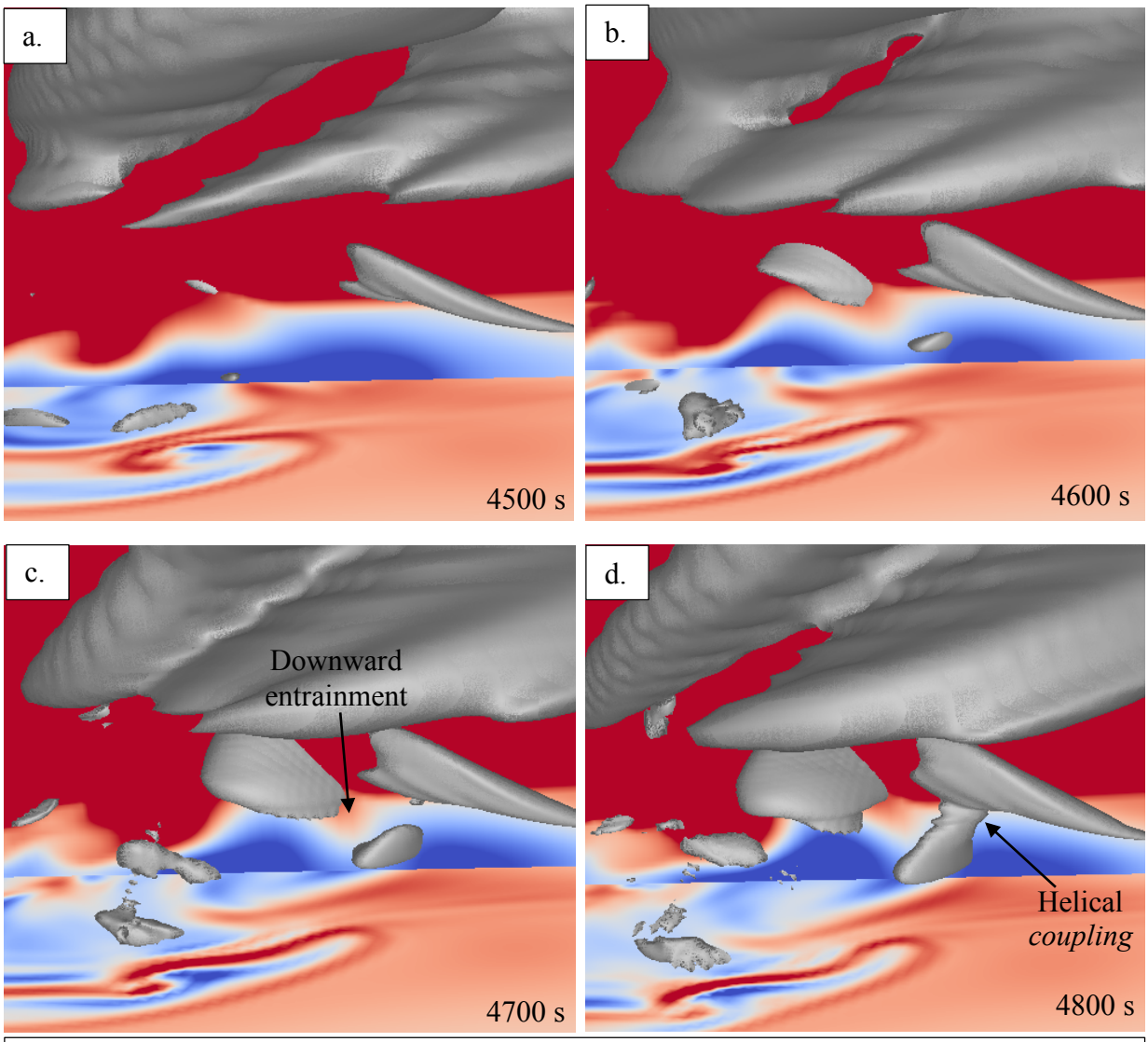

Figure 4.27: Entrainment of environmental air from above during development of helical structure. Evolution of helical flow and vertical potential temperature structure along surging outflow during the genesis phase of the TOR-S simulation. Isosurface and surface shading as in Fig. 4.24. West-east vertical slice is now of potential temperature (θ) where warm colors indicate

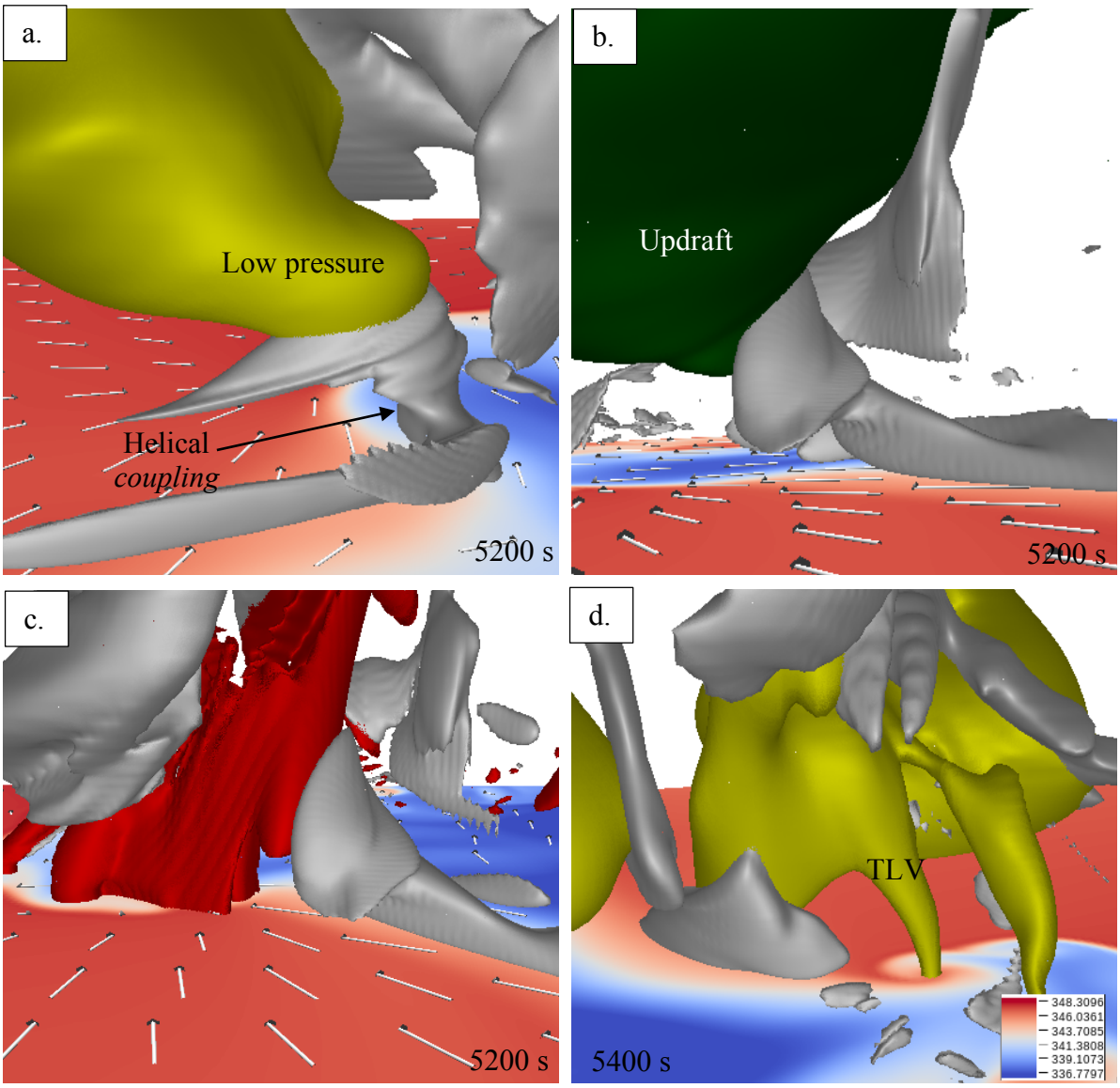

Figure 4.28: Helical dynamic coupling of surface based vertical vorticity and the storm's updraft during TLV genesis in the TOR-S simulation. In all panels, the gray isosurface is rotational helicity of 0.45 ms^{-2} and the surface is each is shaded by equivalent potential temperature (see panel d) and overlaid with surface wind vectors in (a) – (c). In (a) and (d) the yellow isosurface is pressure perturbation of -2 hPa. In (b) green isosurface is 20 ms^{-1} updraft velocity. In (c) the red isosurface is vertical vorticity at 0.025s^{-1}. The viewing angle is from the north-east for (a) and (b), from the south-east for (c) and the north-west for (d). Model time is displayed.

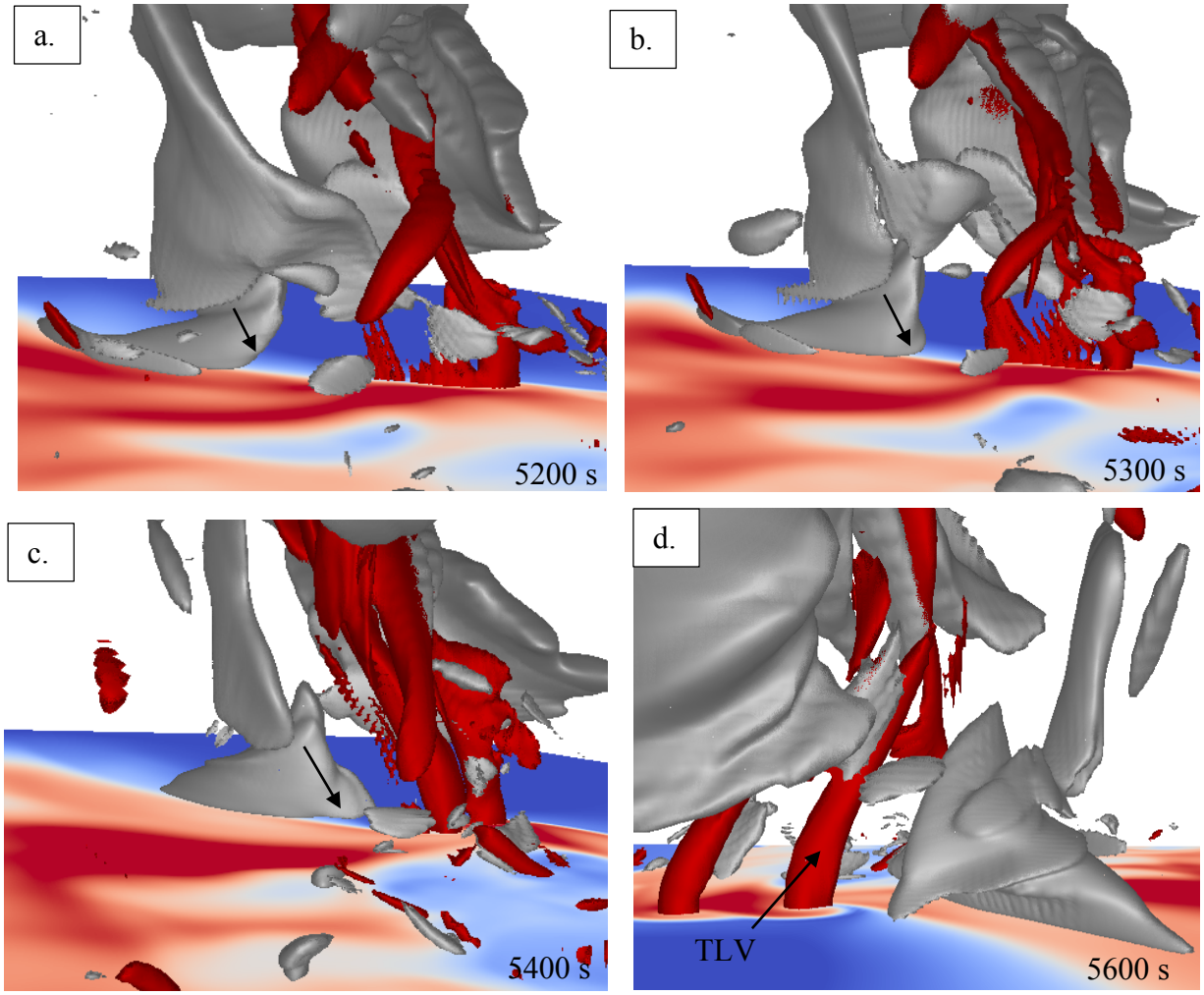

Figure 4.29: Evolution of rotational helicity and vertical vorticity during TLV genesis. As in Fig. 4.27*c* but vertical vorticity (red) isosurface is now 0.05s^{-1}. The view in (a) – (c) is from the north-west looking from the cold pool at the cool side of the coupled helical structure and (d) is viewed from the east in the inflow region of the storm.

To better assess the vertical structure of the environment in the vicinity of the genesis process, model derived soundings were taken in the left-flank outflow region, forward-flank inflow region and inflow region to the south-east of the storm at 4500 s and 4900 s (Figs. 4.30, 4.31 & 4.32). During this time of these soundings, a deep layer of helical flow developed upwards near the base of the updraft and supported intense vertical vortex growth. Each region analyzed with the soundings contains low-level flow directed toward the base of the storm's updraft, therefore each of these regions is a potential source region for updraft rotation. Therefore, the streamwise vorticity present in the storm-relative flow was analyzed in each region. Although all three regions demonstrated a significant increase in the amount of streamwise vorticity during TLV-genesis, the left-flank exhibited, by some margin, the most drastic change (Fig. 4.30). Additionally, the forward-flank and south-east inflow regions were characterized by extremely favorable wind profiles for low-level rotation prior to the TOR-S storm's genesis phase where the left-flank was not until this time. This suggests that the most important change in the storm during its TLV genesis phase occurred in the left-flank outflow region. This evolution was associated with a momentum surge, reorientation of the cold pool boundary and development of helical flow on the cool side of the boundary and very low levels. Another interesting feature seen on the left-flank sounding at 4500 s is the presence of significant potential instability if the air is able to be lifted to 2.5 km AGL (Fig. 4.30). It is possible that this aided in rapid vertical acceleration of the vorticity-rich outflow air during the helical coupling process.

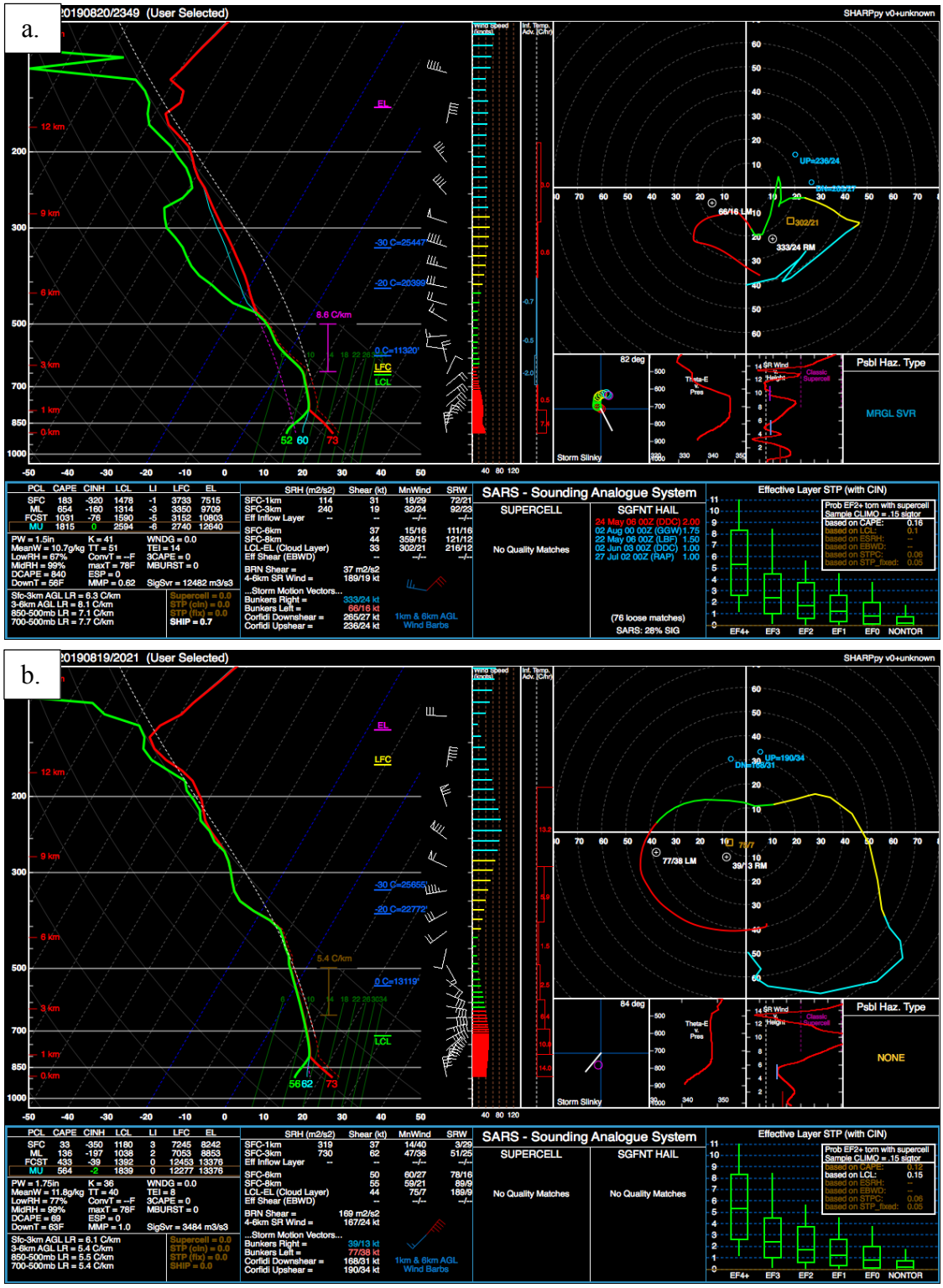

Figure 4.30: Intensification of helical flow in the left-flank of TOR-S storm. Model derived sounding and hodograph from the left-flank of the TOR-S simulation at 4500 s (a) and 4900 s (b).

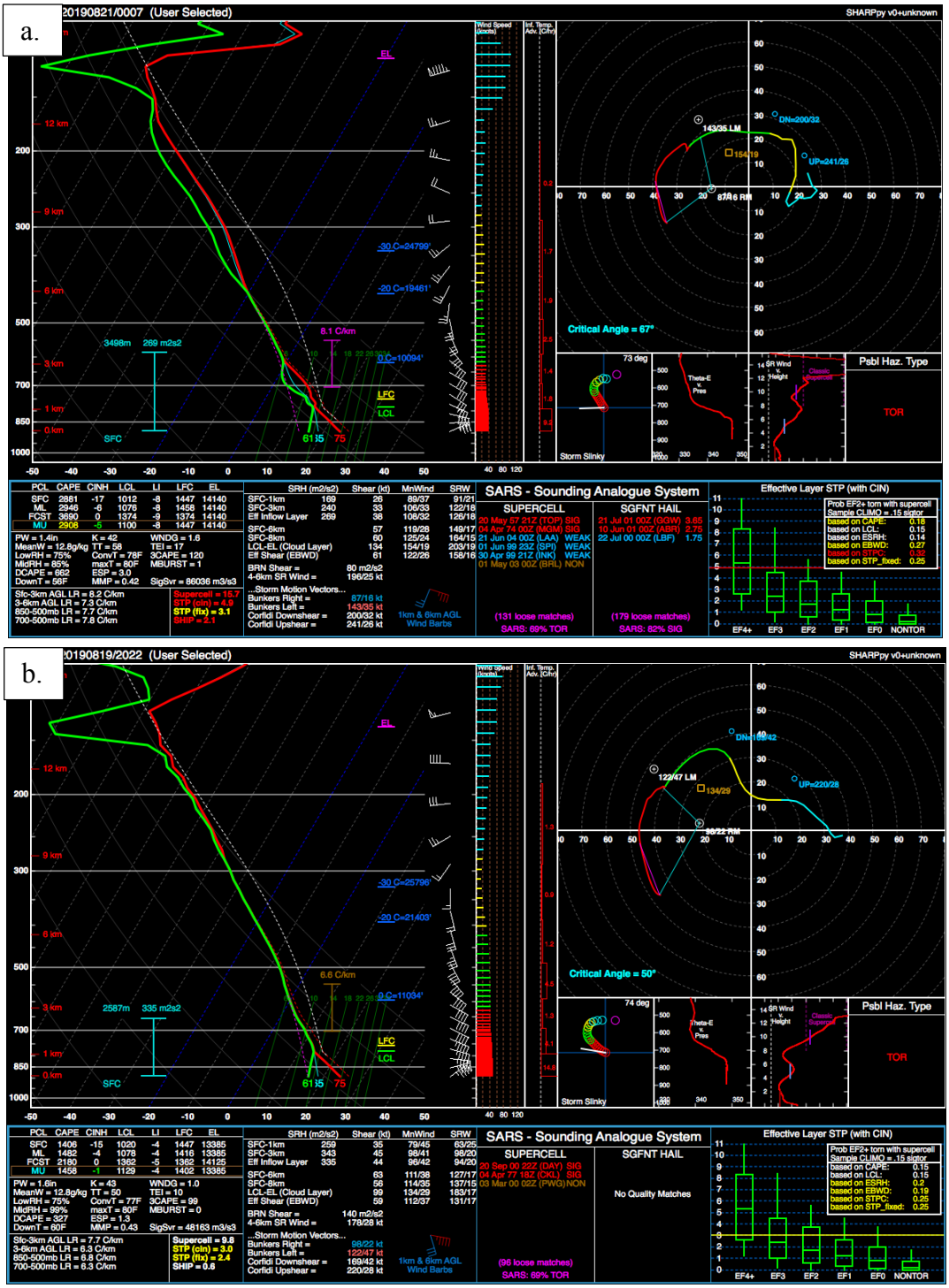

Figure 4.31: Vertical structural change in the forward-flank of the TOR-S storm. As in Fig. 4.60 but for the forward-flank inflow region to the north-east of the TOR-S storm.

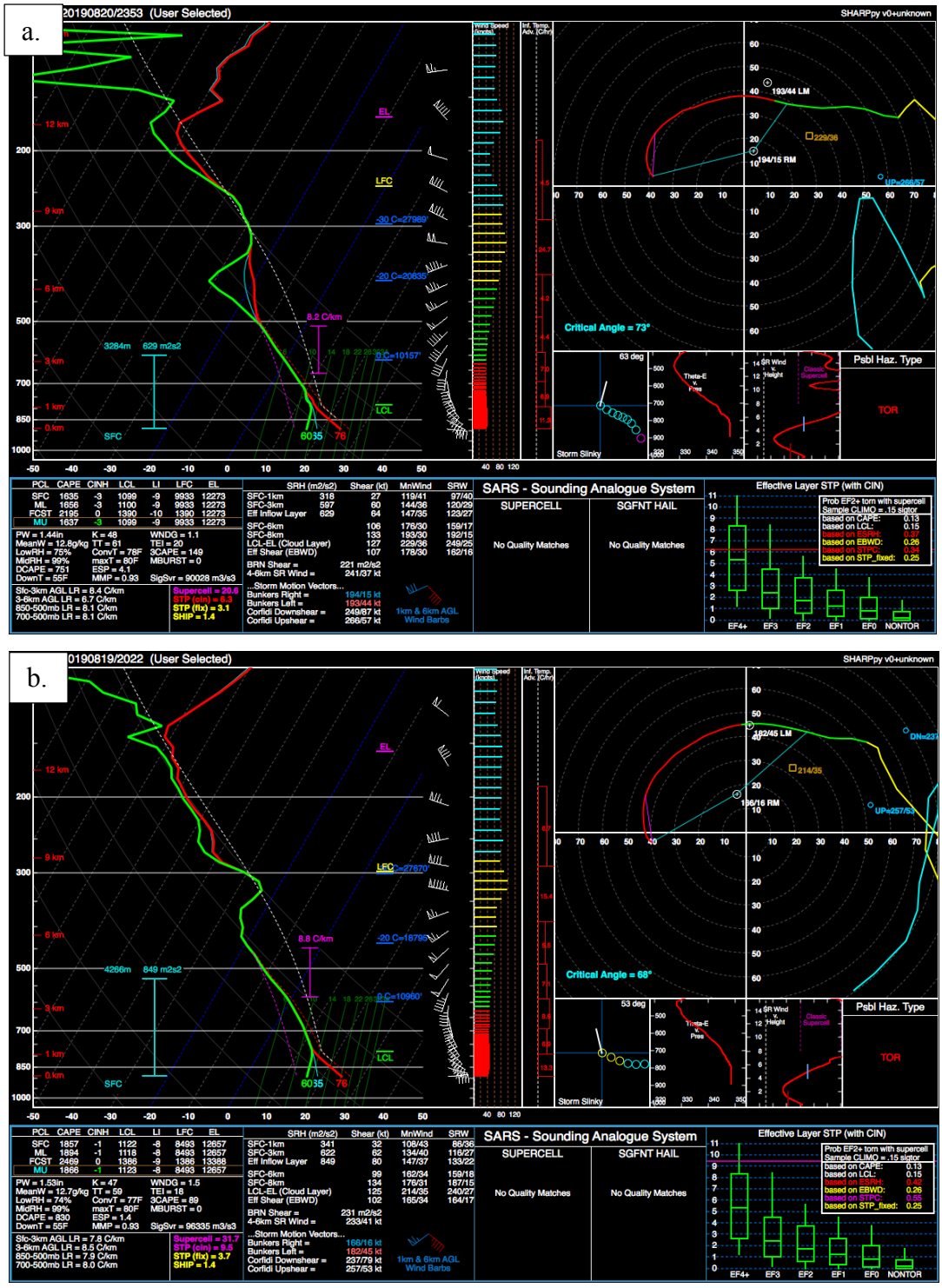

Figure 4.32: Vertical structural change in the inflow region of the TOR-S storm. As in Fig. 4.60 but now for the near-inflow region to the south-east of the TOR-S storm.

b. TLV maintenance

Analysis of the genesis phase of the TOR-S supercell demonstrated that the supercell's left-flank developed significant helical rotational flow in the lowest 500 m AGL during the 1000 s preceding TLV genesis. Apparent "coupling" of this structure with helical low-level inflow of the storm's main updraft region effectively produced a dynamic connection between the rotating updraft and the surface-based vorticity. Soon after this process occurs, surface-based vertical vorticity originating along the left edge (looking in the direction of its propagation) of the low-level helical structure intensifies rapidly upward from low-levels. This vertical vorticity ultimately becomes the dominant TLV during the 5400 – 5800 s timeframe. The evolution of this TLV and the apparent supporting role of rotational helical structures in continued dynamic connection between the updraft and surface is examined in this section.

Although a TLV first forms 5500 s into the TOR-S simulation, it lasts for some 2000 s and undergoes two distinct periods of re-intensification, which is a commonly observed phenomenon in long-tracked supercell tornadoes (Fig. 4.33). Each period of intensification closely follows an intensification in rotational helicity over the 0-1 km layer. The second intensification event at 6600 s is focused on in this section due to the dominating magnitude of the event during the TLV period.

Similar to the immediate pre-genesis phase of the storm, intense helical rotation exists in the lowest 500 m AGL during the 6000 – 6400 s period (Fig. 4.34). Between approximately 6300 and 6400 s, the low-level maximum begins to ascend in height and at the same time a separate maximum aloft begins to descend. The two maxima interact at 6400 s in a vertically coherent manner in the 500 – 1000 m AGL layer. A rapid acceleration of its upward development takes place at this time. Although the upward intensification of rotational helicity appears to reach only

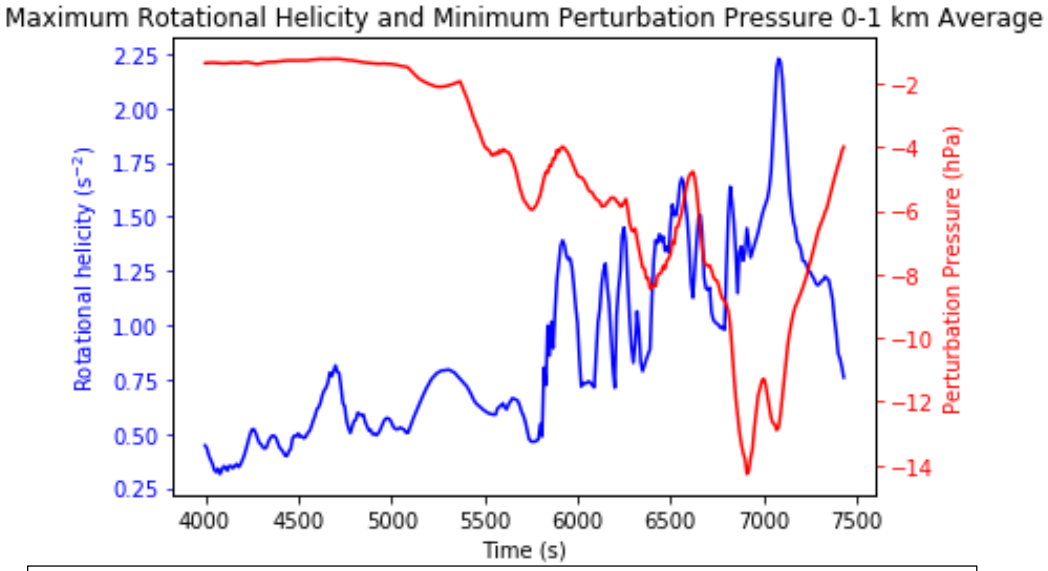

Figure 4.33: Maximum rotational helicity and minimum pressure perturbation over the 0-1 km AGL for the 4000 – 7500 s period of the TOR-S simulation.

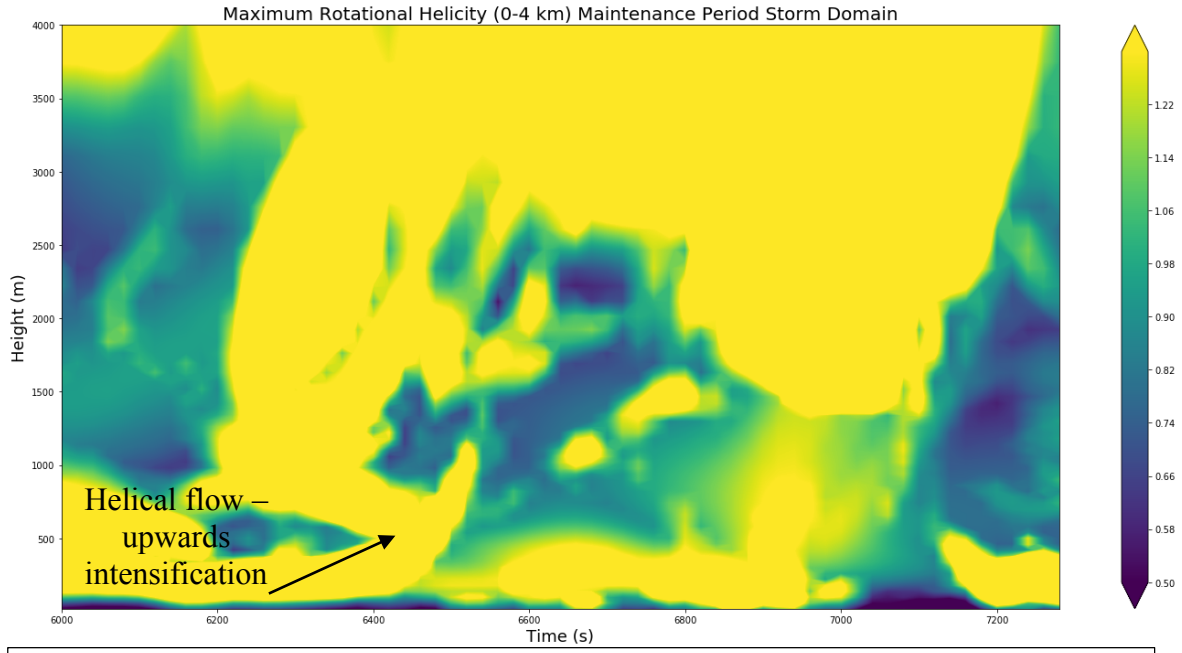

Figure 4.34: Evolution of helical rotation during TLV maintenance. As in Fig. 4.18*a* but for the 6000 – 7300 s period of the TOR-S simulation.

a little above 1000 m, it is clear that it is associated with a deeper communication with the overlying storm when studying other parameters alongside it (Figs. 4.34, 4.35, 4.36 & 4.37). The most illuminating of which is the *upward* development of a maximum in updraft velocity that not only correlates in time-height space with the upward intensification of rotational helicity but extends with a magnitude of 20 ms^{-1} into the lowest 250 m AGL where it first develops (Fig. 4.35). Updraft intensification occurs at low-levels first and ascends during the period of the interaction between the maxima in rotational helicity.

At this time, there is a vertical superposition of helical rotational structures in the vicinity of the TLV (Fig. 4.38). From 6200 to 6400 s the updraft intensifies over the lowest 1 km AGL in the vicinity of this vertical juxtaposition and intensification of the I^2 field appears to occur upwards in association with a helical interaction between the two structures. During this particular intensification period the helical interaction occurred between a horizontal helical structure winding cyclonically around the incipient TLV in the storm's rear-flank region. Interestingly, once the TLV undergoes re-intensification it develops large values of rotational helicity at its core associated with downward motion inside the vortex (Fig. 4.39).

Lastly, it is worth drawing attention to the supply of vertical vorticity associated with the low-level helical rotation in the storm's left and forward flanks (Fig. 4.40). Such upward intensification of vertical vorticity and surface-based vortex development to the north of the updraft appears to occur periodically through the TLV's lifecycle. Each time that this occurs, it is preceded by a helical structure along the left-flank convergence boundary in the lowest 500 m AGL which interacts with the helical inflow of the low-level mesocyclone aloft.

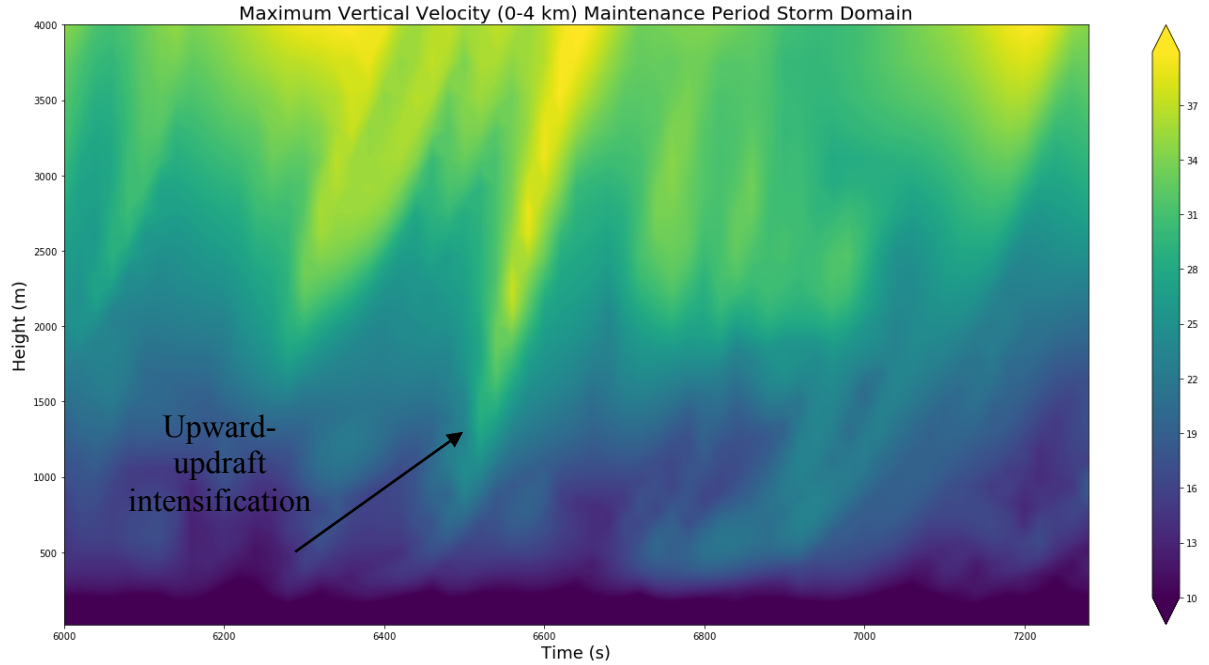

Figure 4.35: Evolution of maximum updraft velocity over the 0-4 km AGL for the 6000 – 7300 s period of the TOR-S simulation for a full storm domain.

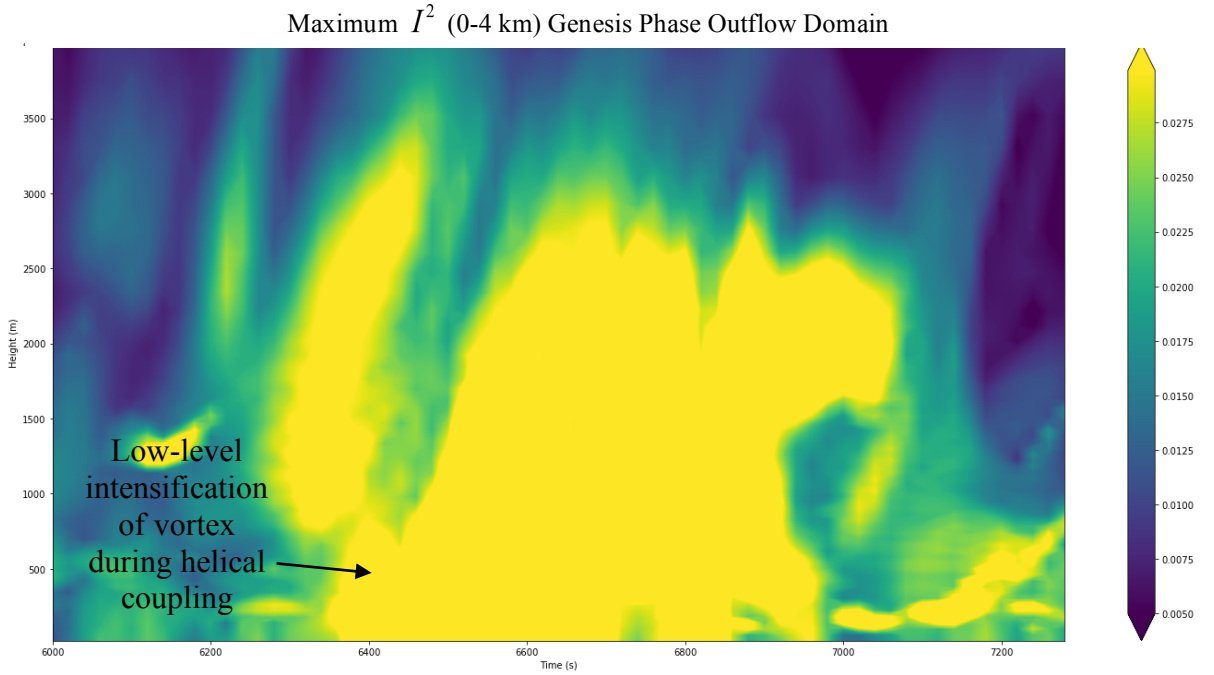

Figure 4.36: Evolution of maximum I^2 over the 0-4 km AGL for the 6000 – 7300 s period of the TOR-S simulation for a full storm domain.

Minimum Pressure Perturbation (0-4 km) Genesis Phase Outflow Domain

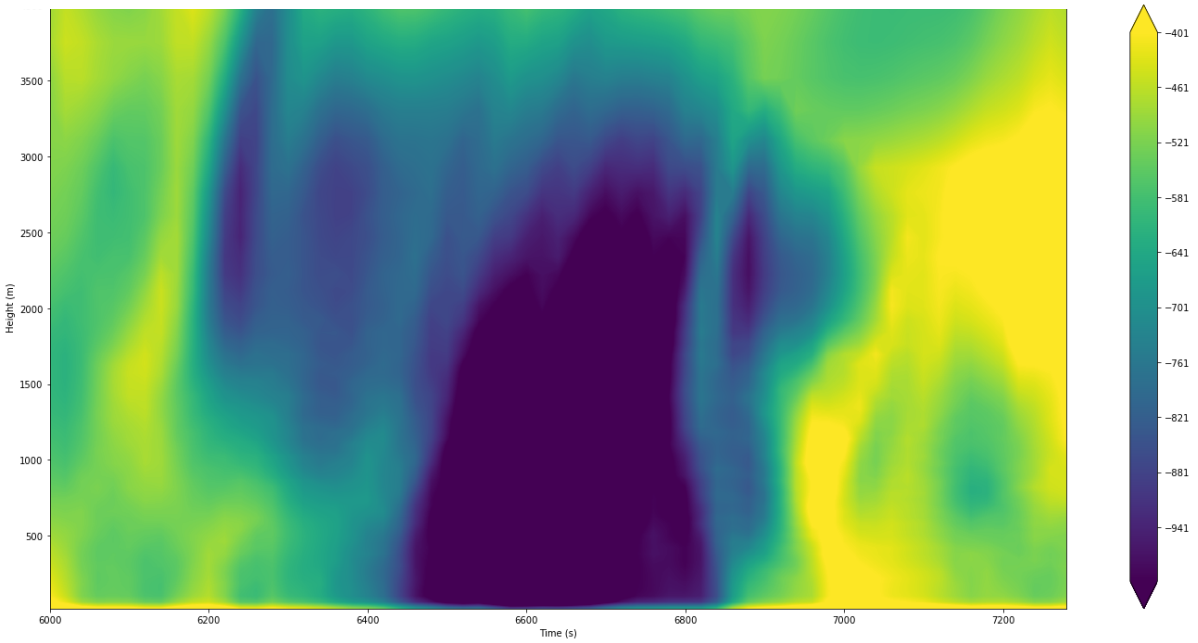

Figure 4.37: Evolution of minimum pressure perturbation over the 0-4 km AGL for the 6000 – 7300 s period of the TOR-S simulation for a full storm domain.

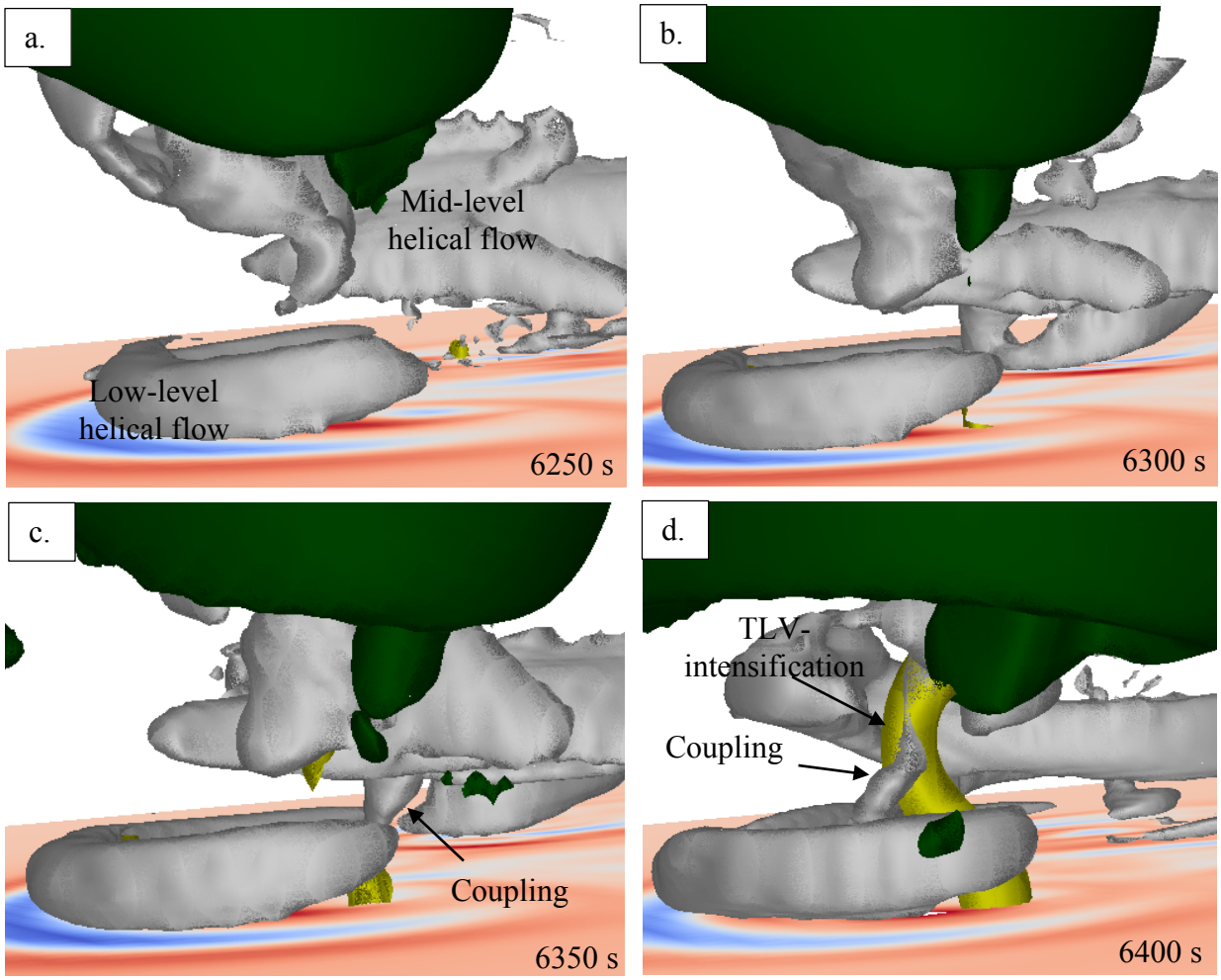

Figure 4.38: TLV intensification associated with helical coupling. Vertical coupling of helical structures associated with an intensification of the low-level updraft and re-intensification of the ongoing TLV. 0.5 ms^{-2} magnitude of rotational helicity is represented by the gray isosurface, 20 ms^{-1} updraft velocity is green and 0.03 s^{-2} I^2 is yellow.

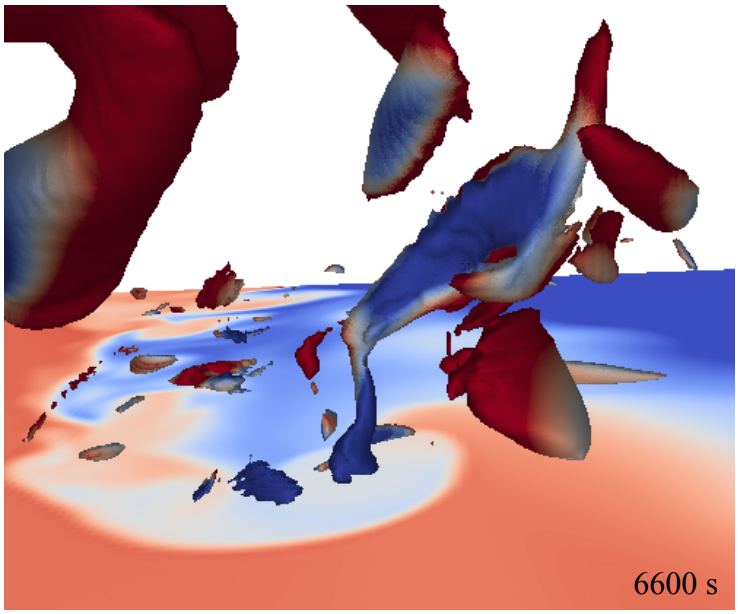

Figure 4.39: Helical flow associated with descending air at the core of the TLV. Rotational helicity isosurface of 1 ms^{-2} colored by vertical velocity where red shading is upward vertical velocity and blue indicates downward vertical velocity. The surface is shaded by equivalent potential temperature at the lowest model level where warmer colors are higher values.

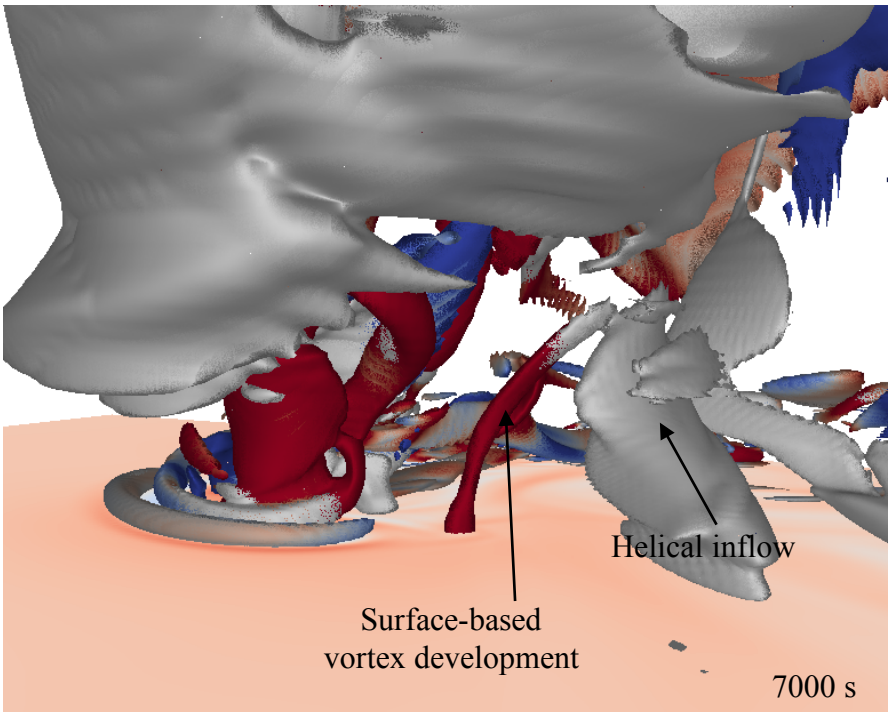

Figure 4.40: Vertical vorticity development associated with helical rotation in the inflow layer. 0.45 ms^{-2} rotational helicity is represented by the gray isosurface and 0.05 s^{-1} total vorticity isosurface is shaded by the vertical component of vorticity where red are positive values. The surface is shaded by convergence. As horizontal displacement between helical flow at mid-levels and at low-levels increases the supply of surface-based vertical vorticity is reduced.

4.2.2 VORTEX2 simulations: Tornado-Like-Vortex failure (TOR-F simulation)

In order to put the results of the prior section into perspective, the following two sections look at cases of TLV-failure in the tornadic VORTEX2 environment (this section) and non-events in the nontornadic VORTEX2 environment (next section), during period of strongest surface-based rotation (determined by I^2). The approach in these two sections will be more direct by identifying key differences in the storm's evolution between the success case (TOR-S) and the cases of failure and non-events.

a. TLV failure and comparisons with TOR-S

The failure stage of the TOR-F simulation came at nearly a nearly identical time of the model integration to the TOR-S simulation and in many ways closely resembled the TOR-S simulation. The structure of the surface condensate field was qualitatively similar approximately 900 s before the time of genesis in the TOR-S simulation and failure in the TOR-F simulation (Figs. 4.9 & 4.41). However, at the time of TLV-failure in TOR-F and genesis in TOR-S, the surface condensate structure exhibited critical differences (Fig. 4.42). While the TOR-S simulation maintained a coherent, north-south oriented band of high surface condensate from the left-flank region to the low-level circulation, higher values in the TOR-F simulation were oriented in an east-west fashion and became disjointed from the low-level circulation.

Both simulations exhibited a significant maximum in rotational helicity prior to surface pressure falls and associated maxima in I^2 (Figs. 4.43 & 4.44). However, the I^2 maximum in the TLV-failure period of the TOR-F simulation was five times weaker than the TOR-S simulation and the surface pressure perturbation did not drop below -5 hPa (Fig. 4.44). Using the

same techniques employed to study TLV genesis in the TOR-S simulation, reasons for TLV-failure in the TOR-F simulation were investigated.

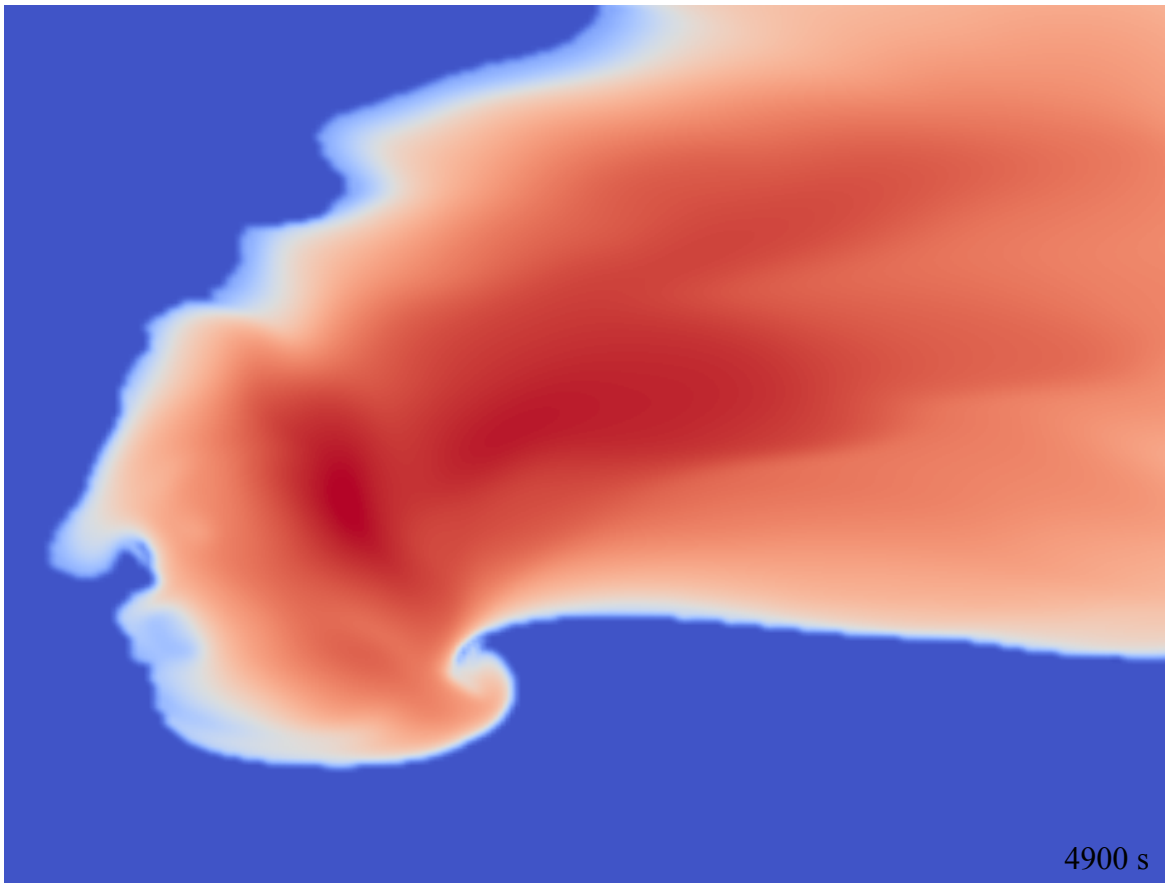

Figure 4.41: Surface condensate in the TOR-F simulation 900 s before TLV-failure. As in Fig. 4.9 but for the TOR-F simulation at 4900 s.

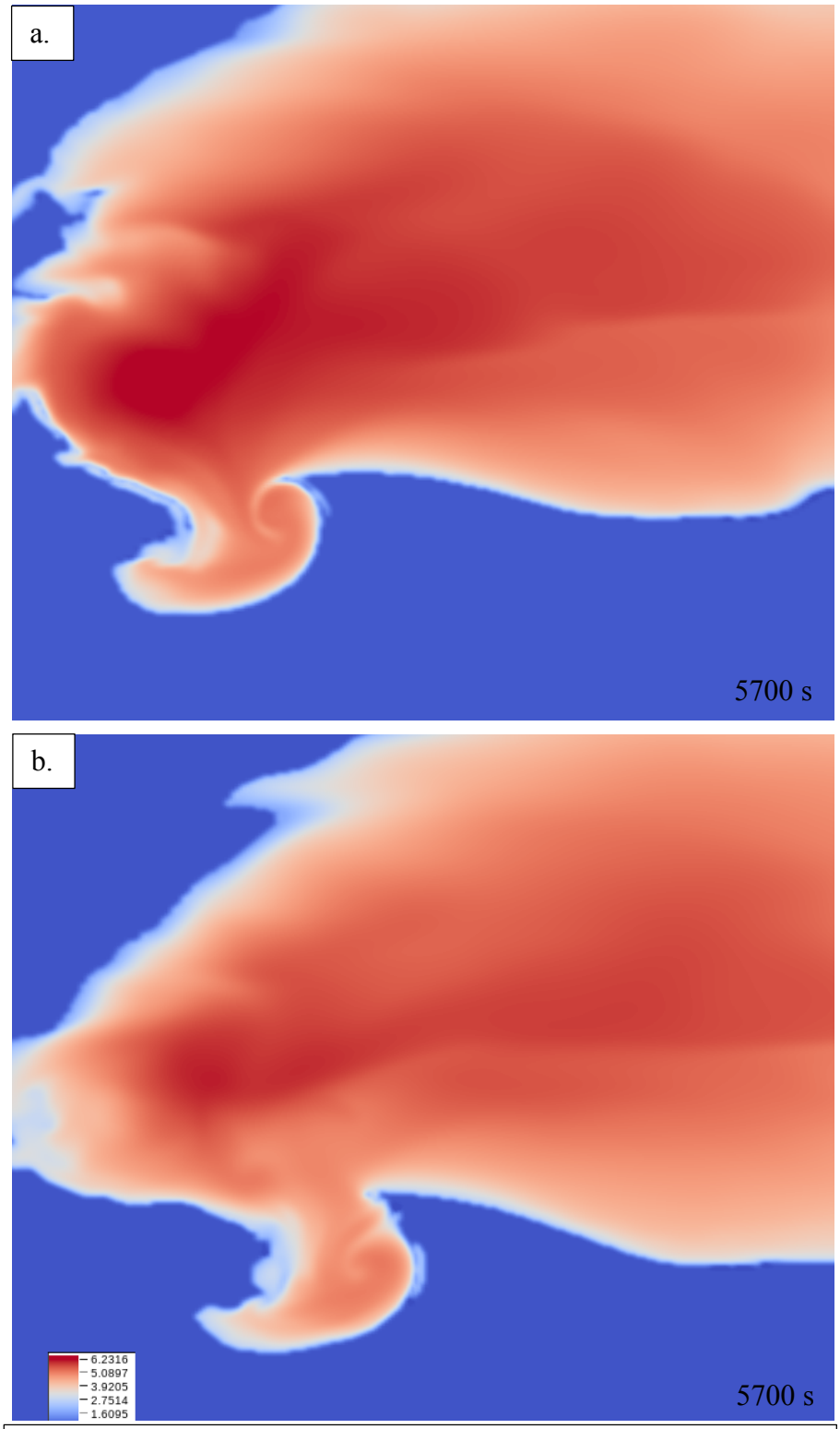

Figure 4.42: Differences between TOR-S and TOR-F simulations during TLV-success and failure events. As in Fig. 4.9 but for the TOR-S simulation at 5700 s (a) and the TOR-F simulation at 5700s (b).

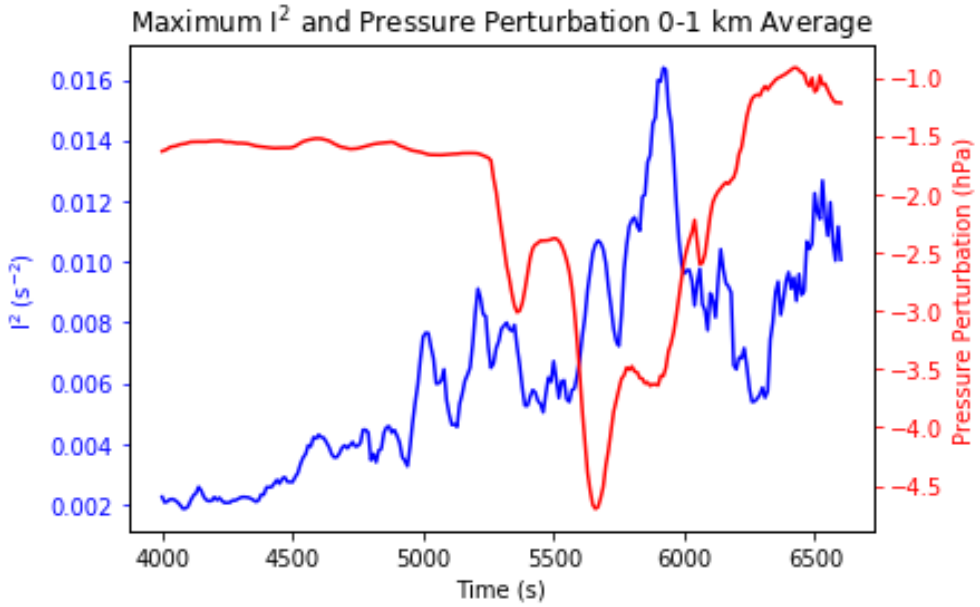

Figure 4.43: I^2 and minimum pressure perturbation (0-1 km layer) during TLV-failure. As in Fig. 4.15 but for the TOR-F simulation for the 4000 – 6700 s period.

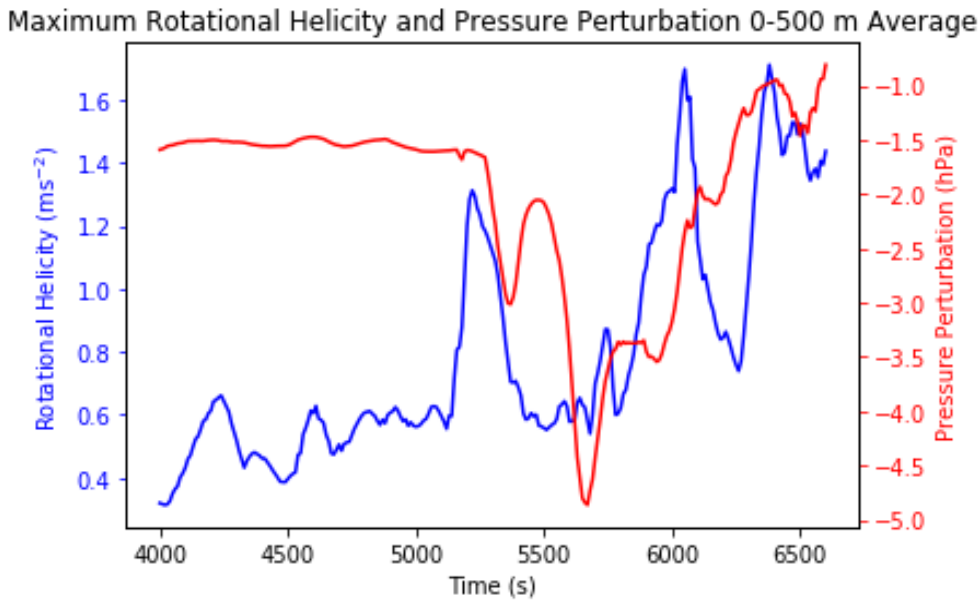

Figure 4.44: Rotational helicity and minimum pressure perturbation (0-500 m layer) during TLV-failure. As in Fig. 4.12 but for the TOR-F simulation for the 4000 – 6700 s period and pressure perturbation calculated over the 0-500 m layer.

Significant vertical vorticity was present in the lowest 500 m of the domain for much of the simulation prior to TLV-failure at 5600 s (Fig. 4.45). Vertical vorticity intensified in this layer at the time of greatest surface pressure perturbation but reached a more significant maximum over a deep layer between 5800 and 6000 s as the surface pressure perturbation was *weakening* (Figs. 4.44, 4.45 & 4.46). During intensification of the surface pressure perturbation and low-level vertical vorticity there was an upward-strengthening maxima in rotational helicity (Fig. 4.47), which similarly to the TOR-S simulation during genesis was associated with an upward intensification of the updraft (Fig. 4.48) and a minimum in pressure perturbation (Fig. 4.46). However, in each case the magnitude was substantially weaker. The rotational helicity field in time-height space was far less coherent and organized in the TOR-F simulation. Where in the TOR-S simulation there was significant maxima in horizontal helical rotation in both the 0-500 m and 1000-1500 m layers, there was a comparative lack of such coherency or longevity in these layers in the TOR-F simulation.

Similar to the TLV-genesis period of the TOR-S simulation, the pre-TLV-failure period of the TOR-F simulation also exhibited significant internal momentum surging in the left-flank region and also appeared to be driven by intense precipitation falling to the north of the updraft (Fig. 4.49). Significantly, however, intense precipitation also falls into the forward-flank inflow region during this period, which has substantial impacts on the evolution of the low-level wind field during the time of TLV failure (Fig. 4.49*c,d*). Low-level divergence develops in association with the intense precipitation in the forward-flank causing flow to turn toward the main updraft region further east and well ahead of the north-south convergence boundary in the left-flank compared with the TOR-S simulation.

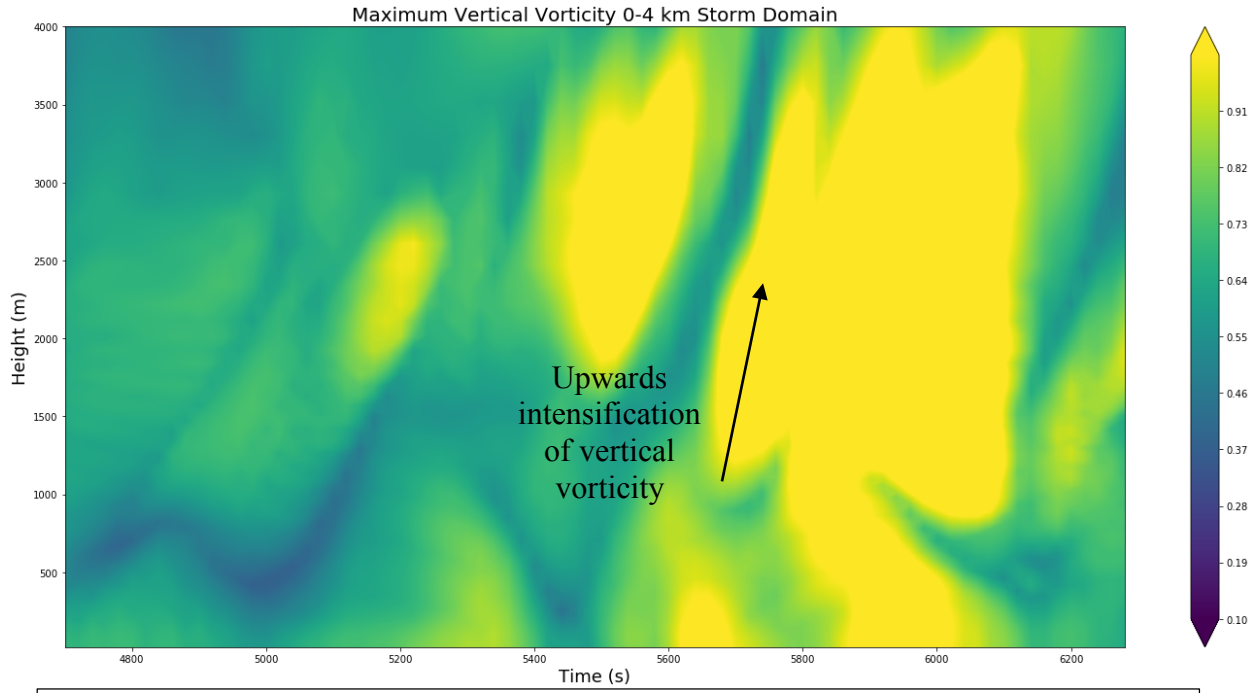

Figure 4.45: Vertical vorticity evolution during TLV-failure. As in Fig. 4.21*b* but for the TOR-F simulation in the 4700 – 6300 s period for the full storm domain.

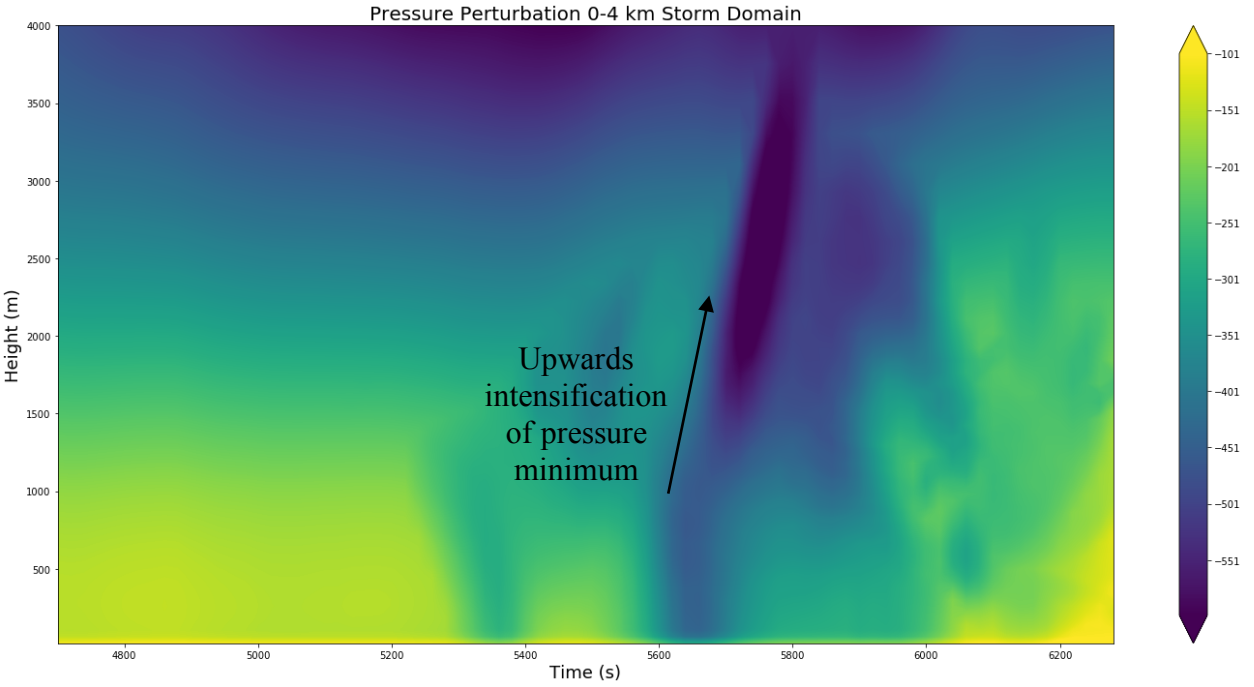

Figure 4.46: Evolution of minimum pressure perturbation during TLV-failure. As in Fig. 4.20*a* but for the TOR-F simulation in the 4700 – 6300 s period.

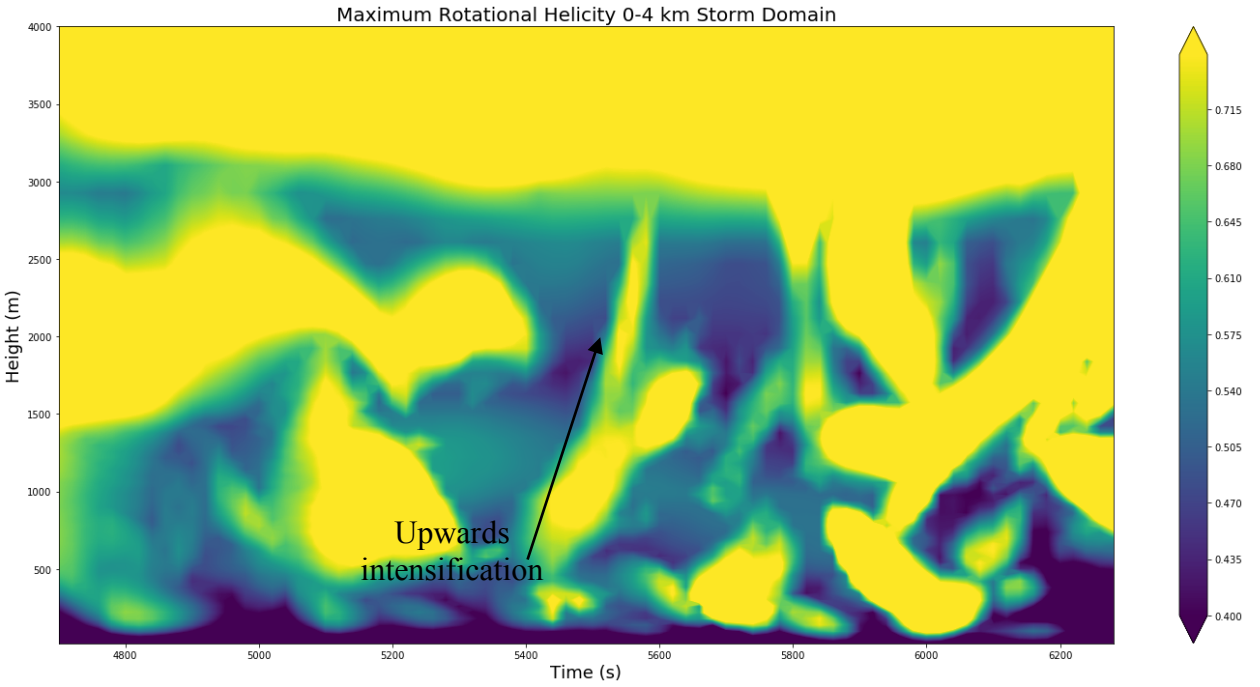

Figure 4.47: Rotational helicity evolution during TLV-failure. As in Fig. 4.18*a* but for the TOR-F simulation for the 4700 – 6300 s period.

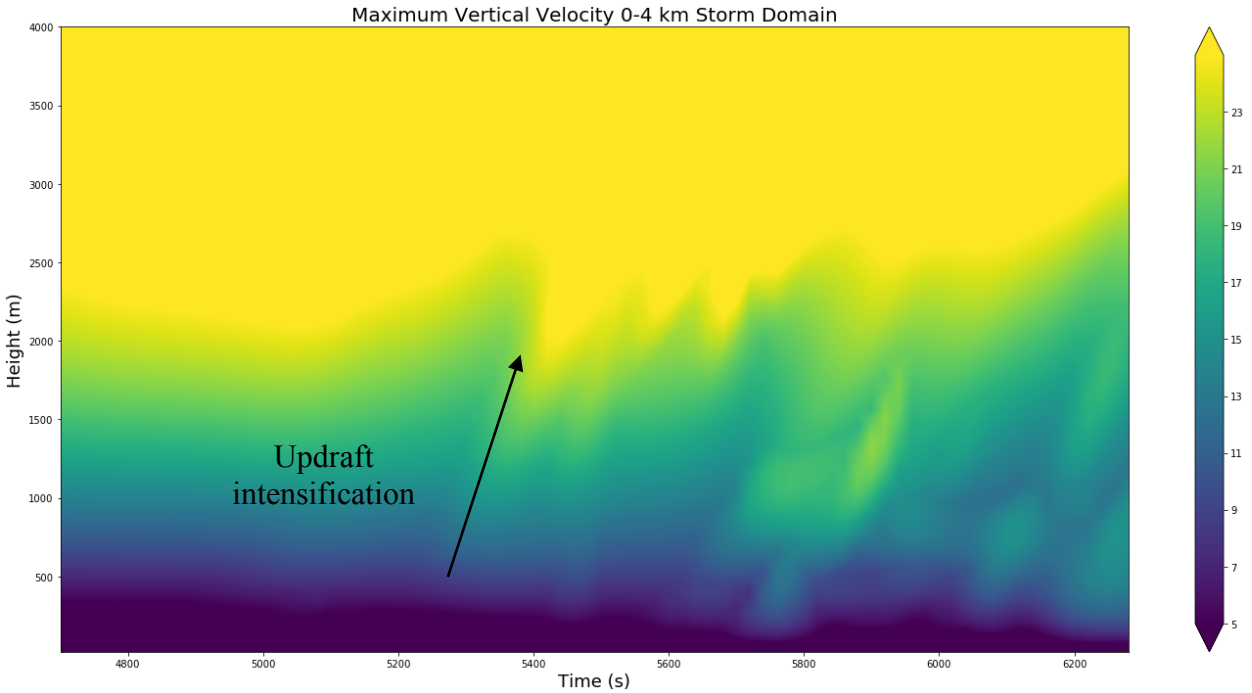

Figure 4.48: Updraft evolution during TLV-failure. As in Fig. 4.60 but for the TOR-F simulation for the 4700 – 6300 s period.

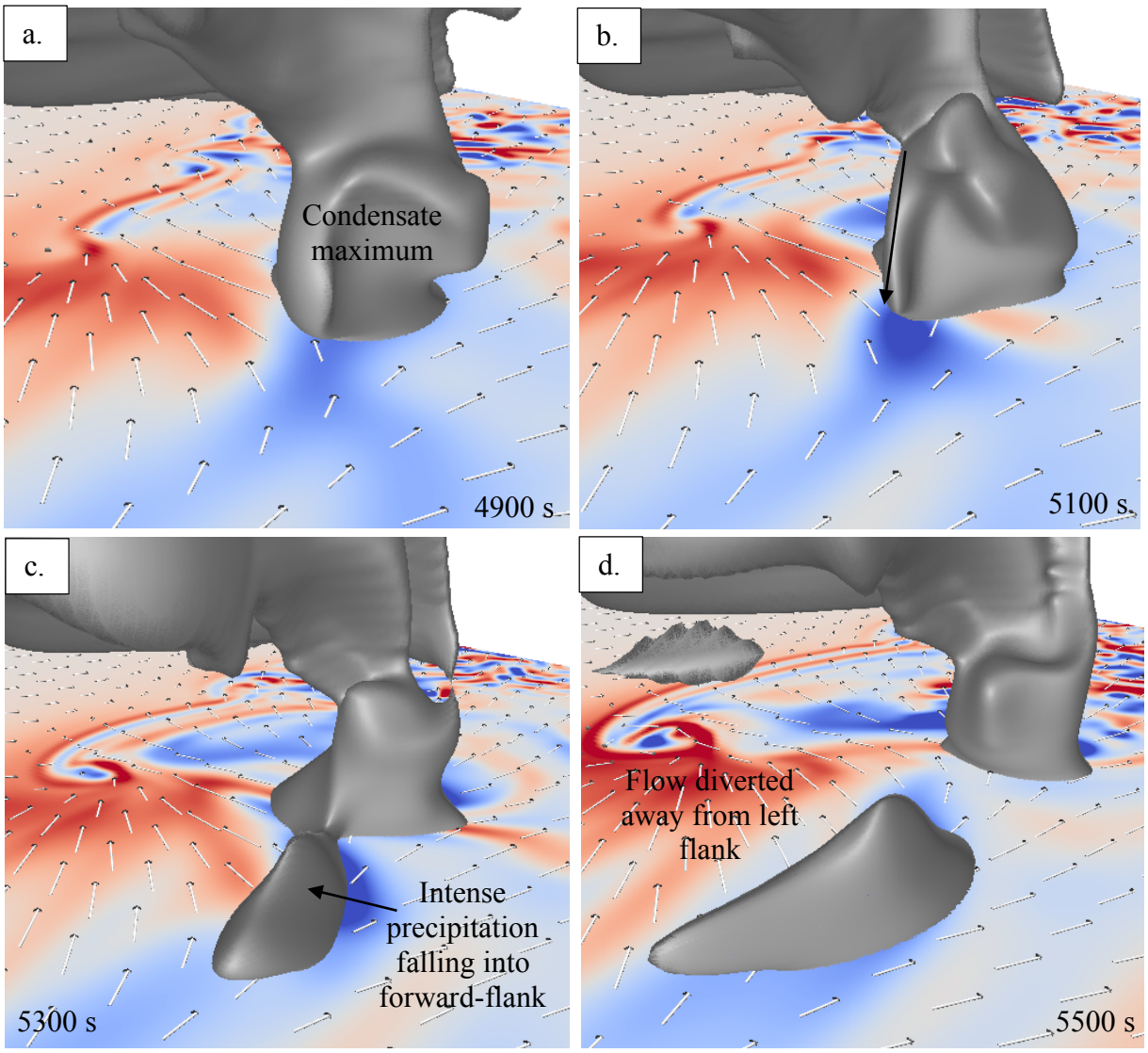

Figure 4.49: Evolution of condensate during TLV-failure. As in Fig. 4.23 but for the TOR-F simulation during the development of a surface-based vortex that fails to intensify into a TLV.

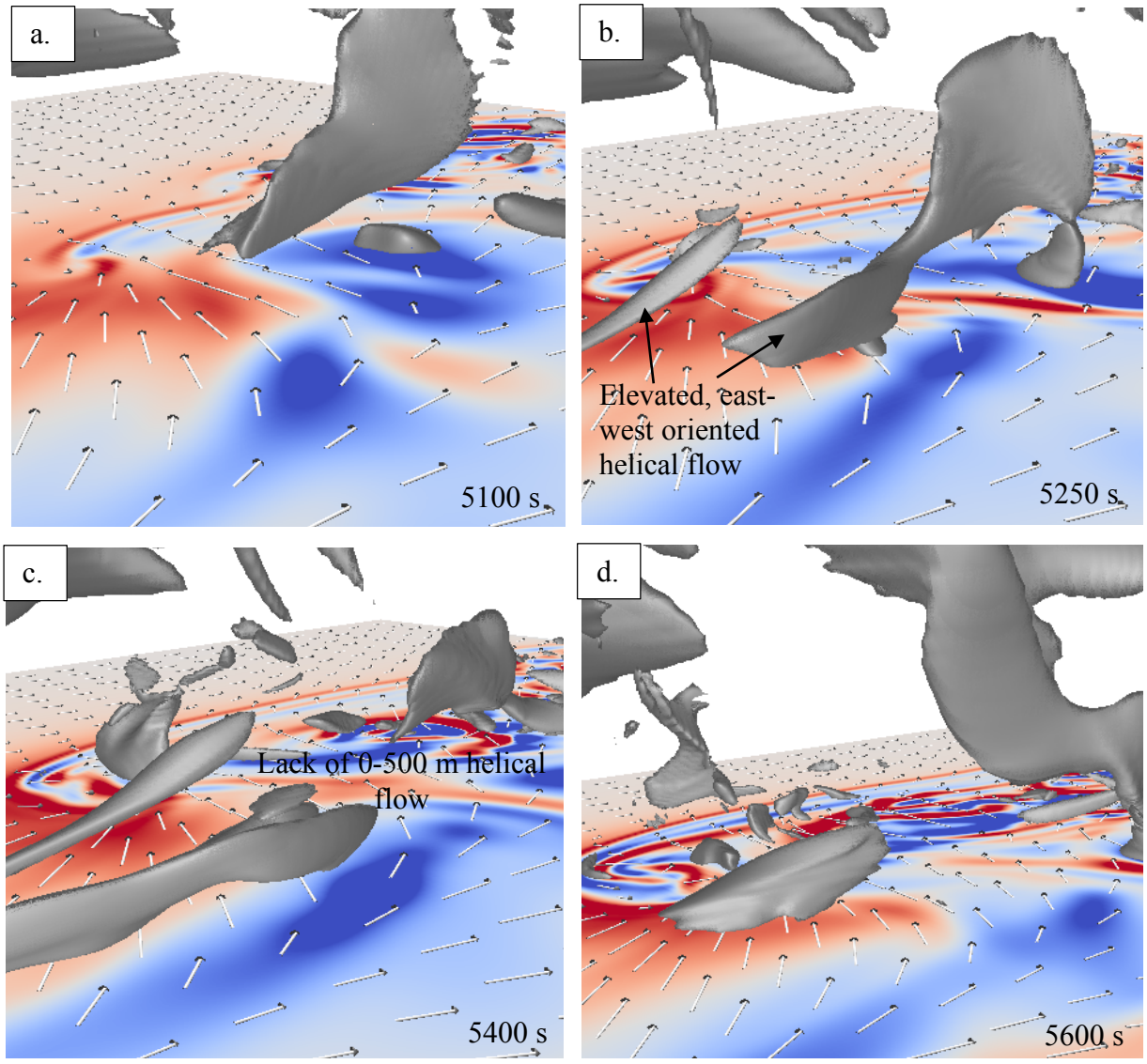

Figure 4.50: Three-dimensional rotational helicity evolution during TLV-failure. As in Fig. 4.25 but for the TOR-F simulation during the development of a surface-based vortex that fails to intensify into a TLV.

The evolution of intense precipitation in the forward-flank appears to prevent significant interaction of the low-level inflow with the north-south oriented convergence line along the periphery of the TOR-F outflow region (Fig. 4.49). As a result, rotational helicity is much weaker along the left-flank boundary during this time (Fig. 4.50). Helical flow still develops in the forward-flank inflow region but remains elevated above the lowest 500 m as it approaches and lifts into the main updraft.

Vertical cross-section analysis reveals an absence of downward entrainment of less negatively (or positively) buoyant air from the low-level environment in the vicinity of the left-flank convergence boundary (Fig. 4.51*a,b*). The vertical potential temperature gradient remains stably stratified and the outflow surges horizontally in a westward direction relative to the storm. Following this, the outflow region of the TOR-F supercell becomes highly disorganized and low-level storm-relative easterly flow penetrates right through the cold pool region, effectively cutting off the low-level circulation in the rear flank from the rest of the outflow (Fig. 4.52). The surface-based vortex development occurs along the surging head of the RFD much like the baroclinic arching theory discussed in chapter two (Fig. 4.53). Rapid upward development of vertical vorticity, initially in the form of a sheet-like structure, occurs as deep convergence along the rear-flank allows the surface-based vertical vorticity to interact with the overlying updraft and develop into a deep but weak cyclonic vortex. Studying three-dimensional rotational helicity, perturbation pressure and updraft at this time in a similar fashion to the TOR-S storm reveals the vertical vorticity development along the RFD is substantially displaced, horizontally, from any significant low-level helical flow, which primarily resides in the forward-flank region (Fig. 4.54). The updraft and pressure anomalies in the lower portion of the updraft and mesocyclone are much weaker than in the TOR-S supercell during TLV-genesis. The primary reason for this

appears to be the large horizontal displacement of the mid-level rotation and the misoscale helical rotation in the forward-flank inflow. This is consistent with the results of Coffer and Parker (2015; 2017; 2018) who found nontornadic storms simulated with the VORTEX2 environments using the CM1, generally suffered (in their ability to sustain strong low-level rotation) from horizontally displaced mid-level and low-level mesocyclones.

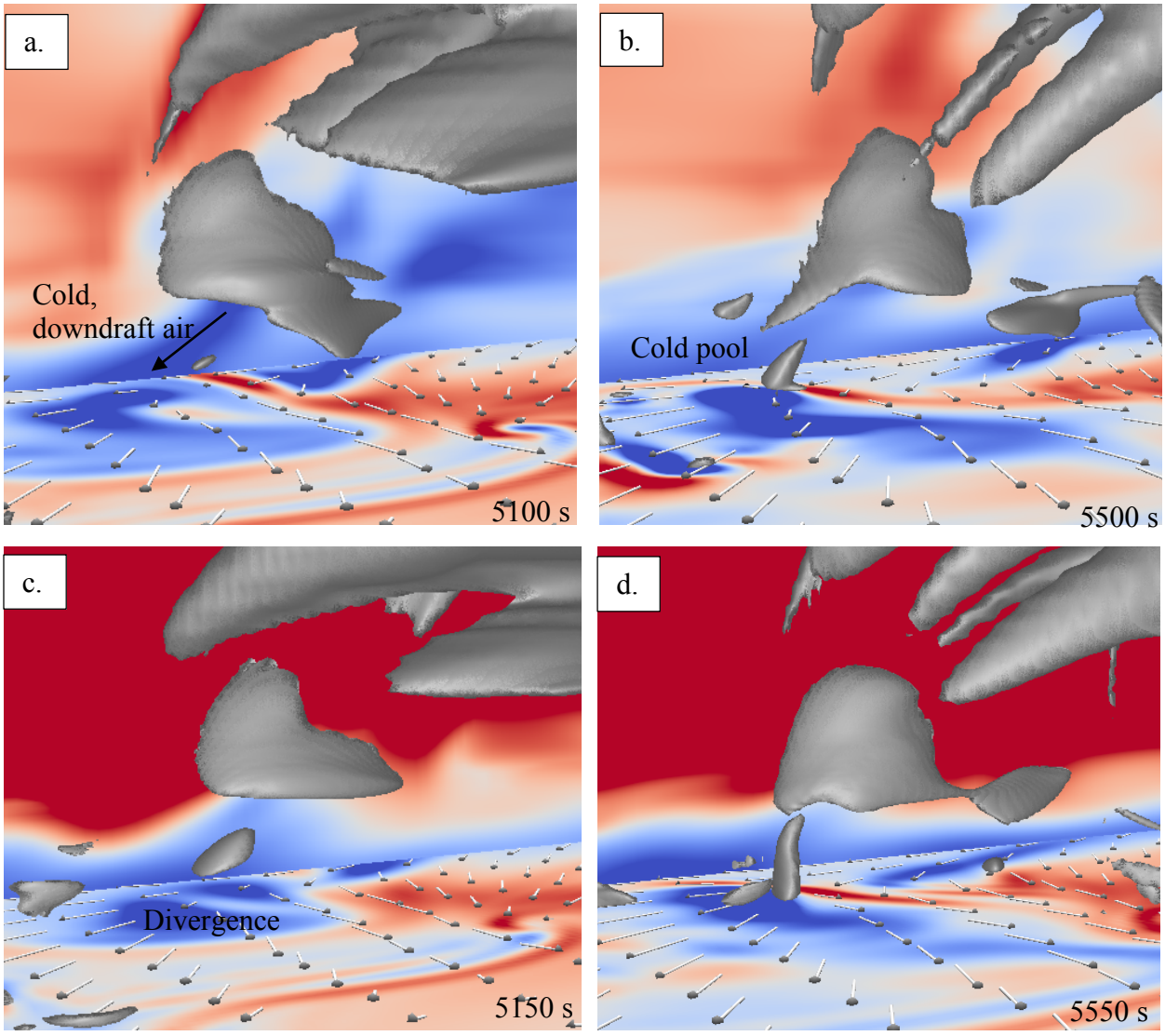

Figure 4.51: Vertical cross section of virtual-virtual potential temperature and potential temperature during TLV-failure. As in Fig. 4.27 for (a), (b) and Fig. 4.28 for (c), (d) but viewing angle is from the south for the TOR-F simulation during TLV-failure.

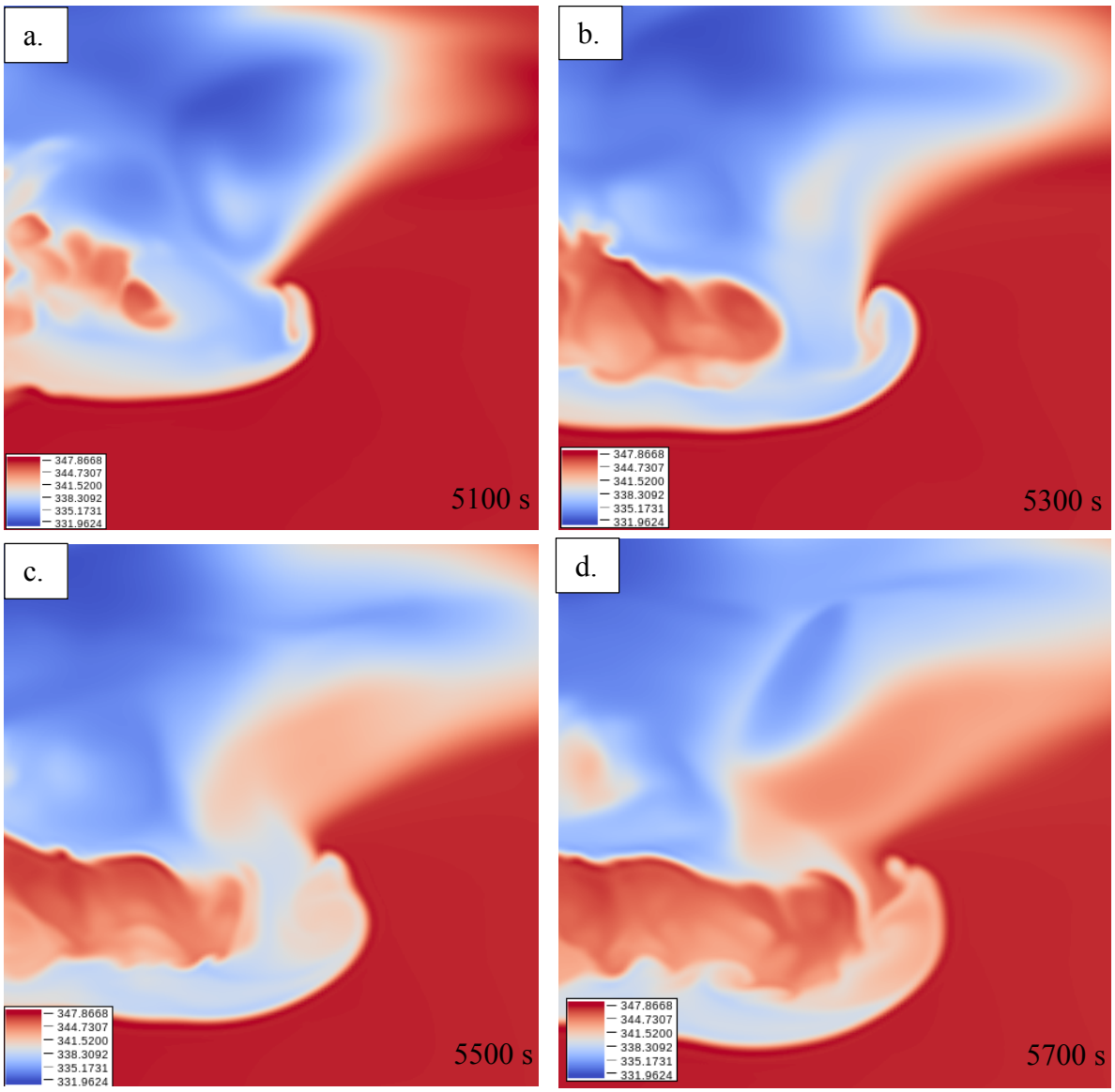

Figure 4.52: Distortion of the outflow structure during TLV failure in the TOR-F simulation. Surface (lowest model level) shaded by equivalent potential temperature (θ_e).

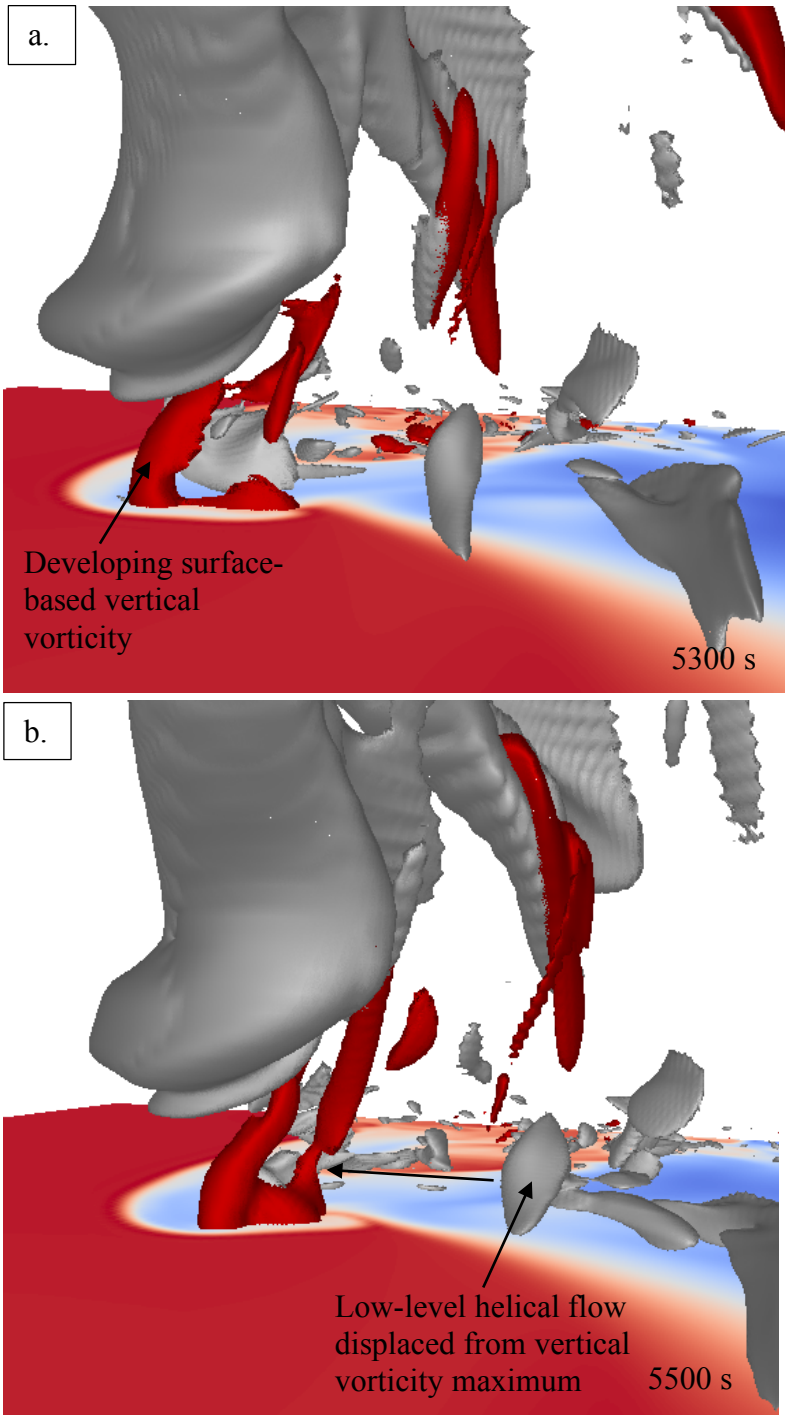

Figure 4.53: Surface-based vortex development that fails to mature into a TLV. Vertical vorticity is rendered in red at 0.25 s^{-1} and rotational helicity is the gray isosurface with a magnitude of 0.45 ms^{-2}.

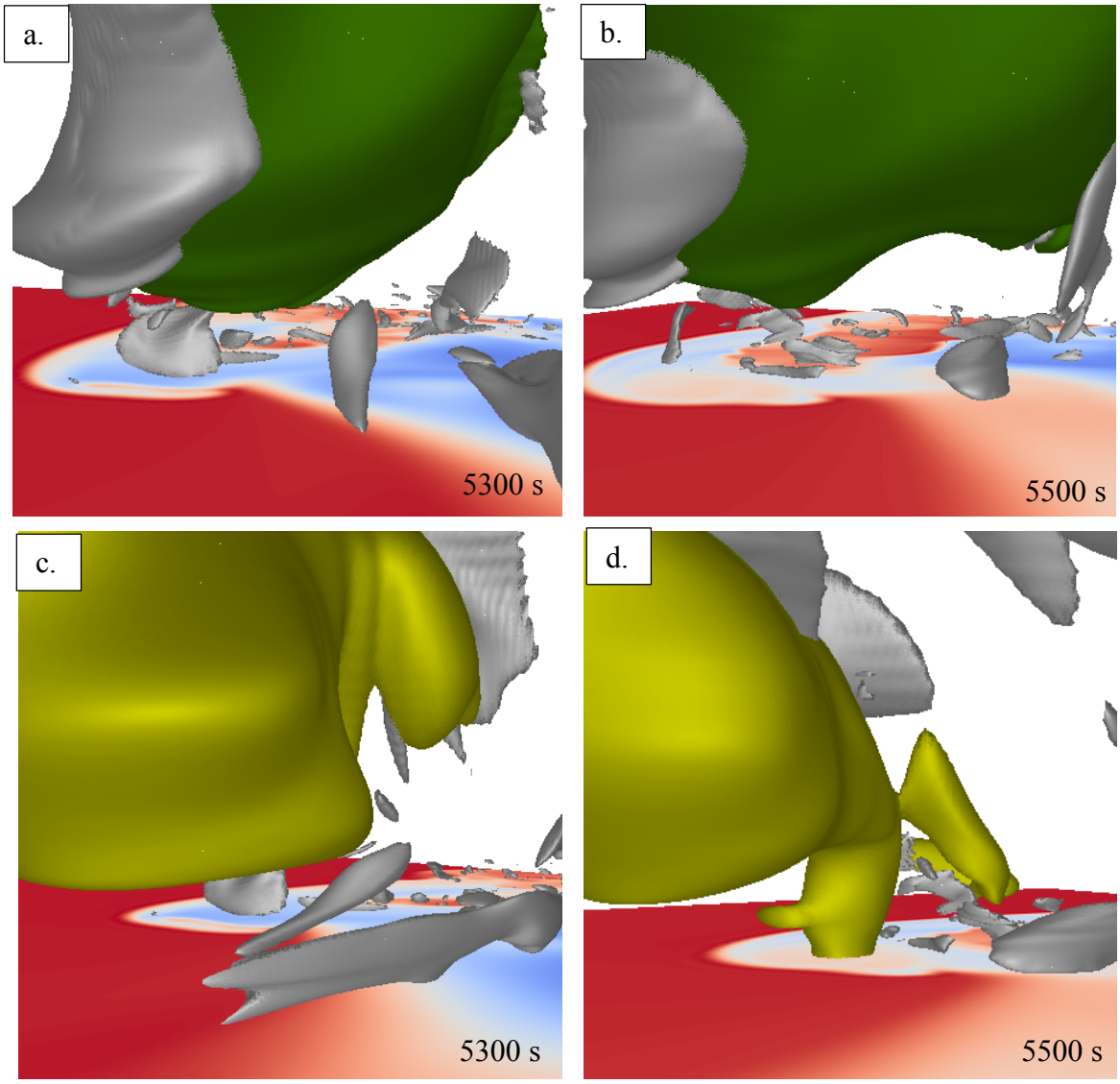

Figure 4.54: Displacement of low-level helical flow and surface-based vortex during TLV-failure. The evolution of the low-level updraft, rotational helicity and pressure perturbation during the time the TOR-F simulation has the most intense surface-based vortex. Isosurfaces are as in Fig. 4.27*b* for (a), (b) and Fig. 4.27*a* for (c), (d).

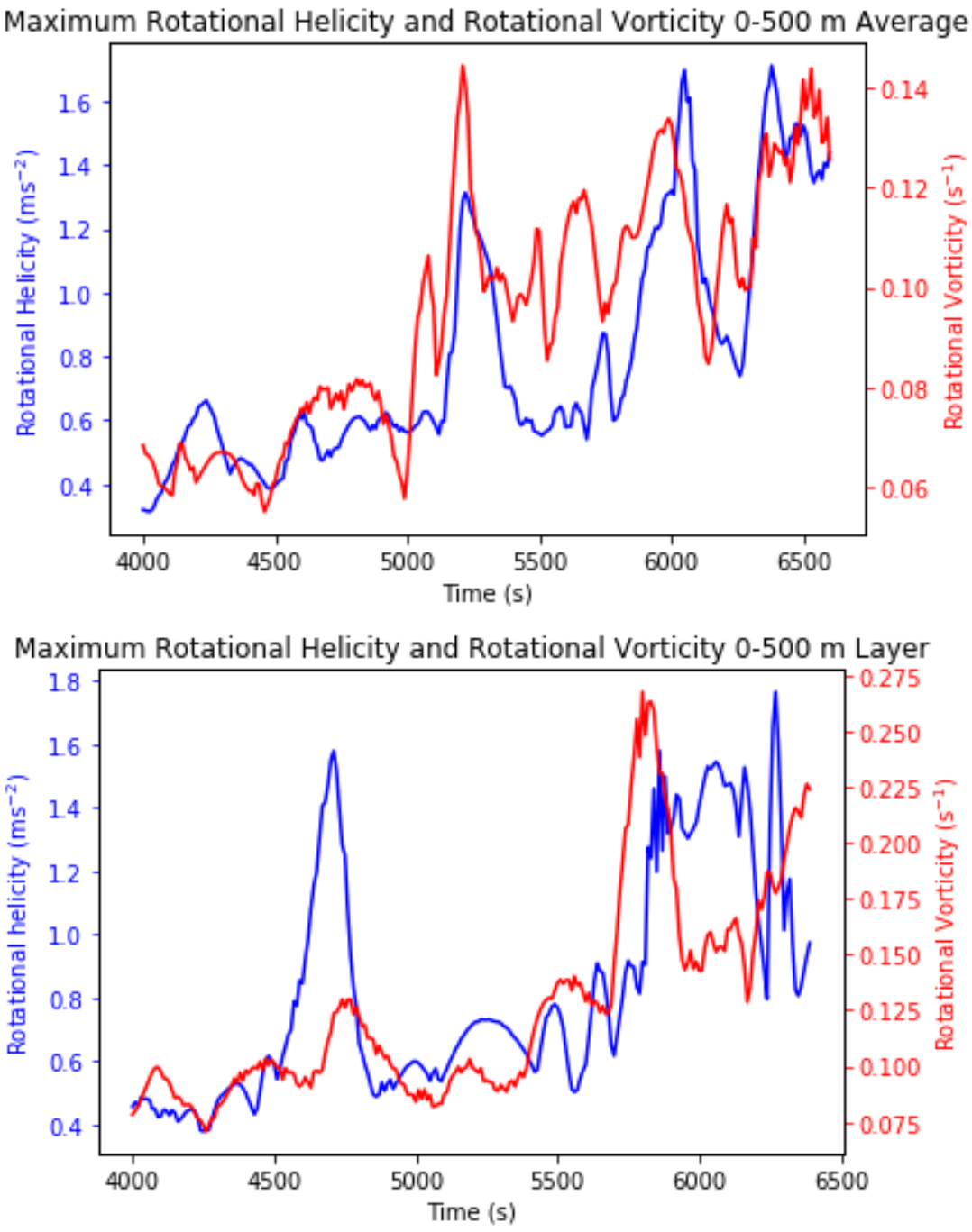

Figure 4.55: Rotational vorticity vs. rotational helicity. A comparison of maximum rotational vorticity and rotational helicity in the lowest 500 m of the domain for the TLV failure phase of the TOR-F simulation(a) and the TLV genesis phase of the TOR-S simulation (b).

b. Rotation vs. helical flow in understanding TLV failure vs. success

Using diagnostic technique developed in chapter three, it was shown in the TOR-S storm that helical flow developed in the lowest 500 m of the model domain in the 1000 s prior to TLV-success along a baroclinic convergence zone in the left-flank region. This low-level helical rotation subsequently developed a sustained interaction with a separate region of helical rotation elevated from the surface and associated with the rotation of the lower potions of the main updraft. This *helical coupling* appeared to have a critical role in the explosive growth of surface-based vertical vorticity during TLV-genesis. Conversely, during TLV-failure in the TOR-F storm, intense precipitation falling out ahead of the updraft into the forward-flank inflow region caused a substantial region of low-level divergence, which prevented the inflow air from interacting with this convergence boundary as it was modified by an internal momentum surge. While a weak surface-based vortex did eventually evolve along the storm's rear-flank gust front, it was displaced to the south of the low-level helical rotation in the forward-flank and *cut off* from the denser cold pool region well to the north of the low-level circulation. The absence of any robust helical structures in the vicinity of the surface-based vortex developing in the RFD region of the TOR-F storm marks a drastic departure from the TOR-S simulation during TLV-genesis.

Interestingly, in the TOR-F simulation, rotational vorticity and rotational helicity correlate extremely well in the lowest 500 m AGL, whereas during TLV-success in TOR-S, rotational helicity exhibits a substantial departure from rotational vorticity in this layer (Fig. 4.55). This suggests that the maxima in rotational helicity are largely driven by an intensification of rotation and not by a conversion of rotation to helical flow in the TLV-failure case. In the TLV-success case, it is evident that there is a conversion of *crosswise* rotational flow to *helical* rotational flow

at low-levels prior to TLV-success because of the significant departure between rotational vorticity and helicity during this time. Analysis of the characteristic vertical thermodynamic and kinematic profiles during TLV-failure in the TOR-F supercell clearly demonstrates stark differences to the TOR-S storm in the left-flank (Fig. 4.56*c*). Throughout the TLV-failure period, the inflow regions in the forward-flank and to the south-east of the updraft are characterized by substantial values of streamwise vorticity and are qualitatively similar to the TOR-S simulation at the time of genesis (compare Fig. 4.56*a,b* with Figs. 4.30 & 4.31).

From the preceding analysis of characteristic TLV-success and failure in the NMS simulations, it appears TLV-genesis in the tornadic VORTEX2 environment depends upon a sustained interaction of helical flow between outflow-driven rotation in the lowest 500 m AGL and rotation associated with the storm's low-level mesocyclone aloft. This interaction involves coherent *misoscale* regions of helical rotation and is clearly distinguishable from the background vorticity and mesocyclone of the supercell during TLV-genesis using the diagnostics developed through this research. The process is modulated substantially by distribution of precipitation relative to the updraft's low-level inflow and due to the prevalence of intense surges in precipitation in the storms simulated with the NMS, it is a considerably chaotic process. The orientation of dominant low-level convergence boundaries relative to storm-relative easterly flow appears to impact the ability for the storm to generate a helical interaction between outflow- and inflow-associated rotational flow. Therefore, the positioning, orientation and intensity of downdraft surges is critical for TLV-genesis in the NMS simulations.

a.

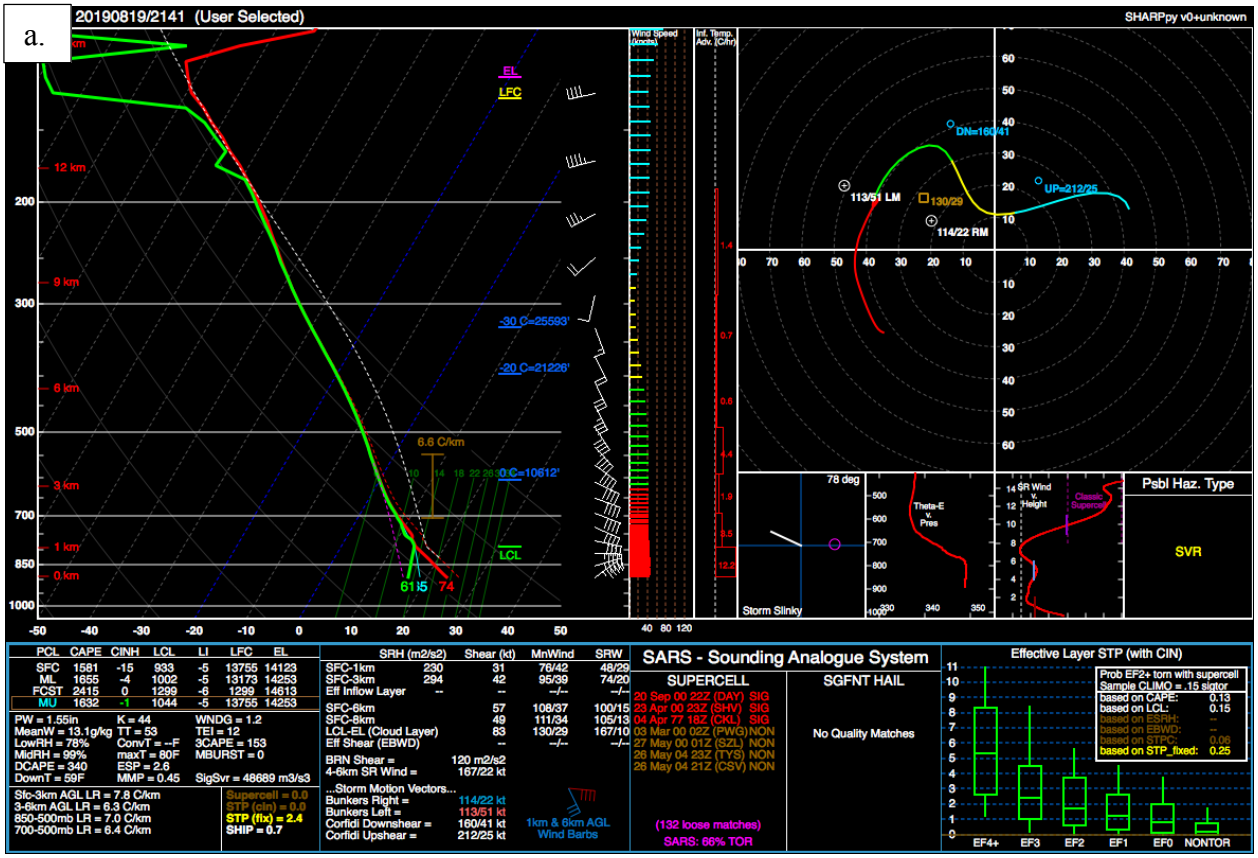
20190819/2141 (User Selected)
SHARPpy v0+unknown
EL
LFC
12 km
9 km
6 km
3 km
1 km
0 km
-30 C=25593'
-20 C=21226'
0 C=10612'
6.6 C/km
LCL
61 65 74
DN=160/41
113/51 LM
130/29
114/22 RM
UP=212/25
78 deg
Storm Slinky
Psbl Haz. Type
SVR
PCL CAPE CINH LCL LI LFC EL
SFC 1581 -15 933 -5 13755 14123
ML 1655 -4 1002 -5 13173 14253
FCST 2415 0 1299 -6 1299 14613
MU 1632 -1 1044 -5 13755 14253
PW = 1.55in K = 44 WNDG = 1.2
MeanW = 13.1g/kg TT = 53 TEI = 12
LowRH = 78% ConvT = --F 3CAPE = 153
MidRH = 99% maxT = 80F MBURST = 0
DCAPE = 940 ESP = 2.6
DownT = 59F MMP = 0.45 SigSvr = 48689 m3/s3
Sfc-3km AGL LR = 7.8 C/km
3-6km AGL LR = 6.3 C/km
850-500mb LR = 7.0 C/km
700-500mb LR = 6.4 C/km
Supercell = 0.0
STP (cin) = 0.0
STP (fix) = 2.4
SHIP = 0.7
SRH (m2/s2) Shear (kt) MnWind SRW
SFC-1km 230 31 76/42 48/29
SFC-3km 294 42 95/39 74/20
Eff Inflow Layer -- -- --/-- --/--
SFC-6km 57 108/37 100/15
SFC-8km 49 111/34 105/13
LCL-EL (Cloud Layer) 83 130/29 167/10
Eff Shear (EBWD) -- --/-- --/--
BRN Shear = 120 m2/s2
4-6km SR Wind = 167/22 kt
...Storm Motion Vectors...
Bunkers Right = 114/22 kt
Bunkers Left = 113/51 kt
Corfidi Downshear = 160/41 kt
Corfidi Upshear = 212/25 kt
1km & 6km AGL Wind Barbs
SARS - Sounding Analogue System
SUPERCELL
20 Sep 00 22Z (DAY) SIG
23 Apr 00 23Z (SHV) SIG
04 Apr 77 18Z (CKL) SIG
03 Mar 00 02Z (PWG) NON
27 May 00 01Z (SZL) NON
26 May 04 23Z (TYS) NON
26 May 04 21Z (CSV) NON
(132 loose matches)
SARS: 66% TOR
SGFNT HAIL
No Quality Matches
Effective Layer STP (with CIN)
Prob EF2+ torn with supercell
Sample CLIMO = .15 sigtor
based on CAPE: 0.13
based on LCL: 0.15
based on ESRH: --
based on EBWD: --
based on STPC: 0.06
based on STP_fixed: 0.25
EF4+ EF3 EF2 EF1 EF0 NONTOR

b.

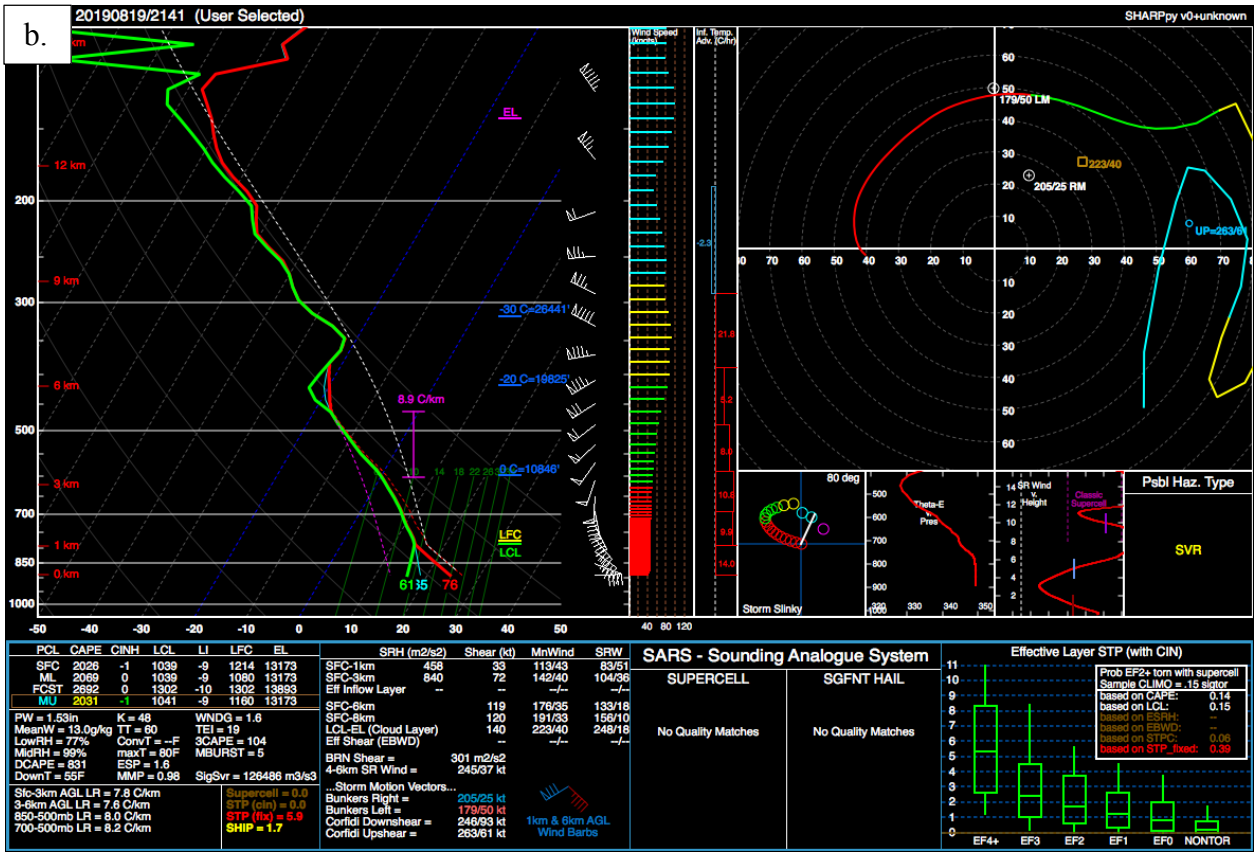
20190819/2141 (User Selected)
SHARPpy v0+unknown
EL
LFC
12 km
9 km
6 km
3 km
1 km
0 km
-30 C=26441
-20 C=19825
0 C=10846'
8.9 C/km
LCL
61 65 76
179/50 LM
223/40
205/25 RM
UP=263/61
80 deg
Storm Slinky
Psbl Haz. Type
SVR
PCL CAPE CINH LCL LI LFC EL
SFC 2026 -1 1039 -9 1214 13173
ML 2069 0 1039 -9 1080 13173
FCST 2692 0 1302 -10 1302 13893
MU 2031 -1 1041 -9 1160 13173
PW = 1.53in K = 48 WNDG = 1.6
MeanW = 13.0g/kg TT = 60 TEI = 19
LowRH = 77% ConvT = --F 3CAPE = 104
MidRH = 99% maxT = 80F MBURST = 5
DCAPE = 831 ESP = 1.6
DownT = 55F MMP = 0.98 SigSvr = 126486 m3/s3
Sfc-3km AGL LR = 7.8 C/km
3-6km AGL LR = 7.6 C/km
850-500mb LR = 8.0 C/km
700-500mb LR = 8.2 C/km
Supercell = 0.0
STP (cin) = 0.0
STP (fix) = 5.9
SHIP = 1.7
SRH (m2/s2) Shear (kt) MnWind SRW
SFC-1km 458 33 113/43 83/51
SFC-3km 840 72 142/40 104/36
Eff Inflow Layer -- -- --/-- --/--
SFC-6km 119 176/35 133/18
SFC-8km 120 191/33 156/10
LCL-EL (Cloud Layer) 140 223/40 248/18
Eff Shear (EBWD) -- --/-- --/--
BRN Shear = 301 m2/s2
4-6km SR Wind = 245/37 kt
...Storm Motion Vectors...
Bunkers Right = 205/25 kt
Bunkers Left = 179/50 kt
Corfidi Downshear = 246/63 kt
Corfidi Upshear = 263/61 kt
1km & 6km AGL Wind Barbs
SARS - Sounding Analogue System
SUPERCELL
No Quality Matches
SGFNT HAIL
No Quality Matches
Effective Layer STP (with CIN)
Prob EF2+ torn with supercell
Sample CLIMO = .15 sigtor
based on CAPE: 0.14
based on LCL: 0.15
based on ESRH: --
based on EBWD: --
based on STPC: 0.06
based on STP_fixed: 0.39
EF4+ EF3 EF2 EF1 EF0 NONTOR

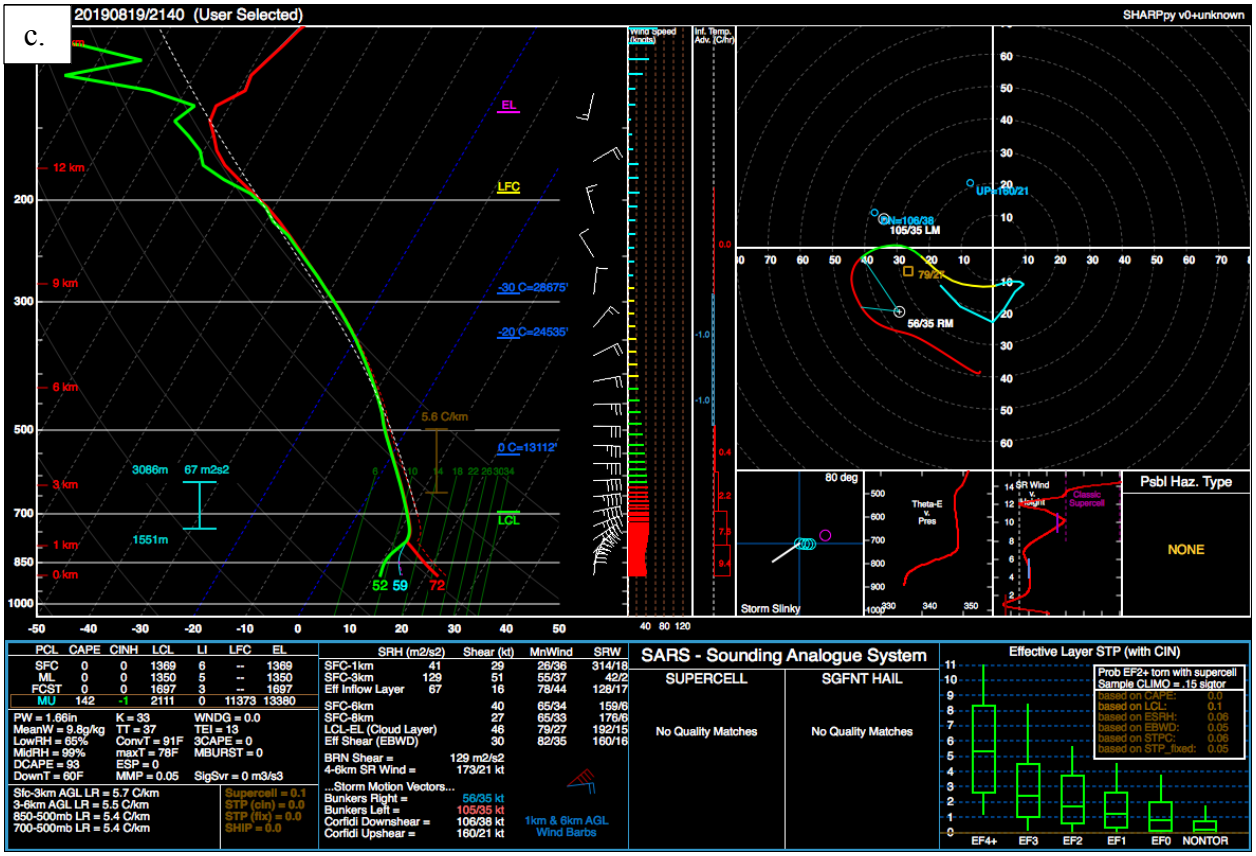

Figure 4.56: Characteristic vertical thermodynamic and kinematic structure of the forward-flank (a), inflow (b) and left-flank regions of the TOR-F supercell at 4900 s.

4.2.3 VORTEX2 simulations: Nontornadic (NOTOR simulation)

All supercells simulated with the NMS with the nontornadic VORTEX2 environment failed to produce TLVs. A characteristic example of one of these simulations is chosen for comparison with results from the tornadic simulations presented in the previous section. Herein, this will be referred to as the NOTOR supercell. The focus of the analysis will be on the period of the simulation in which the storm produced the maximum intensity of surface vertical vorticity and I^2.

a. Outflow structural differences with tornadic simulations

The first thing that becomes apparent when comparing the simulated supercells in the tornadic VORTEX2 environment with those in the nontornadic environment is the differences in structure of the precipitation and cold pool regions around the updraft. The most intense precipitation associated with the simulated supercells in the tornadic environment tended to fall to the north of the updraft leading to the momentum surging and helical flow development in the near-surface layer of the left-flank region. In contrast, the more intense condensate reaching the lowest model level in the NOTOR simulation was predominantly found to the north-east of the updraft in the forward flank region of the storm (Fig. 4.57). This orientation of precipitation in the NOTOR supercell led to primary downdraft-driven momentum surging in the *forward*-flank region leading to a chaotic mixture of low-level environmental air and storm-processed outflow air approaching the low-level updraft (Fig. 4.58). Interestingly, inflowing air from the ambient

environment was frequently forced to the surface in the forward-flank through dynamic interactions with the intense precipitation and associated high density cold pool air (Fig. 4.59).

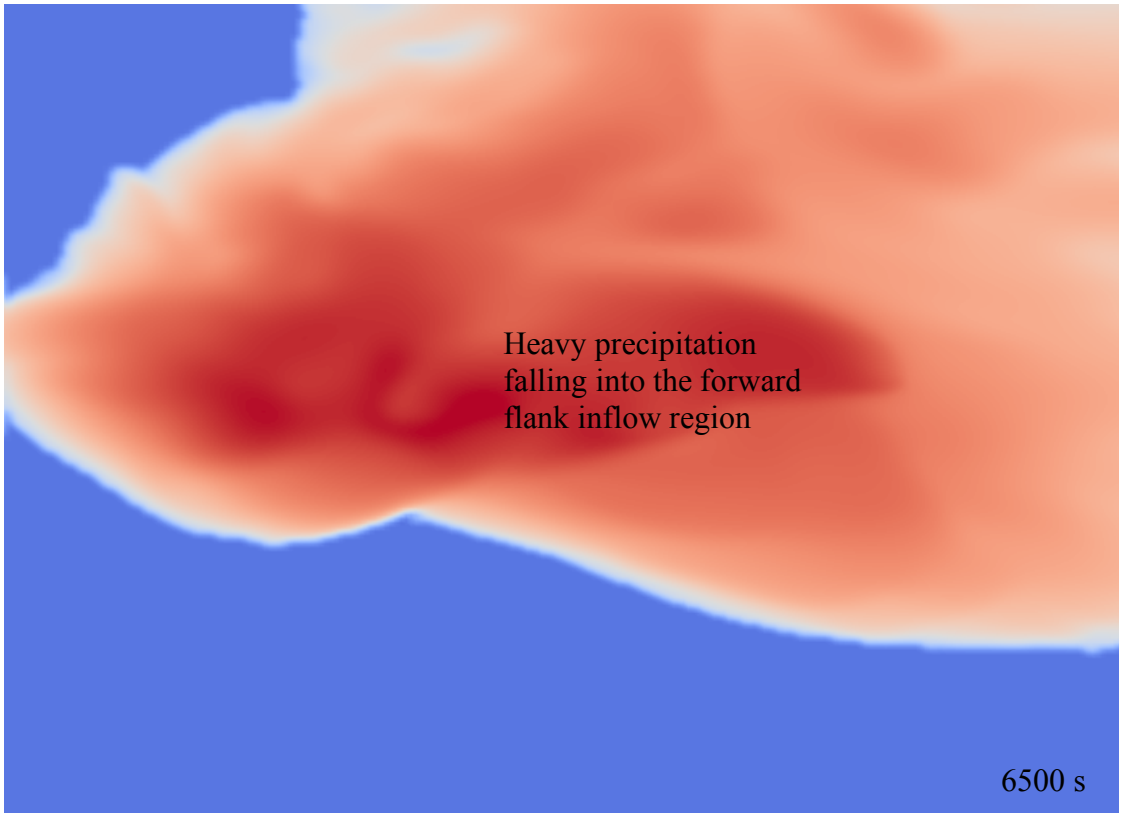

Figure 4.57: Typical surface condensate distribution in the NOTOR simulation. As in Fig. 4.9 but for the NOTOR supercell simulation at 6500 s.

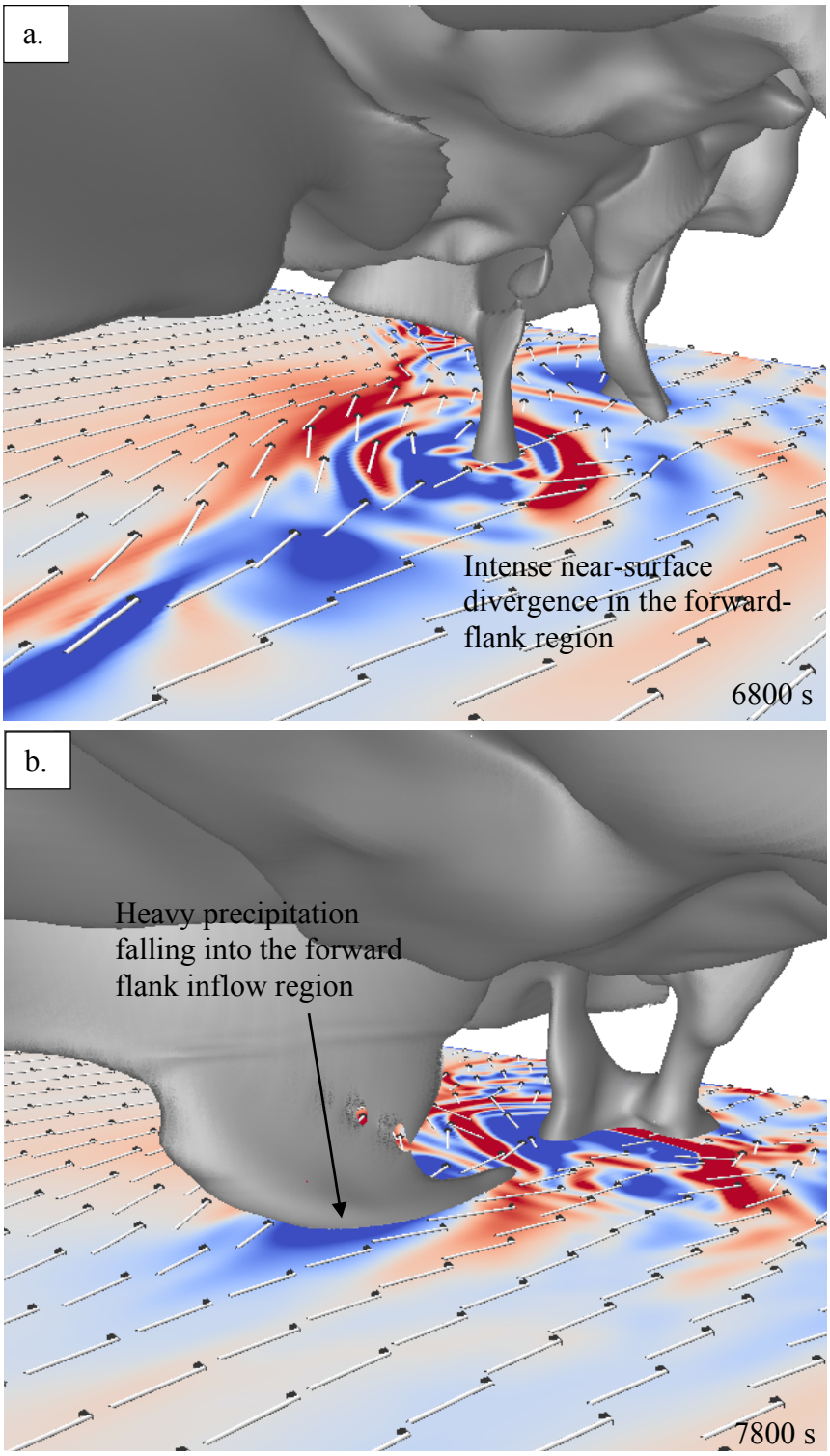

Figure 4.58: Evolution of condensate in the NOTOR simulation. As in Fig. 4.23 but for the NOTOR supercell simulation at 6800 s (a) and 7800 s (b).

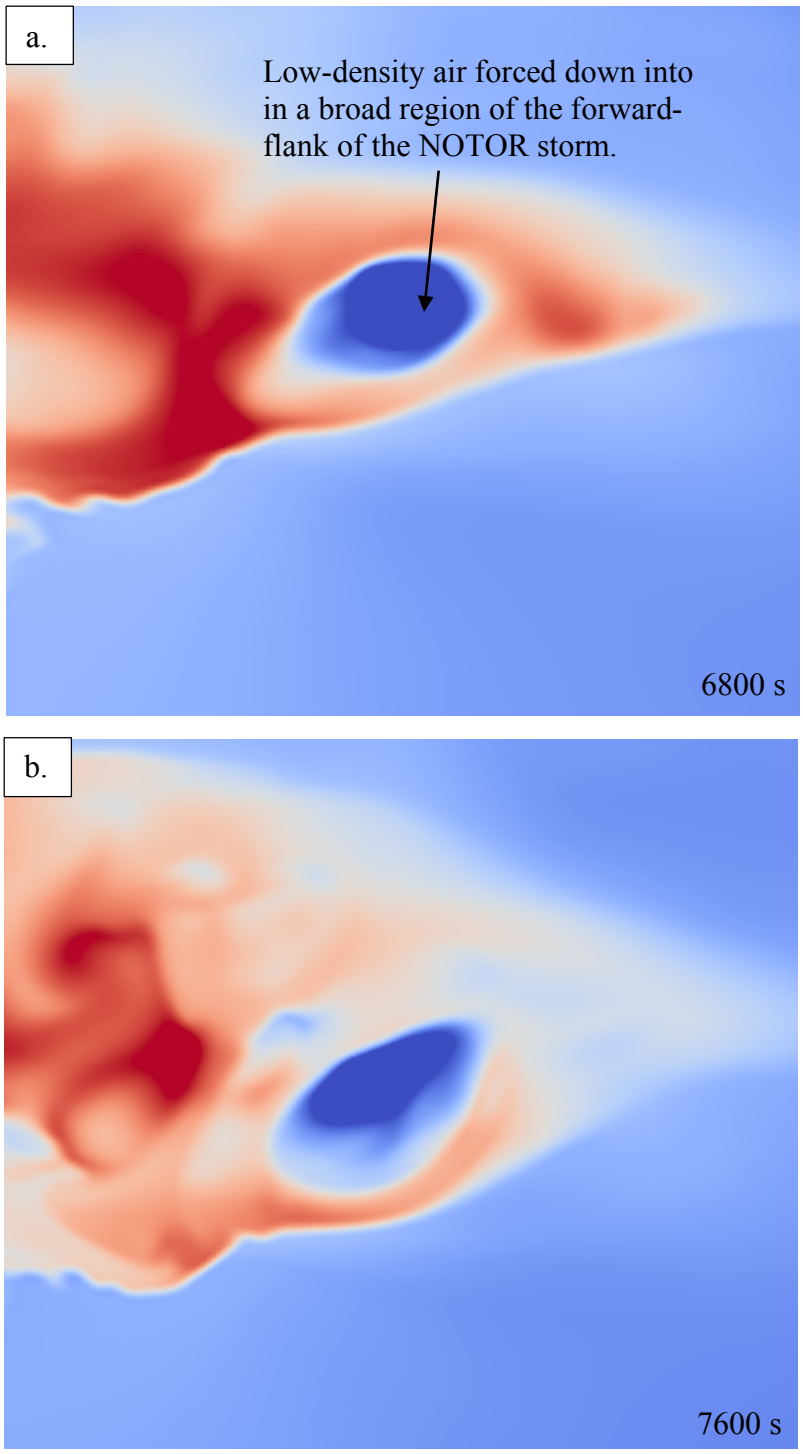

Figure 4.59: Evolution of surface perturbation density in the NOTOR simulation. Perturbation density at the lowest model level in the NOTOR simulation at 6800 s (a) and 7600 s (b). Warm colors are associated with positive perturbation density and blue colors are associated with negative perturbation density.

As opposed to the TOR-S simulation, in which relatively low-density environmental air was dynamically-forced into the outflow to the north of the low-level updraft in an isolated region, the low-density air in the forward-flank of the NOTOR storm was driven into the outflow constantly over a large region by intense precipitation. Additionally, the outflow generally accelerated westward rapidly relative to the storm above, continuously displacing developing low-level circulations from the main updraft of the storm (Fig. 4.60). The more organized, steady dynamic integration of low-level environmental air in the TOR-S simulation was driven by rotation rather than deformation as in the unsteady surging NOTOR simulation. This suggests that storms capable of sustaining horizontal, helical rotational structures such as those seen in the TOR-S simulation are more likely to occur in steadier outflows in which downdraft surging does not impede the low-level flow from the forward-flank. The rotational structures appear to, in return, further help organize and steady the cold pool structure of the supercell's outflow region.

Major differences in vertical atmospheric structure in the outflow region were found between the TOR-S and NOTOR simulations. From a thermodynamic perspective, the lower relative humidity of the NOTOR boundary layer led to lower saturation points, and higher LCLs and LFCs when compared with the TOR-S and TOR-F simulations (Fig. 4.61). There were weaker lapse rates aloft compared with those in the TOR-S and TOR-F simulations, particularly close to 6 km AGL where the dewpoint inversion was observed in the original composite sounding. From a kinematic perspective, the kink in the low-level portions of the original hodograph leads to less sustained helical inflow in the NOTOR storm, which is associated with weaker low-level updraft and inflow. The mid-level mesocyclone effectively sits atop the cold pool in the NOTOR storm with a lack of conditionally unstable inflow air entering its base from the forward-flank. Additionally, with stronger easterly relative momentum just

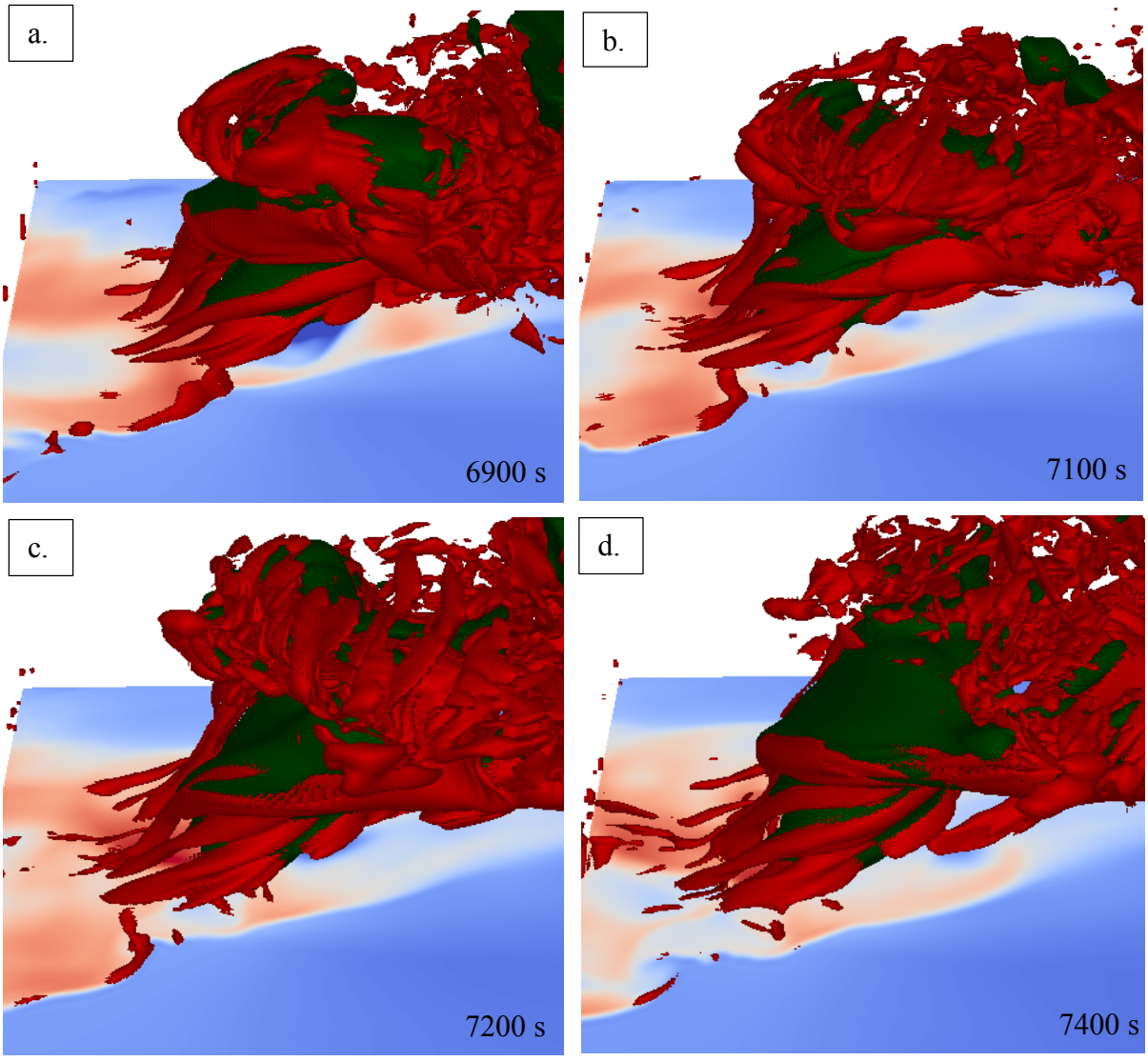

Figure 4.60: Dissociation of low-level and mid-level vertical vorticity fields in the NOTOR simulation. Surface is shaded as in Fig. 4.60, red isosurface is a 0.02s^{-1} rendering of vertical vorticity and green is the 20 ms^{-1} updraft velocity at 6900 s (a), 7100 s (b), 7200 s (c) and 7400 s (d). View is elevated from the south.

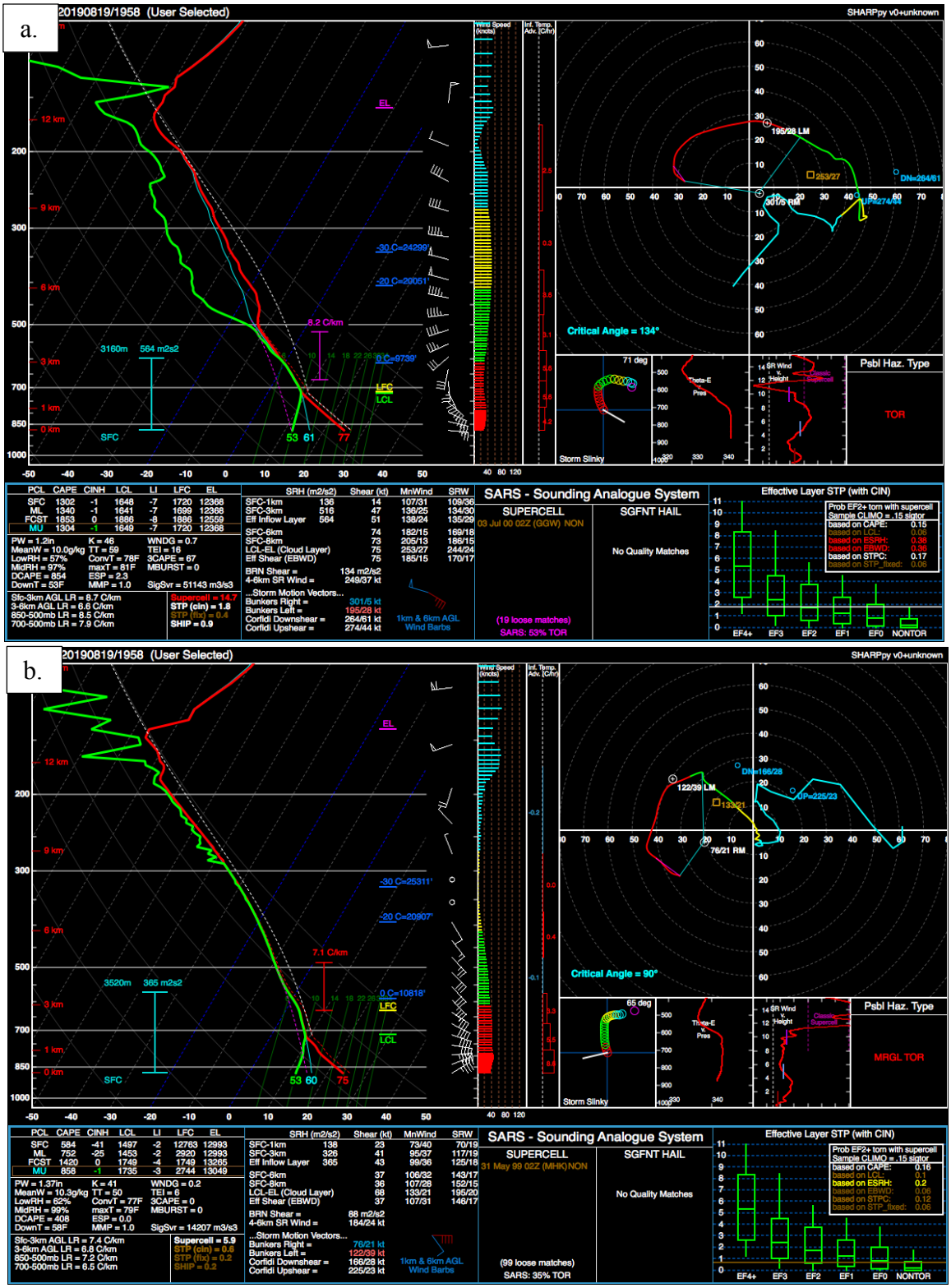

Figure 4.61: Vertical thermodynamic and kinematic structure of NOTOR storm. Characteristic sounding taken in the inflow layer (a) and left-flank (b) of the NOTOR supercell at 7000 s.

above the surface layer owing to the kink in the hodograph, downdrafts bringing down this momentum from aloft tended to accelerate more quickly to the west than in the tornadic simulations.

b. Surface-based vertical vorticity development

The poorly organized outflow region of the NOTOR supercell and weak low-level updraft prevented sustained interactions between surface-based vorticity and the mesocyclone (Fig. 4.60). As a result, the vertical vorticity magnitude in the lowest 500 m AGL peaked at 0.1 s^{-1} (Fig. 4.62). A low-level helical structure approaching the updraft from the east supported more substantial vertical vorticity growth during this time (Fig. 4.64). However, there was a clear lack of a deep helical interaction as was apparent in the TOR-S storm. The rapid westward propagation of the low-level helical structure relative to the storm's updraft precluded any meaningful interaction or intensification.

Time-height analysis of the maximum rotational helicity and vertical velocity fields reveals a stark contrast of the evolution of helical rotation with the TOR-S simulation (Fig. 4.65). Despite development of transient low-level maxima in rotational helicity, no helical rotation develops upward, rather, the most significant values are associated with *descending* structures likely generated along the periphery of intense pulses of precipitation. Upward vertical velocities are substantially weaker than with the TOR-S supercell and there is a complete absence of helical flow in the 1000 – 1500 m AGL layer, which was found to be a necessary component of the upward intensification of helical rotation involved in genesis of the TLV in the TOR-S simulation.

In supercell simulations using VORTEX2 environments with the CM1, the outflow regions of the storms tended to be far steadier than those simulated with the NMS and resulted in more sustained low-level helical interactions. These simulations will briefly be presented in the following section and compared to the NMS simulations already presented.

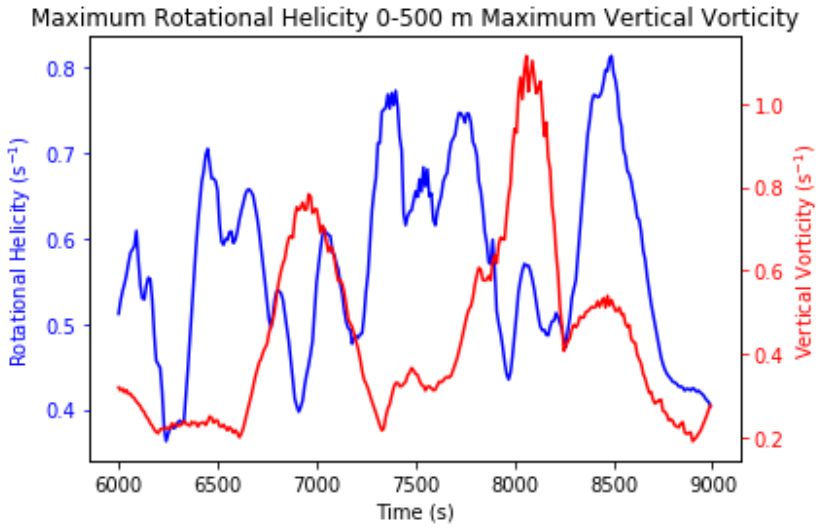

Figure 4.62: Low-level rotational helicity and vertical vorticity in the NOTOR simulation. Maximum rotational helicity and vertical vorticity in the lowest 500 m AGL in the 6000 – 9000 s period of the NOTOR simulation.

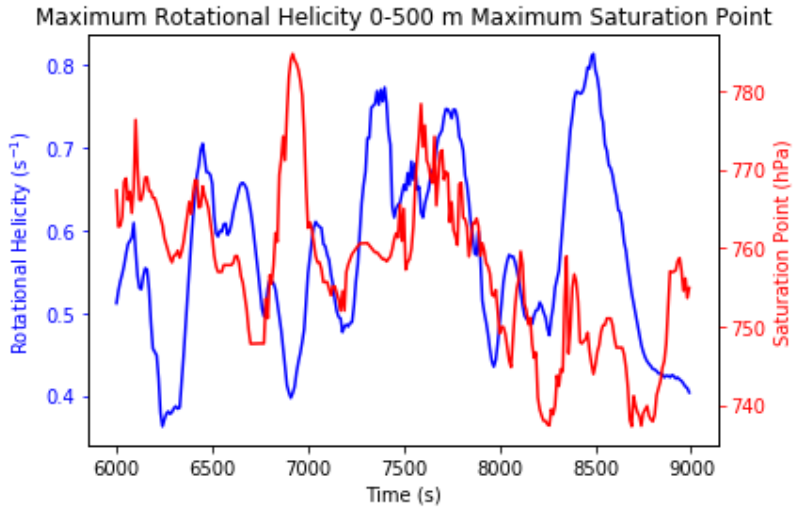

Figure 4.63: Low-level rotational helicity and saturation point in the NOTOR simulation. As in Fig. 4.20 but for the 6000 – 9000 s period of the NOTOR simulation.

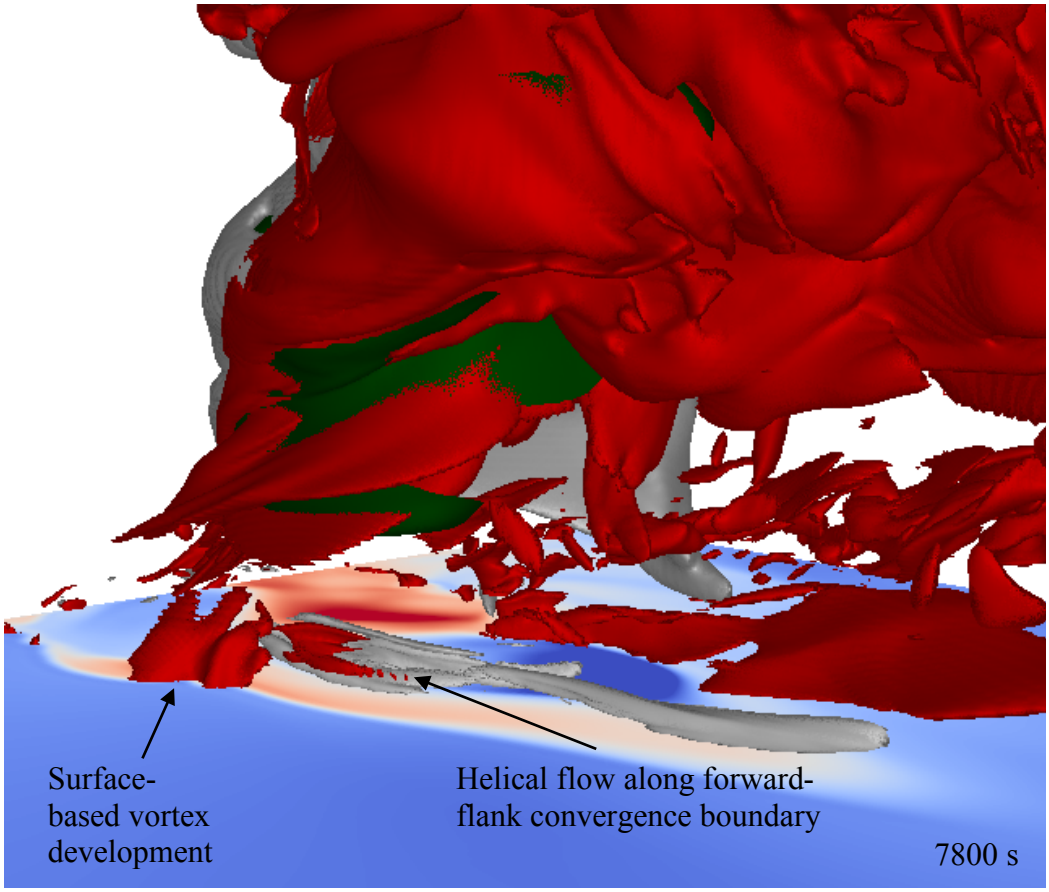

Figure 4.64: Failed surface-based vortex development in the NOTOR simulation. An east-west oriented convergence boundary associated with a westward propagating helical rotational structure supports surface-based vertical vorticity growth but does not intensify upward. As in Fig. 4.60 but with rotational helicity rendered at 0.4 ms^{-2} in the gray isosurface and looking from the south-east and at

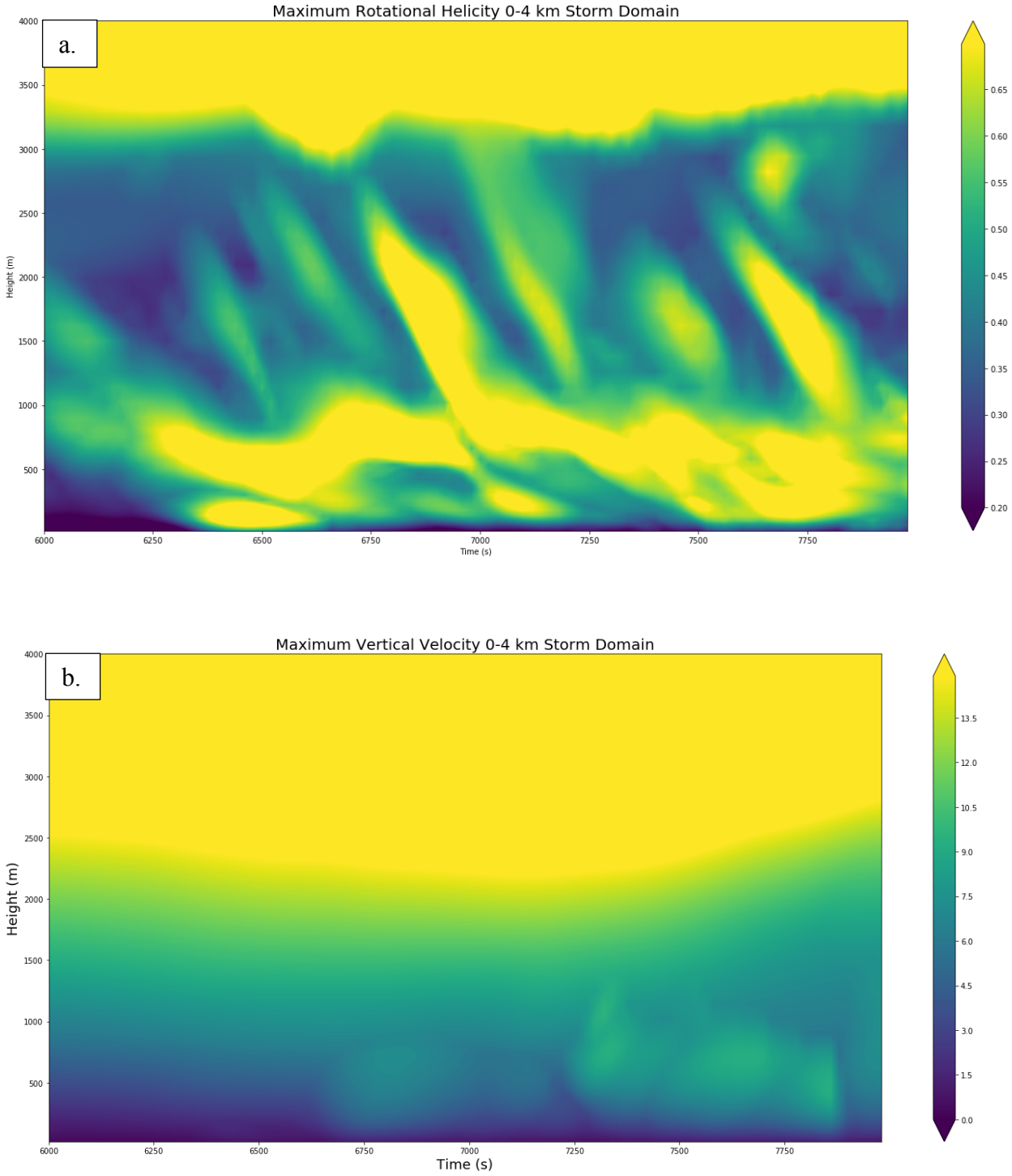

Figure 4.65: Maximum rotational helicity (a) and vertical velocity (b) over the 0-4 km layer of the NOTOR storm domain from 6000 – 8000 s.

4.2.4 VORTEX2 simulations: Comparisons with CM1 simulations

The VORTEX2 composite soundings were used to initialize the CM1 using the same base model configuration as in Orf et al. (2017) in order to test the veracity of the results acquired from the NMS simulations. Supercells initialized in the tornadic and nontornadic environments are briefly compared in this section.

a. Tornadic environment (TOR-CM1)

A significant distinguishing feature of the CM1 VORTEX2 simulations was the relative "steadiness" of the outflow regions compared with the NMS. While obvious cold pool surging did occur, it did not do so with nearly the same frequency or intensity as in the NMS. Fig. 4.66 illustrates a characteristic structure of the tornadic outflow region in the CM1, which can be evaluated against Figs. 4.22, 4.24, 4.49 and 4.52 for comparison. Almost no downdraft surges occurred away from the left-flank marking a stark difference from the NMS. As a result, each tornadic simulation appeared to proceed toward TLV development less abruptly. Less intense and more spatially contained outflow surging led to a quasi-steady left-flank convergence boundary, which occurred only transiently along the periphery of momentum surges in the NMS simulations. The reasons for this are unclear and beyond the scope of the research goals set out by this dissertation. However, it is certainly worthy of future investigation to study the reasons for the contrast in outflow structure between the models given results presented herein that suggest the orientation of internal convergence boundaries are critical to tornadogenesis in the simulated storms. Some further thoughts on this are provided later in this section.

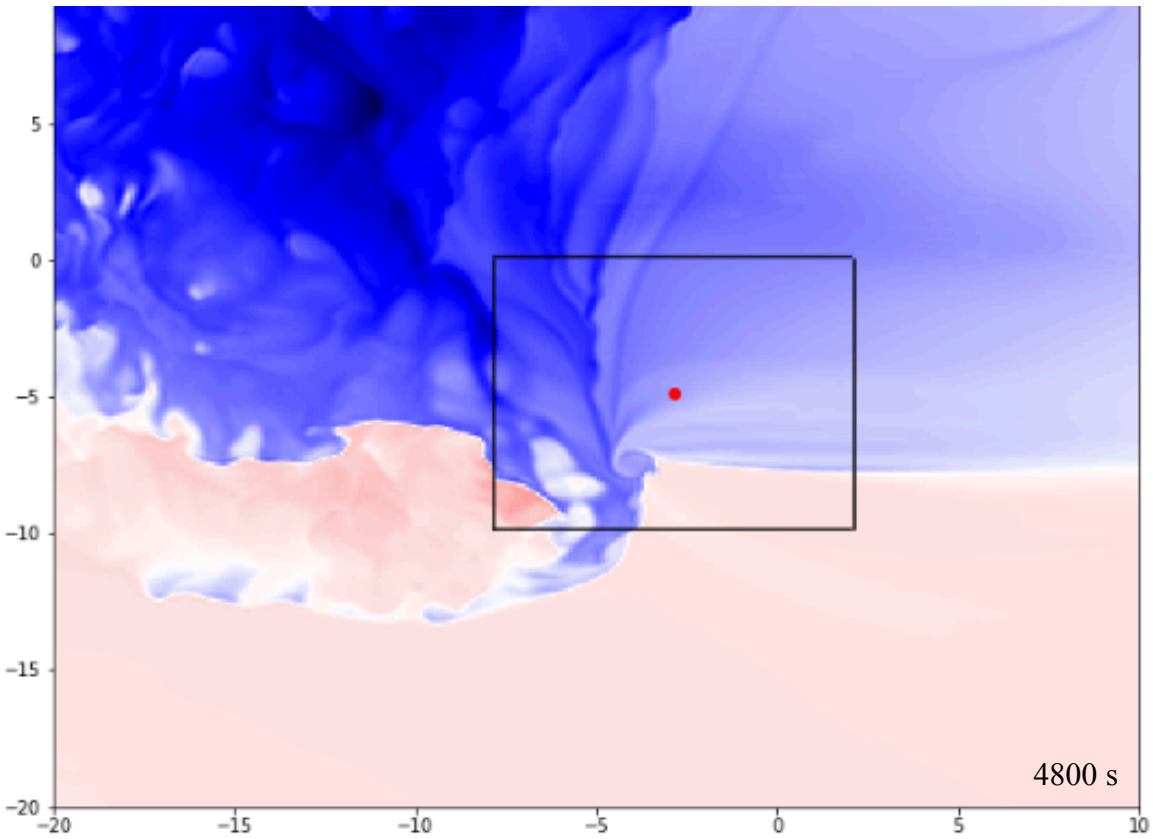

Figure 4.66: Characteristic outflow structure of TOR-CM1 simulation and box area used for time-height analysis. Top-down view of the TOR-CM1 supercell outflow region with box chosen to analyze variables in time-height space relative to the updraft maximum at 4 km AGL (red dot) at 4800 s. The surface is shaded by lowest model level perturbation density potential temperature (θ'_ρ ; Markowski and Richardson, 2011, pp. 13), where blues are associated with positive perturbations and therefore more negatively buoyant air.

Despite the significant differences in *evolution* of the outflow, its structure in the CM1 was an almost spitting image of the TOR-S outflow during their respective genesis phases. This encouraging result motivated the theory that although the storm evolution may be different between the models, TLV genesis may be driven by the same physical processes in each. Using the box area shown in Fig. 4.66, time-height analysis was performed just prior to rapid intensification of surface vertical vorticity. Maxima in rotational helicity were, as in the TOR-S simulation, evident at two distinct heights at 4600 s; around 1000 m AGL and in the lowest 500 m AGL (Fig. 4.67*a*). The low-level maximum intensified and ascended from very close to the surface and can be followed coherently up into the maximum associated with the mid-level mesocyclone at 4 km AGL. During the ascent of this maximum and, in particular, once it interacts with the helical flow of the mesocyclone aloft during the 4600 – 5000 s period of the TOR-CM1 simulation, vertical vorticity intensifies, first at the surface and subsequently deepens quickly over lowest 4 km of the domain in a remarkably similar fashion to the NMS TOR-S simulation (Fig. 4.67*b*).

Investigation of the three-dimensional rotational helicity and vertical vorticity fields illuminates a helical rotational structure along the left-flank baroclinic boundary (see Fig. 4.66), which supports significant surface-based vertical vorticity maxima (Fig. 4.68). The perpendicular orientation of this structure relative to the low-level flow in the forward-flank and the upward intensification of helical flow qualitatively resembles the TOR-S structures at a similar phase of TLV-genesis. It is perhaps more apparent in TOR-CM1 than TOR-S that this structure is associated with the upward growth of vertical vorticity from the surface during TLV-genesis. Interestingly, the upper portion of the surface-based vortices developing along the helical structure in the left-flank of TOR-CM1 appear to be helical or at least encased by helical flow

where they merge with the supporting helical structure. An isosurface of streamwise vorticity provides further intriguing information 4.69).

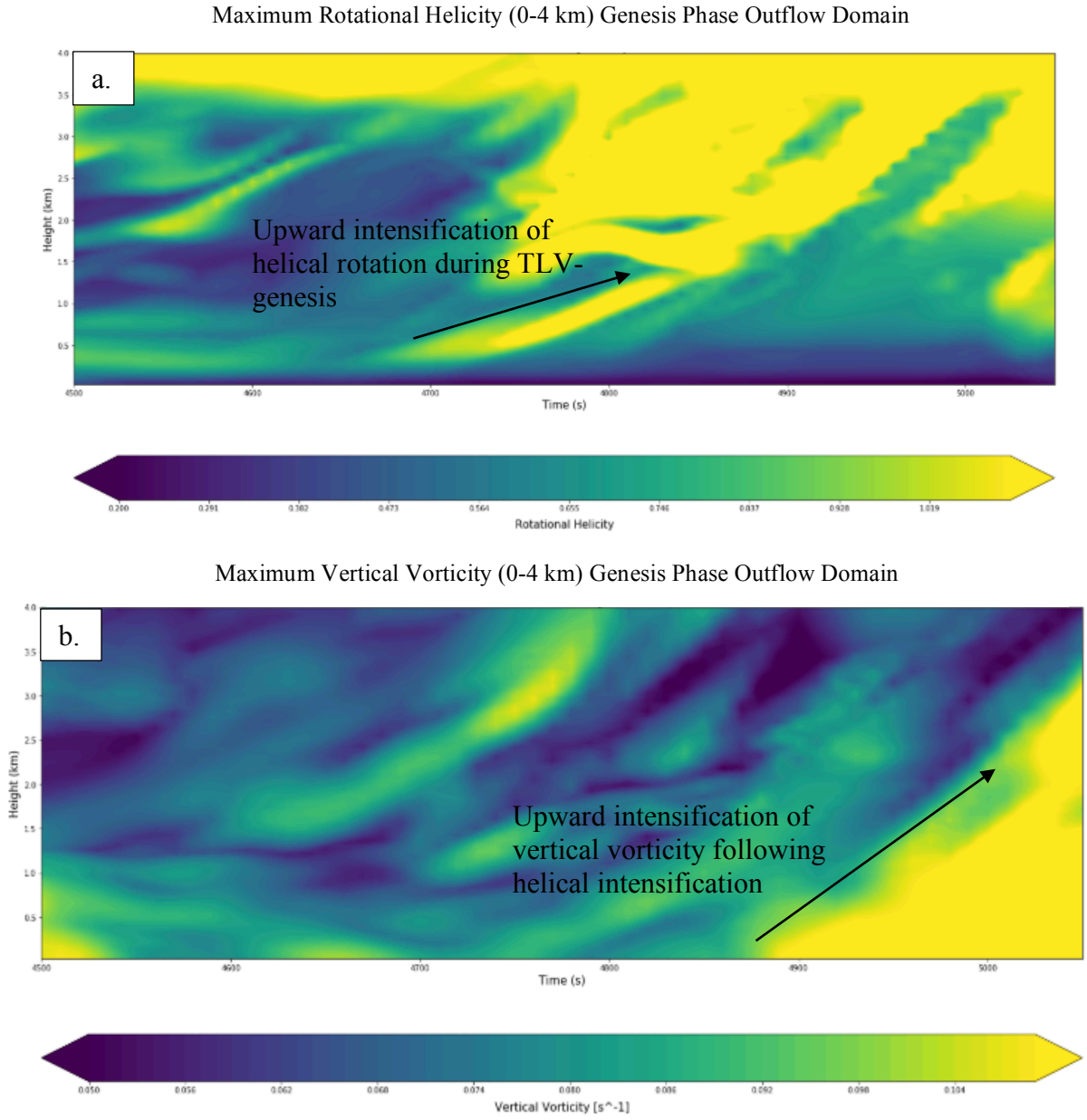

Figure 4.67: Evolution of rotational vorticity and vertical vorticity in TOR-CM1 during TLV-genesis. Time-height analysis of maximum rotational helicity (a) and vertical vorticity (b) over the 0-4 km layer in the TOR-CM1 simulation during its TLV genesis phase calculated in the box area shown in Fig. 4.65.

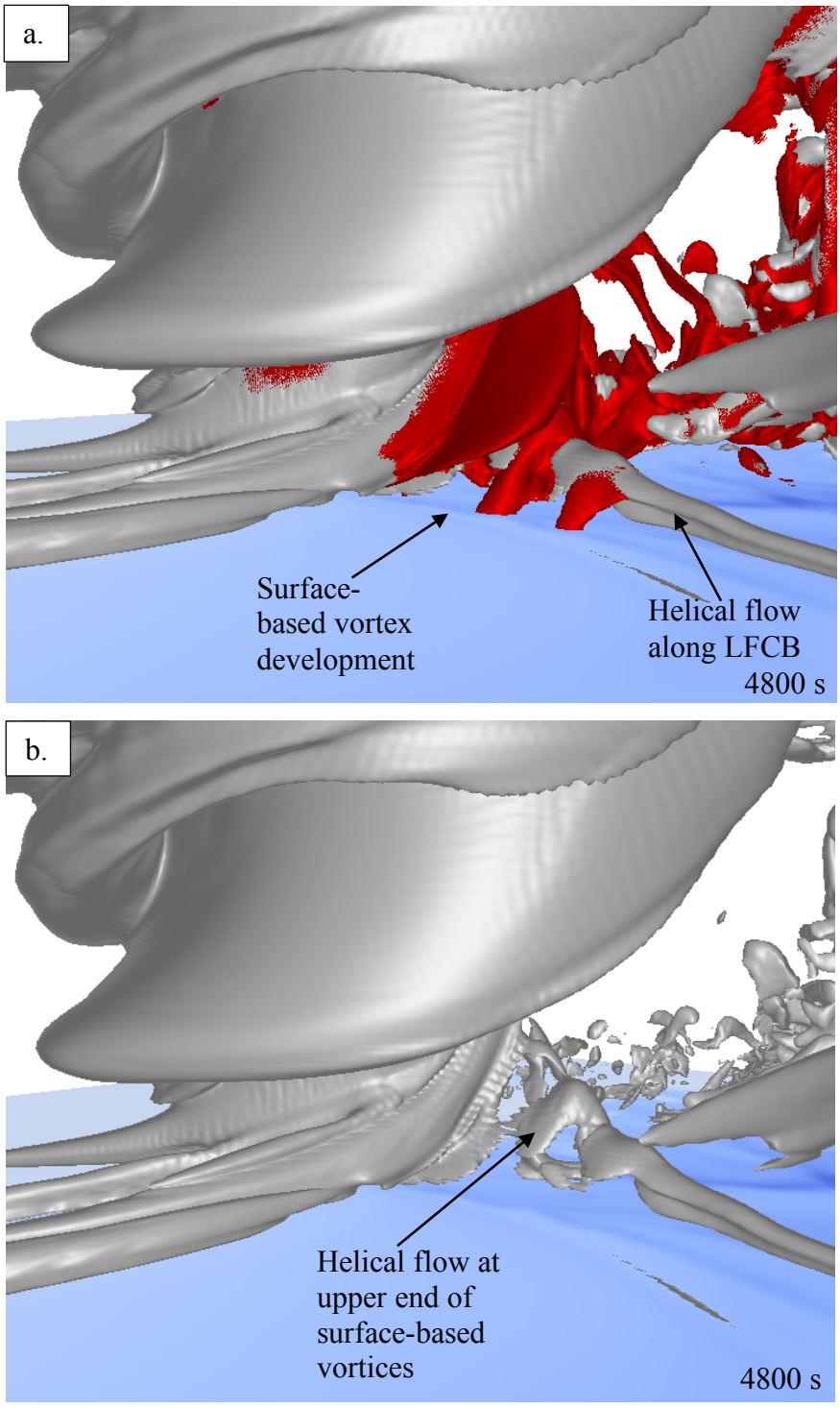

Figure 4.68: Low-level helical rotation supporting surface-based vertical vorticity growth during TLV-genesis in the TOR-CM1 simulation. Time-height analysis of maximum rotational helicity and vertical vorticity over the 0-4 km layer in the TOR-CM1 simulation during its TLV genesis phase calculated in the box area shown in Fig. 4.65. Rotational helicity is the gray isosurface at 0.4 ms^{-2} and vertical vorticity is the red isosurface at 0.15 s^{-1}.

A ‘sheet’ of streamwise vorticity associated with low-level shear of the environmental inflow approaches the helical structure along the internal baroclinic boundary and appears to be “wrapped” around it as it ascends toward the updraft. While the streamwise vorticity entering the updraft further to the south along the FFGF ascends in a sheet-like form for significant height before acquiring three-dimensional rotation (compare Fig. 4.68 with Fig. 4.69), the portion that interacts with the baroclinic boundary acquires rotation in close proximity to the ground.

Davies-Jones and Markowski (2013) rigorously demonstrated that vorticity associated with low-level shear of the environment could not be abruptly tilted into the vertical along a density interface to generate surface-based vertical vorticity because it is lifted ahead of the structure by local high pressure caused by deformation. Therefore, the vertical vortices along the boundary are likely baroclinically-generated. However, this analysis suggests that the role of the low-level environmental streamwise vorticity in TLV-development is more likely through their helical interaction with baroclinic structures in the outflow on its approach to the updraft. This theory will be returned to in chapter five.

It is reasonable to conclude that a number of the processes important to genesis of TLVs were common to both sets of simulations with the NMS and CM1. Ultimately, to determine rigorously whether this was the case, quantitative analysis of vorticity and vertical motion budgets are required. This approach can be performed through tendency analysis along modeled air parcel trajectories. While out of the scope of this dissertation, the author is actively pursuing this research, which will be discussed in greater detail in section 5.3.

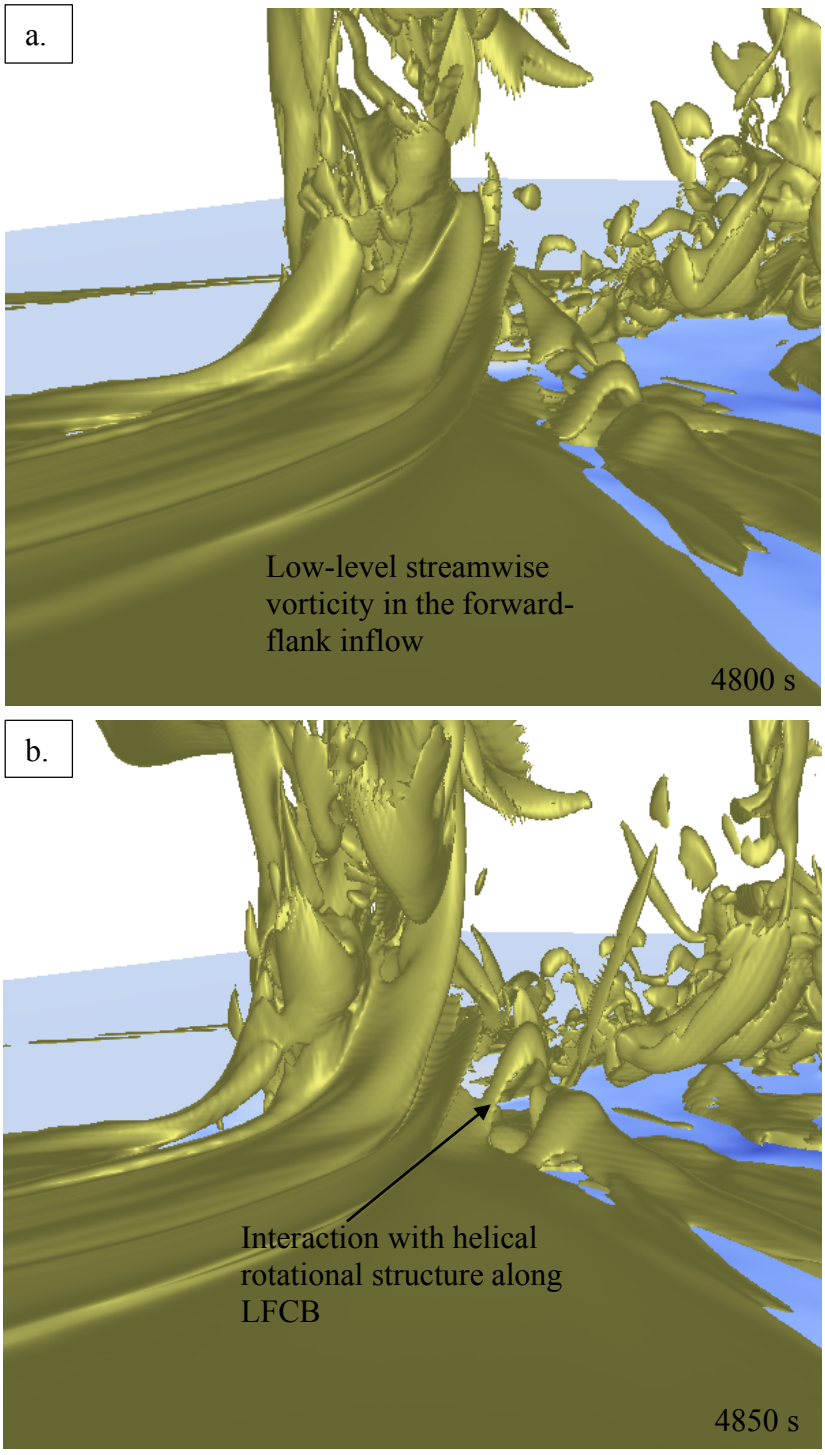

Figure 4.69: Interaction of low-level streamwise vorticity with baroclinic boundary in the left-flank of the TOR-CM1 storm. Streamwise vorticity rendered at 0.4 ms^{-1} (gold isosurface) demonstrating its interaction with the helical rotational structure on the LFCB during genesis of the TOR-CM1 TLV. Viewing angle is from the north-east, looking through the forward-flank region.

b. Nontornadic environment

As in the nontornadic VORTEX2 simulations with the NMS, the CM1 supercells also failed to generate TLVs in this composite environment. Once again, the supercell's outflow region was dramatically different to the tornadic simulations (compare Figs. 4.70 & 4.66). Despite the vivid differences between the chaotic outflow of the NOTOR NMS supercell and the relative quiescence of that in the CM1-NOTOR, there are significant qualitative similarities between the simulations with the two models. The orientation of the outflow in both CM1-NOTOR and NOTOR is aligned in an east-west direction and does not exhibit the four characteristic regions of their tornadic counterparts. Intriguingly, both CM1-NOTOR and NOTOR have *less*-dense outflow relative to their immediate environments despite evolving in environments with less boundary layer relative humidity, which should lead to more negatively buoyant downdrafts through increased evaporational cooling. The author theorizes that this result is due to the more widespread precipitation in the storm's forward-flank producing greater mixing with low-level environmental air from the east.

Much like in NOTOR, surface-based vertical vorticity was weak throughout the NOTOR-CM1 simulation, and was generally poorly organized and confined to the rear flank of the storm (Fig. 4.71). The evolution of both vertical vorticity and rotational helicity in a time vs. height sense clearly lacks vertical coherency that was evident in the tornadic simulations (Fig. 4.72). However, a deep vortex arch did develop in association with the RFD region with well-defined cyclonic and anticyclonic branches (Fig. 4.73). A weak ascending maximum in rotational helicity was noted at this time, but it is uncertain whether this structure had anything to do with the development of the arched vortex. The surface-based vortex arch did not, however, intensify into a TLV by the criteria used herein.

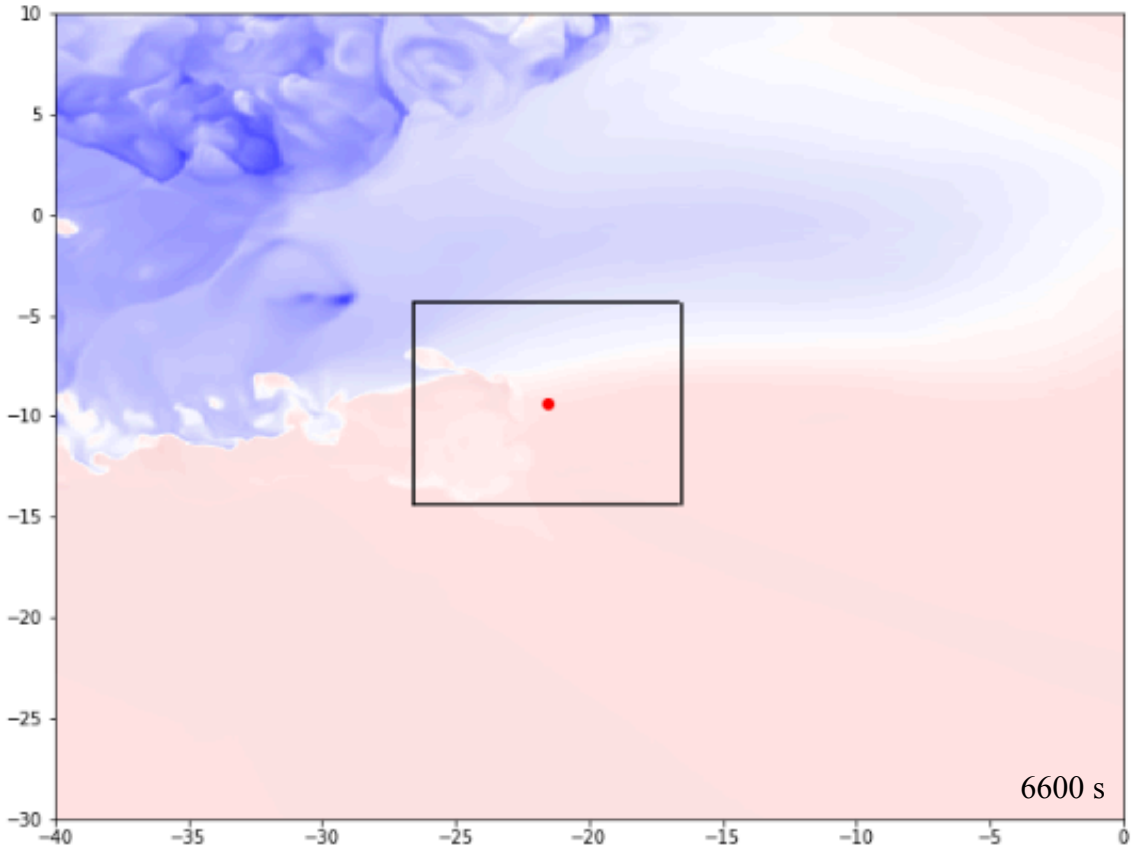

Figure 4.70: Characteristic outflow structure of the CM1-NOTOR simulation. As with Fig. 4.66 but for the CM1-NOTOR supercell at 6600 s.

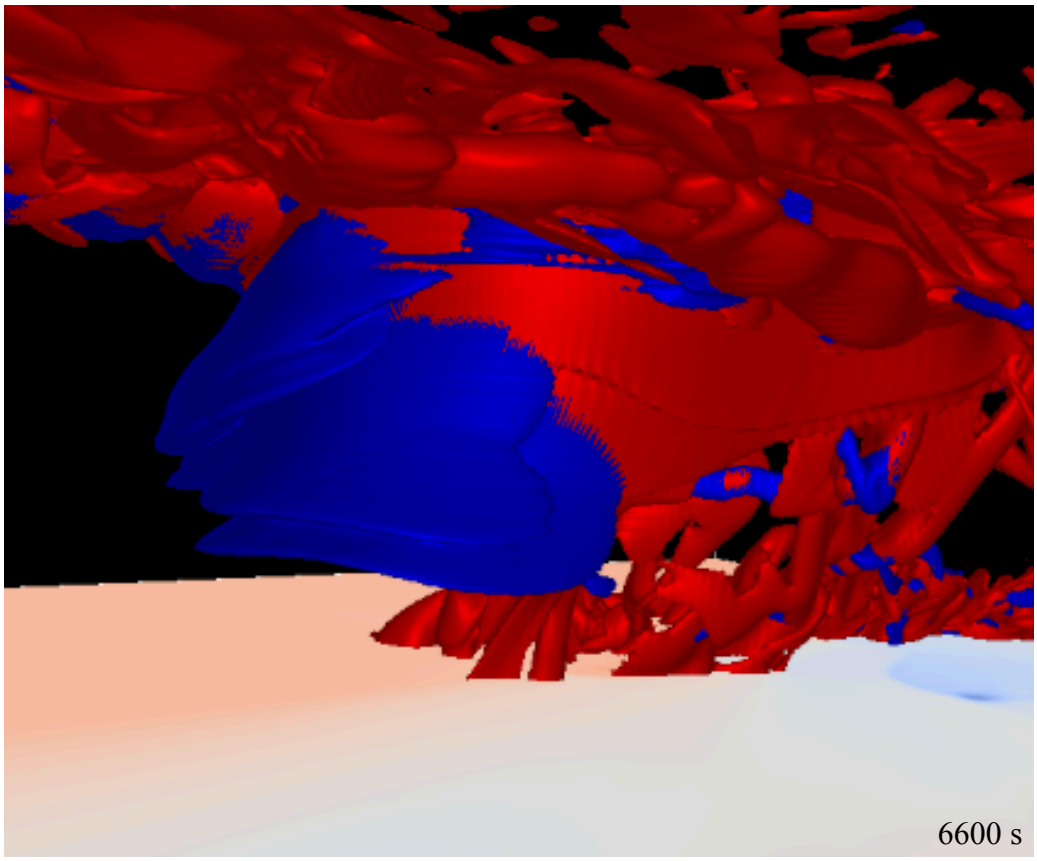

Figure 4.71: Snapshot of rotational helicity and vertical vorticity in CM1-NOTOR. Rotational helicity of 0.4 ms^{-2} (blue isosurface) and vertical vorticity of 0.05 s^{-1} (red isosurface) in the CM1-NOTOR simulation at 6600 s. The surface is shaded as in

Maximum Rotational Helicity (0-4 km) Storm Domain

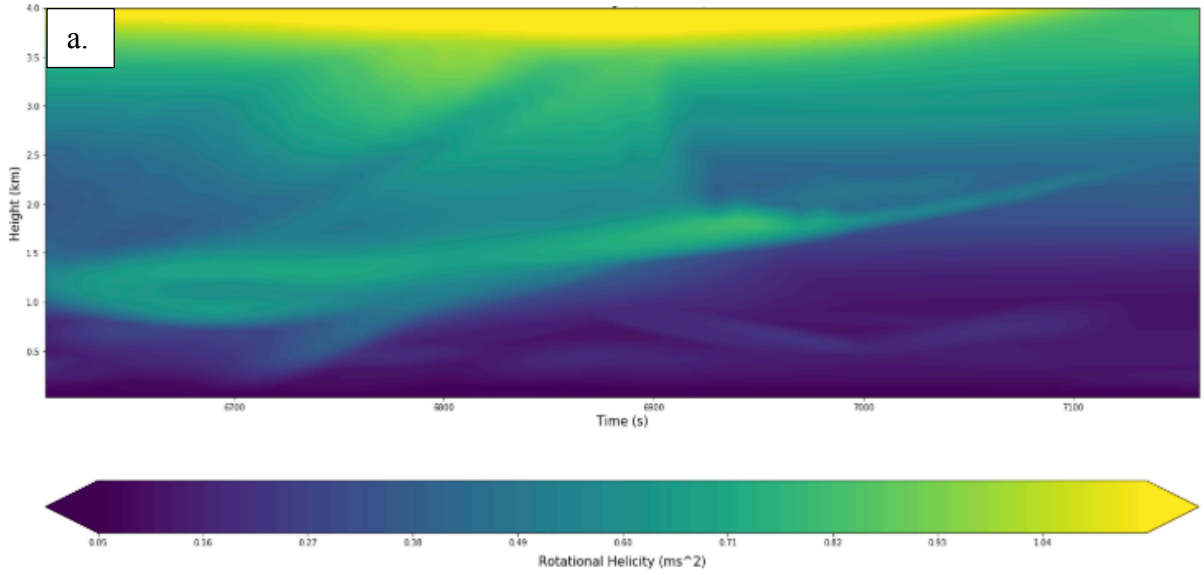

Maximum Vertical Vorticity (0-4 km) Genesis Phase Outflow Domain

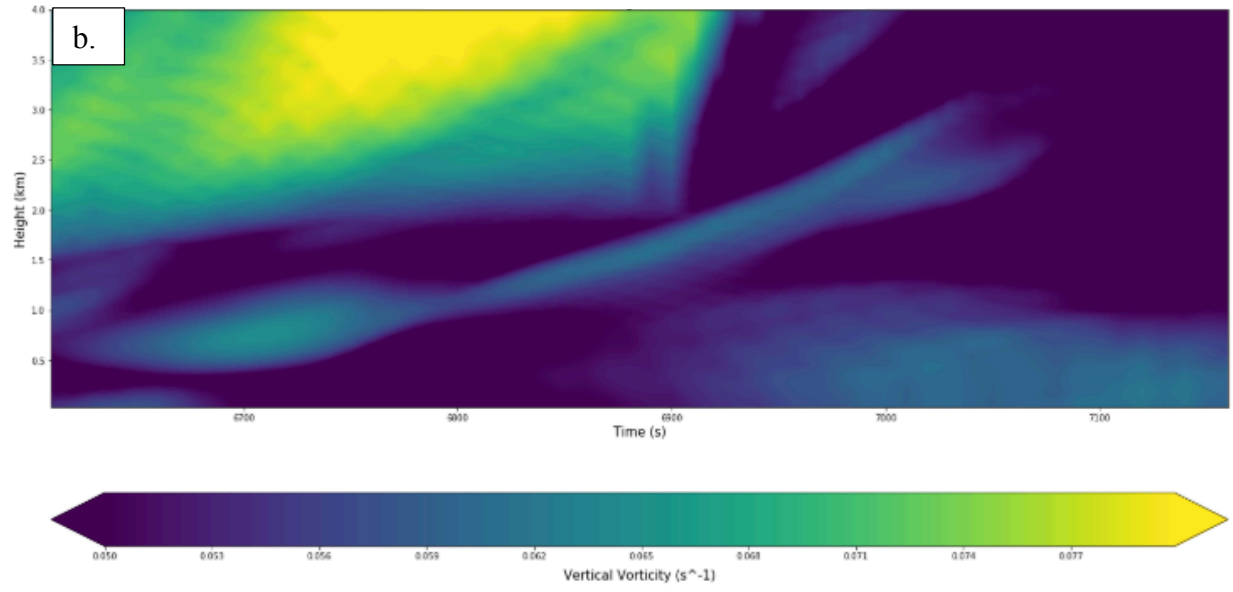

Figure 4.72: Time vs. height of rotational helicity and vertical vorticity in CM1-NOTOR. As in Fig. 4.67 but for CM1-NOTOR during development of an RFD "arch" vortex.

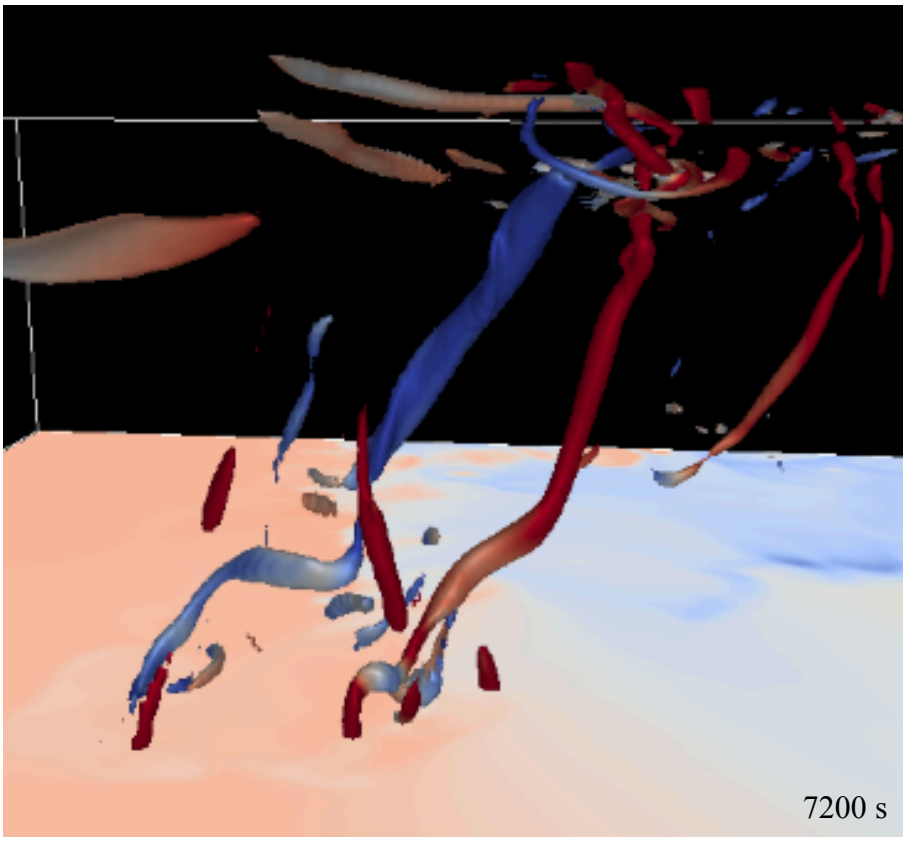

Figure 4.73: RFD arch in CM1-NOTOR. RFD "arch" vortex straddling the diffuse rear-flank outflow region of the CM1-NOTOR supercell at 7200 s. The isosurface is I^2 of 0.01 s^{-2} and is shaded by the vertical component of voriticity where blues are negative and reds are positive values. View is from the east.

The RFD-arching mechanism of surface-based vortex-genesis is inefficient and does not lead to TLV-genesis in the numerical simulations with the NMS presented in this dissertation. This appears to be primarily due to the lack of supporting helical rotational structures that provide a direct dynamical link with the rotation of the storm's updraft and transition the upper portion of the surface-based vortex from crosswise to progressively helical flow. This transition generates a vertical mass flux through the surface-based vortex prompting rapid, intense stretching because the vortex is dynamically "sealed" at the ground protecting the core low pressure as mass is removed from it. Without a helical interaction between inflow and outflow, a dynamic conduit between the surface-based vorticity field and rotating updraft allowing vertical mass-flux through the surface vertical vortex becomes substantially more difficult.

The author did find cases in which at least weak TLVs were apparently generated through this mechanism in sensitivity tests with the CM1, in which the wind profile associated with the tornadic VORTEX2 composite sounding was replaced with the nontornadic wind profile (Figs. 4.74, 4.75). In this simulation, a deep, vertically erect arch associated with the RFD region was sustained for more than 900 s of simulation time and supported surface pressure perturbations of -35 hPa. The author postulates that the free-slip lower boundary condition used in the CM1 simulations may have allowed such a non-helical (crosswise) rotational structure to persist at the lowest model level while being forced vertically by the overlying updraft and acquiring gust-front sheet vorticity in a *spindle-like* manner. It is possible that the theoretical concept of vortex-line arching and splicing proposed by Markowski and Richardson (2014) operates in such cases of weak RFD-generated TLVs. While these structures exist almost ubiquitously in supercell simulations with the NMS as they do in real-world supercells, the process by which vertical vortex generation occurs is far more chaotic compared to the methodical process found to occur

in TLV-genesis in the TOR-S and CM1-TOR simulations. In the author's modeling experience, the RFD-generated TLV process is rarely associated with significant TLVs.

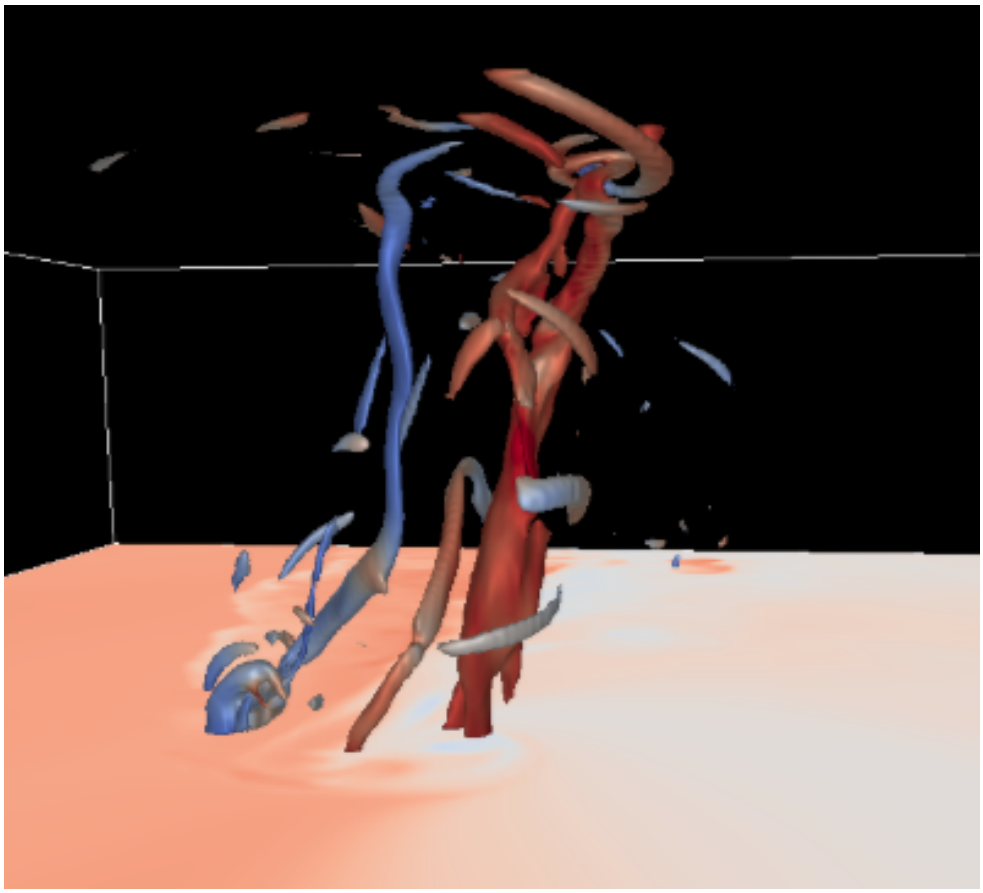

Figure 4.74: RFD-arch TLV in CM1 sensitivity experiment. As in Fig. 4.70 but for an RFD-arch that developed into a TLV in a tornadic thermodynamics and non-tornadic wind profile sensitivity experiment with the CM1.

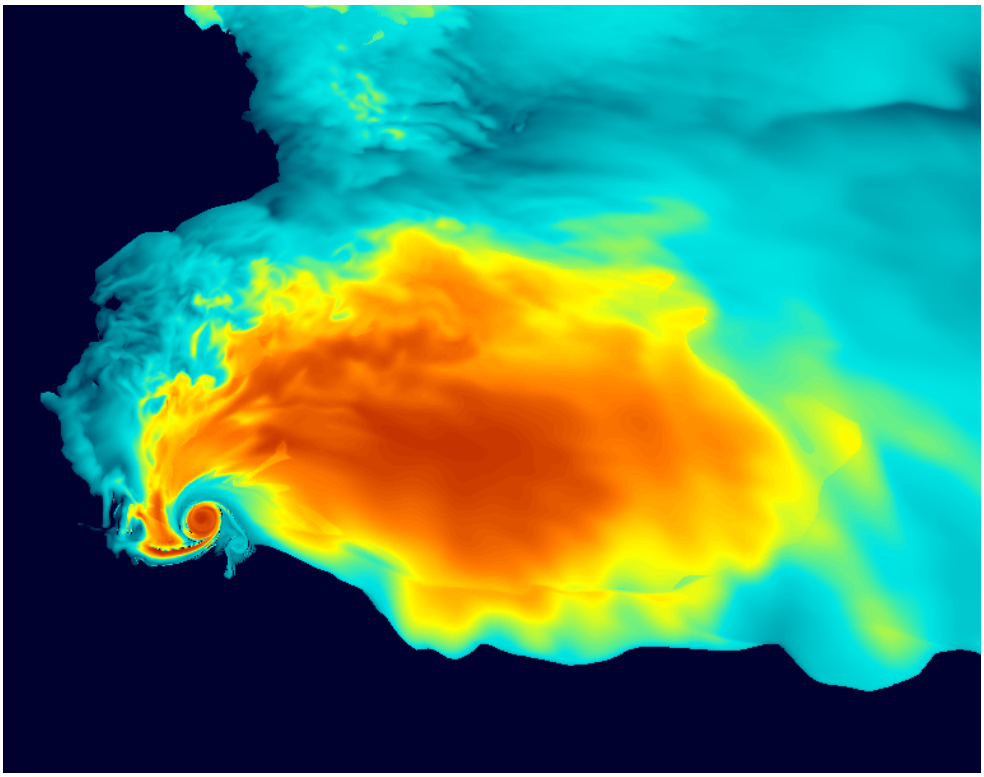

Figure 4.75: Model-derived surface reflectivity for tornadic phase of the CM1 sensitivity experiment described in-text. Figure from Kelton Halbert.

Part III. Comparisons with Weisman-Klemp idealized sounding

A popular idealized atmospheric sounding to study supercells using numerical models is the Weisman-Klemp (1982) sounding (herein, WK). Because this sounding has been used to successfully produce TLVs in simulated supercells with the NMS, a comparison with the TLV-producing storms in the VORTEX2 environment is readily made. To remain consistent with the VORTEX2 simulations present in the preceding sections, the WK sounding was used to initialize the NMS with identical model configuration to the VORTEX2 experiments and is analyzed with the same diagnostic approach in this section.

a. TLV-genesis

The precipitation and outflow structure of WK closely resembled other tornadic simulations presented in this chapter (Figs. 4.76 & 4.77). During its genesis phase, the WK supercell has a meridionally-oriented, skinny region of dense cold pool air in the left-flank outflow region, which was associated with ingestion of positively-buoyant, environmental air from the forward-flank on its approach to the low-level updraft (Fig. 4.78). This was associated with a north-south oriented rotational helicity maximum that developed along the convergence boundary in response to outflow surging and is clearly identifiable in the integral data in the 5000 – 5500 s period of WK (Fig. 4.79a). Similar to the TOR-S storm, a maximum in surface vertical vorticity was also noted during the same period (Fig. 4.79b). Findings from the VORTEX2 simulations suggested it was critical for helical rotation to be present over a deep layer of the lower-troposphere during TLV-genesis. In WK, rotational helicity was also found to intensify over a deeper layer at the time of surface-based vortex intensification (Fig. 4.80).

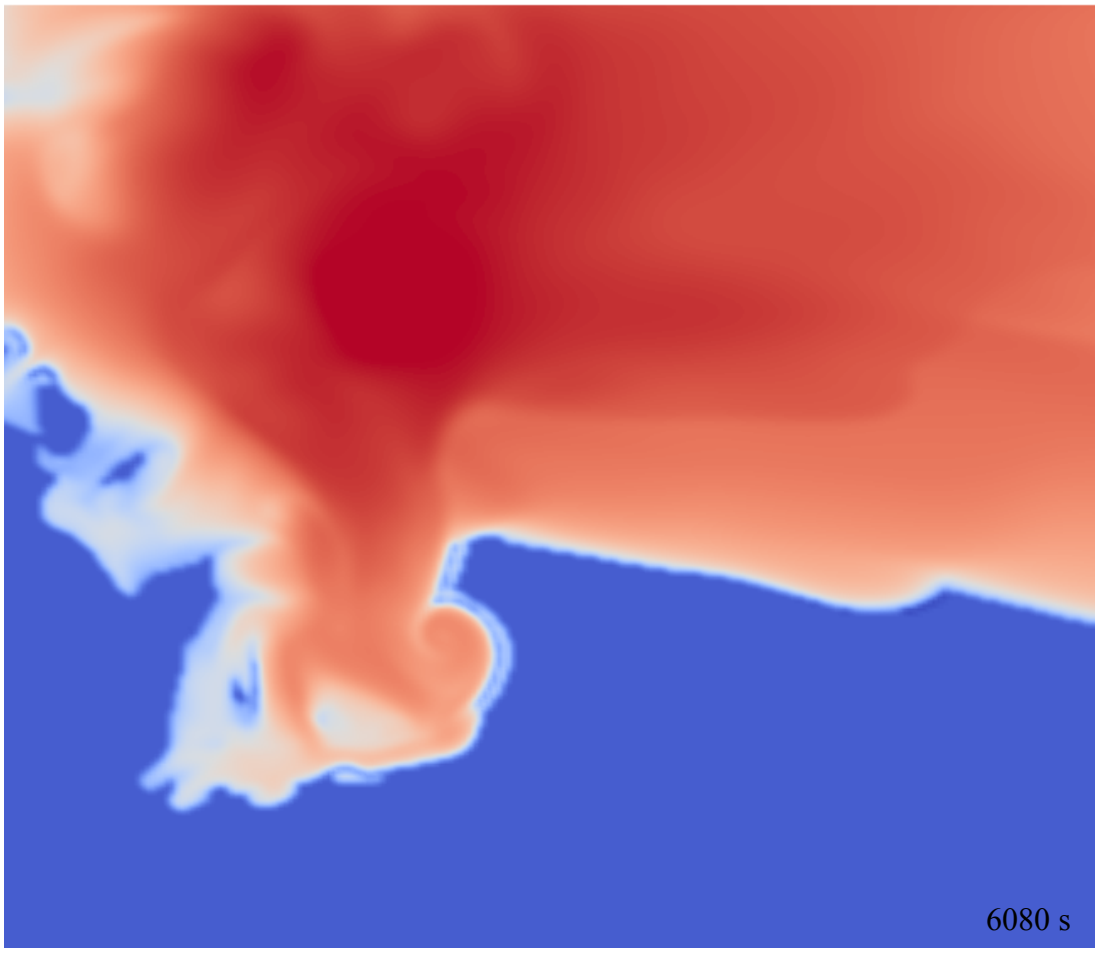

Figure 4.76: Surface condensate distribution during TLV-genesis of WK. As in Fig. 4.9 but for WK at 6080 s.

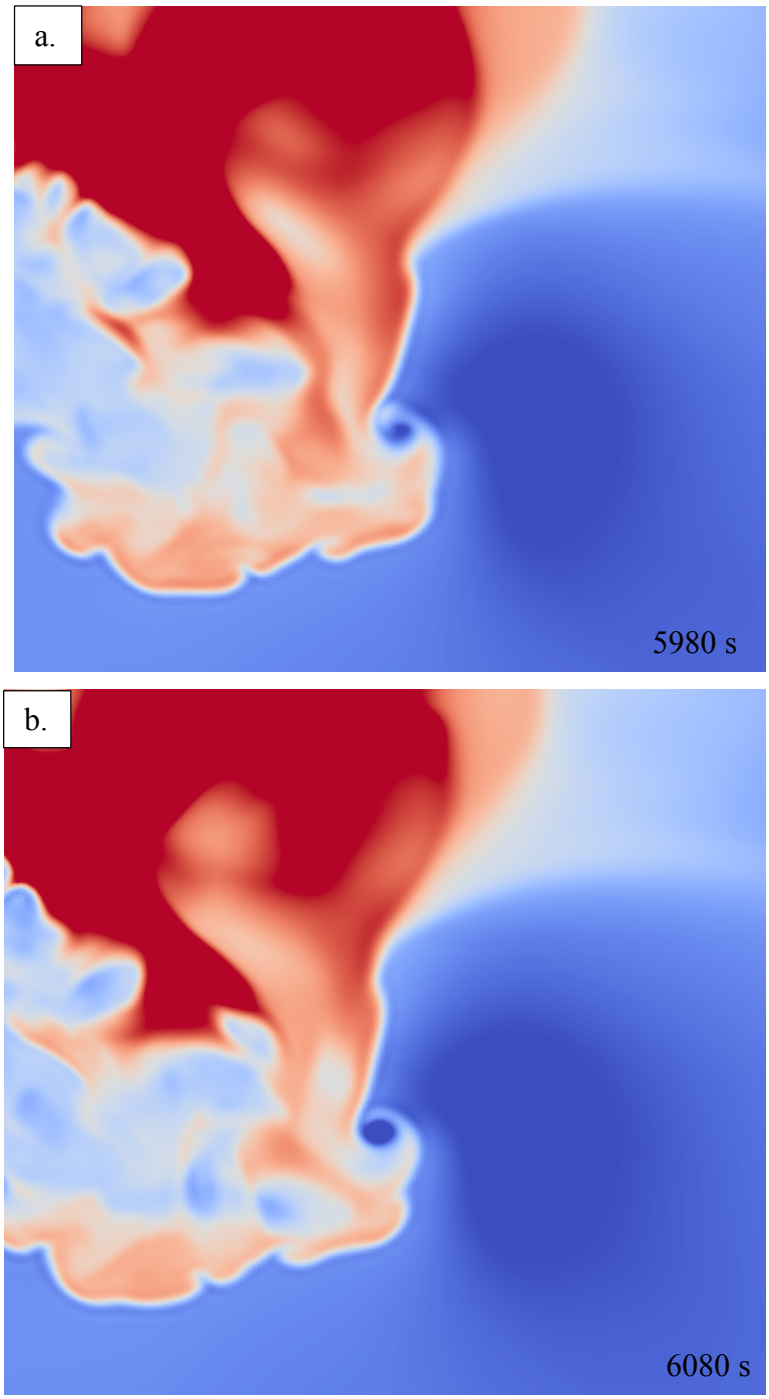

Figure 4.77: Evolution of surface perturbation density during TLV-genesis of WK. As in Fig. 4.9 but for WK at 5980 s (a) and 6080 s (b) showing entrainment and progression of environmental air in the outflow region.

A qualitatively similar dynamic process leads to initial surface-based vertical vortex development during this period but appears to fail to fully couple with the surface and weakens quickly before a rapid intensification ensues just before 6000 s (Fig. 4.80). The initial weakening of the surface-based vortex appears to result from a slightly elevated helical structure (not evident below 200 m; Fig. 4.80a) and weaker vorticity in the immediate above ground layer (Fig. 4.80b). During reintensification and TLV-success, substantial helical flow develops downward toward the surface and is associated with reinvigorated upward vertical growth of vorticity from the surface. Through this analysis, the author hypothesizes that the vertical vorticity production mechanism was not yet associated with a robust baroclinic boundary that could sustain surface-based production during intense vertical stretching associated with it's the first attempt at 5000 s. I^2 also demonstrated a lack of coherency in the lowest layers of the initial vortex and was not associated with a substantial low-level pressure perturbation (Fig. 4.81).

During the successful TLV period, a similar structural evolution of rotational helicity and vertical vorticity to TOR-S can be seen (Fig. 4.82). A local maximum of horizontal helical rotation approaches the updraft from the north in the lowest 500 m AGL, associated with which, surface-based vertical vorticity develops on its immediate left edge (looking in the direction of propagation toward the updraft; Fig. 4.82a) and rapidly intensifies upwards in the following 100 s (Fig. 4.82b). A short while thereafter, this upward-developing vertical vortex merges with the pre-existing surface-based circulation and acquires significant helical rotation extending to the lowest model level (Fig. 4.81c). As the TLV continues to intensify, the low-level, horizontal, helical structure wraps cyclonically around it at low levels (Fig. 4.81d).

All tornadic (TLV-producing) storms analyzed during this dissertation research were characterized by significant helical flow initially elevated from the surface in their forward-flank

inflow regions during their TLV-genesis periods. This helical flow appeared to be effectively inactive from a TLV-genesis standpoint until outflow-driven helical flow develops in the lowest 500 m and interacts with it this separate maximum from below. As a result of the elevated nature of the inflow-associated helical structure, it does not readily support surface-based vertical vortex generation. Furthermore, the helical flow in this region is generally characterized by weak density contrasts across it, rendering the surface-based vorticity production extremely weak directly under the updraft. This is not the case for *baroclinic* outflow-generated helical flow development at very low elevations that was shown to be associated with TLV-success cases. While helical flow in the forward-flank inflow is consistently present through much of the CM1 and NMS tornadic supercells, the left-flank boundary possesses significant helical flow more transiently during the storm's lifecycle. Crucially, however, when the helical flow develops in this region it is in direct contact with the surface layer and supports substantial baroclinic vorticity generation (see section 5.1.2). During TLV-genesis, the left-flank boundary consistently demonstrates a robust helical flow maximum just on the cool side of the baroclinic boundary with the forward-flank inflow. Helical flow first intensifies in this region at very low-levels before intensifying upward in time and subsequently interacting with the storm's buoyant updraft above. This upwards intensification is ubiquitously *followed* (in rapid succession) by explosive upward growth of vertical vorticity from the surface.

Analysis of helical flow evolution in tornadic and nontornadic storms with the new rotational helicity diagnostic illuminated the primary role of a low-level helical structures that appear to be qualitatively similar to the SVC first identified by Orf et al. (2017). In section 5.1.2, the WK sounding will be returned to with results from additional simulations and compared with

analysis of the Orf et al. (2017) storm to provide supporting evidence for the conceptual model of supercell tornadogenesis presented in the following section.

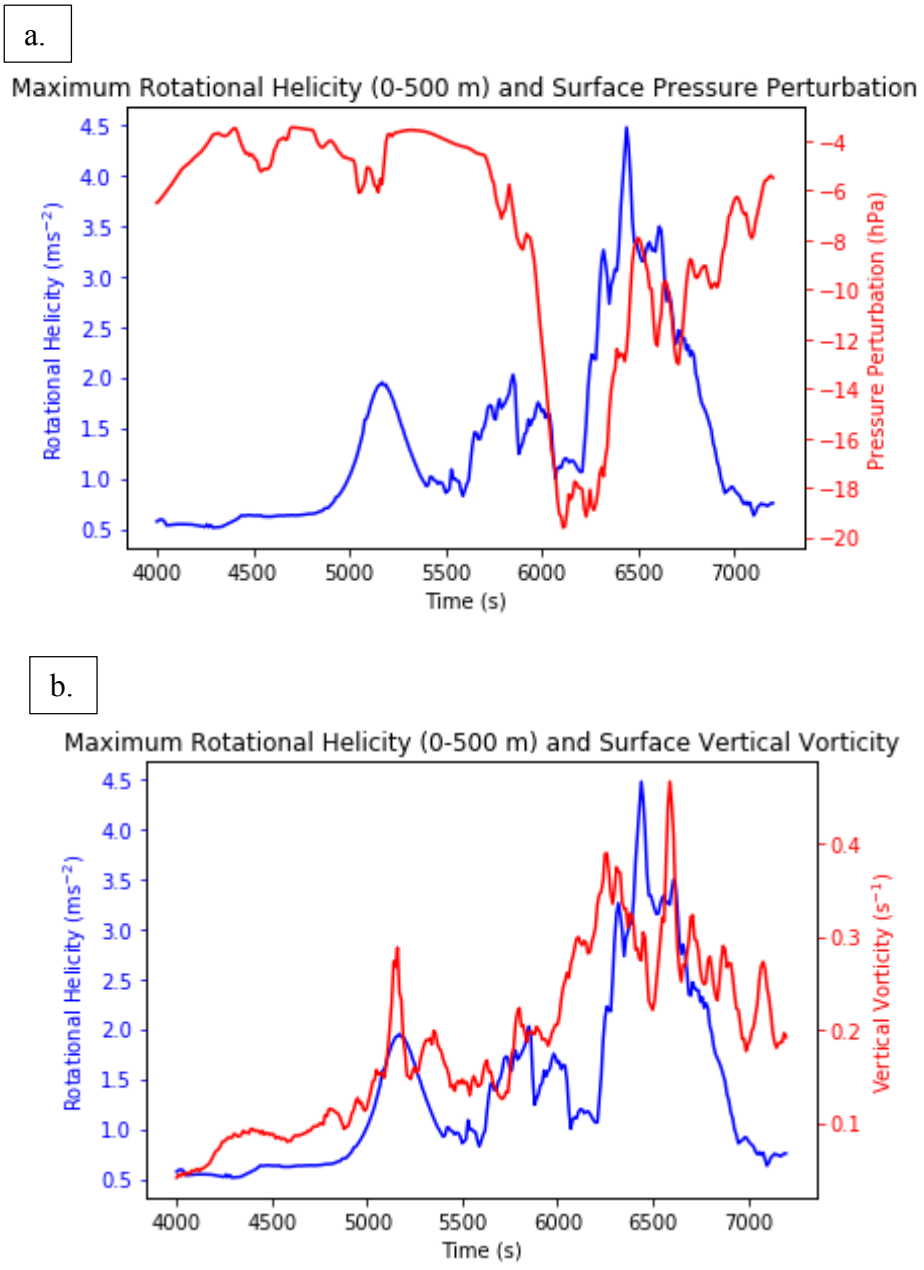

Figure 4.78: Rotational helicity, surface pressure perturbation and vertical vorticity evolution in WK during TLV-genesis. As in Fig. 4.60 (a) and 4.60 (b) but for WK during its TLV genesis phase.

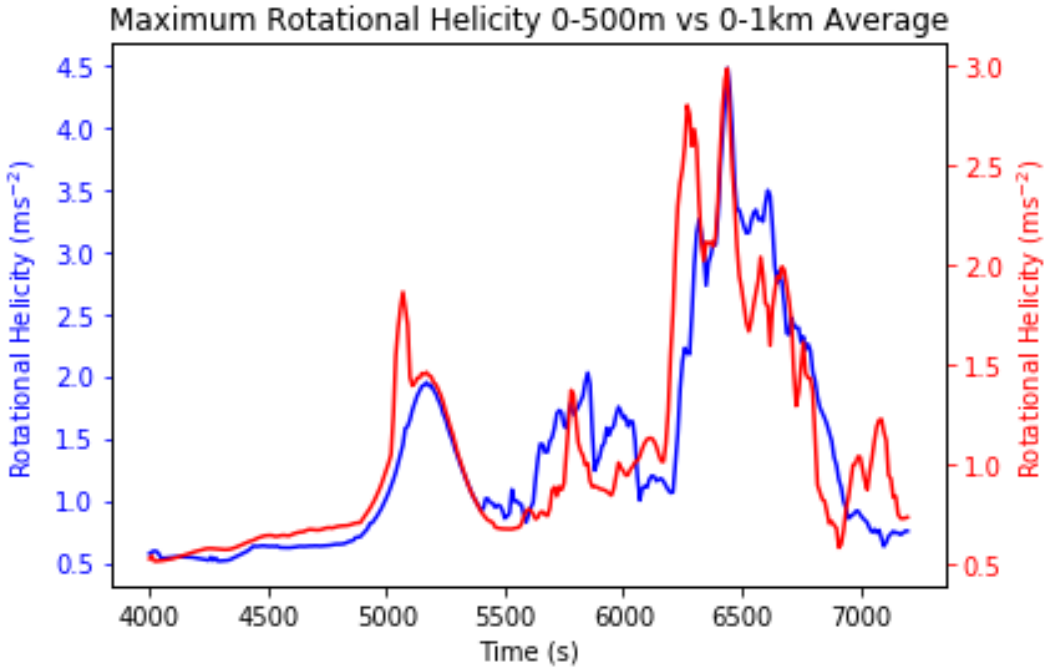

Figure 4.79: A comparison of maximum rotational helicity in the 0-500 m and 0-1 km AGL layers for WK during its TLV genesis phase.

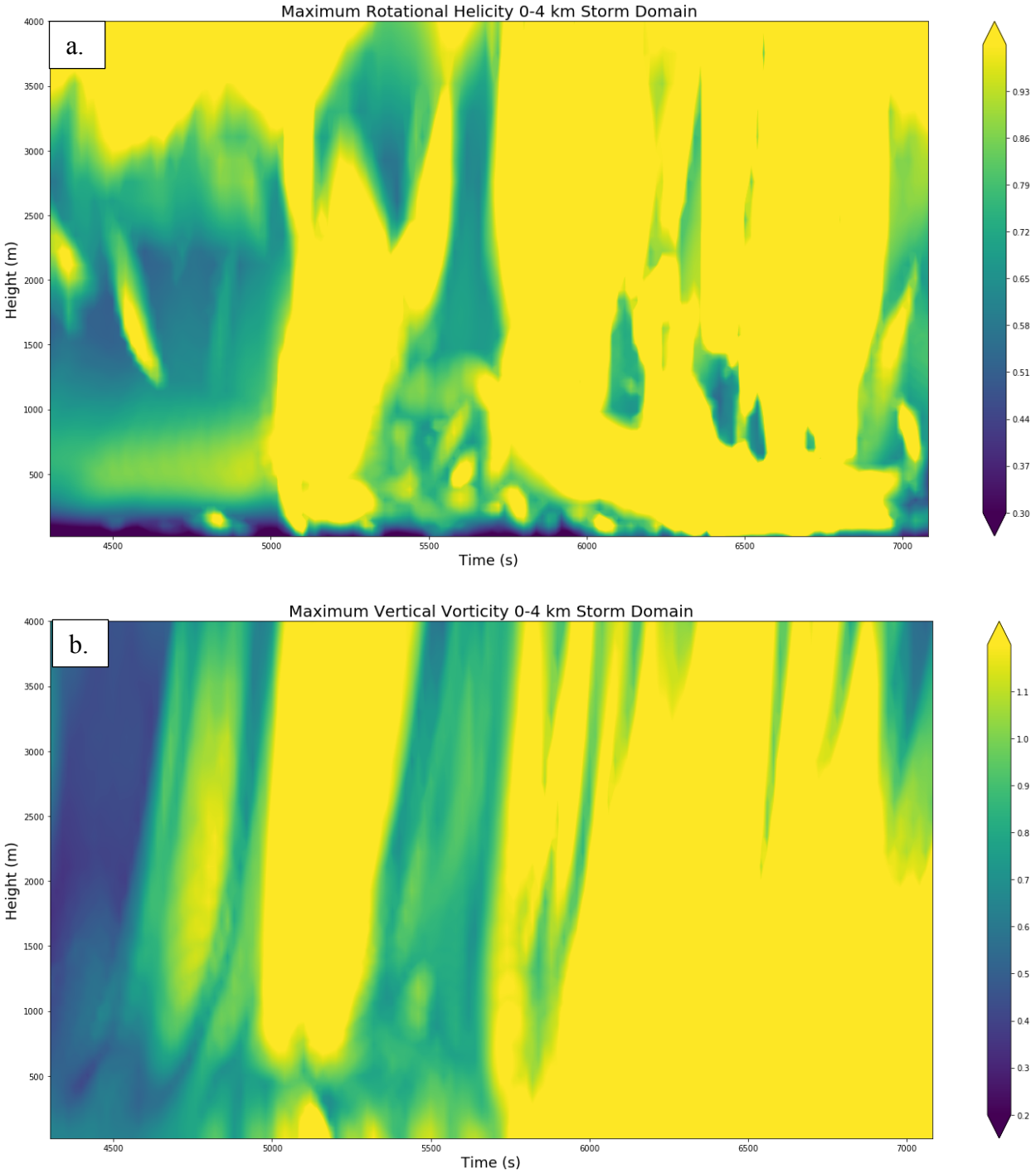

Figure 4.80: Time vs. height evolution of rotational vorticity and vertical vorticity during TLV-genesis in WK. As in Fig. 4.23 (a) and Fig. 4.27 (b) but for WK during TLV-genesis phase.

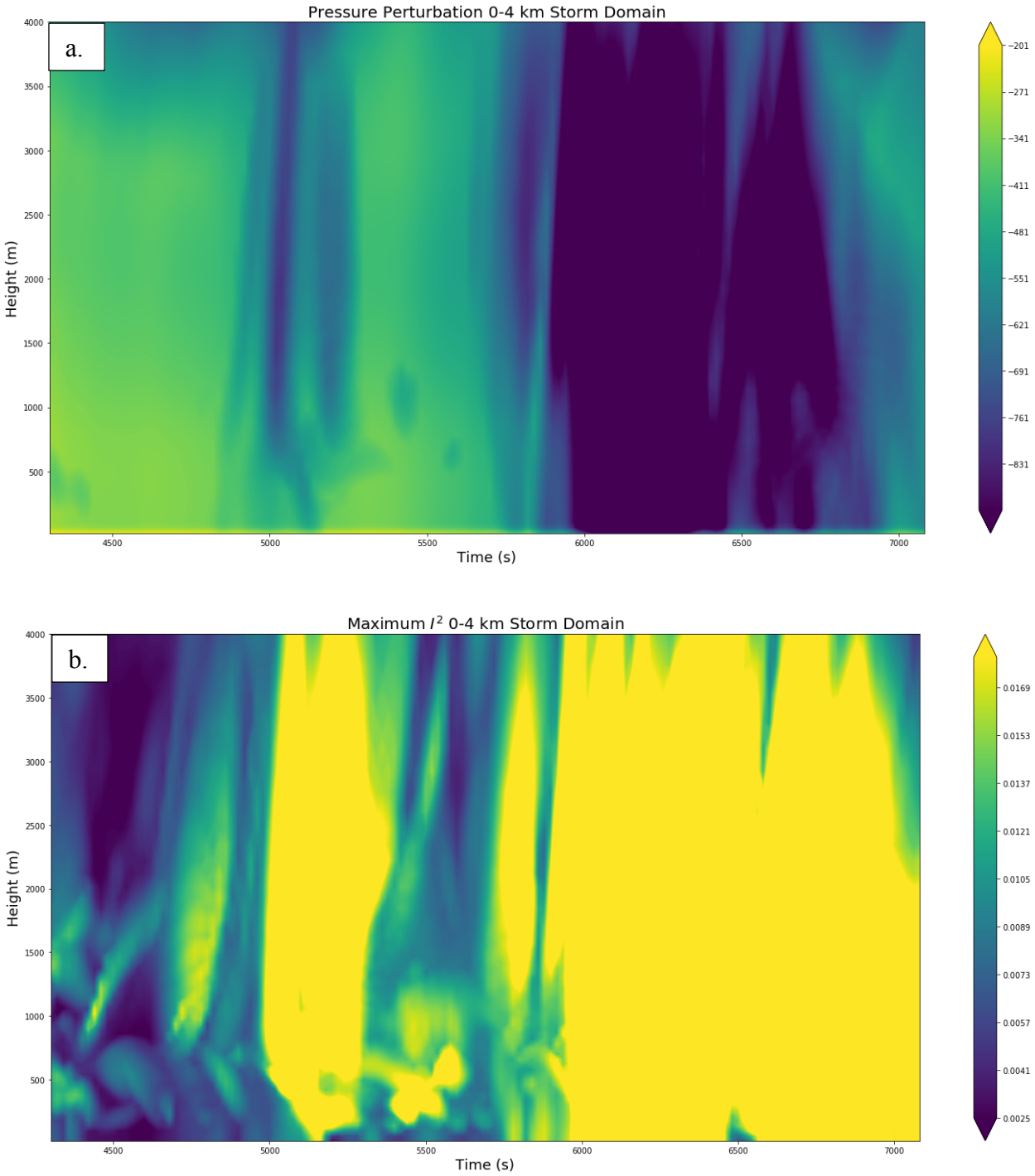

Figure 4.81: Time vs. height evolution of pressure perturbation and I^2 during TLV-genesis of WK. As in Fig. 4.60 (a) and Fig. 4.60 (b) but for WK during genesis phase.

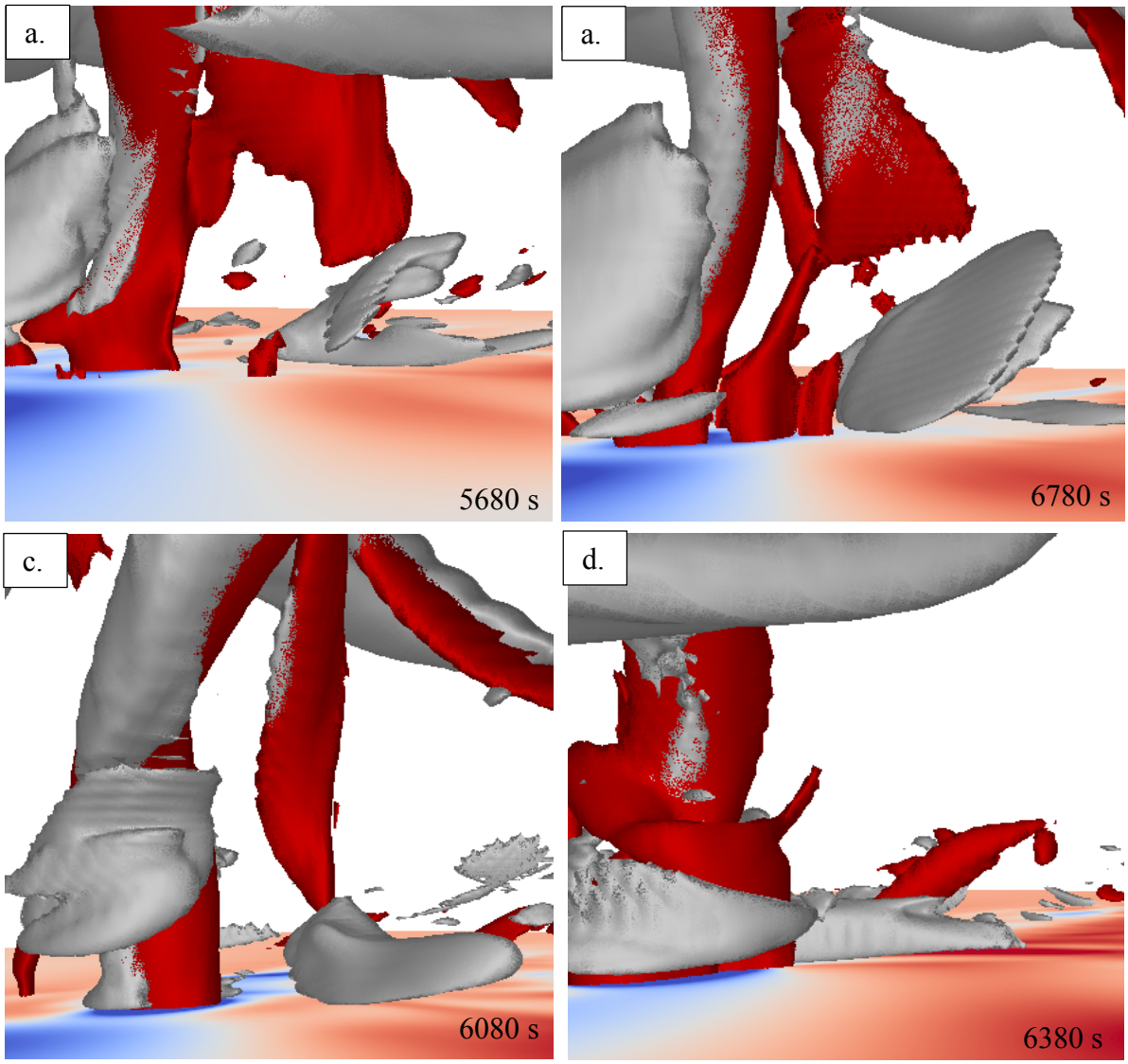

Figure 4.82: Three-dimensional evolution of rotational helicity and vertical vorticity during TLV-genesis of WK. As in Fig. 4.60 but for WK during genesis (a,b; 5680 s and 5780 s respectively) and maintenenance (c,d; 6080 s and 6380 s respectively) as the vertical vortex becomes progressively more helical.

Chapter Five: Synthesis and future direction

In chapter four, traditional vorticity analysis was combined with new diagnostics developed from fundamental theory of fluid rotation to study evolution of rotational structures in numerous numerical model simulations of supercells in tornadic and nontornadic supercell environments. The new theoretical approach illuminated what appeared to be a critical interaction between low-level helical inflow in a supercell's forward-flank region and near-surface helical rotation along density-gradient interfaces to the north of the storm's updraft. The results presented herein were analyzed in the context of fluid dynamics theory presented in chapter three, which prompts a new conceptual model of supercell tornadogenesis presented in section 1.1 of this chapter. This model is then applied to understand development of rotation in extremely high-resolution data of a violently-tornadic supercell simulated in the CM1 by Orf et al. (2017) in section 1.2. Synthesis and discussion of the results and implications of the conceptual model are provided in part two of this chapter, followed by the author's ongoing and future research direction in part three.

Part I. Conceptual model of supercell tornadogenesis

5.1.1 Model

a. Theoretical discussion of a helical coupling process

Through application of a new parameter; rotational helicity, it was demonstrated that helical flow first developed within the lowest 500 m AGL along what is commonly referred to as the supercell's left-flank convergence boundary. Combining theoretical fluid dynamics and recent advancements in our understanding of low-level vorticity generation in the mesoscale atmospheric sciences literature, it is determined that this likely occurs through a conversion of *crosswise*-oriented baroclinically-generated vorticity to *streamwise* vorticity as horizontal flow acceleration occurs toward the incipient updraft during its approach from the north. As the helical flow intensifies along the baroclinic boundary, low-level streamwise vorticity associated with the environmental low-level shear, interacts with this structure. Given the helical nature of both the low-level inflow and outflow-generated vortex structure, the author theorizes that this interaction occurs in a helical *coiling* manner as described in fluid dynamics theory discussed in chapter three. The interaction appears to be initially driven by dynamic accelerations just on the cool (internal) edge of the left-flank convergence boundary as a low-level helical structure intensifies and generates intense near surface divergence, which begins to dynamically-drive environmental air down around it.

As streamwise vortex lines associated with the low-level inflow are dynamically forced to descend around the baroclinic structure, they are able to interact with the streamwise vortex lines of the baroclinic vortex. This rotational structure can then be thought of as *coupled*, dynamically connecting the environmental vorticity to the baroclinic, surface-based vorticity of

the outflow. The significance of this is a portion of the air parcel trajectories winding helically toward the upward along the baroclinic boundary are associated with low-level environmental air and are positively buoyant. As the air-parcels approach the low-level mesocyclone and updraft, the sign of the vertical dynamic pressure forcing changes from downward-directed to upward-directed, causing positively buoyant inflow parcels to erupt upwards into the updraft. Once this occurs, the storm's buoyantly-driven updraft aloft and vorticity is effectively connected to the surface-based vorticity-generation regions of the outflow through the coupled-helical structure. Explosive upward growth of vertical vorticity appears to occur in response along the periphery of the baroclinic structure from the surface.

In the author's investigation of the fluid dynamics literature, a number of theoretical works resonated with the supercell dynamics discussed in this dissertation. Perhaps none more so, however, than a paper describing three-dimensional vortex structure and flow topology by Dallmann (1988). Simple conceptual illustrations of fluid motion and vortex structures presented by Dallmann are extremely useful for visualizing the evolution of three-dimensional vortical flow. One such diagram that is particularly relevant to the current investigation of helical rotation in supercells depicts a region of flow separation in initially laminar boundary layer flow (Fig. 5.1). This figure conceptually illustrates the vortex structure resulting from a shock interaction of an initially laminar boundary layer as described in section 3.3.2a. Through the application of the new rotational helicity parameter in the author's study of rotation in supercells, an important connection between the flow structures in the boundary layer experiments of Dallmann and the numerical supercell simulations presented herein can be inferred.

In Fig. 5.1, a vortex sheet is depicted along the edge of the separated boundary layer flow such as occurs along the periphery of a surging baroclinic outflow region of a supercell. At its

upper periphery, it "rolls-up" into a coherent vortex structure (depicted with the tubes in Fig. 5.1). Resulting from downstream acceleration, a portion of this flow becomes helical (streamwise) in the elevated "head" region of the vortex roll structure. A portion of the vortex lines then separate and reconnects to the surface on the cyclonic side of the head of the surge. A separate vortex line that is coiling helically around the first described, separates toward the downstream edge of the surge and propagates out of the opposing plane remaining elevated from the surface.

Using the results presented in this dissertation as a theoretical basis, this concept is extrapolated to a supercell outflow region in which a horizontal baroclinic vortex structure becomes progressively helical and dynamically forces an interaction with the low-level environmental inflow. If the low-level shear of the inflowing air from the forward-flank side of a supercell is characterized by sufficient streamwise vorticity, a helical coiling of vortex lines between the *negatively* buoyant, baroclinic outflow vorticity and *positively* buoyant, environmental vorticity associated with low-level wind shear can occur. The orientation of the baroclinic vortex and, therefore, the convergence boundary with which it is associated, appears to be critical in determining the quality of this interaction. It can be theoretically reasoned that this is due to the period with which the low-level flow is subject to the dynamic forcing on the cool side of the boundary during its approach to the updraft and the degree to which the low-level inflow is forced to interact with the baroclinic structure. If this interaction is sustained, low-level streamwise vorticity of the environment can theoretically undergo a helical coiling mechanism with the baroclinic structure during its approach to the incipient updraft. If an intense and persistent low-level mesocyclone is present, the dynamic lifting of air in this region combined with increasing low-level convergence at its base, will cause the positively-buoyant

environmental flow to suddenly erupt upwards from the near-surface layer, where it was effectively held "dynamically captive" by the accelerations associated with the horizontal rotation until this point. During its approach, the helical structure forces continued surface-based vertical vorticity development along its immediate warm edge by violently tilting baroclinic vorticity produced along flow trajectories that descend along its cool side into the vertical on its leading and warm edge. While these baroclinc vortex lines, through the process of flow separation and reconnection discussed in section 3.3.2, terminate at the surface along the left edge of the boundary, the vortex lines associated with the low-level inflow are rapidly stretched vertically into the buoyant updraft aloft during their upwards ascent, akin to releasing a coiled spring. Through the deep, helically coupled rotational structure, the intense vertical acceleration produced by buoyancy aloft can almost instantaneously be communicated to the surface, causing explosive upward vertical vortex growth of the baroclinic vorticity on the warm edge of the low-level helical structure. Because these vortex lines effectively terminate at the ground a pressure adjustment rapidly occurs on the compressible timescale and a cyclostrophic balance develops. Vertical mass flux through the upper portion of the coupled structure leads to rapid surface pressure falls because the cyclostrophic balance extending to the surface provides a quasi-sealed region from which mass can rapidly be removed. The result is tornado development occurring on the misoscale at the surface first and erupting vertically-upward. A general conceptual diagram of this proposed mechanism of supercell tornadogenesis is given in Fig. 5.2.

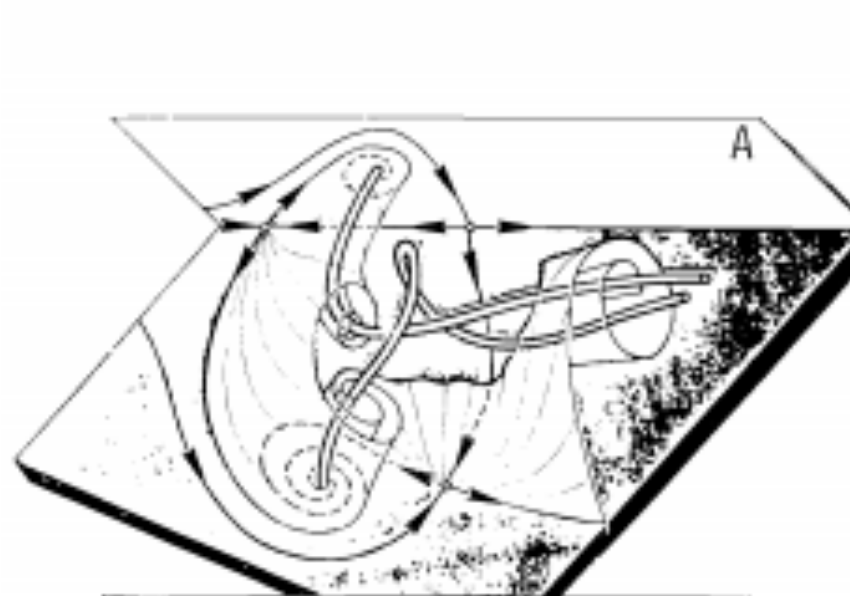

Figure 5.1: Diagram of flow topology and vortex structure associated with flow separation in an unsteady boundary layer. Transparent surface is a crosswise vortex sheet that terminates at the surface and rolls up at its upper end where it is associated with helical vortex tubes (white cylinders). One vortex tube becomes vertically oriented and associated with cyclonic, surface-based rotation on the structures left edge, while the other vortex tube remains elevated from the surface and is shown to bend out to the right through the vertical plane denoted with an 'A'. Adapted from Dallmann (1988).

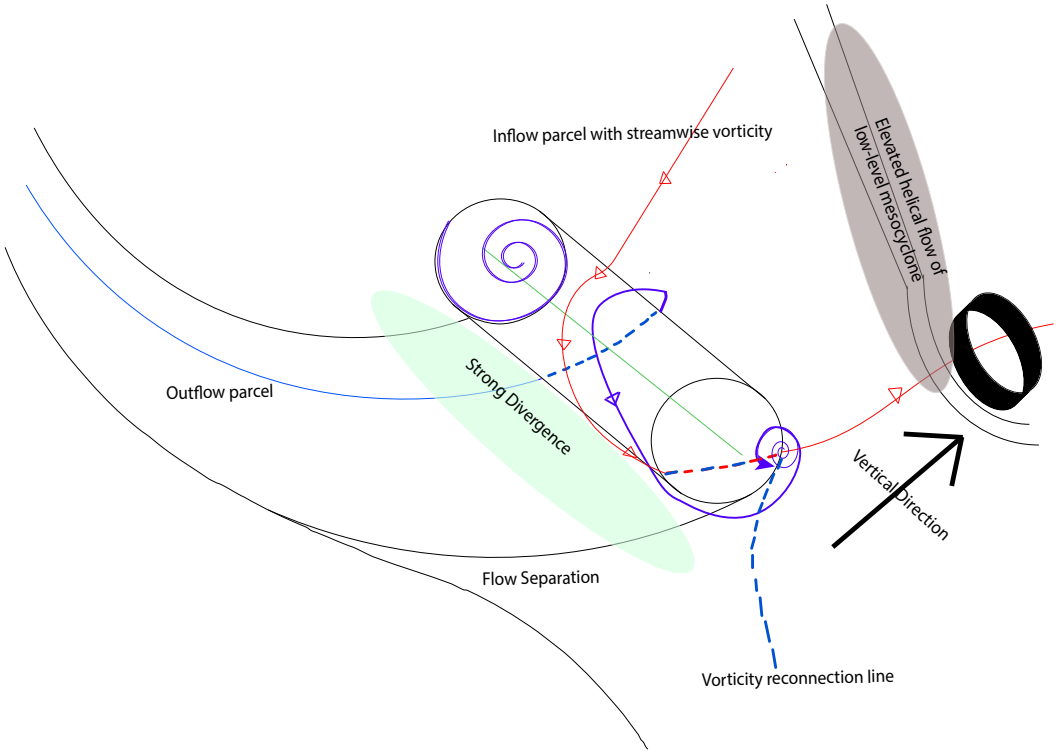

Figure 5.2: Idealized conceptual model of supercell tornadogenesis from tornadic numerical simulations by the author. Blue line is outflow parcel path, red line is inflow parcel path, red and blue dashed line represents a coupled vortex line associated with the inflow and outflow-originating vortex lines and green shaded region indicates dynamically-driven near-surface divergence. Black arrow indicates vertical plane and black circle represents the low-level mesocyclone and updraft. Black cylinder denotes the crosswise roll on edge of downdraft and green line at its center represents the streamwise component of vorticity.

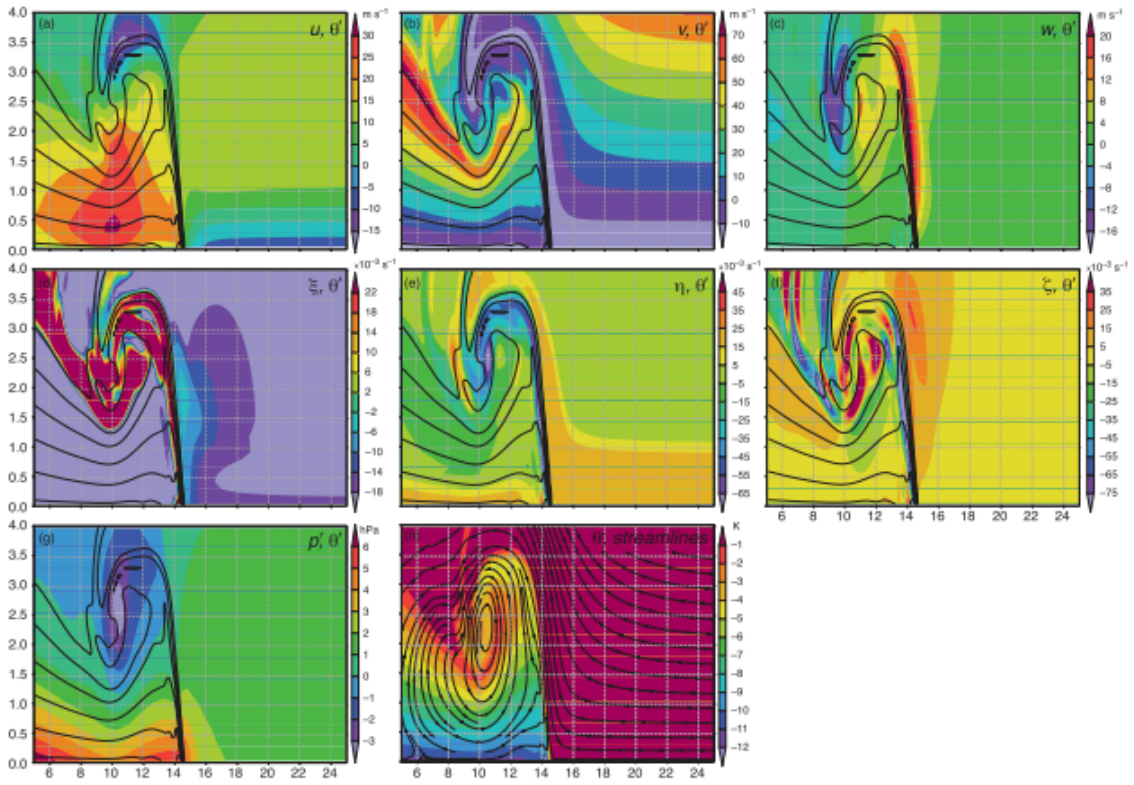

Figure 5.3: Idealized outflow simulations with the CM1 demonstrating surface-based vertical vorticity is not generated through intense tilting of ambient wind shear from Davies-Jones and Markowski (2013). Plane is a vertical cross section through the edge of the density current. Streamlines are black lines; color shading is labeled in top-right corner of each panel. Figure reproduced with permission from Journal of the Atmospheric Sciences.

b. Consistencies with current literature

This theoretical conceptual model of supercell tornadogenesis is consistent with much of the existing literature of supercell dynamics. It is well understood that tornadoes are favored in environments characterized by predominantly streamwise vorticity in the lower troposphere (e.g. Coffer et al. 2017). This is consistent with the requirement for streamwise vorticity to interact with a baroclinic helical structure generated along the periphery of the supercell's cold pool in the proposed model. Additionally, it is consistent with the observations that significantly negatively buoyant supercell outflow is unfavorable for tornadogenesis (e.g. Markwoski, 2002). If the outflow is too dense relative to its surrounding environment, penetration of the ambient air into the cold pool will not occur as readily through the rotationally-driven divergence mechanism proposed by this theory, which is necessary for the helical coupling process to take place. Therefore, the theory is also consistent with observation that tornadic supercells are favored in environments with low LCLs and significant boundary layer moisture (e.g. Thompson et al. 2012).

Another significant consistency with current understanding but which contributes additional dynamical explanation is the requirement for near-neutrally stratified boundary layers in the vicinity of supercells for significant tornadogenesis (e.g. Parker, 2015). Current literature suggests that the importance of weak or neutral stability in a tornadic supercell's boundary layer arises from the requirement for upward-directed, *dynamic* accelerations of low-level vorticity-rich air to intensify through stretching because buoyancy cannot directly supply this vertical acceleration in the near-surface layer. If there is significant static stability, air parcel displacement via dynamic effects are reduced. This is also an important component of the author's proposed mechanism because it enables a deep coupled helical interaction to occur

between the helical inflow and outflow air for both the downward-directed and upward-directed dynamic acceleration of low-level air-parcels. However, another critical aspect of the model that relies on weak low-level stratification is the ability for the air to begin to rotate about the horizontal axis. This will not occur without near-neutral stability, without which a robust horizontal helical structure will not evolve on the cool side of the convergence boundary by the theoretical baroclinic conversion mechanism proposed. This may also help explain why, in the author's modeling experience, these structures are generally associated with air that has a very high saturation point (low condensation level). Regions of high saturation point can locally reduce the stability and allow horizontal rotation to evolve.

Furthermore, it has recently been found that tornado-initiating (or at least tornadogenesis-*associated*) momentum surges are more likely to be forced dynamically by downward-directed vertical perturbation pressure gradient forces (e.g. Skinner et al. 2014; 2016). A number of studies have concluded that this results from intensification of rotation at the ground leading to a local perturbation low pressure that initiates a downdraft. While the theoretical model proposed here is consistent with the result that tornado-initiating outflow surging is likely to be at least partly dynamically driven, the manner in which it occurs differs to current literature. To the author's best knowledge, the theory that the dynamically-induced momentum surges result from intensifying horizontal rotation on the periphery of a cold pool has not been used to explain these surges. Additionally, the initial momentum surge that drives the development of the horizontal streamwise vortex structure responsible for the generation of the horizontal baroclinic structure is almost certainly driven by negative buoyancy or an intense core of precipitation (DRC) that ia able to generate the intensity of near-surface divergence and convergence necessary for such a structure to evolve. In the author's modeling experience with the NMS, these surges are

ubiquitously associated with intense descending cores of precipitation, which is consistent with observations demonstrating the presence of descending reflectivity cores (DRCs) prior to tornadogenesis (e.g. Byko et al. 2007; Markowski et al. 2018).

Finally, the model is consistent with the ever-growing body of literature that finds baroclinic generation of vorticity to be the dominant mechanism of vertical vorticity production associated with low-level rotation in supercells (e.g. Kosiba et al. 2013; Dahl et al. 2014; Dahl et al. 2015). Air parcels descending through the downdraft of the initial momentum surge along buoyancy gradients will tend to acquire non-zero baroclinic vorticity. In the traditional baroclinic mechanism, an air parcel is considered along a cyclonically curving trajectory that descends relatively steadily around the low-level updraft (e.g. Dahl, 2015). However, in the mechanism proposed in this dissertation, while the trajectories steadily descend in the region behind the baroclinc helical structure, they are forced violently downwards and then upwards in the immediate vicinity of the horizontal rotation and so the baroclinic mechanism and "riverbend effect" (e.g. Brooks et al. 1993) ensues with more intensity in the idealized mechanism presented by Dahl (2015). In the new model, tilting of the baroclinic vorticity into the vertical occurs via intense differential horizontal divergence and convergence across the helical structure in a similar fashion to the barotropic effect described in the baroclinic mechanism. Interestingly, Klemp and Rottuno (1983) captured the essence of the model, albeit without much needed additional detail, several decades ago: "Strong horizontal vorticity, contained within the environmental shear and generated along horizontal buoyancy gradients, is tilted into the vertical and then greatly converged as it approaches the low-level center of circulation."

c. Departures from current literature

The theory proposed in this dissertation may explain why it is possible to simulate realistic tornado-like vortices with a free-slip lower boundary condition, which has been the subject of recent debate. In traditional models of supercell tornadogensis (e.g. Trapp and Davies-Jones, 1997; Davies-Jones, 2015), which revolve around contracting rotation on the mesocyclonic scale to the tornado scale through a deep layer of convergence, friction is required to intensify the convergence near the surface leading to an "overshoot" of cyclostrophic balance associated with inward-spiraling air parcels (see Davies-Jones, 2015). In the proposed model, however, surface friction is not required to generate the convergence necessary for development of a surface-based vertical vortex. Rather, a deep, dynamically coupled rotational structure develops surface-based rotation on the smallest scales *first* through unstable roll-up of vertically oriented, baroclinically-generated vorticity initially in the form of a sheet along the warm edge of a supercell's internal convergence boundary. While this process effectively begins on the microscale in a physical atmosphere, in numerical model simulations it will occur at the scale at which the grid resolution permits.

Tornadogenesis has been known to be associated with outflow momentum surging or more generally with downdrafts for a number of years (e.g. Davies-Jones, 2008; Markowski et al. 2012*a,b*). Numerous theories have evolved in order to explain this, most of which include the transport or generation of low-level vorticity by the surge and subsequent upward connection with the updraft. The mechanism by which the low-level vorticity becomes associated with the mid-level rotation of a supercell is through an "arching" and "splicing" mechanism (see section 2.2.2). Opposed to the vortex line arching and splicing theory discussed in Markowski and Richardson (2014*a*), the theory proposed herein involves a *helical dynamic coupling* between

horizontally-oriented vortex lines associated with a supercell's inflow and those associated with its baroclinic outflow. This first occurs at very low levels along density current peripheries as inflow trajectories are forced down around the baroclinic vortex structure and in doing so, curve and parallel the boundary on their approach to the low-level updraft. During this process, the low-level inflow interacts with the baroclinic boundary in a helical manner due to the conversion of initially *crosswise* baroclinic vorticity to *streamwise* vorticity in the baroclinic head of the outflow periphery due to downstream-acceleration toward the updraft. Therefore, helical rotation develops first through baroclinic generation and horizontal momentum surging and subsequently intensifies upwards as it interacts with streamwise vorticity associated with inflow trajectories. This mechanism does not require a "splicing" of vortex lines but rather a helical coiling of vortex lines. However, the author does note that the vortex lines associated with the surface-based baroclinic vorticity may well "splice" or *reconnect* with those of the environment through intense deformation as the coupled structure is subject to intense buoyancy acceleration in the storm's updraft. The reconnection of vortex lines in this manner helps explain how vortex lines initially forming closed loops can reconnect to the surface at the lower boundary and to the helical rotation at their upper portions.

5.1.2 Supporting evidence: Weisman-Klemp sounding

Previous NMS simulations with the WK sounding provide supporting numerical evidence for the new theory proposed in the previous section. Trajectory analysis was performed during TLV-genesis in a region characterized by a similar horizontal helical structure that also appeared to be involved in genesis of a TLV in one of these previous numerical simulations with the WK sounding (see Fig. 5.6 for three-dimensional rendering of the structure). Several source regions for air participating in evolution of the horizontal rotational structure were identified (Fig. 5.4). Air originating to the south of the updraft at approximately 3 km AGL took a path cyclonically around the updraft and descended in the left-flank region during a significant surge event that was associated with the initial formation of the low-level horizontal rotation. This surge generated a qualitatively similar *helical* structure those presented in chapter four along its density interface with the low-level environmental air. During this time, inflow parcels to the east of the updraft, initially at approximately 1 km AGL, lift on their approach toward the structure and then sharply descend on its cool side and turn southwards toward the low-level updraft. These parcels ascend more readily than the green parcels, which have origins in the outflow region. While the trajectories originating to the south of the updraft at mid-levels surge outward to form the RFGF, the parcels from the low-level inflow region and outflow region both ascend through the updraft. The air parcels originating in the inflow region wind helically upward through the updraft as may be expected with the helical portion of the structure. The outflow parcels ascend in a relatively straight path indicative of parcels associated with a developing TLV. A top down view provides some perspective on how these air streams are brought together in this region during TLV genesis (Fig. 5.5).

Vorticity tendency analysis was performed on a separate set of trajectories that best ended up in the developing TLV (Fig. 5.6). It was found that these trajectories generally approached the helical structure from the cool side to its north-west and first descended before being turned abruptly upward on its warm side. This is evident between 300 and 400 s through the trajectory integration where the characteristic parcel temporarily acquires negative vertical vorticity before becoming quickly large and positive on the warm side of the structure. The trajectory anslysis concludes that this vertical vorticity is baroclinically generated during descent along the cool edge of the baroclinic boundary.

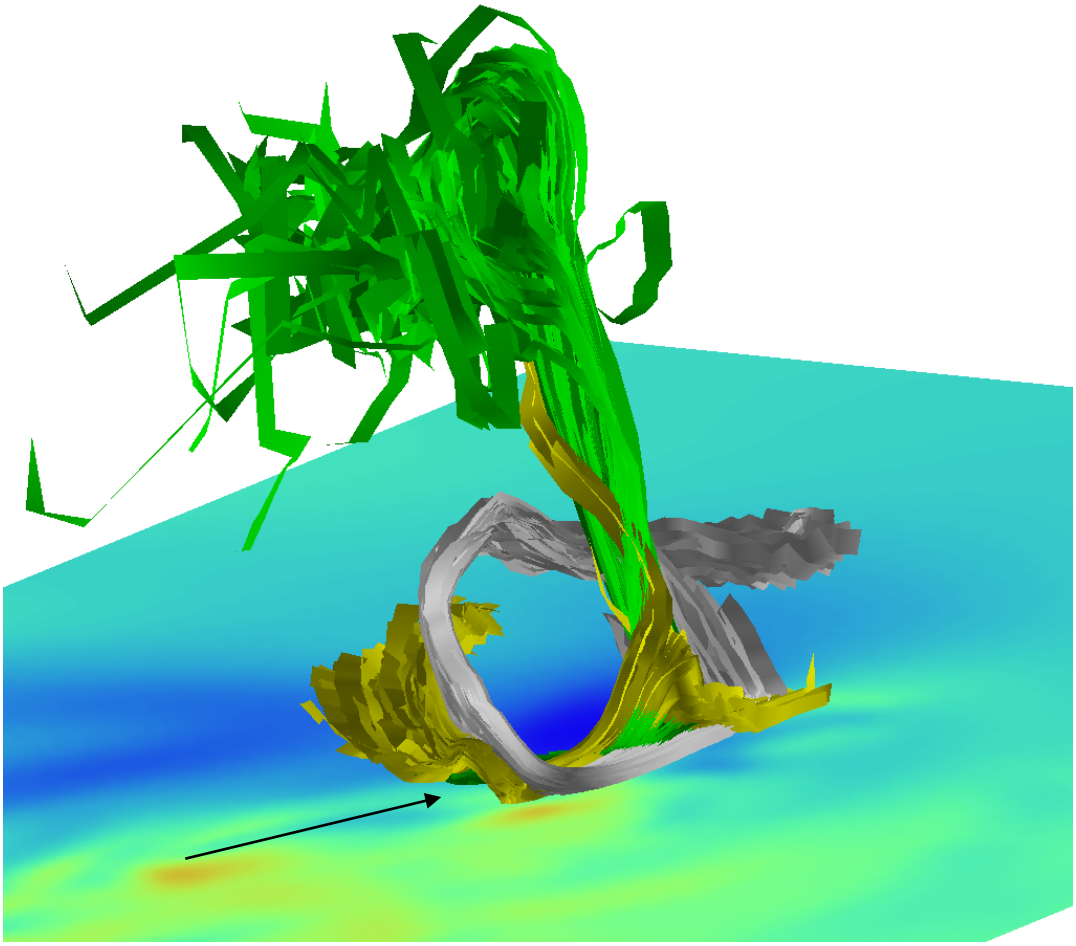

Figure 5.4: Air parcel trajectories associated with a horizontal helical structure and TLV genesis in a prior WK simulation. Green trajectories are trajectories that enter the base of the developing TLV vortex from very low levels. Yellow trajectories are forward-flank inflow parcels that are forced over and then down into the cold pool on the cool side of the helical structure, the relative position of which is indicated with the black arrow. The yellow and green trajectories are seen to wind helically around one another during their ascent into the updraft. The white trajectories originate to the south of the updraft aloft and participate in the initial surge in the left flank but do not interact directly with the structure along the convergence boundary. These parcels then surge out in the rear-flank region. Surface is shaded by pressure perturbation where cooler colors are associated with negative pressure perturbation and warmer colors are associated with positive pressure perturbation.

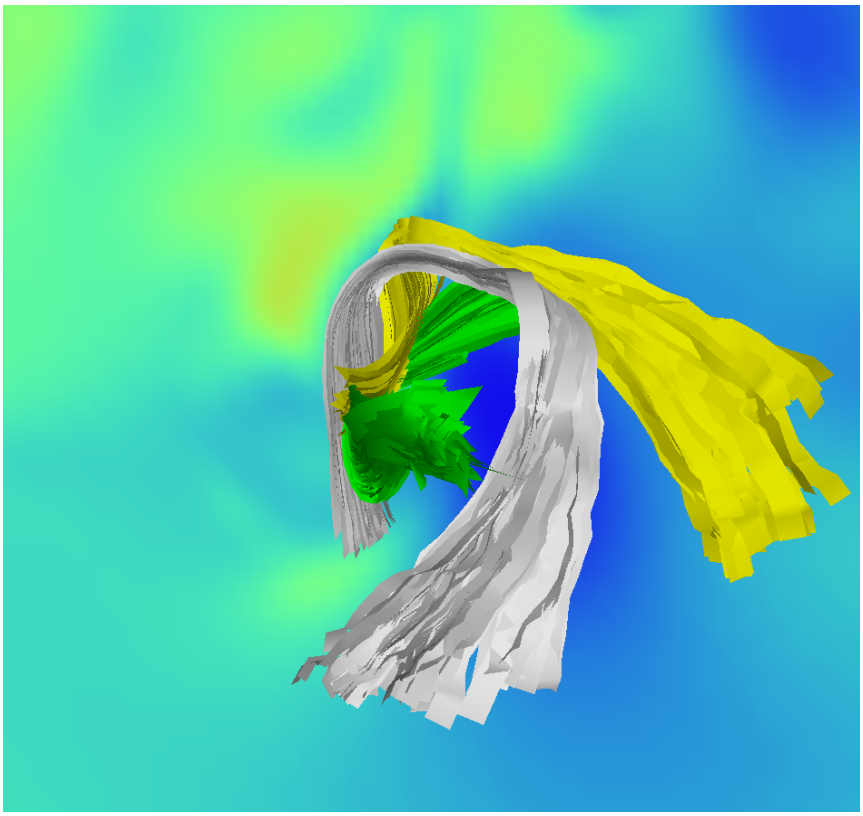

Figure 5.5: Top-down view of air-parcel trajectories involved in low-level helical structure evolution during TLV-genesis of a second WK simulation. As in Fig. 5.4 but looking from the top-down and 100 s earlier in the trajectory integration for visual clarity.

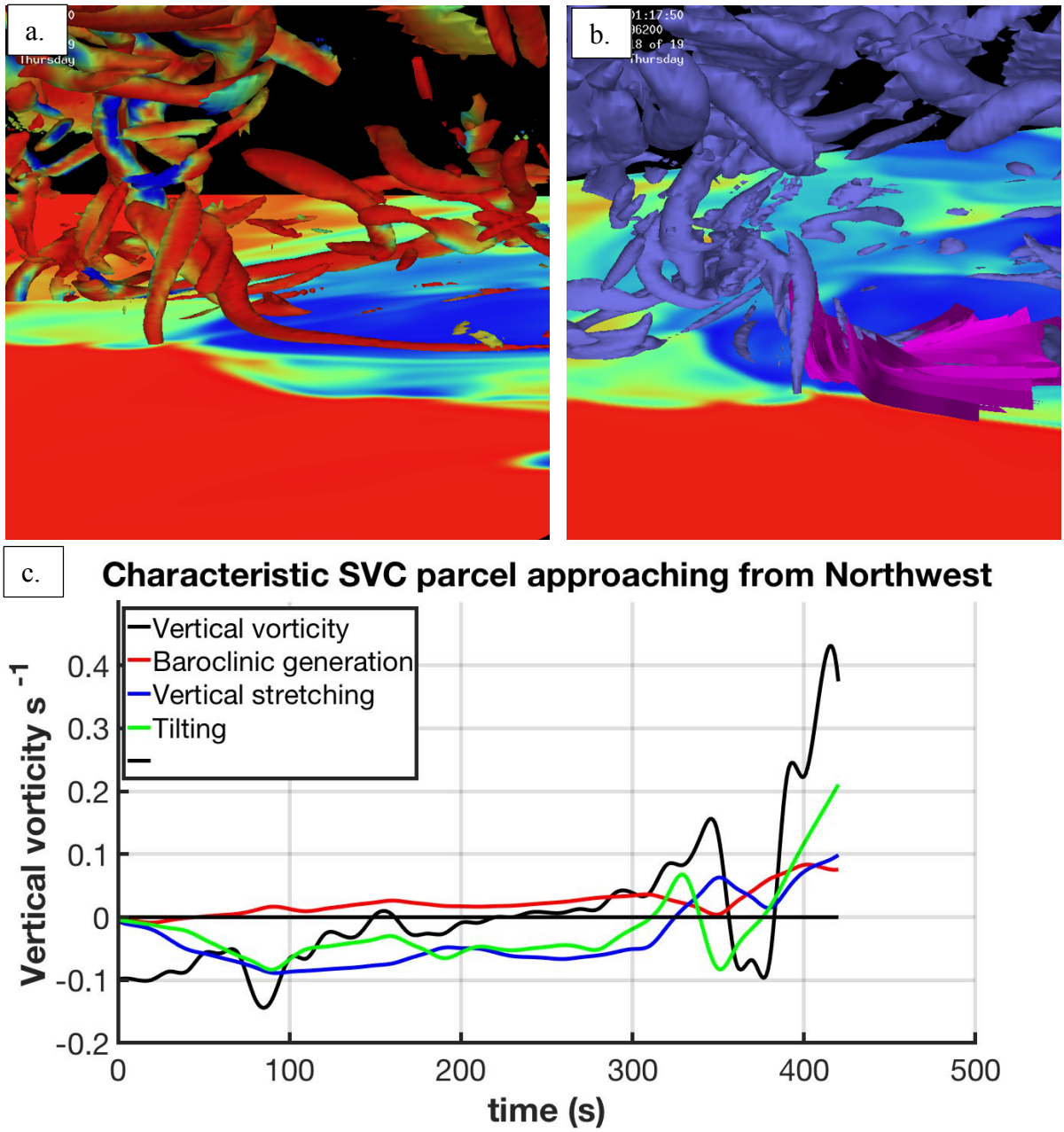

Figure 5.6: Trajectory analysis of parcels entering surface-based vortex during TLV-genesis in a second WK simulation. Repeat of Fi. 2.19, copied here for expansion. A fourth set of trajectories for the WK simulation in Figs. 5.4 & 5.5 (purple ribbons in b.), which are associated with the surface-based vortex that becomes the TLV. A characteristic parcel from this set is chosen to display in (c) showing the resulting vorticity tendency during interaction with the helical structure.

5.1.3 Supporting evidence: May 24 2011 storm analysis

Collaborative efforts with Dr. Leigh Orf at the University of Wisconsin's Space Science and Engineering Center (SSEC) made possible the application of the new diagnostic approach presented in this dissertation to extremely high-resolution numerical model data from a violently tornadic supercell. Orf et al. (2017) identified an important helical structure in the simulation that intensified during and following tornadogenesis, which they called the streamwise vorticity current (SVC).

Analysis of the 24 May storm using the new diagnostics highlights the SVC as a significantly helical structure that supports significant surface-based vertical vorticity (Fig. 3.10). Additionally, the analysis illuminated another region of interest that resembled much of the theoretical and numerical results presented in this dissertation, which serves to further support the theoretical model presented in this chapter.

Tornadogenesis in the 24 May storm occurred at approximately 3800 s (black dashed line in Fig. 5.7). In the time preceding this there was an intense maximum in stretching in the immediate above-surface layer from 3400 – 3800 s, peaking soon after 3600 s (Fig. 5.7). Such a localized maximum in height prompted a detailed time-height analysis of different sectors around the storm's updraft in a similar fashion to the method of analysis for the VORTEX2 simulations. A clear correlation between the maximum in stretching and rotational helicity was found in the box area shown in Fig. 5.8, along an internal baroclinic boundary to the north-west of the low-level updraft (Fig. 5.9). Rotational helicity exhibited a pronounced maximum in the lowest few hundred meters above ground during the time of the maximum in vertical stretching and attained substantial values at the lowest scalar grid level at approximately the same time as

the peak in vertical stretching. At this time, a significant I^2 maximum develops in contact with the surface and subsequently ascends rapidly into the overlying updraft indicating substantial surface-based vortex development that *ascended* with time (Fig. 5.10a). Shortly afterwards, vertical vorticity intensifies rapidly in the lowest 1 km in the full storm domain indicating that tornadogenesis had occurred (Fig. 5.10b).

While the baroclinic boundary to the north of the updraft remains relatively steady throughout tornadogenesis, the left edge of the wedge of dense air approaching the updraft from the north-west exhibits some unsteadiness during the same period (Fig. 5.11). To investigate the evolution of this boundary, a vertical slice of perturbation density potential temperature was taken in the yz (meridional) plane, which illuminated the presence of substantial Kelvin-Helmholtz-type circulations (Fig. 5.12). Analysis of rotational helicity during this time revealed that the billows were associated with low-level helical misoscale structures approaching the base of the updraft from the north-west (Fig. 5.12). While further analysis is required to determine cause and effect, it is reasonable to theorize from the preceding numerical analysis and theoretical discussion that the helical structures forced the billows on the upward branch of their horizontal circulations.

The vertical vorticity field evolved from a relatively disorganized state into remarkable focus during this same time period (Fig. 5.13). Through a combination of the rotational helicity diagnostic and vertical vorticity, a stark similarity with the VORTEX2 runs was found in association with this region of low-level helical flow during the genesis phase of the May 24 2011 storm (Fig. 5.14). Interestingly, however, the surface-based vertical vorticity development in the immediate surface layer in association with these structures occurs on their *cold* side. As can be seen in Fig. 5.12, less dense and therefore more positively buoyant air is ingested

underneath these structures from the south and wrapped around the structures in the *opposite* manner to the baroclinic structures in the VORTEX2 simulations. The resulting helical coupling process remains qualitatively the same in this case despite this variation. Positively buoyant air is forced, dynamically into direct contact with the outflow air in the immediate above-surface layer and ascends rapidly into the updraft from the north-west. The significant difference in this case is that the vertical vorticity growth seen in the time-height analysis and in the three-dimensional renderings must be *barotropic* in origin due to the necessary orientation of vortex lines associated with these structures.

Nevertheless, intense helical rotation is ingested into the updraft from the near surface layer during the time of maximum vertical stretching in the lowest few hundred meters above ground. Made possible by the extremely high-resolution data set provided by Dr. Leigh Orf, the application of the new diagnostics and theoretical approach developed during the author's dissertation research to study rotational structures at extremely high-resolution was made possible. The ability of the diagnostic approach to illuminate a potentially important region of helical flow in addition to the SVC region attests its utility.

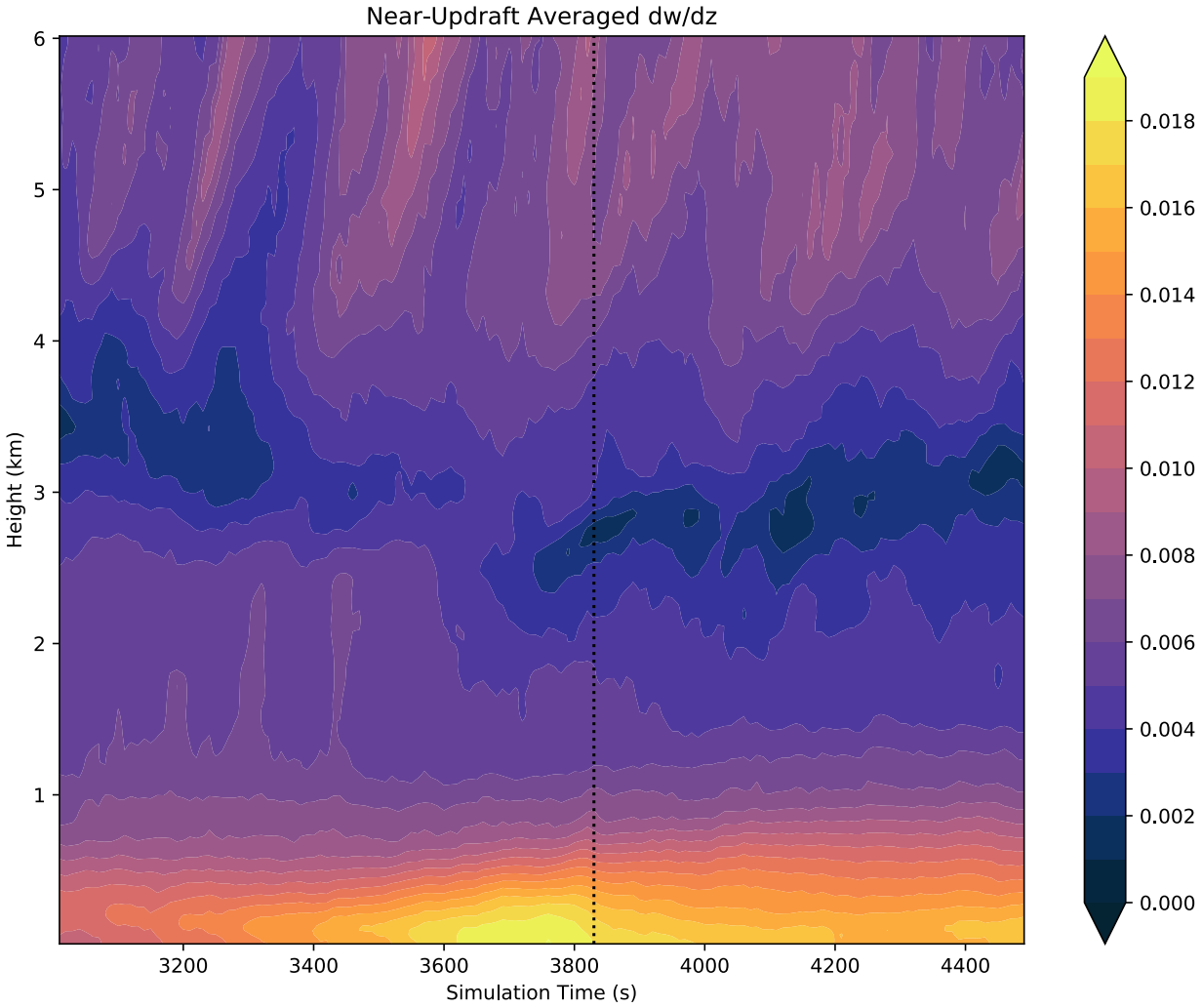

Figure 5.7: Vertical stretching in the May 24 2011 storm during its tornadogenesis phase. Color shading is dw/dz and black line indicates time of tornadogenesis. Figure and permission to use provided by Kelton Halbert.

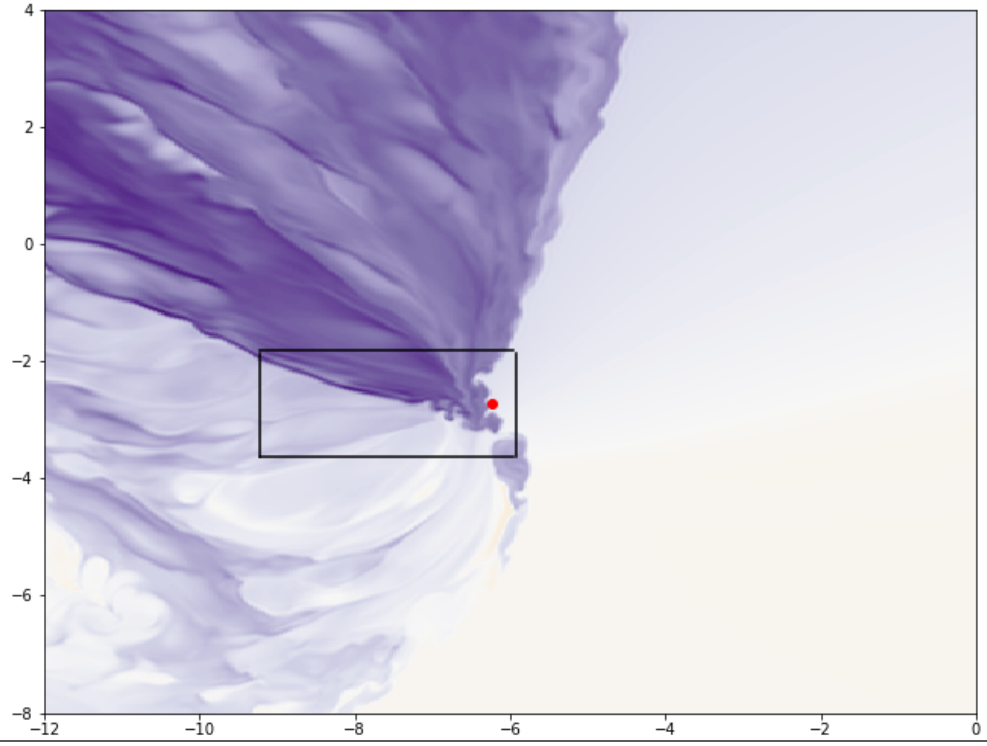

Figure 5.8: Box-area used for subsequent time-height analysis of the May 24 tornadogenesis phase. Surface is shaded by lowest scalar model level perturbation density potential temperature.

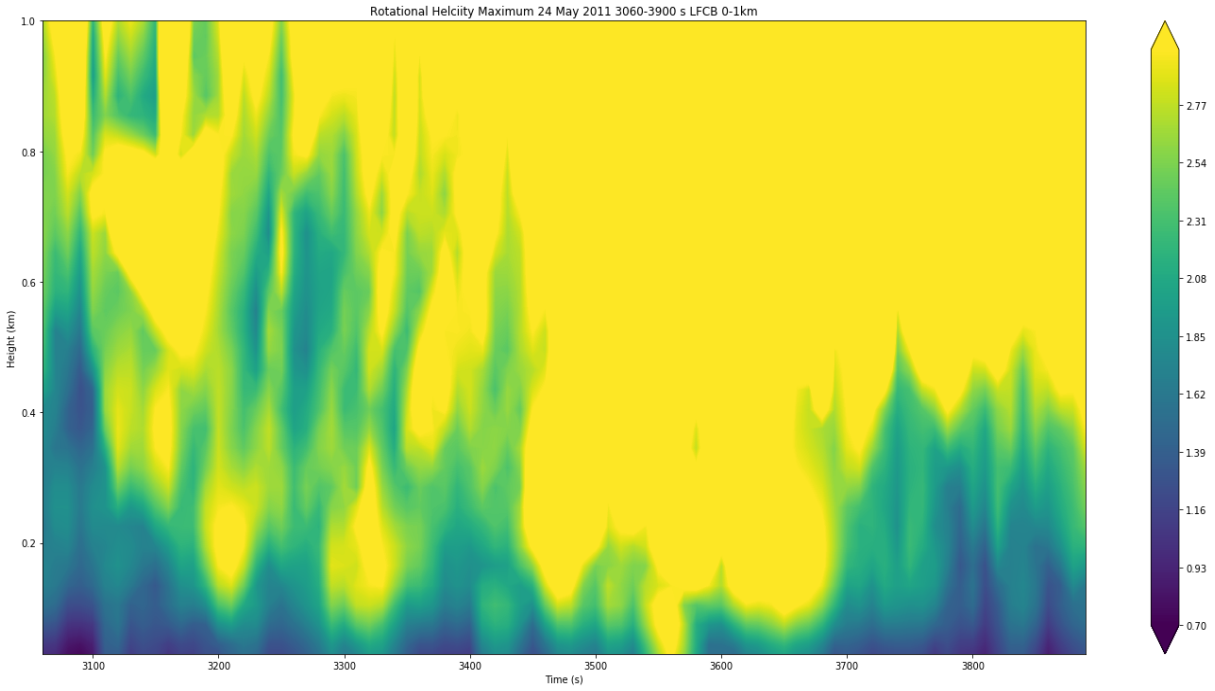

Figure 5.9: Maximum rotational helicity over the 0-1 km layer calculated in box area in Fig. 5.8 for the May 24 storm between 3000 and 3900 s.

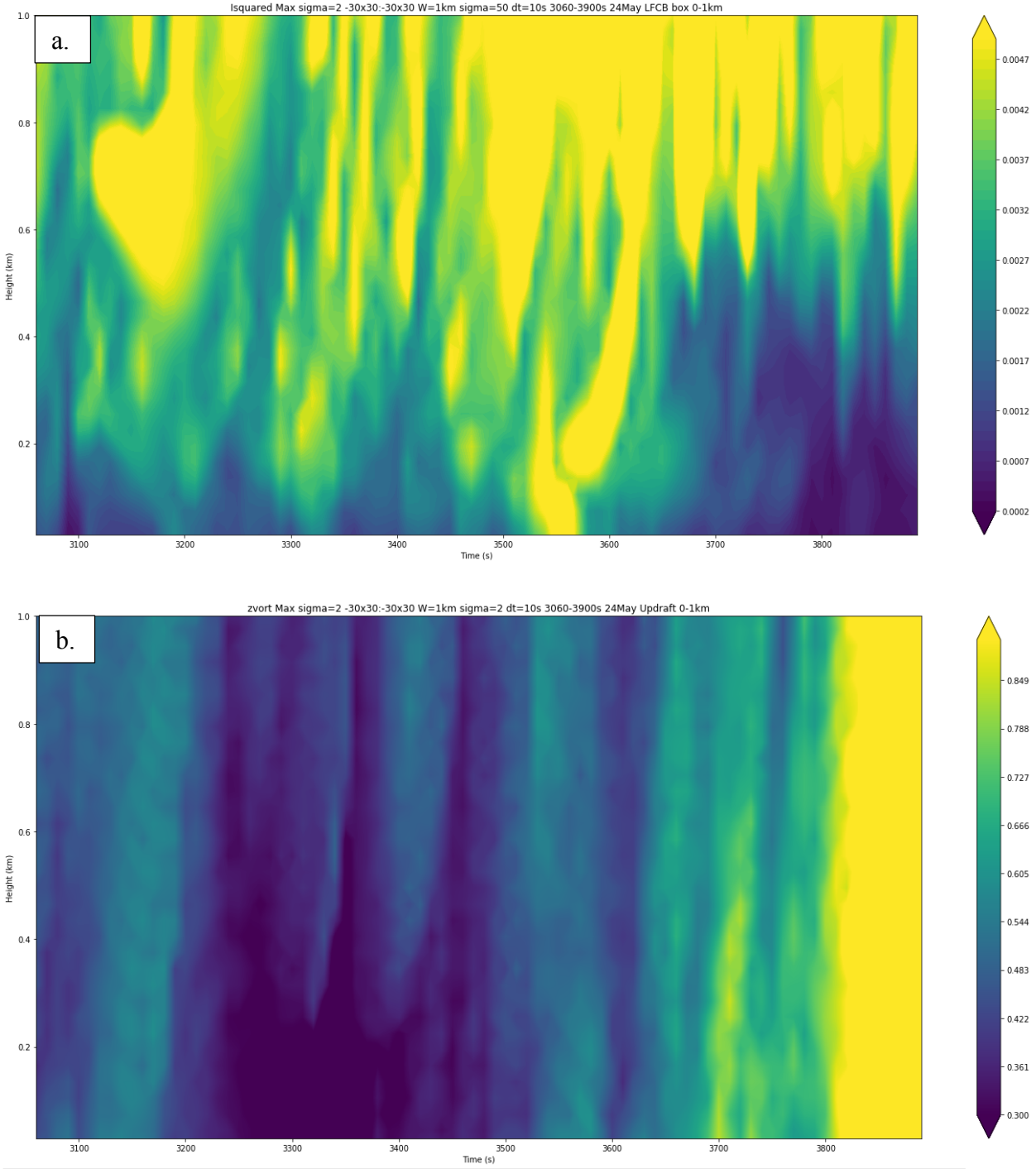

Figure 5.10: Time vs. height analysis of I^2 and vertical vorticity in the 0-1 km layer of the May 24 2011 storm. As in Fig. 5.8 but for I^2 (a) and vertical vorticity (b).

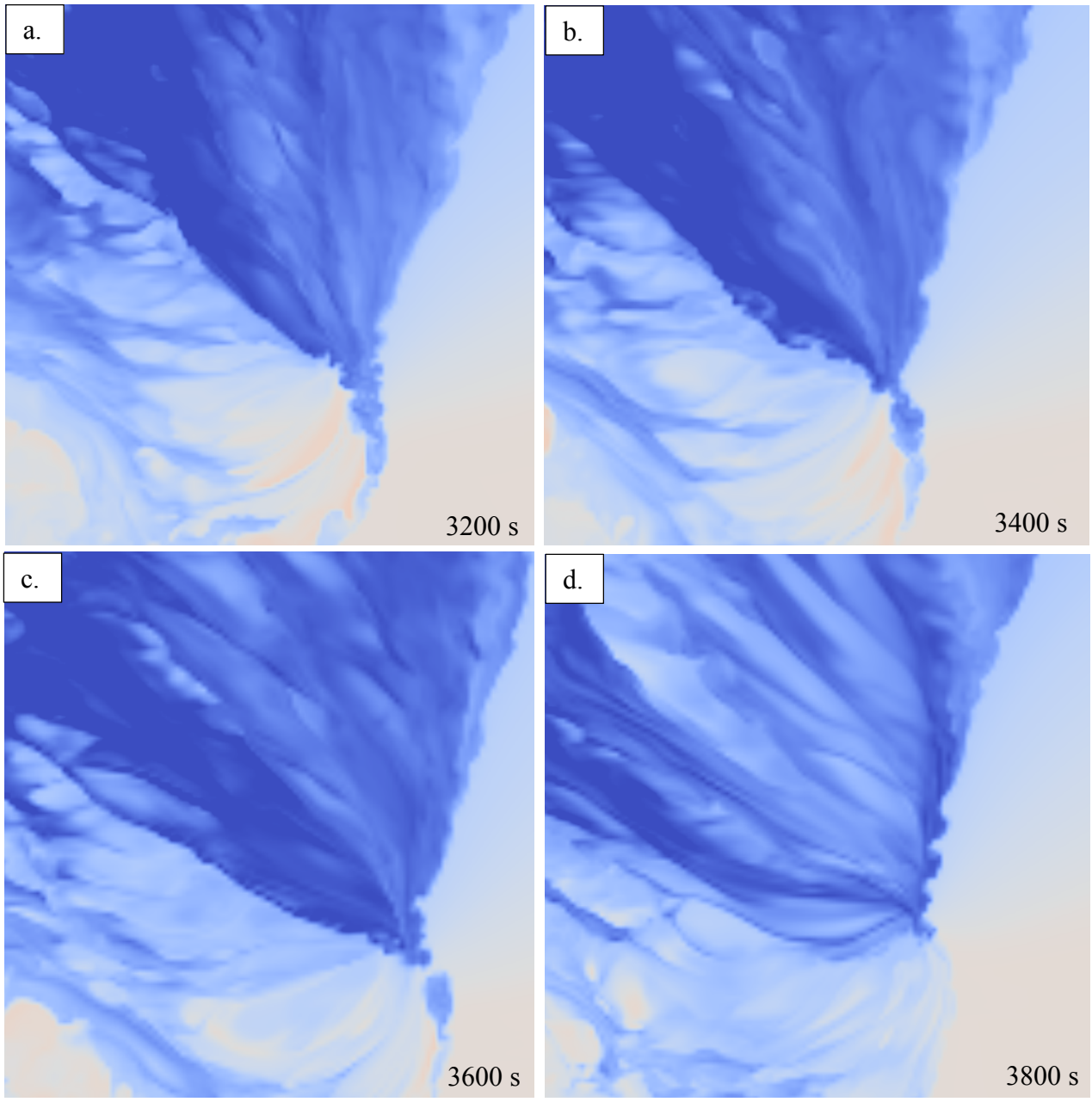

Figure 5.11: Evolution of the left-flank outflow region during tornadogenesis genesis of the May 24. Surface is shaded by perturbation density potential temperature at the lowest scalar model level.

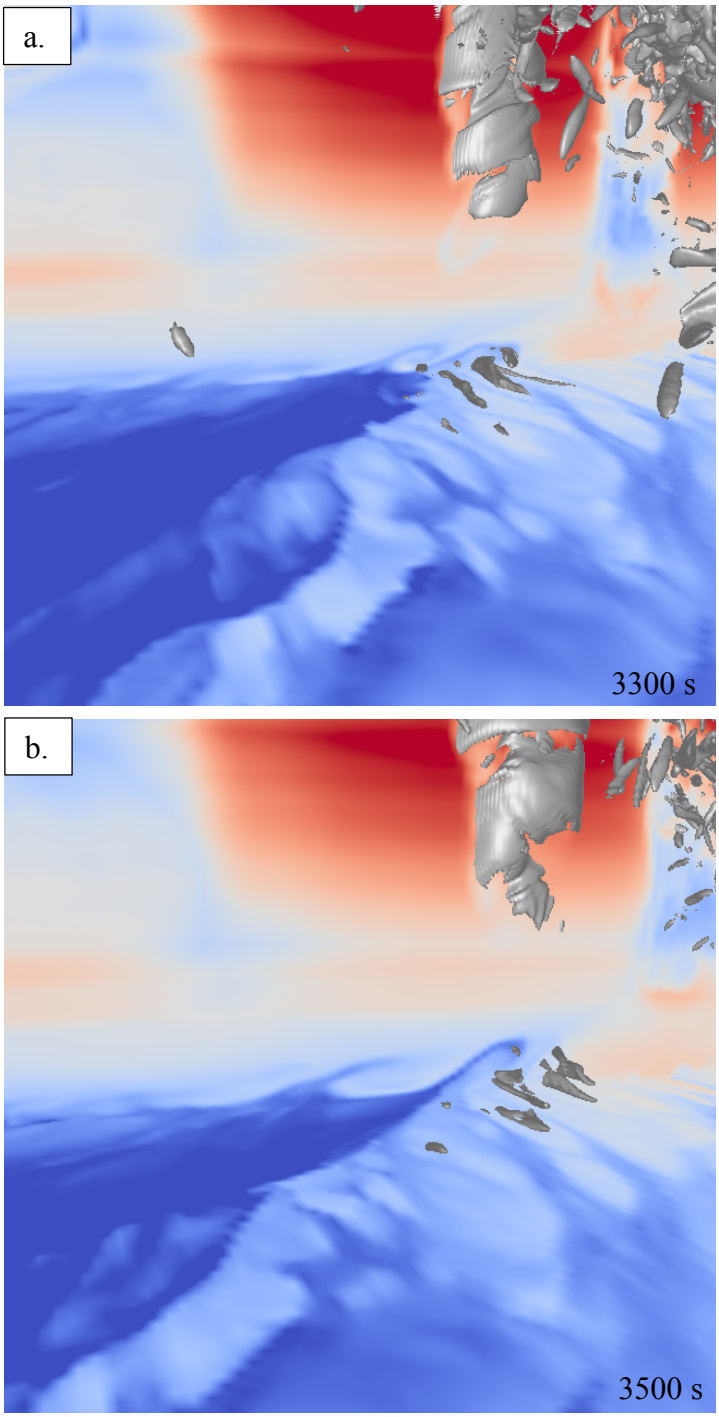

Figure 5.12: Development of horizontal Kelvin-Helholtz-type billows in association with helical structures in the immediate surface layer during tornadogenesis in the May 24 storm. Surface is shaded by perturbation potential temperature where blues indicate positive density perturbations. Vertical slice is also perturbation potential temperature taken in the yz plane and gray isosurface is rotational helicity at 3 ms^{-2}.

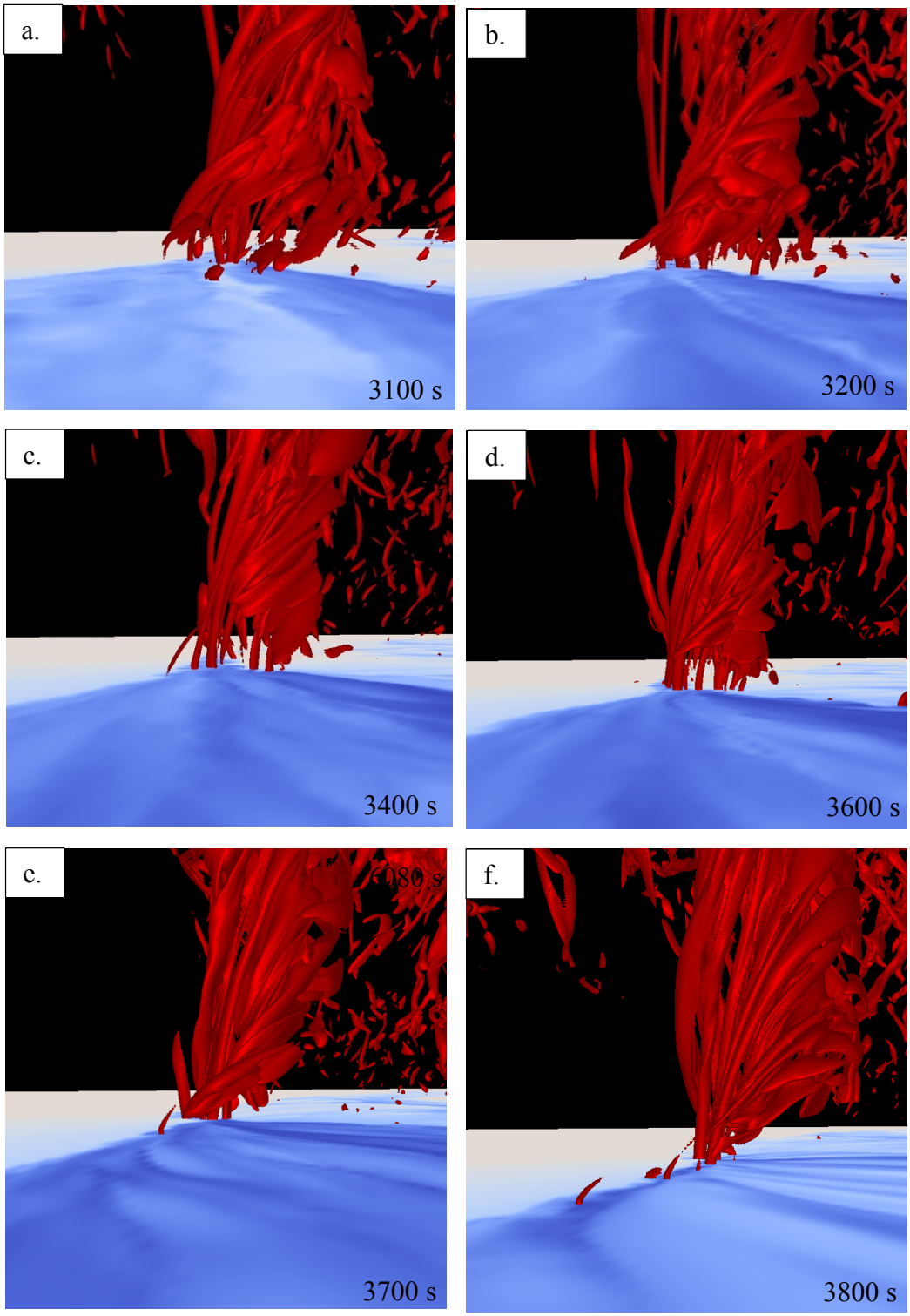

Figure 5.13: Consolidation and intensification of vertical vorticity along baroclinic boundaries in the tornadogenesis phase of the May 24 storm. Vertical vorticity is the red isosurface at 0.15 s^{-1}, surface is shaded by perturbation density potential temperature and the view is from the north.

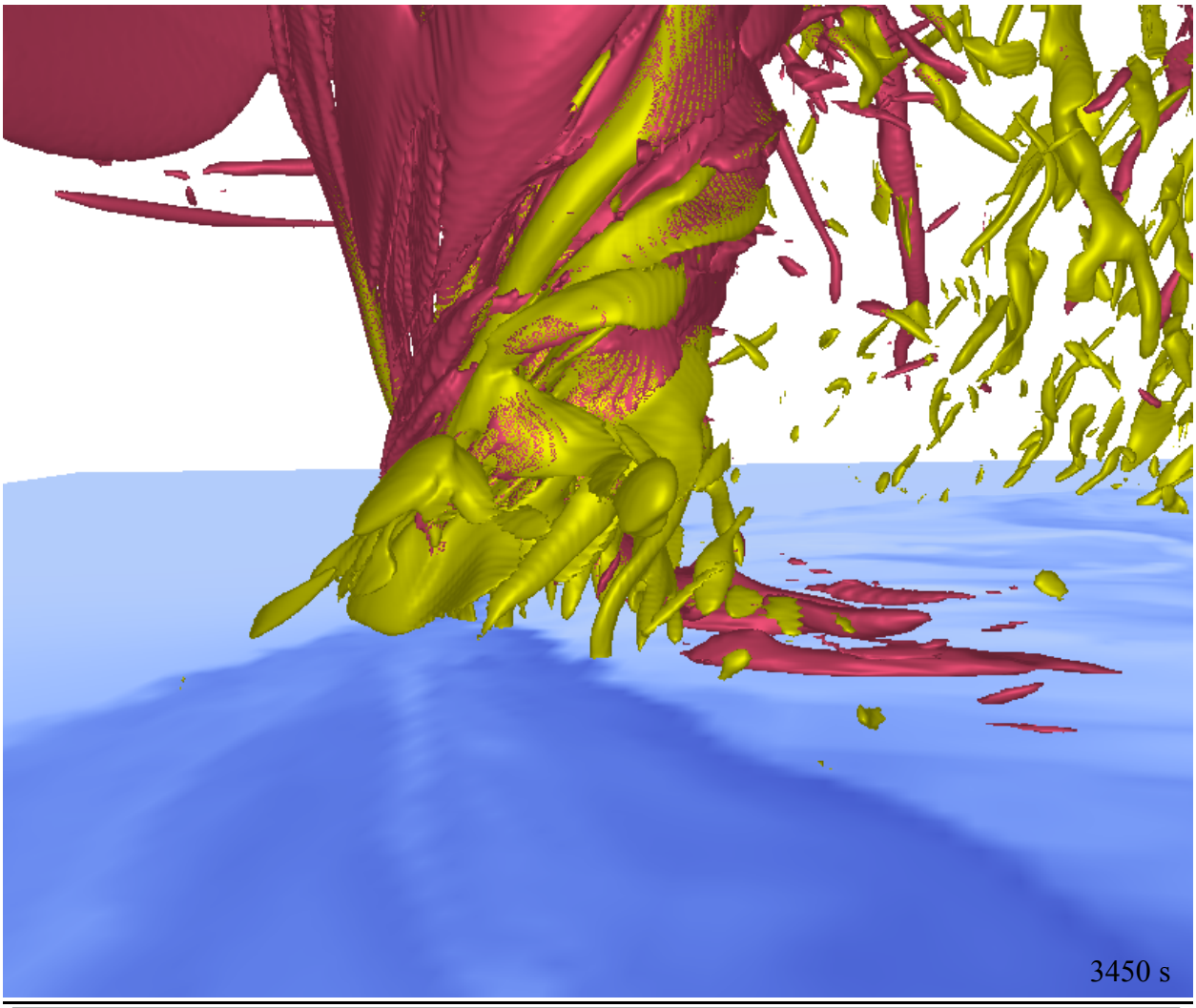

Figure 5.14: Association of pre-tornadic surface-based vertical vortices along helical, near-surface rolls being ingested into the base of the May 24 updraft during its tornadogenesis phase. Rotational helicity is pink isosurface at 3 ms^{-2}, yellow isosurface is vertical vorticity at 0.15 s^{-1} and surface is shaded by perturbation density potential temperature. View is from the north-east.

Figure 5.15: Helical structure ingested into the updraft at time of maximum near-surface vertical stretching in the May 24 2011 simulation. Rotational helicity being tilted and stretched from the near-surface layer deep into the overlying updraft at 3500 s model time during the observed maximum in vertical stretching. Isosurface is rotational helicity at 3 ms^{-2} and surface is shaded by perturbation density potential temperature.

Part II. Synthesis and future work

In this dissertation, rotation of atmospheric flow applicable to mesoscale dynamics in supercell thunderstorms was reviewed in order to develop a fundamental basis from which to study rotational structures involved in the dynamics of supercell tornadogenesis. Through which, in chapter three of this dissertation, new diagnostic approach was developed and subsequently applied to study processes and interactions associated with *coherent* rotational structures in numerical simulations of supercells with the UWNMS and CM1 numerical research models' in chapter four. Tornado-like vortex success was shown to be correlated with sustained helical rotation along internal baroclinic boundaries of a supercell outflow region. Sustained interaction between this low-level helical rotation and the low level streamwise vorticity of the environment was found to occur during an upward intensification of helical flow, and subsequently, explosive upward growth of vertical vorticity occurred from the surface on its periphery. In the context of relevant fluid dynamics' theory, the author presents a new conceptual paradigm for supercell tornadogenesis from these results in chapter five.

The goal of this research was to demonstrate the utility of the diagnostic approach developed during the course of the author's PhD research. The illumination of a dominant role of *horizontal* helical rotational along internal convergence boundaries of numerical supercells demonstrated that the approach advances our diagnostic capabilities. Specifically, through combined application of a new, *rotational helicity* parameter with traditional vorticity diagnostics to study the evolution of misoscale rotation in a supercell's outflow region, a new theoretical tornadogenesis paradigm was offered in the conclusion of the dissertation. This new conceptual model was discussed in the context of current supercell tornadogenesis theory and was found to

be consistent with a significant portion of our current understanding of the evolution of low-level rotation in supercells. Where it diverged from current theory, supporting discussion and evidence was drawn from theory and numerical modeling results.

However, further work is required to confirm many of the theoretical assertions made throughout this dissertation. Firstly, a more comprehensive theoretical study of the fluid dynamics associated with helical flow interactions is necessary in order to formerly understand the helical coupling process proposed herein. Additionally, although out of the scope of the current work, substantially more quantitative-based analysis of vorticity and vertical motion tendency analysis along air parcel trajectories involved in the development, interaction and evolution of the coupled helical structure is warranted to confidently conclude the reasons for its development and upward intensification.

Despite this, the author is highly confident in the following findings:

- Helical flow associated with development of TLVs in numerical simulations presented herein first develops and intensifies in the lowest 500 m AGL
- Subsequent upward intensification relies on interaction with the low-level environmental streamwise vorticity and sustained helical inflow of the low-level updraft
- Surface-based vertical vortex-genesis occurs along the ascending branch of initially horizontally oriented helical structures in the lowest 500 m AGL *baroclinically* in association with dynamic forcing of air parcels to the near-surface layer before being abruptly tilted into the vertical along the ascending edge of helical rotation
- Buoyancy forcing of the updraft is *communicated* to the surface via helical rotation during tornadogenesis allowing for the observed explosive growth of rotation

- Tornadogenesis in the simulations presented in this dissertation occurs primarily through a "bottom-up" process

The process proposed in this dissertation resembles an instability in the supercell's lifecycle. The *coupling* of the positively buoyant inflow air to the negatively buoyant outflow air in a helical manner is conceptually similar to pulling on two ends of a coiled spring. Once the helical coupling occurs and becomes buoyantly unstable, it is inevitable (barring any sudden storm-scale structural changes) that intense vortex-genesis will take place. Thinking of supercell tornadogenesis as an instability raises the question as to whether the instability is *triggered* or occurs as a steady process. While the process of helical coupling occurs theoretically as a steady process, there may be an event that triggered such a process to occur. The proposed theory can occur in both ways, which likely depends on the steadiness of the storm's outflow and inflow interaction. If there is a constant "pushing and shoving" between the two it is likely that if tornadogenesis were to occur through the model presented here that it is triggered by an *event* in the storm's lifecycle such as a downdraft-driven momentum surge. However, it is conceivable that if the mesoscale environment was ideal and a highly steady inflow and outflow region were maintained that the coupling mechanism may occur gradually until the point at which the updraft is connected to the surface-based vorticity through the coupled helical inflow-outflow structure.

The author is further exploring the veracity of these findings through environmental sensitivity tests with a variety of different sounding environments. With this research, the author hopes to isolate more rigorously what controls the ability of the helical coupling process to occur in simulated supercells, which may help forecasters better understand dynamical connections

between local mesoscale environments in the vicinity of ongoing supercells and the storm-generated flow and therefore their likelihood for generating tornadoes.

Additionally, in order to isolate the specific mechanisms at work in the initial generation of the helical rotational structure associated with a supercell's outflow generated convergence boundaries, the author is pursuing idealized downdraft experiments excluding the full-physics of the storm. Through this, processes unique to the outflow dynamics discussed in this dissertation may be studied in isolation before applying them to a full storm situation. This is the subject of ongoing and future research at the University of Wisconsin-Madison.

Although the diagnostic approach used in this dissertation has been shown to be a powerful tool, it is not quantitative. Ultimately, through further theoretical research, the author hopes to develop a prognostic equation for rotational flow, which could be calculated along air parcel trajectories much in the same fashion as traditional vorticity tendency analysis. This would drastically improve on traditional vorticity tendency analysis and on the diagnostic approach presented in this dissertation because it would explicitly determine the sources of intensification of rotation rather than requiring theory to bridge the gaps between *vorticity* development and *vortex* development.

Lastly, the analytical results presented in chapter three involving the divergence equation and the inertial frequency parameter as a measure of stability can be applied to any scale of atmospheric motion. By including the terms dropped for the scale of interest, the inertial stability and therefore its *resistance* against the pressure gradient can be determined for a wide-range of scales. Work in tropical cyclone dynamics by the authors' advisor, Professor Gregory J. Tripoli, has found that applying this diagnostic approach to studying the outflow regions of tropical

cyclones can help predict how rapidly a tropical system is able to remove mass away from its column in order to intensify.

References

Abbs, D.J. and Pielke, R.A., 1986. Thermally forced surface flow and convergence patterns over northeast Colorado. *Monthly weather review*, *114*(12), pp.2281-2296.

Adlerman, E.J., Droegemeier, K.K. and Davies-Jones, R., 1999. A numerical simulation of cyclic mesocyclogenesis. *Journal of the atmospheric sciences*, *56*(13), pp.2045-2069.

Anderson-Frey, A.K., Richardson, Y.P., Dean, A.R., Thompson, R.L. and Smith, B.T., 2016. Investigation of near-storm environments for tornado events and warnings. *Weather and Forecasting*, *31*(6), pp.1771-1790.

Arakawa, A. and Lamb, V.R., 1981. A potential enstrophy and energy conserving scheme for the shallow water equations. *Monthly Weather Review*, *109*(1), pp.18-36.

Atkins, N.T., Glidden, E.M. and Nicholson, T.M., 2014. Observations of wall cloud formation in supercell thunderstorms during VORTEX2. *Monthly Weather Review*, *142*(12), pp.4823-4838.

Barnes, L.R., Gruntfest, E.C., Hayden, M.H., Schultz, D.M. and Benight, C., 2007. False alarms and close calls: A conceptual model of warning accuracy. *Weather and Forecasting*, *22*(5), pp.1140-1147.

Bedard, A. and Georges, T., 2000. Atmospheric infrasound. *Acoustics Australia*, *28*(2), pp.47-52.

Beck, J. and Weiss, C., 2013. An assessment of low-level baroclinity and vorticity within a simulated supercell. *Monthly Weather Review*, *141*(2), pp.649-669.

Bell, G.D. and Keyser, D., 1993. Shear and curvature vorticity and potential-vorticity interchanges: Interpretation and application to a cutoff cyclone event. *Monthly weather review*, *121*(1), pp.76-102.

Bernard, P.S., 2019. On the inherent bias of swirling strength in defining vortical structure. *Physics of Fluids*, *31*(3), p.035107.

Bippes, H. and Turk, M., 1984. *Oil flow patterns of separated flow on a hemisphere cylinder at incidence*. Wiss. Berichtswesen d. DFVLR.

Bippes, H., 1987. Experimental investigation of topological structures in three-dimensional separated flow. In *Boundary-Layer Separation* (pp. 379-381). Springer, Berlin, Heidelberg.

Bluestein, H.B., 1993. Synoptic-dynamic meteorology in midlatitudes. Volume II. Observations and theory of weather systems.

Bluestein, H.B., 2008. Surface boundaries of the Southern Plains: Their role in the initiation of convective storms. In *Synoptic—Dynamic Meteorology and Weather Analysis and Forecasting* (pp. 5-33). American Meteorological Society, Boston, MA.

Bluestein, H.B., 2013. Severe convective storms and tornadoes. *Springer*, *10*, pp.978-3.

Bluestein, H.B., Gaddy, S.G., Dowell, D.C., Pazmany, A.L., Galloway, J.C., McIntosh, R.E. and Stein, H., 1997. Doppler radar observations of substorm-scale vortices in a supercell. *Monthly weather review*, *125*(6), pp.1046-1059.

Bluestein, H.B. and Gaddy, S.G., 2001. Airborne pseudo-dual-Doppler analysis of a rear-inflow jet and deep convergence zone within a supercell. *Monthly weather review*, *129*(9), pp.2270-2289.

Bluestein, H.B., Weiss, C.C. and Pazmany, A.L., 2003. Mobile Doppler radar observations of a tornado in a supercell near Bassett, Nebraska, on 5 June 1999. Part I: Tornadogenesis. *Monthly weather review*, *131*(12), pp.2954-2967.

Bluestein, H.B., French, M.M., Tanamachi, R.L., Frasier, S., Hardwick, K., Junyent, F. and Pazmany, A.L., 2007. Close-range observations of tornadoes in supercells made with a dual-polarization, X-band, mobile Doppler radar. *Monthly weather review*, *135*(4), pp.1522-1543.

Brandes, E.A., 1981. Finestructure of the Del City-Edmond tornadic mesocirculation. *Monthly Weather Review*, *109*(3), pp.635-647.

Brandes, E.A., 1984. Vertical vorticity generation and mesocyclone sustenance in tornadic thunderstorms: The observational evidence. *Monthly weather review*, *112*(11), pp.2253-2269.

Brandes, E.A., Davies-Jones, R.P. and Johnson, B.C., 1988. Streamwise vorticity effects on supercell morphology and persistence. *Journal of the atmospheric sciences*, *45*(6), pp.947-963.

Brandes, E.A. and Ziegler, C.L., 1993. Mesoscale downdraft influences on vertical vorticity in a mature mesoscale convective system. *Monthly weather review*, *121*(5), pp.1337-1353.

Bryan, G.H. and Fritsch, J.M., 2002. A benchmark simulation for moist nonhydrostatic numerical models. *Monthly Weather Review*, *130*(12), pp.2917-2928.

Bryan, G.H., Wyngaard, J.C. and Fritsch, J.M., 2003. Resolution requirements for the simulation of deep moist convection. *Monthly Weather Review*, *131*(10), pp.2394-2416.

Boruff, B.J., Easoz, J.A., Jones, S.D., Landry, H.R., Mitchem, J.D. and Cutter, S.L., 2003. Tornado hazards in the United States. *Climate Research*, *24*(2), pp.103-117.

Bourchtein, A. and Bourchtein, L., 2010. On ellipticity of balance equations for atmospheric dynamics. *Journal of computational and applied mathematics*, *234*(4), pp.1017-1026.

Brooks, E.M., 1949. The tornado cyclone. *Weatherwise*, *2*(2), pp.32-33.

Brotzge, J., Erickson, S. and Brooks, H., 2011. A 5-yr climatology of tornado false alarms. *Weather and Forecasting*, *26*(4), pp.534-544.

Buban, M.S., Ziegler, C.L., Rasmussen, E.N. and Richardson, Y.P., 2007. The dryline on 22 May 2002 during IHOP: Ground-radar and in situ data analyses of the dryline and boundary layer evolution. *Monthly weather review*, *135*(7), pp.2473-2505.

Bunkers, M.J., Johnson, J.S., Czepyha, L.J., Grzywacz, J.M., Klimowski, B.A. and Hjelmfelt, M.R., 2006. An observational examination of long-lived supercells. Part II: Environmental conditions and forecasting. *Weather and forecasting*, *21*(5), pp.689-714.

Brown, R.A., 1991. *Fluid mechanics of the atmosphere* (Vol. 47). Academic Press.

Brooks, H.E., Doswell III, C.A. and Davies-Jones, R., 1993. Environmental helicity and the maintenance and evolution of low-level mesocyclones. *Washington DC American Geophysical Union Geophysical Monograph Series*, *79*, pp.97-104.

Byko, Z., Markowski, P., Richardson, Y., Wurman, J. and Adlerman, E., 2009. Descending reflectivity cores in supercell thunderstorms observed by mobile radars and in a high-resolution numerical simulation. *Weather and Forecasting*, *24*(1), pp.155-186.

Church, C.R., Snow, J.T. and Agee, E.M., 1977. Tornado vortex simulation at Purdue University. *Bulletin of the American Meteorological Society*, *58*(9), pp.900-909.

Church, C., Snow, J.T., Baker, G.L. and Agee, E.M., 1979. Characteristics of tornado-like vortices as a function of swirl ratio: A laboratory investigation. *Journal of the Atmospheric Sciences*, *36*(9), pp.1755-1776.

Coffer, B.E. and Parker, M.D., 2015. Impacts of increasing low-level shear on supercells during the early evening transition. *Monthly Weather Review*, *143*(5), pp.1945-1969.

Coffer, B.E. and Parker, M.D., 2017. Simulated supercells in nontornadic and tornadic VORTEX2 environments. *Monthly Weather Review*, *145*(1), pp.149-180.

Coffer, B.E. and Parker, M.D., 2018. Is there a “tipping point” between simulated nontornadic and tornadic supercells in VORTEX2 environments?. *Monthly Weather Review*, *146*(8), pp.2667-2693.

Coffer, B.E., Parker, M.D., Dahl, J.M., Wicker, L.J. and Clark, A.J., 2017. Volatility of tornadogenesis: An ensemble of simulated nontornadic and tornadic supercells in VORTEX2 environments. *Monthly Weather Review*, *145*(11), pp.4605-4625.

Dahl, J.M., 2006. *Supercells: their dynamics and prediction*(Doctoral dissertation).

Dahl, J.M., 2015. Near-ground rotation in simulated supercells: On the robustness of the baroclinic mechanism. *Monthly Weather Review*, *143*(12), pp.4929-4942.

Dahl, J.M., 2017. Tilting of Horizontal Shear Vorticity and the Development of Updraft Rotation in Supercell Thunderstorms. *Journal of the Atmospheric Sciences*, *74*(9), pp.2997-3020.

Dahl, J.M., Parker, M.D. and Wicker, L.J., 2014. Imported and storm-generated near-ground vertical vorticity in a simulated supercell. *Journal of the Atmospheric Sciences*, *71*(8), pp.3027-3051.

Dallmann, U., 1988. Three-dimensional vortex structures and vorticity topology. *Fluid Dynamics Research*, *3*(1-4), p.183.

Davies, J.M., 2004. Estimations of CIN and LFC associated with tornadic and nontornadic supercells. *Weather and forecasting*, *19*(4), pp.714-726.

Davies-Jones, R.P., 1982. Observational and theoretical aspects of tornadogenesis. In *Intense Atmospheric Vortices*(pp. 175-189). Springer, Berlin, Heidelberg.

Davies-Jones, R.P., 1986. Tornado dynamics. *Thunderstorm morphology and dynamics*, *2*, pp.197-236.

Davies-Jones, R., 2002. Linear and nonlinear propagation of supercell storms. *Journal of the atmospheric sciences*, *59*(22), pp.3178-3205.

Davies-Jones, R., 2008. Can a descending rain curtain in a supercell instigate tornadogenesis barotropically?. *Journal of the Atmospheric Sciences*, *65*(8), pp.2469-2497.

Davies-Jones, R., 2015. A review of supercell and tornado dynamics. *Atmospheric Research*, *158*, pp.274-291.

Davies-Jones, R. and Brooks, H., 1993. Mesocyclogenesis from a theoretical perspective. *Washington DC American Geophysical Union Geophysical Monograph Series*, *79*, pp.105-114

Davies-Jones, R., Trapp, R.J. and Bluestein, H.B., 2001. Tornadoes and tornadic storms. In *Severe convective storms*(pp. 167-221). American Meteorological Society, Boston, MA.

Doswell III, C.A., 1991. A review for forecasters on the application of hodographs to forecasting severe thunderstorms. *Natl. Wea. Dig*, *16*(1), pp.2-16.

Doswell, C.A. and Bosart, L.F., 2001. Extratropical synoptic-scale processes and severe convection. In *Severe Convective Storms* (pp. 27-69). American Meteorological Society, Boston, MA.

Doswell III, C.A., Brooks, H.E. and Dotzek, N., 2009. On the implementation of the enhanced Fujita scale in the USA. *Atmospheric Research*, *93*(1-3), pp.554-563.

Drazin, P.G. and Howard, L.N., 1966. Hydrodynamic stability of parallel flow of inviscid fluid. In *Advances in applied mechanics* (Vol. 9, pp. 1-89). Elsevier.

Droegemeier, K.K., Lazarus, S.M. and Davies-Jones, R., 1993. The influence of helicity on numerically simulated convective storms. *Month*

Fanelli, P.F. and Bannon, P.R., 2005. Nonlinear atmospheric adjustment to thermal forcing. *Journal of the atmospheric sciences*, *62*(12), pp.4253-4272.

Fiedler, B.H. and Rotunno, R., 1986. A theory for the maximum windspeeds in tornado-like vortices. *Journal of the atmospheric sciences*, *43*(21), pp.2328-2340.

Fiedler, B.H., 1994. The thermodynamic speed limit and its violation in axisymmetric numerical simulations of tornado-like vortices. *Atmosphere-ocean*, *32*(2), pp.335-359.

Fiedler, B.H., 1998. Wind-speed limits in numerically simulated tornadoes with suction vortices. *Quarterly Journal of the Royal Meteorological Society*, *124*(551), pp.2377-2392.

Fujita, T., 1958. Mesoanalysis of the Illinois tornadoes of 9 April 1953. *Journal of Meteorology*, *15*(3), pp.288-296.

French, M.M., Bluestein, H.B., PopStefanija, I., Baldi, C.A. and Bluth, R.T., 2013. Reexamining the vertical development of tornadic vortex signatures in supercells. *Monthly Weather Review*, *141*(12), pp.4576-4601.

Gaudet, B.J. and Cotton, W.R., 2006. Low-level mesocyclonic concentration by nonaxisymmetric transport. Part I: Supercell and mesocyclone evolution. *Journal of the atmospheric sciences*, *63*(4), pp.1113-1133.

Gaudet, B.J., Cotton, W.R. and Montgomery, M.T., 2006. Low-level mesocyclonic concentration by nonaxisymmetric transport. Part II: Vorticity dynamics. *Journal of the atmospheric sciences*, *63*(4), pp.1134-1150.

Georges, T.M. and Greene, G.E., 1975. Infrasound from convective storms. Part IV. Is it useful for storm warning?. *Journal of Applied Meteorology*, *14*(7), pp.1303-1316.

Gilmore, M.S. and Wicker, L.J., 1998. The influence of midtropospheric dryness on supercell morphology and evolution. *Monthly weather review*, *126*(4), pp.943-958.

Grams, J.S., Thompson, R.L., Snively, D.V., Prentice, J.A., Hodges, G.M. and Reames, L.J., 2012. A climatology and comparison of parameters for significant tornado events in the United States. *Weather and forecasting*, *27*(1), pp.106-123.

Grasso, L.D. and Cotton, W.R., 1995. Numerical simulation of a tornado vortex. *Journal of the atmospheric sciences*, *52*(8), pp.1192-1203.

Guarriello, F., Nowotarski, C.J. and Epifanio, C.C., 2018. Effects of the low-level wind profile on outflow position and near-surface vertical vorticity in simulated supercell thunderstorms. *Journal of the Atmospheric Sciences*, *75*(3), pp.731-753.

Van Den Heever, S.C. and Cotton, W.R., 2004. The impact of hail size on simulated supercell storms. *Journal of the atmospheric sciences*, *61*(13), pp.1596-1609.

Haller, G., 2005. An objective definition of a vortex. *Journal of fluid mechanics*, *525*, pp.1-26.

Harlow, F.H. and Stein, L.R., 1974. Structural analysis of tornado-like vortices. *Journal of the Atmospheric Sciences*, *31*(8), pp.2081-2098.

Herman, G.R., Nielsen, E.R. and Schumacher, R.S., 2018. Probabilistic verification of Storm Prediction Center convective outlooks. *Weather and Forecasting*, *33*(1), pp.161-184.

Jeevanjee, N. and Romps, D.M., 2015. Effective buoyancy, inertial pressure, and the mechanical generation of boundary layer mass flux by cold pools. *Journal of the Atmospheric Sciences*, *72*(8), pp.3199-3213.

Johns, R.H. and Doswell III, C.A., 1992. Severe local storms forecasting. *Weather and Forecasting*, *7*(4), pp.588-612.

Kennedy, A., Straka, J.M. and Rasmussen, E.N., 2007. A statistical study of the association of DRCs with supercells and tornadoes. *Weather and Forecasting*, *22*(6), pp.1191-1199.

Klemp, J.B., 1987. Dynamics of tornadic thunderstorms. *Annual review of fluid mechanics*, *19*(1), pp.369-402.

Klemp, J.B. and Wilhelmson, R.B., 1978. The simulation of three-dimensional convective storm dynamics. *Journal of the Atmospheric Sciences*, *35*(6), pp.1070-1096.

Klemp, J.B. and Rotunno, R., 1983. A study of the tornadic region within a supercell thunderstorm. *Journal of the Atmospheric Sciences*, *40*(2), pp.359-377.

Knox, J.A., 1997. Generalized nonlinear balance criteria and inertial stability. *Journal of the atmospheric sciences*, *54*(8), pp.967-985.

Kosiba, K.A. and Wurman, J., 2013. The three-dimensional structure and evolution of a tornado boundary layer. *Weather and Forecasting*, *28*(6), pp.1552-1561.

Kolář, V., 2007. Vortex identification: New requirements and limitations. *International journal of heat and fluid flow*, *28*(4), pp.638-652.

Kottmeier, C., Kalthoff, N., Barthlott, C., Corsmeier, U., Van Baelen, J., Behrendt, A., Behrendt, R., Blyth, A., Coulter, R., Crewell, S. and Di Girolamo, P., 2008. Mechanisms initiating deep convection over complex terrain during COPS. *Meteorologische Zeitschrift*, *17*(6), pp.931-948.

Lee, B.D. and Wilhelmson, R.B., 1997. The numerical simulation of nonsupercell tornadogenesis. Part II: Evolution of a family of tornadoes along a weak outflow boundary. *Journal of the atmospheric sciences*, *54*(19), pp.2387-2415.

Lee, B.D., Finley, C.A. and Karstens, C.D., 2012. The Bowdle, South Dakota, cyclic tornadic supercell of 22 May 2010: Surface analysis of rear-flank downdraft evolution and multiple internal surges. *Monthly Weather Review*, *140*(11), pp.3419-3441.

Lemon, L.R., Burgess, D.W. and Brown, R.A., 1978. Tornadic storm airflow and morphology derived from single-Doppler radar measurements. *Monthly Weather Review*, *106*(1), pp.48-61.

Lemon, L.R. and Doswell III, C.A., 1979. Severe thunderstorm evolution and mesocyclone structure as related to tornadogenesis. *Monthly Weather Review*, *107*(9), pp.1184-1197.

Lewellen, W.S., 1976, June. Theoretical models of the tornado vortex. In *Proc. Symp. on Tornadoes: Assessment of Knowledge and Implications for Man* (pp. 107-143).

Lewellen, D.C. and Lewellen, W.S., 2007. Near-surface intensification of tornado vortices. *Journal of the Atmospheric Sciences*, *64*(7), pp.2176-2194.

Lighthill, M., 1963. Attachment and separation in laminar boundary layers. *Laminar Boundary Layers*.

Lilly, D.K., 1983. Dynamics of rotating thunderstorms. In *Mesoscale Meteorology—Theories, Observations and Models*(pp. 531-543). Springer, Dordrecht.

Lilly, D.K., 1986. The structure, energetics and propagation of rotating convective storms. Part I: Energy exchange with the mean flow. *Journal of the atmospheric sciences*, *43*(2), pp.113-125.

Lily, D.K., 1986. The structure, energetics and propagation of rotating convective storms: Part II. Helicity and storm stabilisation. *J. Atmos. Sci*, *43*, pp.126-140.

Lin, J.C., Howard, F.G. and Selby, G.V., 1990. Small submerged vortex generators for turbulent flow separation control. *Journal of Spacecraft and Rockets*, *27*(5), pp.503-507.

Markowski, P.M., 2002. Hook echoes and rear-flank downdrafts: A review. *Monthly Weather Review*, *130*(4), pp.852-876.

Markowski, P. M., A Review of the Various Treatments of the Surface Momentum Flux in Severe Storms Simulations: Assumptions, Deficiencies, and Alternatives, *29th Conference on Severe Local Storms*, Stowe, VT, American Meteorological Society, 7.3.

Markowski, P.M., Straka, J.M. and Rasmussen, E.N., 2002. Direct surface thermodynamic observations within the rear-flank downdrafts of nontornadic and tornadic supercells. *Monthly weather review*, *130*(7), pp.1692-1721.

Markowski, P., Richardson, Y., Rasmussen, E., Straka, J., Davies-Jones, R. and Trapp, R.J., 2008. Vortex lines within low-level mesocyclones obtained from pseudo-dual-Doppler radar observations. *Monthly Weather Review*, *136*(9), pp.3513-3535.

Markowski, P.M. and Richardson, Y.P., 2009. Tornadogenesis: Our current understanding, forecasting considerations, and questions to guide future research. *Atmospheric Research*, *93*(1-3), pp.3-10.

Markowski, P. and Richardson, Y., 2011. *Mesoscale meteorology in midlatitudes* (Vol. 2). John Wiley & Sons.

Markowski, P.M., Richardson, Y., Majcen, M., Marquis, J. and Wurman, J., 2011. Characteristics of the wind field in three nontornadic low-level mesocyclones observed by the Doppler on Wheels radars. *E-Journal of Severe Storms Meteorology*, *6*(3).

Markowski, P., Richardson, Y., Marquis, J., Wurman, J., Kosiba, K., Robinson, P., Dowell, D., Rasmussen, E. and Davies-Jones, R., 2012. The pretornadic phase of the Goshen County, Wyoming, supercell of 5 June 2009 intercepted by VORTEX2. Part I: Evolution of kinematic and surface thermodynamic fields. *Monthly Weather Review*, *140*(9), pp.2887-2915.

Markowski, P., Richardson, Y., Marquis, J., Davies-Jones, R., Wurman, J., Kosiba, K., Robinson, P., Rasmussen, E. and Dowell, D., 2012. The pretornadic phase of the Goshen County, Wyoming, supercell of 5 June 2009 intercepted by VORTEX2. Part II: Intensification of low-level rotation. *Monthly Weather Review*, *140*(9), pp.2916-2938.

Markowski, P.M. and Richardson, Y.P., 2014. The influence of environmental low-level shear and cold pools on tornadogenesis: Insights from idealized simulations. *Journal of the Atmospheric Sciences*, *71*(1), pp.243-275.

Markowski, P.M., Hatlee, T.P. and Richardson, Y.P., 2018. Tornadogenesis in the 12 May 2010 Supercell Thunderstorm Intercepted by VORTEX2 near Clinton, Oklahoma. *Monthly Weather Review*, *146*(11), pp.3623-3650.

Marquis, J.N., Richardson, Y.P. and Wurman, J.M., 2007. Kinematic observations of misocyclones along boundaries during IHOP. *Monthly weather review*, *135*(5), pp.1749-1768.

Marquis, J., Richardson, Y., Wurman, J. and Markowski, P., 2008. Single-and dual-Doppler analysis of a tornadic vortex and surrounding storm-scale flow in the Crowell, Texas, supercell of 30 April 2000. *Monthly Weather Review*, *136*(12), pp.5017-5043.

Marquis, J., Richardson, Y., Markowski, P., Wurman, J., Kosiba, K. and Robinson, P., 2016. An investigation of the Goshen County, Wyoming, tornadic supercell of 5 June 2009 using EnKF assimilation of mobile mesonet and radar observations collected during VORTEX2. Part II: Mesocyclone-scale processes affecting tornado formation, maintenance, and decay. *Monthly Weather Review*, *144*(9), pp.3441-3463.

Mashiko, W., Niino, H. and Kato, T., 2009. Numerical simulation of tornadogenesis in an outer-rainband minisupercell of Typhoon Shanshan on 17 September 2006. *Monthly Weather Review*, *137*(12), pp.4238-4260.

Mashiko, W., 2016. A numerical study of the 6 May 2012 Tsukuba City supercell tornado. Part I: Vorticity sources of low-level and midlevel mesocyclones. *Monthly Weather Review*, *144*(3), pp.1069-1092.

Moller, A.R., Doswell III, C.A., Foster, M.P. and Woodall, G.R., 1994. The operational recognition of supercell thunderstorm environments and storm structures. *Weather and Forecasting*, *9*(3), pp.327-347.

Na, Y. and Moin, P., 1998. The structure of wall-pressure fluctuations in turbulent boundary layers with adverse pressure gradient and separation. *Journal of Fluid Mechanics*, *377*, pp.347-373.

Naylor, J. and Gilmore, M.S., 2014. Vorticity evolution leading to tornadogenesis and tornadogenesis failure in simulated supercells. *Journal of the Atmospheric Sciences*, *71*(3), pp.1201-1217.

Nemes, A., Jacono, D.L., Blackburn, H.M. and Sheridan, J., 2015. Mutual inductance of two helical vortices. *Journal of Fluid Mechanics*, *774*, pp.298-310.

Noda, A.T. and Niino, H., 2005. Genesis and structure of a major tornado in a numerically-simulated supercell storm: Importance of vertical vorticity in a gust front. *SOLA*, *1*, pp.5-8.

Noda, A.T. and Niino, H., 2010. A numerical investigation of a supercell tornado: Genesis and vorticity budget. *Journal of the Meteorological Society of Japan. Ser. II*, *88*(2), pp.135-159.

Nowotarski, C.J., Markowski, P.M. and Richardson, Y.P., 2011. The characteristics of numerically simulated supercell storms situated over statically stable boundary layers. *Monthly Weather Review*, *139*(10), pp.3139-3162.

Nowotarski, C.J., Markowski, P.M., Richardson, Y.P. and Bryan, G.H., 2015. Supercell low-level mesocyclones in simulations with a sheared convective boundary layer. *Monthly Weather Review*, *143*(1), pp.272-297.

Odell, L. E., G. J. Tripoli, S. T. Trevorrow, and M. L. Buker, 2014: Vortex genesis and intensification processes associated with an idealized tornadic supercell. Special Symp. on Severe Local Storms: The Current State of the Science and Understanding Impacts, Atlanta, GA, Amer. Meteor. Soc., P810.

Orf, L.G., Semeraro, B.D. and Wilhelmson, R.B., 2007. Vortex detection in a simulated supercell thunderstorm. *Atmospheric Science Letters*, *8*(1), pp.29-35.

Orf, L., Wilhelmson, R., Lee, B., Finley, C. and Houston, A., 2017. Evolution of a long-track violent tornado within a simulated supercell. *Bulletin of the American Meteorological Society*, *98*(1), pp.45-68.

Parker, M.D., 2012. Impacts of lapse rates on low-level rotation in idealized storms. *Journal of the Atmospheric Sciences*, *69*(2), pp.538-559.

Parker, M.D., 2014. Composite VORTEX2 supercell environments from near-storm soundings. *Monthly Weather Review*, *142*(2), pp.508-529.

Parker, M.D., 2017. How much does “backing aloft” actually impact a supercell?. *Weather and Forecasting*, *32*(5), pp.1937-1957.

Parker, M.D. and Dahl, J.M., 2015. Production of near-surface vertical vorticity by idealized downdrafts. *Monthly Weather Review*, *143*(7), pp.2795-2816.

Parsons, D.B., Haghi, K.R., Halbert, K.T., Elmer, B. and Wang, J., 2019. The potential role of atmospheric bores and gravity waves in the initiation and maintenance of nocturnal convection over the Southern Great Plains. *Journal of the Atmospheric Sciences*, *76*(1), pp.43-68.

Rasmussen, E.N., 2003. Refined supercell and tornado forecast parameters. *Weather and Forecasting*, *18*(3), pp.530-535.

Rasmussen, E.N., Straka, J.M., Davies-Jones, R., Doswell III, C.A., Carr, F.H., Eilts, M.D. and MacGorman, D.R., 1994. Verification of the origins of rotation in tornadoes experiment: VORTEX. *Bulletin of the American Meteorological Society*, *75*(6), pp.995-1006.

Robertson, S.D., 2017. *Intensification of the low-level updraft in supercells preceding tornadogenesis* (Masters' thesis).

Roberts, B., Xue, M., Schenkman, A.D. and Dawson, D.T., 2016. The role of surface drag in tornadogenesis within an idealized supercell simulation. *Journal of the Atmospheric Sciences*, *73*(9), pp.3371-3395.

Roth, M. and Peikert, R., 1998, October. A higher-order method for finding vortex core lines. In *Proceedings Visualization'98 (Cat. No. 98CB36276)* (pp. 143-150). IEEE.

Rotunno, R., 1979. A study in tornado-like vortex dynamics. *Journal of the Atmospheric Sciences*, *36*(1), pp.140-155.

Rotunno, R., 2013. The fluid dynamics of tornadoes. *Annual review of fluid mechanics*, *45*, pp.59-84.

Rotunno, R. and Klemp, J.B., 1982. The influence of the shear-induced pressure gradient on thunderstorm motion. *Monthly Weather Review*, *110*(2), pp.136-151.

Rotunno, R. and Klemp, J., 1985. On the rotation and propagation of simulated supercell thunderstorms. *Journal of the Atmospheric Sciences*, *42*(3), pp.271-292.

Rotunno, R., Markowski, P.M. and Bryan, G.H., 2017. "Near ground" vertical vorticity in supercell thunderstorm models. *Journal of the Atmospheric Sciences*, *74*(6), pp.1757-1766.

Sadourny, R., 1975. The dynamics of finite-difference models of the shallow-water equations. *Journal of the Atmospheric Sciences*, *32*(4), pp.680-689.

Scheeler, M.W., Kleckner, D., Proment, D., Kindlmann, G.L. and Irvine, W.T., 2014. Helicity conservation by flow across scales in reconnecting vortex links and knots. *Proceedings of the National Academy of Sciences*, *111*(43), pp.15350-15355.

Scheeler, M.W., van Rees, W.M., Kedia, H., Kleckner, D. and Irvine, W.T., 2017. Complete measurement of helicity and its dynamics in vortex tubes. *Science*, *357*(6350), pp.487-491.

Schenkman, A.D., Xue, M. and Dawson II, D.T., 2016. The cause of internal outflow surges in a high-resolution simulation of the 8 May 2003 Oklahoma City tornadic supercell. *Journal of the Atmospheric Sciences*, *73*(1), pp.353-370.

Schueth, A. and C. C. Weiss, Comparing Observations and Simulations of the Streamwise Vorticity Current in a Tornadic Supercell Storm, *29th Conference on Severe Local Storms*, Stowe, VT, American Meteorological Society, 3B.6.

Skinner, P.S., Weiss, C.C., French, M.M., Bluestein, H.B., Markowski, P.M. and Richardson, Y.P., 2014. VORTEX2 observations of a low-level mesocyclone with multiple internal rear-flank downdraft momentum surges in the 18 May 2010 Dumas, Texas, supercell. *Monthly Weather Review*, *142*(8), pp.2935-2960.

Skinner, P.S., Weiss, C.C., Wicker, L.J., Potvin, C.K. and Dowell, D.C., 2015. Forcing mechanisms for an internal rear-flank downdraft momentum surge in the 18 May 2010 Dumas, Texas, supercell. *Monthly Weather Review*, *143*(11), pp.4305-4330.

Shabbott, C.J. and Markowski, P.M., 2006. Surface in situ observations within the outflow of forward-flank downdrafts of supercell thunderstorms. *Monthly weather review*, *134*(5), pp.1422-1441.

Shapiro, M.A., 1981. Frontogenesis and geostrophically forced secondary circulations in the vicinity of jet stream-frontal zone systems. *Journal of the Atmospheric Sciences*, *38*(5), pp.954-973.

Smith, AMO, 1947. The jet airplane utilizing boundary layer air for propulsion. *Journal of the Aeronautical Sciences*, *14*(2), pp.97-109.

Smith, F.T. and Duck, P.W., 1977. Separation of jets or thermal boundary layers from a wall. *The Quarterly Journal of Mechanics and Applied Mathematics*, *30*(2), pp.143-156.

Snook, N. and Xue, M., 2008. Effects of microphysical drop size distribution on tornadogenesis in supercell thunderstorms. *Geophysical Research Letters*, *35*(24).

Snow, J.T., 1984. The tornado. *Scientific American*, *250*(4), pp.86-105.

Sondergaard, R., Rivir, R.B. and Bons, J.P., 2002. Control of low-pressure turbine separation using vortex-generator jets. *Journal of propulsion and power*, *18*(4), pp.889-895.

Stout, G.E. and Huff, F.A., 1953. Radar records Illinois tornadogenesis. *Bulletin of the American Meteorological Society*, *34*(6), pp.281-284.

Straka, J.M., Rasmussen, E.N., Davies-Jones, R.P. and Markowski, P.M., 2007. An observational and idealized numerical examination of low-level counter-rotating vortices in the rear flank of supercells. *E-Journal of Severe Storms Meteorology*, *2*(8).

Sujudi, D. and Haimes, R., 1995. Identification of swirling flow in 3-D vector fields. In *12th Computational Fluid Dynamics Conference* (p. 1715).

Thompson, R.L. and Edwards, R., 2000. A comparison of Rapid Update Cycle 2 (RUC-2) model soundings with observed soundings in supercell environments. In *Preprints, 20th Conf. on Severe Local Storms, Orlando, FL, Amer. Meteor. Soc* (pp. 551-554).

Thompson, R.L., Edwards, R., Hart, J.A., Elmore, K.L. and Markowski, P., 2003. Close proximity soundings within supercell environments obtained from the Rapid Update Cycle. *Weather and Forecasting*, *18*(6), pp.1243-1261.

Thompson, R.L., Mead, C.M. and Edwards, R., 2007. Effective storm-relative helicity and bulk shear in supercell thunderstorm environments. *Weather and forecasting*, *22*(1), pp.102-115.

Thompson, R.L., Smith, B.T., Grams, J.S., Dean, A.R. and Broyles, C., 2012. Convective modes for significant severe thunderstorms in the contiguous United States. Part II: Supercell and QLCS tornado environments. *Weather and forecasting*, *27*(5), pp.1136-1154.

Trapp, R.J., 1999. Observations of nontornadic low-level mesocyclones and attendant tornadogenesis failure during VORTEX. *Monthly weather review*, *127*(7), pp.1693-1705.

Trapp, R.J. and Davies-Jones, R., 1997. Tornadogenesis with and without a dynamic pipe effect. *Journal of the atmospheric sciences*, *54*(1), pp.113-133.

Trapp, J. R. and Fiedler, B.H., 1995. Tornado-like vortexgenesis in a simplified numerical model. *Journal of the atmospheric sciences*, *52*(21), pp.3757-3778.

Trapp, R.J., Tessendorf, S.A., Godfrey, E.S. and Brooks, H.E., 2005. Tornadoes from squall lines and bow echoes. Part I: Climatological distribution. *Weather and forecasting*, *20*(1), pp.23-34.

Tripoli, G.J., 1992. A nonhydrostatic mesoscale model designed to simulate scale interaction. *Monthly Weather Review*, *120*(7), pp.1342-1359.

Tripoli, G.J. and Smith, E.A., 2014. Introducing Variable-Step Topography (VST) coordinates within dynamically constrained Nonhydrostatic Modeling System (NMS). Part 1: VST formulation within NMS host model framework. *Dynamics of Atmospheres and Oceans*, *66*, pp.28-57.

Uccellini, L.W. and Johnson, D.R., 1979. The coupling of upper and lower tropospheric jet streaks and implications for the development of severe convective storms. *Monthly Weather Review*, *107*(6), pp.682-703.

Viúdez, Á. and Haney, R.L., 1996. On the shear and curvature vorticity equations. *Journal of the atmospheric sciences*, *53*(22), pp.3384-3394.

Wakimoto, R.M. and Wilson, J.W., 1989. Non-supercell tornadoes. *Monthly Weather Review*, *117*(6), pp.1113-1140.

Wakimoto, R.M., Liu, C. and Cai, H., 1998. The Garden City, Kansas, storm during VORTEX 95. Part I: Overview of the storm's life cycle and mesocyclogenesis. *Monthly weather review*, *126*(2), pp.372-392.

Wakimoto, R.M. and Cai, H., 2000. Analysis of a nontornadic storm during VORTEX 95. *Monthly weather review*, *128*(3), pp.565-592.

Wakimoto, R.M. and Murphey, H.V., 2009. Analysis of a dryline during IHOP: Implications for convection initiation. *Monthly Weather Review*, *137*(3), pp.912-936.

Wang, B.C., Bergstrom, D.J., Yin, J. and Yee, E., 2006. Turbulence topologies predicted using large eddy simulations. *Journal of Turbulence*, (7), p.N34.

Ward, N.B., 1972. The exploration of certain features of tornado dynamics using a laboratory model. *Journal of the Atmospheric Sciences*, *29*(6), pp.1194-1204.

Weckwerth, T.M. and Parsons, D.B., 2006. A review of convection initiation and motivation for IHOP_2002. *Monthly weather review*, *134*(1), pp.5-22.

Weisman, M.L. and Klemp, J.B., 1982. The dependence of numerically simulated convective storms on vertical wind shear and buoyancy. *Monthly Weather Review*, *110*(6), pp.504-520.

Weisman, M.L. and Klemp, J.B., 1984. The structure and classification of numerically simulated convective stormsin directionally varying wind shears. *Monthly Weather Review*, *112*(12), pp.2479-2498.

Weisman, M.L. and Klemp, J.B., 1986. Characteristics of isolated convective storms. In *Mesoscale meteorology and forecasting* (pp. 331-358). American Meteorological Society, Boston, MA.

Weisman, M.L. and Rotunno, R., 2000. The use of vertical wind shear versus helicity in interpreting supercell dynamics. *Journal of the atmospheric sciences*, *57*(9), pp.1452-1472.

Weiss, C.C., Dowell, D.C., Schroeder, J.L., Skinner, P.S., Reinhart, A.E., Markowski, P.M. and Richardson, Y.P., 2015. A comparison of near-surface buoyancy and baroclinity across three VORTEX2 supercell intercepts. *Monthly Weather Review*, *143*(7), pp.2736-2753.

Wicker, L.J. and Wilhelmson, R.B., 1995. Simulation and analysis of tornado development and decay within a three-dimensional supercell thunderstorm. *Journal of the atmospheric sciences*, *52*(15), pp.2675-2703.

Wieler, J.G., 1986. Real-time automated detection of mesocyclones and tornadic vortex signatures. *Journal of Atmospheric and Oceanic Technology*, *3*(1), pp.98-113.

Wilhelmson, R.B. and Chen, C.S., 1982. A simulation of the development of successive cells along a cold outflow boundary. *Journal of the Atmospheric Sciences*, *39*(7), pp.1466-1483.

Wegener, A., 1928. Beitrage zur Mechanik der Tromben und Tornados. *Zeitschrift für Meteorologie*.

Wu, J.Z., Ma, H.Y. and Zhou, M.D., 2007. *Vorticity and vortex dynamics*. Springer Science & Business Media.

Wurman, J., Kosiba, K., Markowski, P., Richardson, Y., Dowell, D. and Robinson, P., 2010. Finescale single-and dual-Doppler analysis of tornado intensification, maintenance, and dissipation in the Orleans, Nebraska, supercell. *Monthly Weather Review*, *138*(12), pp.4439-4455.

Wurman, J., Dowell, D., Richardson, Y., Markowski, P., Rasmussen, E., Burgess, D., Wicker, L. and Bluestein, H.B., 2012. The second verification of the origins of rotation in tornadoes experiment: VORTEX2. *Bulletin of the American Meteorological Society*, *93*(8), pp.1147-1170.

Ziegler, C.L., Mansell, E.R., Straka, J.M., MacGorman, D.R. and Burgess, D.W., 2010. The impact of spatial variations of low-level stability on the life cycle of a simulated supercell storm. *Monthly Weather Review*, *138*(5), pp.1738-1766.

http://www.atmospheric-phenomena-ap.com/2017/04/weird-clouds-look-even-better-from.html URL accessed at 22.30 UTC on August 7 2019.

https://vortex.plymouth.edu/ URL accessed at 19.30 UTC on August 8, 2019.